
# RICH detector time alignment and studies of CP violation in the decay $B_s^0 \to \phi\phi$ at the LHCb experiment

*Nicholas A. Styles*

Thesis submitted for the degree of
Doctor of Philosophy

The University of Edinburgh

2009

*We shall not cease from exploration*
*And the end of all our exploring*
*Will be to arrive where we started*
*And to know the place for the first time.*

- T. S. Eliot, Four Quartets, 'Little Gidding'

# Declaration

The work contained in this thesis was carried out within LHCb collaboration, and as such represents the combined effort of myself and many others throughout the experiment. The composition of this thesis is entirely my own work.

(*Nicholas A. Styles*)

# Acknowledgements

I would like to thank a number of people in the Edinburgh Particle Physics Experiments group for their help throughout my PhD: My supervisor, Phil Clark, for general guidance and, along with Franz Muheim and Yuehong Xie, providing extensive B Physics experience, both in theoretical concepts and technical issues such as fitting. Thanks are also extended to Stephan Eisenhardt, for sharing his HPD knowledge, and Greig Cowan, for aiding me with various aspects of distributed computing.

During my time on long-term attachment at CERN, I was very grateful for help with the RICH hardware from Theirry Gys, Ken Wyllie and Johan Morant, and with the operation of the RICH detectors from Carmelo D'Ambrosio. Gloria Corti, Sajan Easo, Antonis Papanestis and Chris Jones provided valuable assistance with the LHCb software. Thanks to Tito Bellunato and Marco Adinolfi for coordinating the RICH test beams in which I participated, and to Mitesh Patel and Ulrich Kerzel who led the subsequent data analyses.

Thanks also to my parents, for their encouragement and support throughout my studies.

# Abstract

LHCb is a high-precision experiment dedicated to measuring the decays of B hadrons. Particle identification at LHCb relies upon two Ring Imaging Cherenkov (RICH) detectors, and this thesis describes work carried out relating to these detectors. It includes an analysis performed to investigate ion feedback in the Hybrid Photon Detectors (HPDs) used as photosensors for the RICH system, and studies of the performance of a RICH prototype in test beam conditions. A time alignment system for the RICH detectors has been designed and implemented, and this work is presented here. Excellent particle identification performance is required for efficient reconstruction of the $b \to s$ penguin decay $B_s^0 \to \phi\phi$, a channel in which visible New Physics effects are possible. An analysis of this decay has been performed, encompassing event selection at trigger and offline levels, resolution, tagging and acceptance studies, and toy monte carlo experiments on sensitivity and systematic errors in measuring the total weak phase. The results are discussed within.

# Contents

# List of Figures

# List of Tables

# Chapter 1

# Introduction

> *Not only is the universe stranger than we imagine, it is stranger than we can imagine.*
>
> - Sir Arthur Eddington

The nature of the Universe in which we find ourselves is still largely a mystery, despite centuries of enquiry by the best minds of countless generations. There have been many dramatic paradigm shifts in our understanding, from the Copernican revolution of the $16^{th}$ Century, through Newton and Maxwell to Einstein and Schrödinger, yet the questions that remain are still among the most fundamental we can possibly ask. Many of these questions have an impact on, or can possibly be answered by, the field of particle physics.

The high energy collisions at particle accelerator facilities are the closest recreation of conditions in the early Universe that we can produce. In combination with the macroscopic observations of astrophysics and cosmology, the microscopic measurements of particle physics give us our best clues about the possible origins, and eventual fate, of the Universe.

## 1.1 The Standard Model and Beyond

Our current understanding of particle physics is based around the Standard Model, which describes the particle content of the Universe and the forces through which the particles interact. It is a very successful model, and many theoretical predictions of the Standard Model have subsequently been confirmed experimentally. However, most particle physicists believe that the Standard Model is only a low-energy effective theory which will become ineffective at some higher energy scale, analogous to Newtonian dynamics which breaks down for velocities an appreciable fraction of the speed of light.

There are a number of reasons for believing this to be the case; amongst these is the vast difference in the energy scale of the gravitational and weak forces, known as the Hierarchy Problem [1]. Another concern is the observed baryon asymmetry in the Universe [2]; the fact that the amount of matter is overwhelmingly larger than the amount of antimatter. The Standard Model also fails to provide a satisfactory candidate for Dark Matter [3].

The Large Hadron Collider will operate at the highest centre-of-mass energy ever attained at a particle accelerator, and not only provides the best opportunity yet to complete the particle content of the Standard Model by allowing observation of the Higgs Boson, but also has the potential to see signs of New Physics effects beyond the Standard Model.

The general purpose LHC detectors, ATLAS and CMS, will be able to search directly for new particles within the energy reach of the LHC. A complementary approach is taken by the LHCb experiment, which is designed in order to make high-precision measurements of many Standard Model parameters. LHCb aims to study loop-level processes with a high degree of accuracy. In loop processes, the presence of New Physics particles - even if too massive to be produced on-shell at the LHC - can cause measurable deviations of parameters from their Standard Model predictions. The LHCb experiment is uniquely suited for this kind of indirect New Physics search at the LHC.

## 1.2 CP Violation and B Physics

The CPT theorem states that the laws of physics should be invariant under the combined inversion of charge, parity and time. For a state $\psi$, this can be expressed as

$$\mathcal{CPT}(\psi) \equiv \psi \tag{1.1}$$

While CPT invariance appears to be a fundamental symmetry of the universe, the C, P and T symmetries individually are not. Violation of the C and P symmetries were both discovered in the 1950s [4], and it was subsequently shown in the decays of neutral kaons [5] that symmetry under the combined inversion of C and P (equivalent to exchanging all particles in a process for anti-particles with opposite handedness and vice-versa) is also violated. This discovery prompted Andrei Sakharov to propose three conditions necessary to generate the baryon asymmetry of the Universe [6]:

- CP violation
- Baryon number violation
- Departure from thermal equilibrium

So far, CP violation is the only one of these conditions that a process for has been experimentally observed, although the level of CP violation in the Standard Model, the mechanism of which will be discussed later, is too small to account for the size of the observed baryon asymmetry [7].

The study of CP violation in kaons continued for many years, through experiments such as NA31 [8] and NA48 [9] at the CERN SPS accelerator, and KTeV [10] at Fermilab's Tevatron accelerator. In addition to kaons, CP violation also manifests itself in the decays of B mesons, the study of which is known as B physics. The BaBar [11] and BELLE [12] experiments both make use of asymmetric $e^+e^-$ colliders operating at the $\Upsilon(4S)$ resonance, the PEP-II and KEK accelerators respectively (collectively known as the B factories), which produced copious amounts of $B^0$ mesons over their lifetimes. The $\Upsilon(4S)$ resonance is just above the threshold for producing pairs of $B^0$ mesons at rest[1], and so measurements in the heavier $B_s^0$ sector were made by BELLE using data taken at the $\Upsilon(5S)$ resonance. Measurements of these decays were also made at the Tevatron, following an upgrade to a centre-of-mass energy of 1.96 TeV, by the CDF [13] and D0 [14] experiments (although these are both general purpose detectors rather than specific B physics experiments).

B physics has been a very active field in the last 10 years, and a large amount of valuable physics has been done. The B factories made the first measurements of direct [15][16] and interference [17][18] CP violation[2] in the B sector, and measured the $B^0$ width and mass difference; the Tevatron experiments measured the $B_s^0$ mixing parameters [19] and, amongst many other measurements, the branching ratio for the decay $B_s^0 \to \phi\phi$ [20].

The LHCb experiment will be able to make use of the extremely high luminosity for $b\bar{b}$ events available at the LHC ($1 \times 10^{12}$ events in 2 $fb^{-1}$, corresponding to a nominal year of data taking). In particular, the production rate of $B_s^0$ mesons is expected to be far greater than has been available to any previous experiment, making excellent measurements of the decays of this meson possible. The decay $B_s^0 \to \phi\phi$ is a sensitive probe for new CP violating effects beyond the Standard Model. Evidence of New Physics in this channel would be an ideal complementary result to other studies at LHCb, helping to give additional clues about the nature of these effects. With measurements like this, and many others, LHCb will extend the valuable work carried out by other experiments in the field of B physics, which could have wide ramifications for the study of particle physics as a whole.

[1] Hence the reason why asymmetric beam energies were used, in order to provide a sufficient Lorentz boost for accurate proper time determination.

[2] The precise meanings of these terms will be explained in section 2.3.

# Chapter 2

# Theory

## 2.1 The Standard Model

### 2.1.1 Particle Content

The fundamental particles in the Standard Model can be divided into two categories; fermions and bosons. Broadly speaking, fermions can be considered as matter particles, while bosons are force particles.

Fermions are spin $\frac{1}{2}$ particles and hence, as the name would imply, obey Fermi-Dirac statistics. Fermions can be further subdivided into quarks and leptons. Quarks are confined within bound states known as hadrons, of which there are two known configurations; mesons, which consist of a quark-antiquark pair ($q\bar{q}$), and baryons which are bound states of three quarks or antiquarks (qqq or $\bar{q}\bar{q}\bar{q}$). As a consequence, we can assign a quantum number known as Baryon Number, giving each quark a baryon number of $\frac{1}{3}$ (and $-\frac{1}{3}$ for each anti-quark), in order that baryonic states have a baryon number of 1 (or -1 for antibaryons), while mesonic states have a baryon number of 0.

In the Standard Model, there are three generations of quarks. There is no a priori reason why the Standard Model should have three generations, in principle more generations are possible. The fact that there are only three generations is an experimental result, based on results from the LEP experiments. Each generation is a doublet comprised of one 'up type' quark with a charge of $+\frac{2}{3}$ and one 'down type' quark with a charge of $-\frac{1}{3}$. This results in 6 discrete quark flavours[1], with the corresponding antiquarks possessing the appropriate anti-flavours.

$$\begin{pmatrix} u \\ d \end{pmatrix} \begin{pmatrix} c \\ s \end{pmatrix} \begin{pmatrix} t \\ b \end{pmatrix} \tag{2.1}$$

[1] Named *up*, *down*, *charm*, *strange*, *top* (or *truth*) and *bottom* (or *beauty*).

There are also three lepton generations. Again, the number of generations is restricted to three only by experimental observations, and there is no theoretical reason in the Standard Model why the number of lepton generations should be the same as the number of quark generations. The fact that there does seem to be the same number of quark and lepton generations could be seen as evidence of underlying physics yet to be discovered.

$$\begin{pmatrix} e \\ \nu_e \end{pmatrix} \begin{pmatrix} \mu \\ \nu_\mu \end{pmatrix} \begin{pmatrix} \tau \\ \nu_\tau \end{pmatrix} \tag{2.2}$$

Each lepton generation contains one charged lepton and one uncharged lepton, called a neutrino. The equivalent of baryon number in the lepton sector is simply called the Lepton Number, and each lepton is assigned a lepton number of 1 (-1 for antileptons), which reflects the fact that unlike quarks, leptons can exist in isolation and are not necessarily confined within bound states.

Bosons are particles with integer spin, obeying Bose-Einstein statistics. As was mentioned, bosons act as force carriers for the fundamental interactions of the Standard Model, so it is sensible to discuss them within the context of the forces with which they are associated.

### 2.1.2 The Strong Interaction

The Strong Interaction is the force which binds quarks within hadrons. The underlying theory behind the strong interaction is Quantum Chromodynamics, or QCD, which acts only on objects with color. The color quantum number explains the existence of states such as the $\Delta^{++}$ baryon. The $\Delta^{++}$ is a bound state of 3 spin-up $u$ quarks, a configuration thought to be forbidden due to the identical quantum numbers of the constituent particles, which would be in violation of Fermi-Dirac statistics. This can be resolved by assigning an additional quantum number to each quark [21], and this is the color. Quark color can take one of three values (rgb), with corresponding anticolors for antiquarks ($\bar{\text{r}}\bar{\text{g}}\bar{\text{b}}$), with the property that a bound state of all three color states (baryons), or any color and its anticolor (mesons), has no overall color. This allows mesons and baryons to be color-neutral objects.

The color structure of Standard Model can be described by the $SU(3)$ gauge group. The properties of this group give rise to 8 gauge bosons, called gluons, which mediate the strong interaction. Gluons exist as color-anticolor states, of which there would seem to be 9 possibilities. However, the strong force does not act on color symmetric objects and three of the color-anticolor states ($\text{r}\bar{\text{r}}$, $\text{b}\bar{\text{b}}$ and $\text{g}\bar{\text{g}}$) are color-symmetric combinations. Since these states cannot interact, they are not physically realisable and hence the two final gluons are the two non-color-symmetric linear combinations of these states [22]. Since gluons are colored, they can self-interact; a consequence of the non-abelian nature of the SU(3) group.

An important property of QCD is asymptotic freedom. The value of the running coupling constant for the strong force, $\alpha_s$, is high at low energies and decreases at higher energies. This has the consequence that quarks behave as free particles (at least

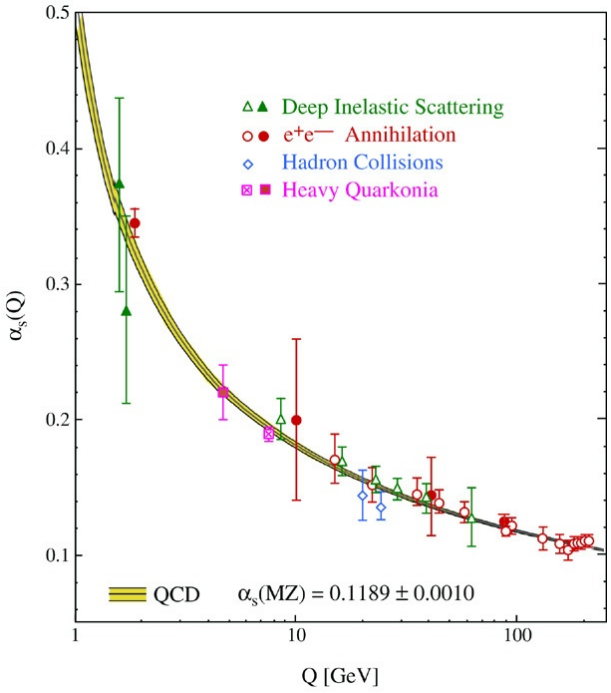


**Figure 2.1:** The running of the strong coupling constant $\alpha_s$ [23].

in terms of the strong interaction) at short distances, but the strength of the strong interaction increases at larger distances, resulting in the confinement of quarks within hadronic bound states [24][25].

### 2.1.3 The Electroweak Interaction

Particles with non-zero electric charge interact via the Electromagnetic force. The existence of this force has long been known, due to its effects being easily visible at a macroscopic level. The gauge boson associated with the electromagnetic interaction is the photon, usually represented as $\gamma$. Since the photon does not carry electric charge, they do not interact with each other. Consequently, Quantum Electrodynamics (QED), the $U(1)$ theory describing electromagnetic interactions does not have to be concerned with self-coupling between its gauge bosons, in contrast to QCD.

The final force which is described by the Standard Model is the Weak interaction. A unique feature of the weak interaction is that it operates solely on left-handed particles. The handedness of a particle refers to its helicity state, which describes the spin of a particle relative to the direction of its momentum, with the possible states called left-

handed and right-handed (or 0 if the particle is spinless):

$$\psi_L = \frac{(1-\gamma^5)}{2}\psi \;\&\; \psi_R = \frac{(1+\gamma^5)}{2}\psi \tag{2.3}$$

where $\psi_L$ and $\psi_R$ are the left and right handed components respectively, and $\gamma^5$ is the product of the four Dirac matrices $\{\gamma^0, \gamma^1, \gamma^2, \gamma^3\}$. The application of the parity operator, $\mathcal{P}$, inverts the helicity of a particle since linear momentum is parity-odd while spin is parity-even, and since the weak interaction only acts on one helicity state it is explicitly parity violating. This is consequence of the $V-A$ (Vector minus Axial) form of the interaction; the Lagrangian contains terms of the form $(1-\gamma^5)$, which projects out the left-handed component of a state [26].

Although the electromagnetic and weak interactions manifest themselves as ostensibly separate forces, at least in the low-energy regime, they are in fact both facets of a unified Electroweak interaction. This unified interaction is described by the $SU(2)_L \times U(1)_Y$ gauge group. The $L$ denotes the fact we are considering only left-handed particles, while the $Y$ denotes the $U(1)$ Weak Hypercharge group, which is not the same as the $U(1)$ group of QED. Weak hypercharge is defined as:

$$Q = T_3 + \frac{Y}{2} \tag{2.4}$$

where $Q$ is the conventional (QED) charge. The $SU(2)_L$ gauge group provides us with three gauge bosons, $W_\mu^{1,2,3}$, while the $U(1)_Y$ gauge group provides one, $B_\mu$. Two of these gauge bosons, $W_\mu^1$ and $W_\mu^2$ give us the physical $W^+$ and $W^-$ bosons. Linear combinations of the remaining gauge bosons give us the physical $Z$ boson and photon (here denoted $A_\mu$)

$$Z_\mu = cos\theta_w W_\mu^3 - sin\theta_w B_\mu \tag{2.5}$$

$$A_\mu = cos\theta_w B_\mu + sin\theta_w W_\mu^3 \tag{2.6}$$

where $\theta_w$ is the Weak Mixing Angle. It is defined such that

$$tan\theta_w = \frac{g}{g'} \tag{2.7}$$

$$gsin\theta_w = g'cos\theta_w = e \tag{2.8}$$

where $g$ and $g'$ denote the coupling of the $SU(2)_L$ and $U(1)_Y$ fields respectively, and $e$ is the electron charge [27].

Processes mediated by the $W^{+/-}$ are known as Charged Current (CC) processes, whereas those mediated by the $Z^0$ are Neutral Current (NC) processes. The weak gauge bosons couple to particles with a quantum number known as Weak Isospin, $T$, which within the Standard Model are the quarks and leptons. These weakly interacting particles appear in doublets with $T = \frac{1}{2}$ , with one particle having $T_3$, the third com-

ponent of weak isospin, equal to $+\frac{1}{2}$ and the other having $T_3 = -\frac{1}{2}$. For the quarks, up-type quarks have $T_3 = +\frac{1}{2}$ , while down-type quarks have $T_3 = -\frac{1}{2}$. Similarly, the charged lepton and neutrino have $T_3 = -\frac{1}{2}$ and $T_3 = \frac{1}{2}$ respectively. The $W^+$ and $W^-$ bosons have $T = 1$, with $T_3 = +1$ and $T_3 = -1$ respectively, and consequently there are self-couplings between the weak gauge bosons. The $Z^0$ has $T = T_3 = 0$, and in contrast with the W bosons, can couple to both left-handed and right-handed states, due to its component from the $U(1)_Y$ gauge boson.

### 2.1.4 Spontaneous Symmetry Breaking and the Higgs Mechanism

Unbroken gauge symmetries must result in massless gauge bosons, such as the photon and the gluons, since mass terms are not invariant under gauge transformation. An unbroken $SU(2)_L \times U(1)_Y$ gauge symmetry would result in four massless gauge bosons. However, this is not what is observed experimentally; the photon is massless, but the W and Z bosons have large masses [28]. Consequently, the electroweak symmetry must be broken in order to accommodate these massive bosons. Breaking the symmetry explicitly by simply adding mass terms also means that the electroweak theory is no longer renormalizable. Renormalization is a procedure that allows divergences in quantum field theories to be dealt with by moving the divergent behaviour into renormalization factors that link the measurable quantities to the bare quantities intrinsic to the theory; the divergences are in a sense 'hidden'. Non-renormalizable quantum field theories lose their predictive power because these divergences become manifest.

Spontaneous, or hidden, symmetry breaking allows the symmetry to be broken without sacrificing the renormalizability of the theory. By introducing a scalar field, with a potential that has a degenerate ground state, the Lagrangian remains symmetric, but the symmetry of the theory is broken by choosing one of the degenerate ground states as the true ground. This requirement can be satisfied by a 'mexican hat' potential (figure 2.2), of the form

$$V(\phi) = \mu^2 |\phi|^2 + \lambda^2 |\phi|^4 \tag{2.9}$$

with $\lambda > 0$, ensuring that the potential has a minimum, and $\mu^2 < 0$ moving the minimum away from $|\phi| = 0$. Spontaneously broken global symmetries result in the appearance of massless Goldstone bosons as a consequence of their degenerate ground states. The Goldstone bosons can be thought of as excitations in the symmetric direction of the field, and it is these excitations that allow the W and Z bosons to become massive. Massless gauge bosons have two degrees of freedom, while massive spin 1 gauge bosons have three degrees of freedom; for spontaneously broken local symmetries, the excitations that would otherwise form the Goldstone bosons can, through gauge transformations, be made to disappear, being 'eaten' and reappearing as the extra degree of freedom required for the gauge bosons to become massive. This is the Higgs Mechanism [29].

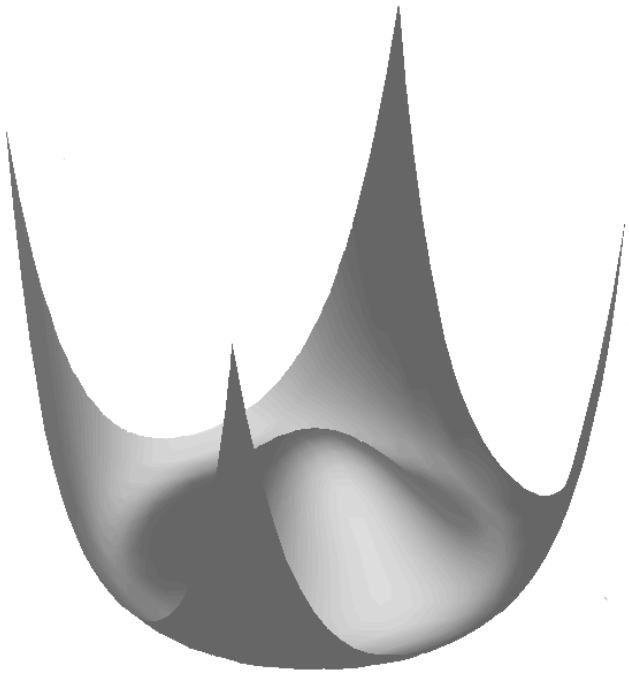

**Figure 2.2:** A 2D 'Mexican Hat' potential, of the form required for spontaneous symmetry breaking to occur.

Additionally, the Higgs Mechanism results in the existence of a massive scalar boson, the Higgs Boson. The Higgs boson is the only remaining particle in the Standard Model whose existence has not been verified experimentally. The discovery of the Higgs boson is one of the primary physics goals of the general purpose LHC experiments, ATLAS and CMS.

## 2.2 Flavour Physics

As described is section 2.1.3, the quarks can be grouped into doublets under the weak interaction; these are the doublets shown in section 2.1.1 for quark generations, and so quark flavours are eigenstates of the weak interaction. However, the physical quark mass eigenstates are not the same as the quark flavours. We can relate the quark mass eigenstates, $q'$, to the flavours, $q$, via a rotation in flavour space [30]. This was first expressed by Cabibbo for the $u$, $d$ and $s$ quarks, using a single angle $\theta_c$, called the Cabibbo angle:

$$\begin{pmatrix} u \\ d' \end{pmatrix} = \begin{pmatrix} u \\ d\ cos\theta_c + s\ sin\theta_c \end{pmatrix} \tag{2.10}$$

The Cabibbo hypothesis was proposed to explain the differences in amplitude between strangeness-changing and strangeness-conserving processes. As a consequence of this quark flavour mixing, flavour-changing processes can occur via the weak interaction.

### 2.2.1 The GIM Mechanism

Flavour-changing processes mediated by the $Z^0$ boson (Flavour-Changing Neutral Current) do not occur at tree level in the Standard Model. The absence of FCNC processes was problematic for a 3 quark model with Cabibbo rotations. The form of the NC in this model is

$$\begin{aligned} J^0 &\sim g(u\overline{u} - d'\overline{d'}) \\ &= g[u\overline{u} - d\overline{d}\ cos^2\theta_c - s\overline{s}\ sin^2\theta_c - (\overline{d}s + \overline{s}d)cos\theta_c sin\theta_c] \end{aligned}$$

which has a non-zero flavour-changing component, in conflict with experimental observations. However, by adding a fourth quark flavour, the $c$ quark, of up-type a second doublet can be formed.

$$\begin{pmatrix} c \\ s' \end{pmatrix} = \begin{pmatrix} s \\ -d\ sin\theta_c + s\ cos\theta_c \end{pmatrix} \tag{2.11}$$

The form of the NC now becomes

$$\begin{aligned} J^0 &\sim g(u\overline{u} + c\overline{c} - d'\overline{d'} - s'\overline{s'}) \\ &= g[u\overline{u} + c\overline{c} - d\overline{d} - s\overline{s}] \end{aligned}$$

where the flavour-changing terms cancel, leaving the NC processes flavour symmetric [31]. This is known as the GIM (Glashow, Iliopoulos and Maiani) mechanism, which predicted the existence of the $c$ quark. While FCNC processes are forbidden at tree level, they can proceed through higher-order diagrams such as the box diagram show in figure 2.3. For these higher-order processes to have non-zero amplitudes in

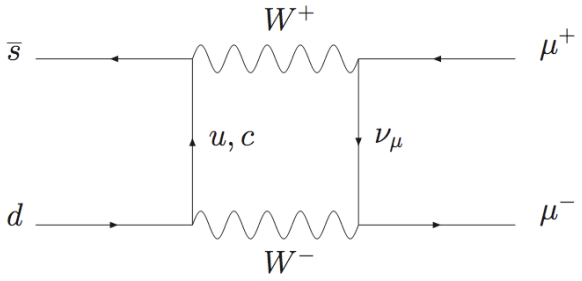


**Figure 2.3:** Box Diagram for the flavour-changing neutral current process $K^0 \rightarrow \mu^+\mu^-$.

this 2 generation model, the $u$ and $c$ quark masses must be non-degenerate, in order that the two contributions do not cancel. Consequently, the GIM mechanism allowed a prediction for the $c$ quark mass to be made, based on the observed branching ratio for $K^0 \rightarrow \mu^+\mu^-$ [32].

### 2.2.2 The CKM Matrix

The extension of this formalism to three generations and 6 quarks flavours is known as the CKM (Cabibbo, Kobayashi and Maskawa) matrix [33]:

$$\begin{pmatrix} d' \\ s' \\ b' \end{pmatrix} = V^{CKM} \begin{pmatrix} d \\ s \\ b \end{pmatrix} \tag{2.12}$$

Where

$$V^{CKM} = \begin{pmatrix} V_{ud} & V_{us} & V_{ub} \\ V_{cd} & V_{cs} & V_{cb} \\ V_{td} & V_{ts} & V_{tb} \end{pmatrix} \tag{2.13}$$

For a process $q_1 \rightarrow q_2$, where $q_1$ and $q_2$ represent two different quark flavours, the probability of this process occurring is related to the CKM matrix element $V_{q_1 q_2}$ .

$$P\left(q_1 \rightarrow q_2\right) \propto \left|V_{q_1 q_2}\right|^2 \tag{2.14}$$

#### The Wolfenstein Parameterisation

The nine CKM matrix elements are not independent, and the form of the CKM matrix shown in equation 2.13 is not its most useful form. The nine elements can in fact all be expressed in terms of 4 parameters. The original Kobayashi and Maskawa parameterisation was in terms of three angles ($\theta_1$, $\theta_2$ and $\theta_3$) and one complex phase ($\delta$). Another popular parameterisation is that of Wolfenstein [34], which uses the parameters $\lambda$, $A$, $\rho$ and $\eta$, and if expressed to third order in $\lambda$ is shown here:

$$\begin{pmatrix} 1-\frac{\lambda^2}{2} & \lambda & A\lambda^3(\rho - i\eta) \\ -\lambda & 1-\frac{\lambda^2}{2} & A\lambda^2 \\ A\lambda^3(1-\rho-i\eta) & -A\lambda^2 & 1 \end{pmatrix} \tag{2.15}$$

#### The Unitarity Triangles

The CKM matrix is a unitary matrix, meaning that $V^\dagger V$ is equal to the identity, $I$. Unitary matrices conserve the length of complex vectors, thus the unitarity condition ensures that the summed quark transition probabilities do not exceed 1. It also implies

$$\sum_i V_{ij}^* V_{ik} = \delta_{jk} \tag{2.16}$$

$$\sum_j V_{ij}^* V_{kj} = \delta_{ik} \tag{2.17}$$

where the subscripts represent quark flavours, which leads to 6 expressions of the form

$$V_{ki}V_{kj}^* + V_{li}V_{lj}^* + V_{mi}V_{mj}^* = 0 \tag{2.18}$$

for $i \neq j$. These expressions can be plotted as triangles in the complex plane, with each term representing a side. While there are in total six possible triangles, only two of these have all three sides of approximately equal length, and these are the two triangles shown in figure 2.4.

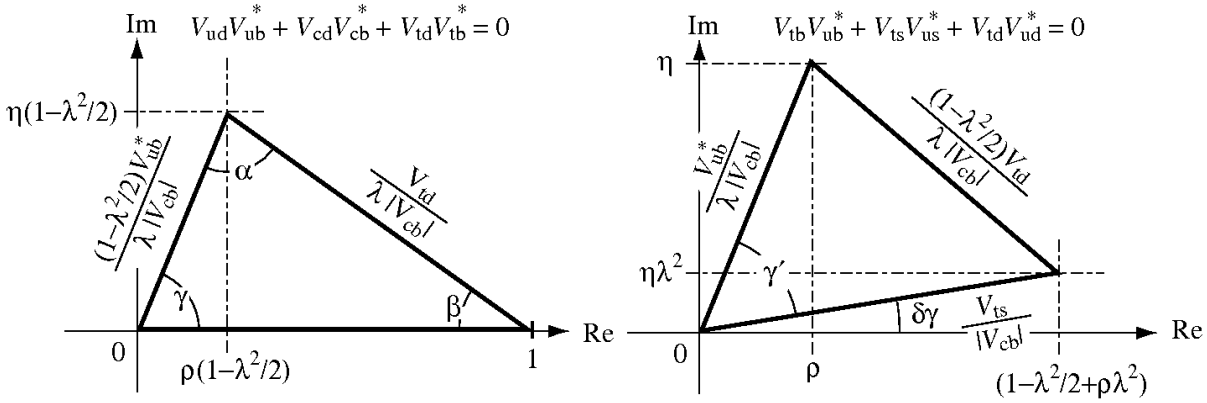


**Figure 2.4:** The 'non-squashed' Unitarity Triangles [35].

The Unitarity Triangle usually refers to the triangle describing the unitarity condition

$$V_{ud}V_{ub}^* + V_{cd}V_{cb}^* + V_{td}V_{tb}^* = 0 \tag{2.19}$$

The three angles of the Unitarity Triangle, $\alpha$, $\beta$ and $\gamma$, offer a test of the Standard Model flavour structure; an unclosed Unitarity Triangle would be a signal of flavour physics beyond the Standard Model. Constraints on these angles can be extracted from measurements of many processes, and combined fits based on current best measurements of Standard Model parameters have been performed by both the CKM fitter [36] and UTfit [37] groups. Figure 2.5 shows a combined fit from the CKM fitter group. Some of the main Unitarity Triangle constraints are:

- $\sin 2\beta = 0.672 \pm 0.023$ from $B^0 \to J/\psi K^0$ [38]
- $\alpha = 90.6^{+3.8}_{-4.2}$ deg. from $B^0 \to \pi\pi, \rho\rho, \rho\pi$ [36]
- $\gamma = 76^{+12}_{-13} \pm 4 \pm 9$ deg. from $B \to D^{(*)}K$ [38]
- $\epsilon_K = 2.23 \pm 0.01 \times 10^{-3}$ from $K^0 - \overline{K}^0$ mixing [28]
- $|V_{ub}| = 0.0042 \pm 0.0003$ from $B \to X_u \ell^- \overline{\nu}_\ell$ [38]
- $\Delta m_{d(s)} = 0.507 \pm 0.005$ $(17.77 \pm 0.10 \pm 0.07)$ ps$^{-1}$ from $B^0_{(s)} - \overline{B}^0_{(s)}$ mixing [28]

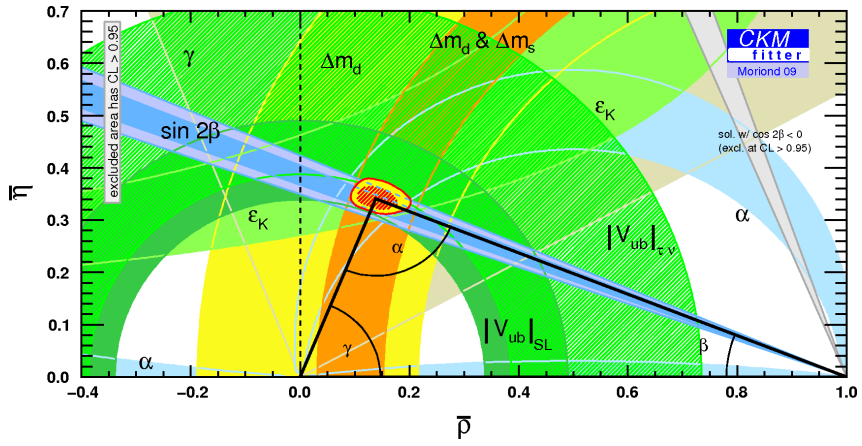


**Figure 2.5:** Current constraints on the Unitarity Triangle, compiled by the CKMfitter group [36].

## 2.3 CP Violation

CP violation corresponds physically to differences between processes and their CP conjugate processes. Since CP conjugate states are related via hermitian conjugation, the presence of complex couplings in the Hamiltonian will break invariance under the CP transformation. The complex phase present in the CKM matrix parameterisations is an example of this.

When applying the Quantum Mechanical $\mathcal{CP}$ operator to a transition $i \to f$, a phase can be introduced:

$$\mathcal{CP}\langle f|T|i\rangle = e^{i\phi}\langle \overline{f}|\overline{T}|\overline{i}\rangle \tag{2.20}$$

where $T$ represents a transition matrix. However, physical observables are determined by the product of two quantum mechanical transition amplitudes, and so any one individual phase of these amplitudes is arbitrary and has no physical meaning. Only phase differences have physical consequences, and so CP Violation can only be observed in processes that have multiple coherent contributions with different phases. The phases appearing in the transition amplitudes can either be CP-odd (if they change sign under CP transformations) or CP-even (if they are invariant under CP transformations), with the two types referred to as 'Weak' and 'Strong' phases respectively.

Naïvely, only the weak phases which change sign under CP conjugation might be expected to be important to CP violation, but strong phase differences are often also necessary in order for CP violation to be non-zero. For example, if the transition $i \to f$ is a superposition of two amplitudes $A_1$ and $A_2$ (whose moduli are invariant under CP) with weak phases $\phi_1$ and $\phi_2$ and strong phases $\delta_1$ and $\delta_2$ respectively

$$|\langle f|T|i\rangle|^2 - |\langle \overline{f}|T|\overline{i}\rangle|^2 = -4A_1A_2\sin(\delta_1-\delta_2)\sin(\phi_1-\phi_2) \tag{2.21}$$

and so CP violation will only be observed if there is both a weak and a strong phase difference.

CP violation without strong phase differences requires transitions to two different final states $i \to f$ and $i \to g$, where the CP violating parameter of interest has the form

$$\langle f|T|i\rangle\langle g|T|\bar{i}\rangle - \langle g|T|i\rangle\langle f|T|\bar{i}\rangle = 2iA_fA_ge^{i(\delta_f+\delta_g)}\sin(\phi_f - \phi_g) \tag{2.22}$$

and the $f$ and $g$ subscripts denote which transition the relevant amplitudes and phases are associated with. In this case, a strong phase difference is not required and only the weak phase difference is important.

In equation 2.22 it has been assumed that $f$ and $g$ are CP eigenstates ($f = \overline{f}$ and $g = \overline{g}$) with the same CP-parity. An example of this type of scenario is the decay of $K^0$ to the final states $\pi^+\pi^-$ and $\pi^0\pi^0$, which are CP eigenstates with CP=+1.

### 2.3.1 CP Violation in Neutral Meson Decays

CP violation in neutral meson decays can be manifested in a process in a number of ways; it is generally classified as one of three types:

- Direct CP violation, or CP violation in Decay
- Indirect CP violation, or CP violation in Mixing
- CP violation from the Interference of Mixing and Decay

These three categories of CP violation are not mutually exclusive, and can all contribute to the overall CP violation observed in a single process. However, it is often useful to consider processes for which a single type of CP violation is dominant, in order to investigate the CP structure of the CKM matrix.

### 2.3.2 Direct CP Violation

Direct CP violation reflects the situation when a process and its CP conjugate do not have the same amplitude. That is to say, if the decay of a $B^0$ meson to a final state $f$ has the amplitude $A_f$, direct CP violation occurs in the following case:

$$|A_f| \neq |\overline{A}_{\overline{f}}| \tag{2.23}$$

This is also called CP violation in decay, as it is manifested in the decay amplitudes. In order for this situation to arise, both weak and strong phase differences are required from at least two interfering amplitudes, as shown in equation 2.21. Unlike the other categories of CP violation, direct CP violation is not exclusive to neutral meson decays, it can also occur in the decays of charged hadrons. As an example, Direct CP violation

can be seen in the decay $B^- \to K^-\rho^0$. The CP asymmetry in this mode can be defined as follows:

$$\mathcal{A}_{\rho^0 K^\mp} = \frac{\Gamma(B^+ \to K^+\rho^0) - \Gamma(B^- \to K^-\rho^0)}{\Gamma(B^+ \to K^+\rho^0) + \Gamma(B^- \to K^-\rho^0)} \tag{2.24}$$

The value of which has been measured to be $\mathcal{A}_{\rho^0 K^\mp} = 0.31^{+0.11}_{-0.10}$ [39][40].

### 2.3.3 B Mixing and Indirect CP Violation

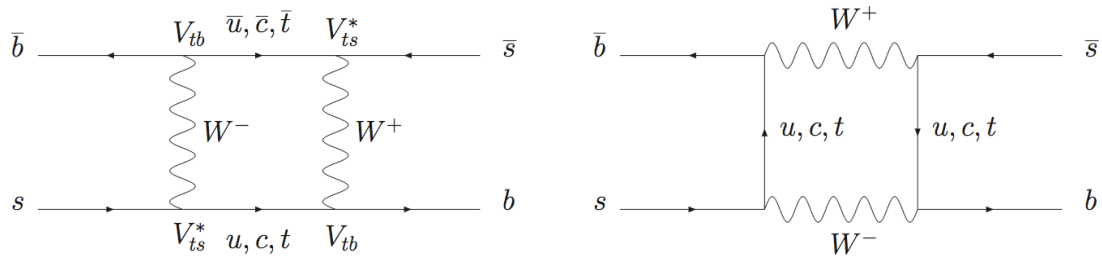


**Figure 2.6:** Two possible diagrams for $B_s^0 - \overline{B_s^0}$ mixing.

Neutral B mesons[2] (such as $B^0$, a $\bar{b}d$ bound state or $B_s^0$, a $\bar{b}s$ bound state) can oscillate between particle and antiparticle states via flavour-changing neutral processes of the kind shown in figure 2.6. The phenomenon of neutral meson mixing is closely related to CP violation. B mixing can be described by a Hamiltonian of the form

$$H \begin{pmatrix} B \\ \overline{B} \end{pmatrix} = \begin{pmatrix} M - \frac{i}{2}\Gamma & M_{12} - \frac{i}{2}\Gamma_{12} \\ M_{12}^* - \frac{i}{2}\Gamma_{12}^* & M - \frac{i}{2}\Gamma \end{pmatrix} \begin{pmatrix} B \\ \overline{B} \end{pmatrix} \tag{2.25}$$

where $M$ and $\Gamma$ are the mass and decay width of the flavour eigenstates, $M_{12}$ relates to virtual $B\overline{B}$ transitions, and $\Gamma_{12}$ comes from physical decays common to both $B$ and $\overline{B}$.

The mass eigenstates for neutral B mesons are

$$|B_L\rangle = p|B\rangle + q|\overline{B}\rangle \tag{2.26}$$

$$|B_H\rangle = p|B\rangle - q|\overline{B}\rangle \tag{2.27}$$

where the L and H subscript denote the 'light' and 'heavy' eigenstates with masses $M - \frac{1}{2}\Delta M$ and $M + \frac{1}{2}\Delta M$ respectively, where

$$\Delta M = 2Re\sqrt{(M_{12} - \frac{\Gamma_{12}}{2})(M_{12}^* - \frac{\Gamma_{12}^*}{2})} \tag{2.28}$$

[2]This section will only deal with the mixing of neutral B mesons, but the mixing of neutral kaons and charmed mesons uses the same theoretical framework.

Similarly, the lifetime difference $\Delta\Gamma = \Gamma_H - \Gamma_L$ for the eigenstates is given by

$$\Delta\Gamma = -4Im\sqrt{(M_{12} - \frac{\Gamma_{12}}{2})(M_{12}^* - \frac{\Gamma_{12}^*}{2})} \tag{2.29}$$

although for $B^0$ mesons, this difference is usually neglected as it is small.

The evolution of a physical neutral B meson state can be described by the equations

$$|B(t)\rangle = g_+(t)|B\rangle + \frac{q}{p}g_-(t)|\overline{B}\rangle \tag{2.30}$$

$$|\overline{B}(t)\rangle = g_+(t)|\overline{B}\rangle + \frac{p}{q}g_-(t)|B\rangle \tag{2.31}$$

Where the paramters $g_\pm$ represent the time-dependent probabilities of the state remaining unchanged (+) or oscillating into its charge conjugate state (-), and are defined as follows:

$$|g_\pm|^2 = \frac{e^{-\Gamma t}}{2}\left[cosh\left(\frac{\Delta\Gamma}{2}t\right) \pm cos\left(\Delta M t\right)\right] \tag{2.32}$$

The dimensionless parameters

$$x = \frac{\Delta M}{\Gamma} \tag{2.33}$$

$$y = \frac{\Delta\Gamma}{2\Gamma} \tag{2.34}$$

can be defined, and are useful for characterising the mixing of neutral mesons. Figure 2.7 shows the effect of varying $x$ and $y$, and demonstrate qualitatively the difference between the mixing of $B^0$ and $B_s^0$ mesons.

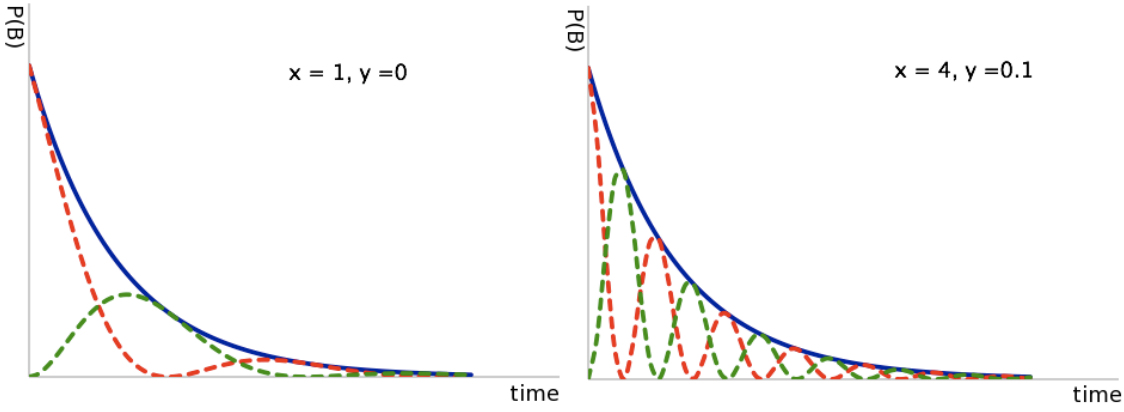


**Figure 2.7:** Lifetime distributions for a neutral $B$ meson. The red and green lines represent the probability of the state being a $B$ or $\overline{B}$ at a given time. The plot on the left shows a distribution like that of $B^0$ mesons, and the right shows the effect of changing the parameters $x$ and $y$. For $B_s^0$ mesons, $x \sim 30$.

We can also define the mixing parameter $\chi$, which is the time integrated probability

that an initial $B/\overline{B}$ state decays as its charge conjugate state, and is given by

$$\chi = \frac{|q/p|^2\chi_0}{1-\chi_0+|q/p|^2\chi_0},\ \chi_0 = \frac{x^2+y^2}{2(1+x^2)} \tag{2.35}$$

For $B^0$ mesons, the current best value is $\chi_d = 0.1878 \pm 0.0024$ [28], and for the mass difference $\Delta M_d = 0.507 \pm 0.005$ ps$^{-1}$. For $B_s^0$ mesons, the current best value of the mixing parameter is $\chi_s = 0.49927 \pm 0.00003$ and the mass difference is $\Delta M_s = 17.77 \pm 0.10 \pm 0.07$ ps$^{-1}$.

The coefficients $p$ and $q$, introduced in equations 2.26 and 2.27, denoting the relative proportions of $B$ and $\overline{B}$ states making up the mass eigenstates, play a fundamental role in Indirect CP violation. For the case where $p = q = \frac{1}{\sqrt{2}}$, the physical mass eigenstates are also CP eigenstates. If $p$ and $q$ are not equal, then this is no longer the case, and CP violation can occur. We have seen in equation 2.20 that any CP transformation will have an arbitrary phase associated, and any quantum mechanical state can be rephased at will, so any physical observable must be invariant under these rephasings. The magnitude of the ratio of the coefficients fulfills this criteria, and so is a good observable. Therefore, in order for Indirect CP violation to occur, we have the following condition:

$$\left|\frac{p}{q}\right| \neq 1 \tag{2.36}$$

This parameter can be measured in flavour-specific decays such as $B^0 \to D^{\mp}\mu^{\pm}\nu_\mu$, by measuring the rate of 'wrong-sign' decays, giving the semileptonic asymmetry $\mathcal{A}_{sl}$:

$$\mathcal{A}_{sl}(t) = \frac{d\Gamma/dt(\overline{B}^0 \to D^-\mu^+\nu_\mu) - d\Gamma/dt(B^0 \to D^+\mu^-\overline{\nu}_\mu)}{d\Gamma/dt(\overline{B}^0 \to D^-\mu^+\nu_\mu) + d\Gamma/dt(B^0 \to D^+\mu^-\overline{\nu}_\mu)} \tag{2.37}$$

### 2.3.4 CP Violation from Interference

CP violation can still occur in a process, even if there is no CP violation in mixing or decay individually, due to interference between their phases. To demonstrate this, it is useful to consider the complex parameter $\lambda_f$, defined as [41]

$$\lambda_f \equiv \frac{q}{p}\frac{\overline{A}_f}{A_f} \tag{2.38}$$

This parameter is invariant under arbitrary rephasings of the initial and final states, and so is a potential observable in neutral-meson decays. The condition for CP violation can be expressed as

$$\lambda_f \neq \frac{1}{\lambda_{\overline{f}}} \tag{2.39}$$

In the absence of any phases, this condition will be fulfilled if CP is conserved in mixing and decay. However, when phases are included, CP violation will occur if

$$arg\ \lambda_f + arg\ \lambda_{\overline{f}} \neq 0 \tag{2.40}$$

This can be observed in channels where the same final state is accessible to both $B$ and $\overline{B}$, so that the asymmetry between decays with $(B \to \overline{B} \to f)$ and without $(B \to f)$ mixing can be measured. Decays to final states which are CP eigenstates, i.e. $f = \overline{f}$, fulfill this criteria; in this case, the condition for CP violation from interference simplifies to

$$arg\ \lambda_f \neq 0 \tag{2.41}$$

$B_s^0 \to \phi\phi$, which will be discussed in detail in chapters 6 and 7, is an example of this. The time-dependent CP asymmetry $\mathcal{A}_{f(CP)}$ can be constructed to quantify effects in this type of decay:

$$\mathcal{A}_{f(CP)}(t) = \frac{d\Gamma/dt(\overline{B}_s^0 \to \phi\phi) - d\Gamma/dt(B_s^0 \to \phi\phi)}{d\Gamma/dt(\overline{B}_s^0 \to \phi\phi) + d\Gamma/dt(B_s^0 \to \phi\phi)} \tag{2.42}$$

In decays of $B^0$ mesons, where the approximations $\Delta\Gamma = 0$ and $|q/p| = 1$ can be made, this time-dependent asymmetry is often expressed in the form

$$\mathcal{A}_{f(CP)}(t) = S\sin(\Delta m t) - C\cos(\Delta m t) \tag{2.43}$$

with the $S$ and $C$ terms describing the contributions from interference and direct CP violation respectively.

## 2.4 Beyond the Standard Model

As discussed in chapter 1, there is an increasing body of evidence suggesting that the Standard Model is only a special case of some more general theory; the Hierarchy Problem, the mechanism of baryogenesis, and the lack of a dark matter candidate have already been mentioned. Other phenomena left unexplained by the standard model are [42]:

- The Strong CP Problem. Given that CP violation is present in the electroweak interactions of quarks, it may also be expected that strong interactions will display CP asymmetry. However, this has been ruled out to a very high precision. This is problematic because there are terms in the Standard Model Lagrangian that would naturally allow CP violation in strong interactions, and only by a fine-tuning of parameters can these terms be made to cancel [43].

- The origin of neutrino masses. Results showing the oscillation of neutrinos from one flavour to another also imply that they must have non-zero masses. The origin of these masses, and the large discrepancy between the neutrino masses and those of the charged leptons are not explained by the Standard Model. Neutrino oscillations also imply lepton flavour violation, which is as yet unobserved in the charged lepton sector.
- The incorporation of gravity. The Standard Model does not include gravity in any form. Any eventual Theory Of Everything must also incorporate terms which provide the attractive force between massive particles.

### 2.4.1 Supersymmetry

The vast difference between the electroweak and Planck scales causes problems with the Higgs mass. New Physics close to the Planck scale (which must be assumed to exist, in order to allow quantum gravitational effects) will cause large corrections to the Higgs mass, making it much larger than expected given the mass spectrum of the Standard Model particles which obtain their masses through interactions with the Higgs potential. This can be resolved by positing an additional symmetry of nature, relating fermions and bosons. This symmetry is referred to as Supersymmetry, or SUSY, and predicts the existence of a bosonic partner to every fermion and vice-versa. The introduction of this symmetry causes the cancellation of higher-order corrections to the Higgs mass, allowing it to occupy the expected range [44].

The simplest SUSY model is the Minimal Supersymmetric Standard Model (MSSM), in which every Standard Model particle has a superpartner. From experiment, these must have larger masses than their SM counterparts, and so SUSY is a broken symmetry. In addition to resolving the Hierarchy problem, SUSY also provides dark matter candidates, and allows unification of all the fundamental forces at high energies, making it an attractive possibility as an extension to the Standard Model [45].

### 2.4.2 Minimal Flavour Violation

Predictions regarding the scale at which New Physics effects will become manifest introduce an issue know as the Flavour Problem. One can define a scale, $\Lambda$, beyond which the Standard Model is no longer valid. The natural[3] scale of $\Lambda$ is of the order 1 TeV. However, measurements of FCNC processes expected to be sensitive to these New Physics effects, such as $K^0 - \overline{K}^0$ and $B^0 - \overline{B}^0$ mixing, show good agreement with Standard Model predictions. These results would suggest $\Lambda > 10^2$ TeV, contradicting the prediction from naturalness [46]. The flavour structure of any extension to the Standard Model must be able to resolve this apparent discrepancy.

[3] I.e. not requiring fine-tuning of parameters.

One hypothesis that has been proposed in order to resolve this is known as Minimal Flavour Violation, or MFV. Flavour is a broken symmetry in the Standard Model, as evinced by the mass hierarchies of the quarks and leptons, and MFV supposes that any breaking of this symmetry in New Physics has the same structure as in the Standard Model. This structure come from the Yukawa interaction, that describes the interactions of quarks and leptons with the Higgs field [47].

### 2.4.3 Other New Physics Models

Beyond SUSY, there are a large number of other New Physics models that have been proposed. Some of the most popular models include the existence of extra dimensions beyond the normal four dimensions of spacetime. These models account for the Hierarchy Problem by suggesting that the gravitational force extends into these extra dimensions (which may be compactified, or 'curled up') while the other forces are restricted to the usual (3 +1) dimensions [48].

There are also models in which the Higgs field is not the source of electroweak symmetry breaking, such as Technicolor [49]. In Technicolor models, a new QCD-like interaction is introduced, with an associated set of force-carrying fields and massless fermions, which are responsible for breaking the electroweak symmetry by forming a condensate (analogous to the formation of Cooper pairs in superconductivity).

It is models like these which the LHC experiments hope to see evidence of, so that a favoured New Physics model can be identified, or at least the phase-space of possible models reduced.

# Chapter 3

# The LHCb Experiment

In this chapter, the design and function of the LHCb experiment will be discussed. This discussion will cover the overall aims of the experiment, and the consequences for its general design. The specific functions and structure of the detector subsystems will then be covered in more detail. The operation of the LHCb detector is entirely dependent on the collisions provided by the LHC accelerator, and so this will be discussed first.

## 3.1 The Large Hadron Collider

The Large Hadron Collider (LHC) is a high-energy proton-proton collider located at CERN, the European Organisation for Nuclear Research. The main accelerator is housed in a tunnel of circumference 27 km, approximately 100 m underground. LHCb is one of four large experiments situated around the LHC ring, along with ATLAS, CMS and ALICE. This is shown in figure 3.1. The LHC is designed to operate at a centre-of-mass energy of 14 TeV, with a luminosity of $10^{34}$ cm$^{-2}$ s$^{-1}$.

The two 7 TeV counter-circulating proton beams each consist of 2808 bunches, with a bunch-crossing frequency of 40 MHz. Each bunch contains approximately $10^{11}$ protons, resulting in an average of 600 million collisions per second[1].

Prior to injection into the LHC, the protons are accelerated by a series of smaller synchrotrons:

- Protons, produced in a Duoplasmatron ion source by bombarding hydrogen gas with electrons from a hot cathode and accelerated to 50 MeV by the CERN Linac2, are injected into the Proton Synchrotron Booster (PSB)
- The PSB accelerates the protons to an energy of 1.4 GeV

[1] For the high-luminosity experiments, ATLAS and CMS.

- These protons are injected into the Proton Synchrotron (PS) and accelerated to 25 GeV
- The Super Proton Synchrotron (SPS) then takes the protons, and accelerates them to 450 GeV, at which point they can be transferred to the LHC

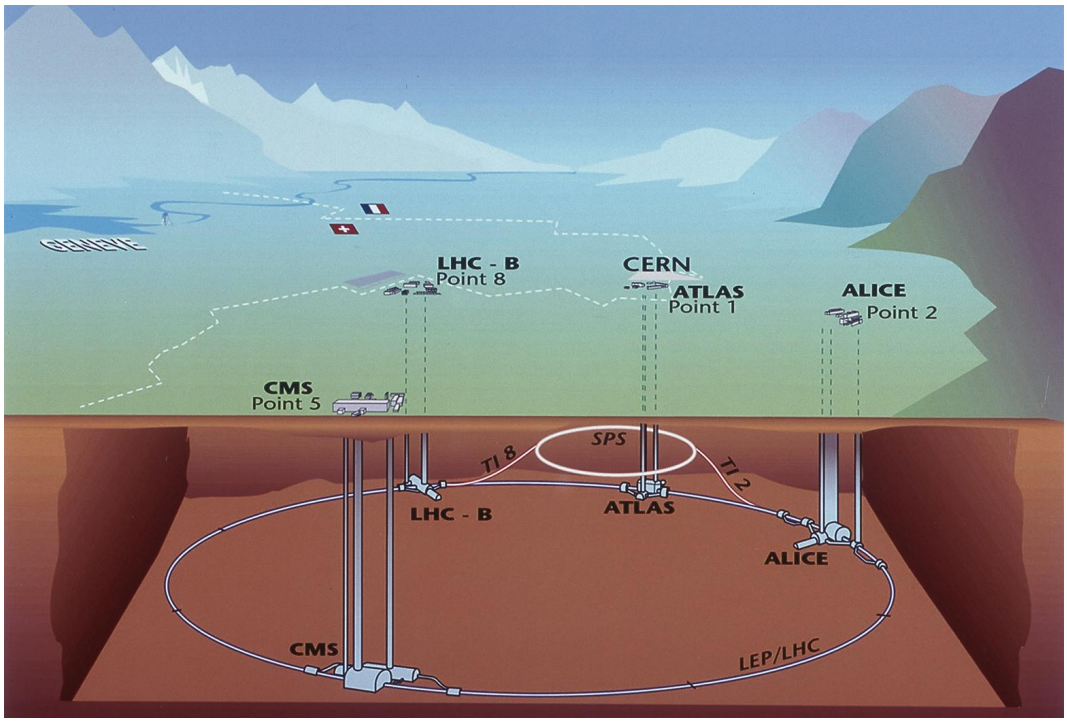


**Figure 3.1:** Overview of the Large Hadron Collider, showing the positions of the four main experiments.

The LHC ring consists of 8 curved arc sections, and 8 straight sections known as 'insertions'. An octant of the ring, beginning and ending in the centre of successive arc sections, and containing an entire insertion is referred to as a 'sector'. Each sector is dedicated to a specific function; four of the sectors are used for the experiments, two are used for beam cleaning, one for the beam dump system, and the final sector is used for the RF (Radio Frequency) cavities which accelerate and compress the bunches.

A wide variety of magnets are employed in the LHC, in order to steer and focus the proton beams. Since the counter-circulating beams have the same charge, two sets of magnets with opposing fields are required. Only at the four beam crossing points, corresponding to the interaction points for the four large experiments, do the beams cross from one magnet bore to the other. The arc sections are comprised mainly of dipole bending magnets. The specific combination of magnets used in an insertion depends on the function of the sector.

The majority of the LHC magnets use superconducting NbTi technology operating at temperatures as low as 1.9 K. One of the drawbacks of superconducting magnets is the risk of 'quenches'. A quench occurs when the magnet leaves the superconducting

regime, and enters the resistive state, discharging the energy stored in its magnetic field in the process. Quenches can reduce the lifetime of superconducting magnets, or in some cases cause permanent damage, and so should be avoided.

Consequently, superconducting magnets require a very well collimated beam, as even small energy deposits into the magnets can cause a magnet to quench; this is the function of the beam cleaning system. Cleaning of the beam 'halo' (beam loss during normal LHC operation) will also reduce backgrounds in the experiments. The beam cleaning system also includes beam loss monitors, which allow the beam to be dumped in the case of abnormal losses. The beam dump system extracts and dilutes the beam, before depositing it in a beam dump absorber block.

## 3.2 The LHCb Detector

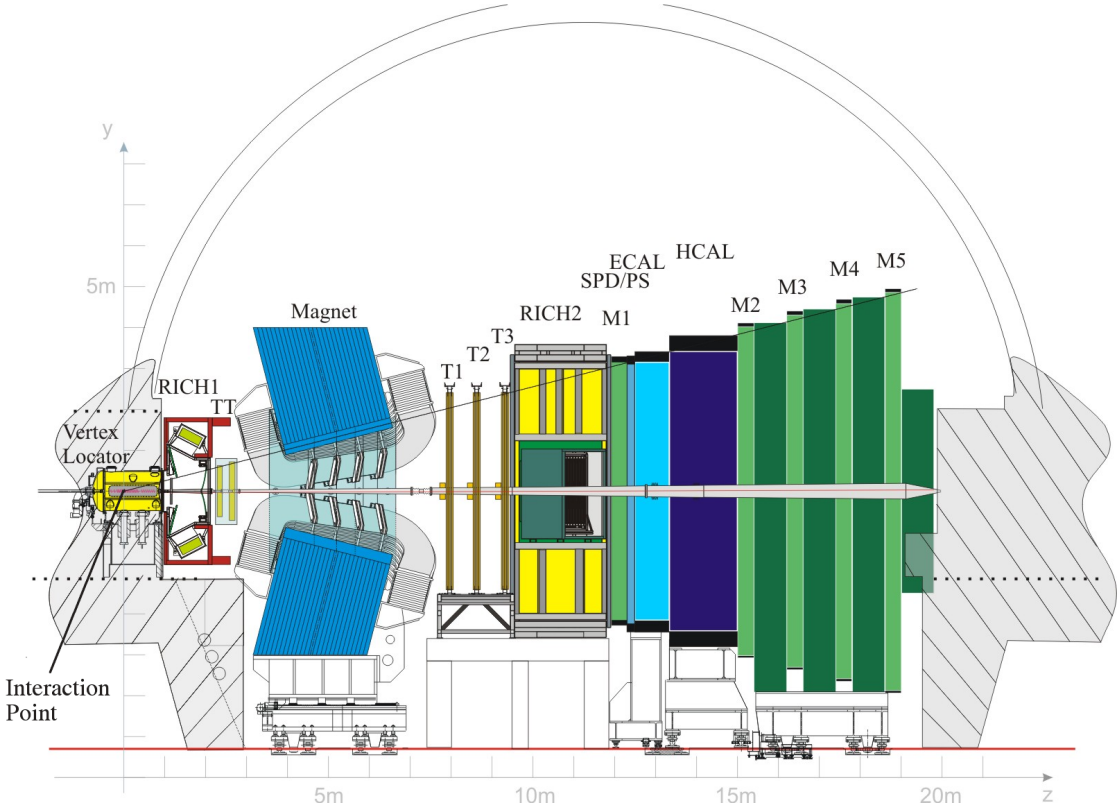


**Figure 3.2:** The LHCb Detector.

LHCb is the dedicated B physics experiment at the LHC. It was designed to be a precision experiment, measuring rare and CP-violating decays of B mesons. In order to do so, it requires excellent proper-time resolution, enabling it to resolve the fast oscillations of $B_s^0$ mesons, and a powerful particle identification system, allowing discrimination between a variety of final state particles. It must also be able to trigger efficiently on B decay signatures.

LHCb operates at a reduced luminosity compared to ATLAS and CMS. The LHC beams are defocused prior to collisions at Intersection Point 8, where LHCb is located, to deliver a luminosity of $2 \times 10^{32}$ cm$^{-2}$ s$^{-1}$. This allows LHCb to operate in the regime in which the probability of a single interaction per bunch crossing is maximised. Working in this regime results in a lower detector occupancy, making the identification of individual B decays considerably easier, and reducing radiation damage to the detector.

LHCb is a single arm spectrometer, in the forward direction, as shown in figure 3.2. It covers the angles $10 < \theta < 300$ mrad in the bending plane of the LHCb magnet, and $10 < \theta < 250$ mrad in the non-bending plane. This single arm design was chosen because $b\bar{b}$ quark-pair production at the LHC is strongly peaked in the forward (and backward) direction, as shown in figure 3.3(a). The production of $b\bar{b}$ quark-pairs occurs primarily through the interaction of gluons and sea quarks, as shown in figure 3.3(b).

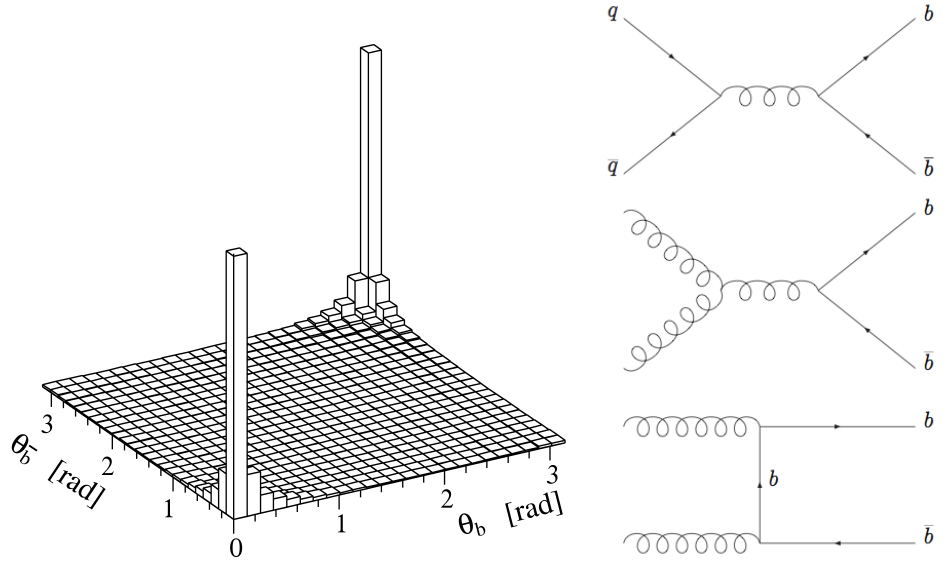


(a) Angular distribution (polar) of $b\bar{b}$ quark-pair production from simulation [35].

(b) Leading-order diagrams for $b\bar{b}$ quark-pair production.

**Figure 3.3:** $b\bar{b}$ quark-pair production at the LHC.

The LHCb detector was constructed in the cavern which formerly housed the DELPHI experiment on the LEP accelerator. In order to make the best use of the space available in the cavern, the interaction point is shifted by -11.25 m in the z direction from the centre of the cavern, as shown in figure 3.2. Given that the LHCb detector extends only in the forward direction from the interaction point, rather than in $4\pi$ surrounding it, this offers the maximum area for the detector to extend into. The LHC beam optics were modified in order to facilitate this displacement.

The focus on the high-rapidity region provides additional challenges, since particles in this region are travelling close to the beam pipe. Interactions with the beam pipe will cause additional secondary particles, which will contribute to the overall detector

occupancy. To minimise these interactions, much of the beam pipe is constructed from beryllium, which has a high radiation length and good rigidity. However, beryllium is fragile and costly, and so features such as flanges, bellows and interfaces with subdectector elements are constructed from aluminium. The beam pipe is 19 m long, and 12 m of this length consists of beryllium, with the remaining length of the beam pipe, outside the critical region for low occupancy, constructed from stainless steel. The narrowest aperture of the beam pipe is 50 mm, and is maintained at a pressure between $10^{-8}$ and $10^{-9}$ mbar.

The LHCb detector is divided into a number of subsystems, each of which is responsible for a particular facet of the overall measurement of a B decay. The function, operating principles, design and performance of each subdetector is outlined in detail in the following sections.

## 3.3 Vertex Locator

The Vertex Locator, or Velo, is responsible for measuring track coordinates close to the interaction point. The Velo allows displaced secondary decay vertices, a characteristic property of b-hadron (and also c-hadron) decays, to be reconstructed. The Velo is the most upstream of the LHCb subdetectors, and surrounds the p-p interaction point. The precise vertex location provided by this subdetector is necessary for LHCb to obtain its required proper-time resolution ($\sim$ 40 fs).

### 3.3.1 Design

The Velo is also necessary for the measurement of particle impact parameters, the measurement of which are greatly improved by reducing the extrapolation distance from the primary vertex, and so the sensitive region of the Velo is positioned as close as possible to the interaction point. The smallest possible distance of the detector from the beam axis is approximately 8mm during physics running [50]. The Velo is designed to be retractable, moving the sensitive elements out of the path of the beam during LHC injection[2], and re-positioning them as close as possible during collisions.

The Velo is enclosed within a secondary vacuum vessel, as shown in figure 3.4, separated from the beam pipe by a 100 $\mu$m aluminium foil, which protects against RF pickup from the beam. Wake field suppressors made from 50 $\mu$m thick copper-beryllium provide the interface to the beam pipe, reducing electromagnetic effects due to sudden changes in geometry around the LHC beam [52]. The detector elements of the Velo are a series of 300 $\mu$m thick silicon sensors. These sensors are approximately semicircular, with a radius of 42 mm. The semicircular elements are positioned on either side of the beam

[2]During which the necessary beam aperture increases.

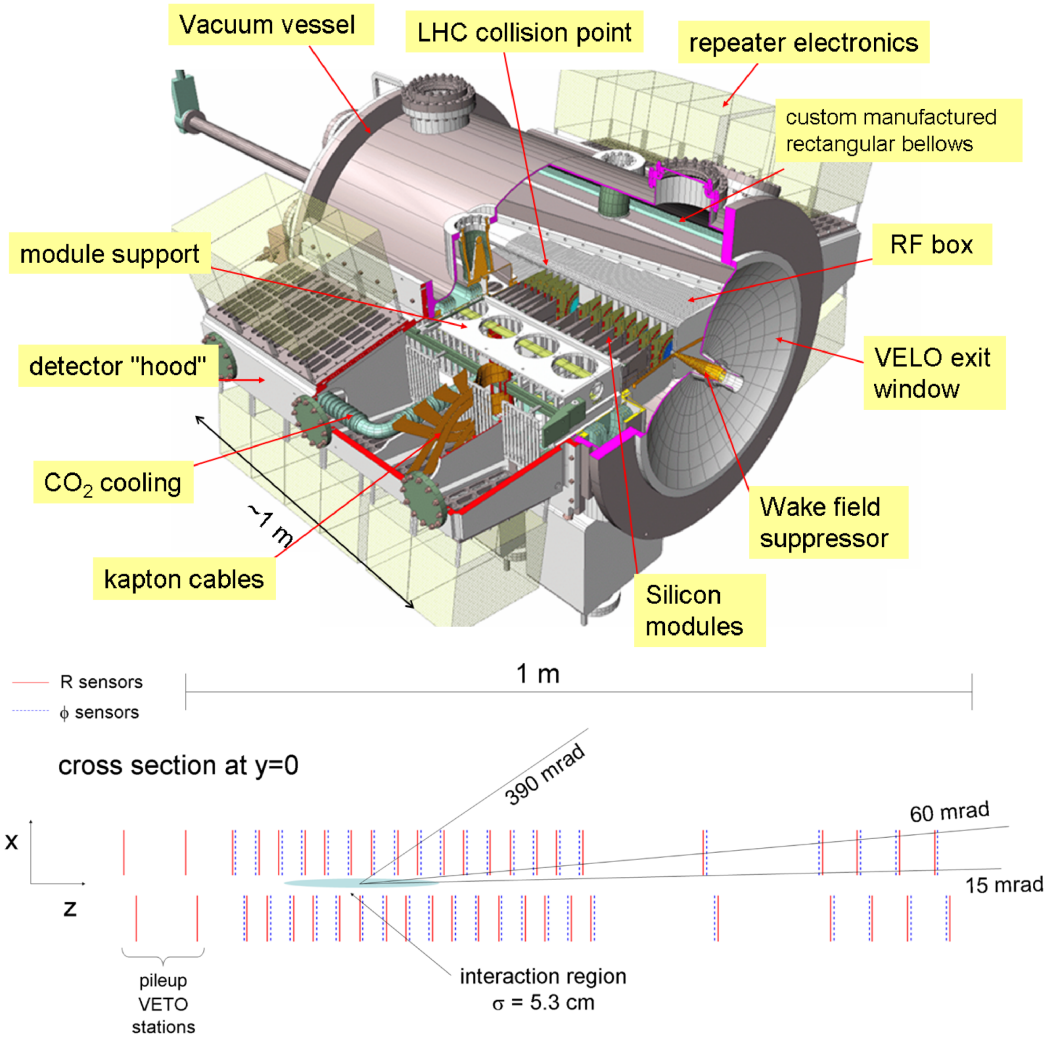


**Figure 3.4:** The Velo vacuum vessel and sensor position[51].

pipe, allowing the two halves to be retracted by a distance of 3 cm during injection. The positions of the sensors on the two detector halves are staggered by 1.5 cm in the z-direction, so that during physics running, they can overlap.

### Sensors

The sensors are divided into two types, r-measuring and $\phi$-measuring, reflecting the cylindrical geometry used for the Velo. The r-measuring sensors provide information on the radial coordinates of the hits, and so are segmented into 512 concentric semi-circular strips, giving a strip pitch of 40 $\mu$m at the inner edge, increasing to 101.6 $\mu$m at the outer edge. The $\phi$-measuring sensors provide azimuthal hit information, and thus are segmented into radial strips. In order to keep strip occupancy at an acceptable

level, the $\phi$-measuring sensors are divided into an inner and an outer region. The inner region comprises 683 strips, and extends to a radius of 17.25 mm on the sensor, with the outer region of 1365 strips making up the rest of the sensor. The strip pitch in the inner and outer regions is 35.5 $\mu$m and 95.6 $\mu$m respectively. The inner region strips are at a larger angle to the radial than the outer region strips, resulting in a 'dog-leg' design, which improves pattern recognition. The layout of these sensors is shown in figure 3.5. Using the z-position of the sensors along the length of the Velo, the hit

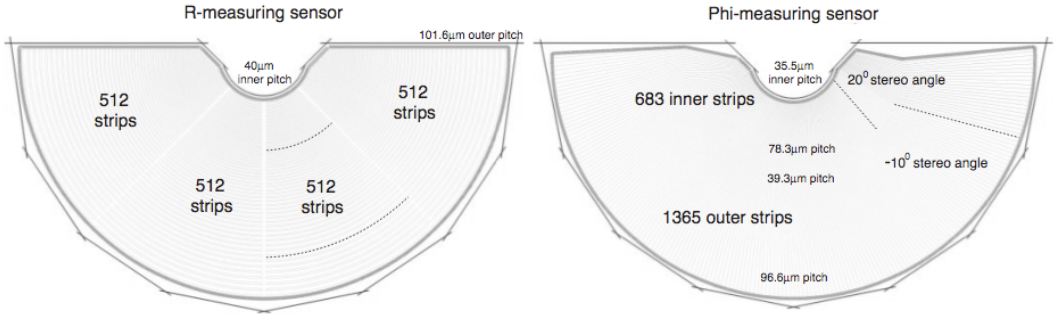


**Figure 3.5:** Layout of the r-and $\phi$-measuring Velo sensors [53].

information allows 3D tracks to be reconstructed. Both sensor types are read out at the outside edge, and each sensor has 2048 readout channels. The sensors are designed to provide a spatial resolution for 100 mrad tracks of approximately 4 $\mu$m, in the region with the smallest strip pitch.

### Modules

The sensors are integrated within Velo 'modules'. Each module contains one r-measuring and one $\phi$-measuring sensor, on opposite faces of the module. The modules also include the readout electronics which interface with the sensors, and provide mechanical support. There are 42 Velo modules in total, 21 in each detector half. The modules are arranged so that sensors of the same type face each other (i.e. the arrangement of sensors in the z-direction is 'rr$\phi\phi$rr' et cetera). The particles passing through the Velo will experience on average 17.5 % of a radiation length. The largest contribution to this comes from the RF shielding foil, followed by the sensors.

The total length of the Velo's sensitive region is approximately 1 m. The position of the modules along the beam axis reflect two conditions; the Velo must cover the entire angular acceptance of the downstream subdetectors corresponding to the pseudorapidity range $1.6 < \eta < 4.9$, and tracks traversing the Velo should intersect at least 3 sets of sensors. The module pitch in the central region closest to the interaction point is 3.5 cm, with the downstream modules at a larger pitch. There are several modules upstream of the nominal interaction point, as seen in figure 3.4, allowing tracks in the backward direction to be partly reconstructed.

#### Pile-Up Veto

Two sets of r-measuring sensors are located further upstream of the IP, and these are known as the Pile-Up Veto. It is used by the LHCb Trigger system, described in section 3.9. It is responsible for distinguishing between beam crossings with single and multiple visible interactions, by measuring the overall track multiplicity. This allows crossings with more than one p-p interaction to be ignored (vetoed) by the trigger.

#### Detector Lifespan

The Velo operates in an extremely high and non-uniform radiation environment. Radiation-tolerant technologies were adopted for all of the detector elements. However, it is still anticipated that the Velo will require replacement after 3 years of normal LHC running. After this time, the inner regions of the detector will have received equivalent damage to being irradiated by $3.9 \times 10^{14}$ neutrons (1 MeV) per $\text{cm}^2$ [50].

## 3.4 RICH Detectors

Particle identification (PID) is crucial for accurate reconstruction of B meson decays at LHCb; of particular importance is the ability to distinguish between pions and kaons, which are common final states in many B meson decays. In addition to suppressing backgrounds, identifying kaons is essential for the LHCb Flavour Tagging system, which determines the initial flavour of the B meson. The PID system of the LHCb experiment consists of two Ring Imaging Cherenkov (RICH) detectors.

### 3.4.1 Operating Principle

As the name suggests, RICH detectors make use of the principle of Cherenkov radiation [54]. Cherenkov radiation is a phenomenon that occurs when charged particles travel through a radiator medium at a velocity greater then the phase velocity of light in that medium. As the charged particle passes through the medium, it causes molecules to become polarised[3]. Upon relaxing from this polarised state, the molecules will emit electromagnetic radiation. If the particle velocity is above threshold, i.e. $\beta n > 1$ where $\beta = \frac{v}{c}$ and $n$ is the refractive index of the medium, constructive interference can occur, as shown diagrammatically in figure 3.6. This results in the emission of photons at a constant angle, the Cherenkov angle $\theta_c$, with respect to the velocity of the charged particle. From simple geometrical considerations, it can be derived that:

$$\cos\theta_c = \frac{1}{n\beta} \tag{3.1}$$

[3]Hence why Cherenkov radiation applies exclusively to charged particles.

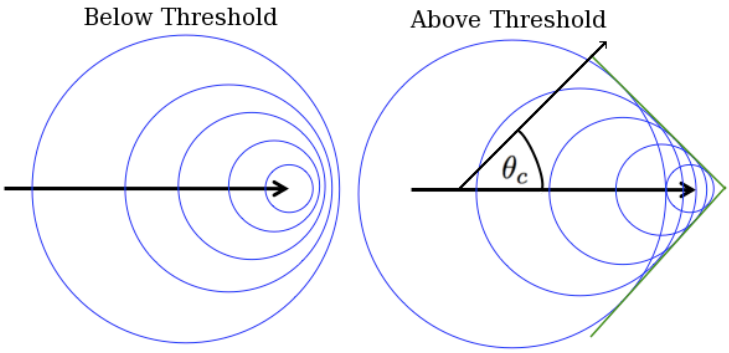


**Figure 3.6:** Waveforms produced by a charged particle travelling through a radiator medium at speeds below and above the threshold velocity for that medium.

Hence, the velocity of a charged particle in a given radiator medium can be determined by measuring $\theta_c$.

In RICH detectors, the cone of Cherenkov photons emitted by a particle as it traverses the radiator medium is focused into a ring (hence 'Ring Imaging') by means of a spherical mirror. The radius of these rings can be used to extract $\theta_c$, and hence the particle velocity. Combining this information with measurements from other subdetectors (the particle momentum in particular) allows a mass hypothesis, and hence a PID hypothesis, to be formulated. The RICH system is expected to provide an average positive kaon identification of 95% over the momentum range 1 - 100 GeV/c, with an average pion misidentification rate of 5%.

### 3.4.2 RICH1

LHCb uses two RICH detectors in order to cover the required momentum range of charged particles. RICH1 covers the lower momentum region within the full LHCb acceptance, and is located after the Velo, upstream of the LHCb spectrometer magnet. It occupies this position as the low-momentum particles which it measures may be swept out of the downstream detector acceptance by the magnet. RICH1 uses two radiator materials; aerogel and $C_4F_{10}$ gas. The silica-based aerogel has a refractive index n = 1.03, and provides $\pi - K$ separation up to approximately 10 GeV/c. The 5 cm thick aerogel tiles are located close to the RICH1 entrance window, surrounding the beam pipe. The Cherenkov photons emitted have wavelengths towards the infrared end of the visible spectrum. The maximum $\theta_c$ for aerogel is 242 mrad. $C_4F_{10}$ gas has a refractive index of n = 1.0014, and a maximum $\theta_c$ of 53 mrad. It provides $\pi - K$ separation up to 60 GeV/c, with the particles traversing approximately 85 cm of the gas which is at standard temperature and pressure.

Two sets of mirrors are used; the spherical mirrors for focusing, and plane mirrors to reflect the photons onto the two photodetector planes, above and below the beam pipe,

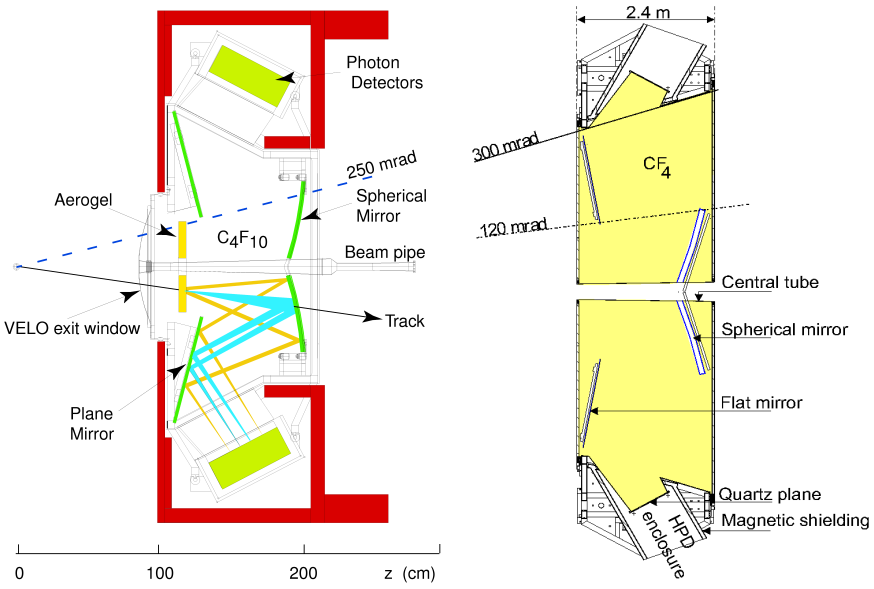


(a) RICH1 Schematic (b) RICH2 Schematic

**Figure 3.7:** The RICH Detectors [51].

as shown in figure 3.7(a). Since the spherical mirrors are within the detector acceptance, they are made of a carbon fibre reinforced polymer substrate, coated with a Al+$MgF_2$ deposition, which contributes less than 2% of a radiation length to the material budget of the detector. Since the plane mirrors are outside the detector acceptance, they are not subject to material budget constraints. They are composed of a glass substrate, with a coating of Al+$SiO_2$+$HfO_2$.

The photosensitive elements, which will be discussed in detail in chapter 4, are located within magnetic shielding boxes, which protect them from the 60 mT fringe field of the LHCb dipole magnet.

### 3.4.3 RICH2

RICH2, shown in figure 3.7(b), provides PID information for higher momentum charged particles (15 GeV/c - 100 GeV/c). It is located downstream of the LHCb magnet and tracking stations, and has a smaller angular acceptance than the upstream detectors, ±120 mrad in the bending plane, and ±100 mrad in the non-bending. A single radiator medium, $CF_4$ gas is used in RICH2, which has a refractive index of n = 1.0005, with a maximum $\theta_c$ = 32 mrad. Charged particles traverse a path length of approximately 167 cm through this gas.

The layout of RICH2 is similar to that of RICH1, rotated by 90° about the z-axis, so that the photodetector planes are located either side of the beam pipe, rather than above and below as in RICH1. Both the plane and spherical mirrors are constructed from 6mm thick Simax glass, coated with the same Al+$SiO_2$+$HfO_2$ deposition as the

RICH1 plane mirrors. RICH2 contributes 15 % of a radiation length to the overall material budget of the detector.

### 3.4.4 Ring Reconstruction

In order to assign a PID hypothesis to a particle, a Cherenkov ring must be matched to a particle track, and each mass hypothesis tried in turn in order to calculate a likelihood which can be maximised. This can either be done locally, for each particle track individually, or globally, maximising simultaneously for all tracks. Procedures for ring reconstruction without tracking information are also being developed.

#### Systematic Uncertainties

There are several sources of systematic uncertainties for the determination of the Cherenkov angle. One of these factors is the error in the emission point of the Cherenkov photons. The photons are assumed to originate from the centre of the radiator, when in fact emission occurs along the entire length of the particle track through the radiator, and beam trajectories that do not pass through the centre of curvature of the spherical mirror will result in distorted rings. Another source of uncertainty is the chromatic error, this is caused by variations in the refractive indices of the radiator media with wavelength. Additional uncertainties are introduced by the finite size of the photon detector pixels, and the error in the tracking information.

#### Performance

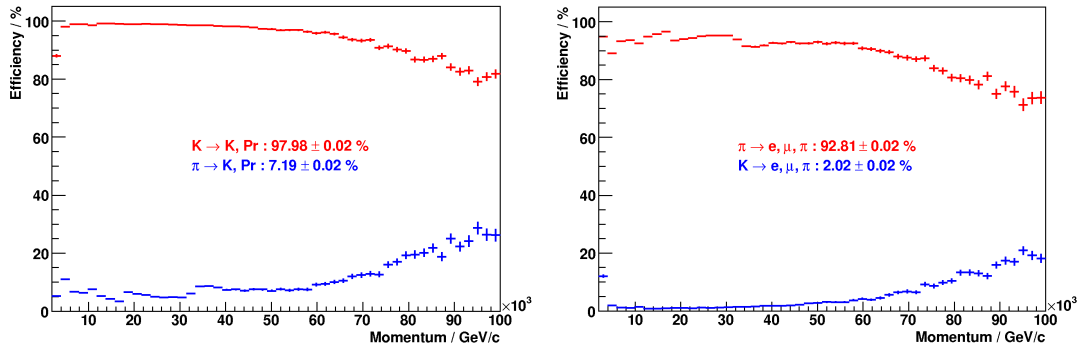


(a) Heavy ID (Kaon, Proton)

(b) Light ID (Pion, Electron, Muon)

**Figure 3.8:** RICH Particle Identification performance for $B_s^0 \to \phi\phi$ signal events.

Figure 3.8 shows the simulated RICH particle identification performance for a sample of $B_s^0 \to \phi\phi$ signal events. The analysis of this channel will be discussed in detail in chapters 6 and 7. Particle identification is important for the reconstruction of this

channel; since there are four kaons in the final state, the kaon identification efficiency will have a large effect on the overall reconstruction efficiency.

Figure 3.8(a) shows the efficiency (red, kaon identified as 'heavy') and purity (blue, kaon identified as 'light') for the kaons in the sample as a function of their momentum, while figure 3.8(b) shows the corresponding performance for the pions. The PID decision shown in these plots is based on the best PID hypothesis for each track, but the required log likelihood difference (DLL) between the various PID hypotheses can be varied in order to tune the balance between efficiency and purity as required by the analysis.

## 3.5 Magnet

In order to determine the momentum of charged particles, a magnetic field is required to deflect the particle trajectories. The integrated magnetic field required to provide sufficient momentum resolution is around 4 Tm for tracks originating near the interaction point [55].

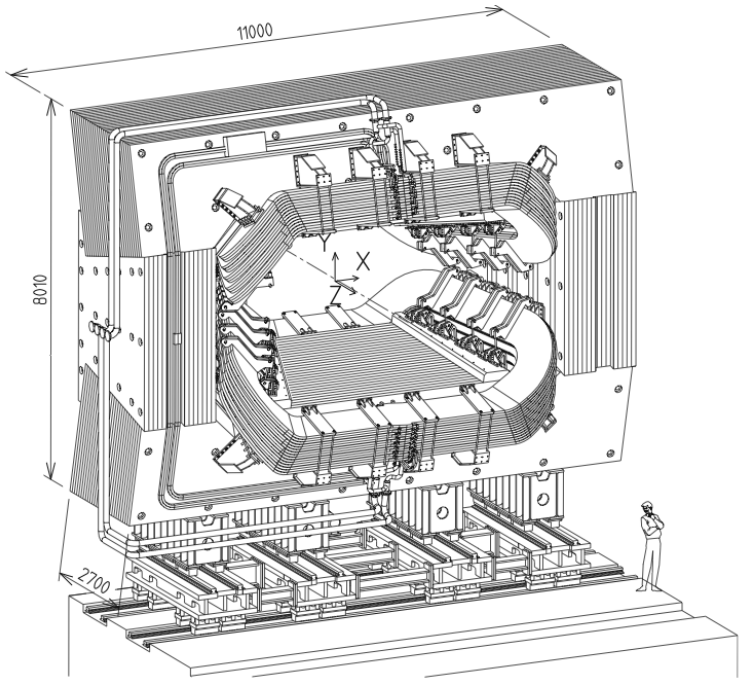


**Figure 3.9:** The LHCb Dipole Magnet [51], dimensions given in millimeters.

Due to cost considerations, a warm magnet was chosen for use in LHCb. It consists of aluminium coils within an iron yoke. The two identical coils above and below the beam pipe have a conical saddle shape, reflecting the angular acceptance of the detector, as shown in figure 3.9, and weigh a total of 54 tons. The yoke shapes and guides the magnetic flux, and weighs a total of 1500 tons.

The magnet produces a maximum magnetic field of just over 1 T. The magnetic field strength is carefully mapped by an array of Hall probes, in order to measure the magnetic field integral $\int Bdl$ and the position of the peak magnetic field. The polarity of the magnet will be periodically reversed in order to counter the effect of charge asymmetric effects within the detector.

## 3.6 Tracking

The LHCb tracking system (Velo aside) consists of 4 tracking stations; the Tracker Turicensis (TT) upstream of the magnet, and three stations (T1-T3) downstream of the magnet. The downstream tracking stations use a combination of silicon and straw-tube technologies in different regions (the Inner and Outer trackers respectively), whereas the TT uses exclusively silicon. The TT and Inner Tracker (IT) will therefore be discussed collectively as the Silicon Tracker. The expected momentum resolution for tracks with hits in all tracking stations is $dp/p < 0.55\%$, and the expected efficiency for finding this type of track for particles with momenta $> 10$ GeV/c is 94%.

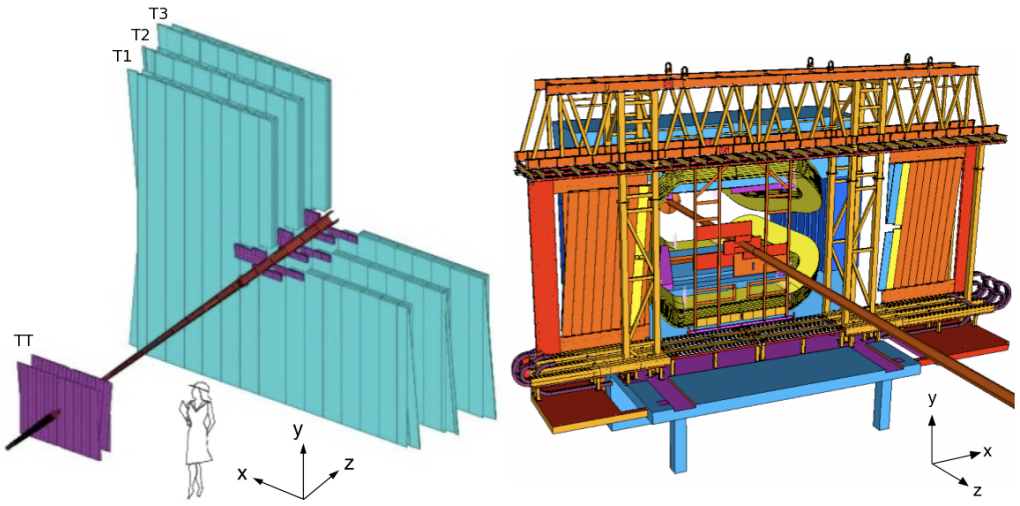


**Figure 3.10:** The LHCb tracking system [51]. In the left hand diagram, the Silicon Tracker is depicted in purple and the Outer Tracker in blue. The figure on the right shows a retracted Outer Tracker (OT) station, and its vertically aligned straw-tube modules.

### 3.6.1 Silicon Tracker

Due to the high-rapidity nature of events at LHCb, very high charged particle fluxes (up to $5 \times 10^5$ cm$^{-2}$s$^{-1}$) are expected in the inner regions of the tracking stations, dropping off rapidly with distance from the beam pipe. Both the TT and the IT use silicon microstrip detectors, with a pitch of around 200 $\mu$m, in order to cope with these high particle fluxes [56].

**Tracker Turicensis**

The TT station is responsible for providing tracking information on low-momentum particles that are swept out of the detector acceptance by the magnet. It consists of 4 layers of silicon microstrips, in an 'x-u-v-x' arrangement. The x-layers have the microstrips in a vertical orientation, while the u and v-layers are rotated by stereo angles of $-5°$ and $+5°$ respectively. The layers are positioned in two pairs, with a separation in the z direction of 27 cm between the second and third layers. All four layers are housed within a light-tight and electrically insulated volume. The volume is kept at a temperature below 5° C, and circulated with nitrogen to prevent condensation. The TT station is constructed in two halves which can be retracted horizontally to allow beam pipe maintenance.

The silicon sensors used in the TT are 500 $\mu$m thick, measure 9.64 $\times$ 9.44 cm, and are subdivided into 512 readout strips. 896 of these sensor modules are used in total (210 each for the first two layers and 238 each for the last two layers, which are wider) giving a total sensitive area of 8.4 $m^2$.

**Inner Tracker**

The Inner Tracker is located in the region closest to the beam pipe of the three downstream tracking stations (T1-T3). Each IT station consists of four boxes, in a cross shape surrounding the beam pipe. Like the TT, each box is light-tight, electrically insulating, and kept below 5° C with nitrogen circulating to prevent condensation. The boxes above and below the beam pipe consist of a single row of seven silicon sensors, which are 7.6 by 11 cm with 384 readout strips at a pitch of 198 $\mu$m. The boxes to the right and left of the beam pipe contain two rows of seven sensors, with the same area as those above and below, but of different thickness (410 compared to 320 $\mu$m).

The boxes above and below the beam pipe are staggered by 4 mm in z with respect to the boxes on the right and left, and overlap by 3 mm in x, to avoid acceptance gaps. Each box contains 4 silicon layers, in the 'x-u-v-x' layout described previously. 504 silicon sensors are used in total in the IT, with an overall active area of approximately 4 m.

For both the TT and the IT, the material budget is a function of pseudorapidity and the azimuthal angle. For the TT, it has an average of around 4% of a radiation length, but this increases to almost 13% in the very forward region. For the IT the material budget varies between 3.5% and up to 30% in some narrow regions.

### 3.6.2 Outer Tracker

The Outer Tracker surrounds the IT at each of the downstream tracking stations in the region where particle fluxes and hence detector occupancy are much lower. The sensitive elements of the OT stations are 4.9 mm diameter straw-tubes [57], filled with Argon (70%) and $CO_2$ (30%). Each OT module consists of two staggered layers (monolayers) of 64 tubes aligned vertically. There are two types of modules, long and short, with the short modules located above and below the beam pipe and the IT boxes, and the long modules extending the entire height of the T station (4.85 m). The long modules are split into two halves, effectively resulting in 256 individual straw-tubes, with the splitting position staggered for the two monolayers to avoid producing a central dead region.

Each OT layer consists of 14 long and 8 short modules, and each downstream tracking station has 4 layers in the 'x-u-v-x' geometry. Like the TT, each station is constructed of two halves that can be retracted horizontally, as shown in figure 3.10. The OT has a total active area of approximately 80.6 $m^2$. The total material in the OT corresponds to 9.6% of a radiation length.

## 3.7 Calorimeters

The LHCb calorimeters are responsible for measuring the energy, position and shower shapes of electrons, photons and hadrons, and using this information, in combination with other subdetectors, to identify them. This information is required by the Level-0 hardware trigger, discussed in section 3.9, and so must be available very quickly. The calorimeters are located downstream of RICH2. The LHCb calorimetry system consists of a Silicon Pad Detector/Preshower, followed by the electromagnetic calorimeter (ECAL), and finally the hadronic calorimeter (HCAL).

### 3.7.1 Silicon Pad Detector and Pre-Shower

The Silicon Pad Detector (SPD) and Pre-Shower (PS) are responsible for verifying the charged and electromagnetic nature respectively, of incoming particles that are subsequently measured by the calorimeters. The SPD/PS system consists of two sets of scintillator tiles, separated by a 15 mm thick sheet of lead, corresponding to 2.5 radiation lengths.

The first set of scintillators, the SPD, identifies charged particles. This allows electron and photon showers to be discriminated. It also aids $\pi^0$ identification, which decay to a pair of photons. For high energy $\pi^0$s, the daughter photons cannot be separated, and provide a background to electrons in the ECAL. The second set of scintillators, the PS,

provides separation between electrons and hadrons (pions in particular) by providing additional information on the shower shape.

The scintillators have an area of 7.6 × 6.2 $m^2$, and are highly segmented. Due to the large variation in hit densities over the surface (two orders of magnitude), it is divided into three regions with different granularities. The inner section, closest to the beam pipe, is comprised of 1472 cells of size approximately 4 × 4 $cm^2$, the middle section has 1792 6 × 6 $cm^2$ cells, while the outer section is the largest and contains 2688 12 × 12 $cm^2$ cells [58].

The scintillation light is transported via wavelength-shifting fibres, and measured by Multi-Anode Photo Multiplier Tubes (MAPMTs). Between 20 and 30 photoelectrons are produced per minimum ionising particle. While the size of the PS signal in each cell must be recorded, the SPD output is a single bit output by a discriminator telling whether a cell has been hit.

### 3.7.2 Electromagnetic Calorimeter

The ECAL is a 'Shashlick' sampling calorimeter (allowing the shower shape in z, as well as the x-y position to be measured), comprised of alternate layers of lead and scintillator. It is responsible for measuring the energy of electromagnetic particles (i.e. photons and electrons) and reconstructing $\pi^0 s$. It has the same segmentation in the x-y plane as the SPD/PS, although each cell is approximately 1.5 % bigger.

The calorimeter is divided in the z-direction into 66 layers. Each layer consists of 2 mm of lead followed by a 4 mm thick scintillator tile, with a 120 $\mu$m layer of white, reflecting TYVEK paper inbetween, to aid reflection of the scintillator light at the tile boundary. This stack has a total thickness of 42 cm, which corresponds to 25 radiation lengths. The Molière radius of the stack is 3.5 cm. The scintillation light is transported by wavelength-shifting fibres and measured by Photo Multiplier Tubes (PMTs).

The ECAL energy resolution is a function of the particle energy, and is described by

$$\frac{\sigma_E}{E} = \frac{10\ \%}{\sqrt{E}} \oplus 1\% \tag{3.2}$$

where the energy is measured in GeV [58].

### 3.7.3 Hadronic Calorimeter

The HCAL is responsible for measuring the energy of hadrons. It is a sampling calorimeter, using iron and scintillator tiles. In contrast to the ECAL, the tiles in the HCAL run parallel to the beam pipe, and are interspersed with 1 cm of iron. This results in a

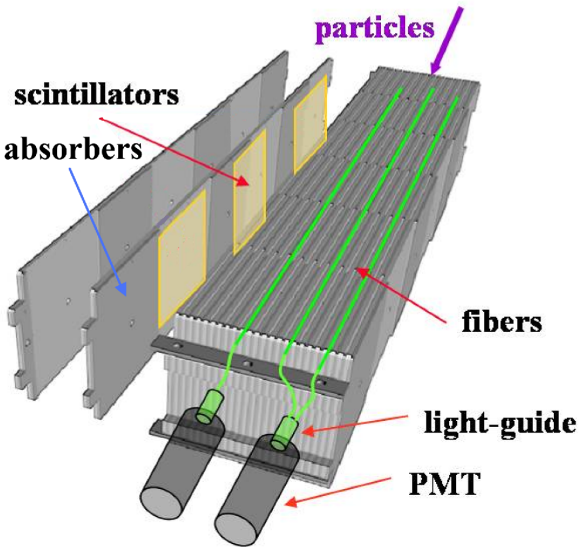


**Figure 3.11:** Structure of the LHCb Hadronic Calorimeter [51].

lateral sampling distance of 2 cm, and a longitudinal sampling distance of 20 cm. The required energy resolution of the HCAL is $80\ \%/\sqrt{E} \oplus 10\%$ (energy in GeV) [58].

In the x-y plane, the HCAL is segmented into cells of two different sizes; in the inner region, the cells measure 131.3 × 131.3 mm, and in the outer region, they measure 262.6 × 262.6 mm. The inner region consists of 860 channels, and the outer region has 608 channels. The HCAL measures 8.4 m by 6.8 m in total, with a depth of 1.65 m which corresponds to 5.6 hadronic interaction lengths. Like the ECAL, the scintillator light is extracted via wavelength-shifting fibres, and measured by PMTs.

## 3.8 Muon System

The final LHCb subdetector is the Muon system, which as the name suggests is responsible for the identification, $p_T$ measurement and triggering of muons. It consists of five stations, M1-M5, the first upstream of the calorimeters and the rest downstream, as shown in figure 3.12.

The position of the first muon station allows increased precision in the $p_T$ measurement. The remaining stations are separated by muon filters, which are 80 cm thick iron absorbers [59]. M1-M3 have high spatial resolution in the x-direction (corresponding to the dipole magnet bending plane) in order to measure the muon $p_T$ with a resolution of 20 %, while M4 and M5 have a lower spatial resolution, and are used for selecting highly penetrating muons. The muon system comprises 20 radiation lengths in total, with a minimum momentum of 6 GeV required for a muon to traverse all five stations.

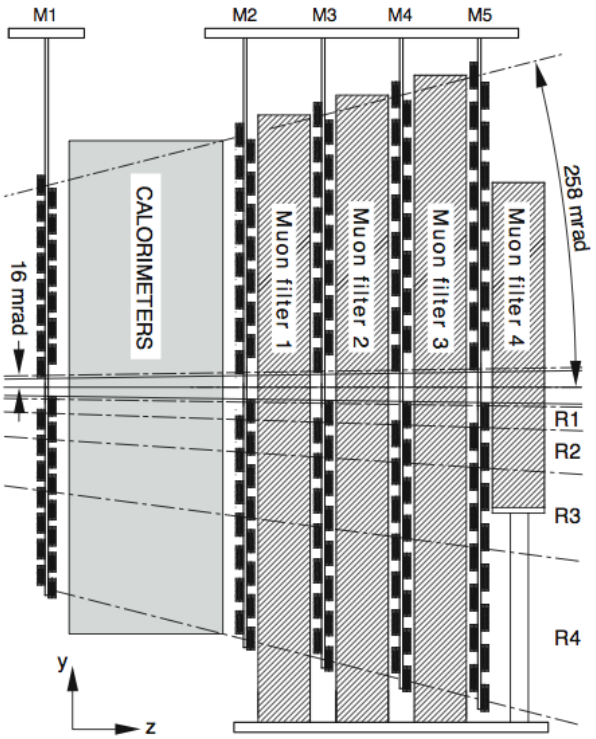


**Figure 3.12:** The LHCb Muon System [51].

### 3.8.1 Multi-Wire Proportional Chambers

The stations themselves are comprised of Multi-Wire Proportional Chambers (MWPCs), with the exception of the central region of M1, which uses triple Gas Electron Multipliers (triple-GEMs) due to aging considerations in this high particle flux region. A muon passing through the MWPCs will ionise the gas (an $Ar/CO_2/CF_4$ mix in the ratio 4:5:1), with the ions and liberated electrons drifting to the cathode pads and anode wires respectively. The gas gap measures 5 mm, and the anode wires have a pitch of 2 mm [60]. The MWPCs in M2-M5 are composed of four ORed gas gaps, while in M1 they use two ORed gas gaps (to reduce the amount of material in front of the ECAL).

### 3.8.2 Gas Electron Multipliers

The triple-GEMs consist of three copper-clad 50 $\mu$m kapton foils between anode and cathode planes. The foils have bi-conical holes with external and internal diameters of 70 $\mu$m and 50 $\mu$m respectively, at a pitch of 140 $\mu$m. A potential difference of around 350 V is applied between the copper cladding, which causes high electric fields within the holes resulting in avalanche effects in the presence of an electron. The foils therefore act as gain stages for electrons produced when a muon traverses the $Ar/CO_2/CF_4$ (in a 45:15:40 ratio) gas. The gas gaps between the cathode/foils/anode are 3/1/2/1

mm [61]. Two ORed triple-GEMs are used in the central M1 region. The response of both the MWPCs and the triple-GEMs are read out as binary information, reporting the presence of a muon hit.

The segmentation of the muon stations, providing the x-y hit coordinates, is defined in four different regions, labelled R1-R4 with increasing distance from the beam pipe. The logical pads (the readout unit into which the MWPC/GEMs are subdivided) in R1 of M1 have size $1 \times 2.5$ cm$^2$, and quadruple in area (while keeping the same aspect ratio) in each subsequent region. In M2 and M3, the pads for each region halve in size (subject to projection corrections due to the detector acceptance) and double in number compared to M1, while in M4 and M5 they double in size and halve in number (subject to the same corrections).

## 3.9 LHCb Trigger

The LHCb Trigger system is responsible for selecting the events that will be stored for offline analysis, and so must select p-p interactions containing B-mesons within the detector acceptance, while keeping the total rate to be written out down to a manageable level. At the LHCb design luminosity of $2 \times 10^{32}$ cm$^{-2}$s$^{-1}$, visible p-p interactions occur at a rate of 10 MHz, and events can be written to storage at a rate of 2 kHz [62]. This 5000-fold reduction is achieved in two stages. Firstly, the Level-0 (L0) trigger, consisting of custom electronics operating synchronously with the LHC machine, reduces the rate to 1 MHz, at which rate the entire LHCb detector can be read out. The High Level Trigger reduces this rate down to 2 kHz asynchronously, using a processor farm.

### 3.9.1 Level-0 Trigger

The L0 trigger selects events based on high $E_T$ and $p_T$ signatures which are indicative of B-meson decays. Three subdetectors are involved in the L0 trigger decision, the Velo Pile-Up Veto, the Calorimeters, and the Muon system. The role of the Pile-Up Veto was discussed in section 3.3.1. The L0 trigger also attempts to reconstruct [62]

- The highest $E_T$ hadron (with $E_T > 3.6$ GeV), electron ($> 2.8$ GeV) and photon ($> 2.6$ GeV) clusters in the Calorimeters
- The two highest $p_T$ muons ($\Sigma p_T > 1.5$ GeV/c) in each quadrant of the Muon system.

The Calorimeter trigger also sums the total HCAL energy deposits to allow discrimination of crossings without visible interactions and muons from the beam halo, and hit occupancy in the SPD allows the charged track multiplicity to be estimated. The in-

formation from each of these subdetectors is sent to the Level-0 Decision Unit (L0DU) in order to be combined to produce the overall trigger decision. The L0 latency is fixed to 4 $\mu$s.

### 3.9.2 High Level Trigger

The HLT is a set of C++ applications that run on approximately 200 computing nodes. The first stage of the HLT is known as HLT1, and is responsible for confirming the L0 decision. This is done by a series of 'alleys', one for each type of L0 trigger; muon and dimuon $p_T$, plus hadron, electron and neutral ($\gamma$ and $\pi^0$) $E_T$. The alleys run a series of algorithms using tracking information to make the decision. An event passing at least one alley will be passed by HLT1.

The final stage of the trigger uses additional information in order to perform more specific reconstructions. A number of algorithms are run, which have been optimised for various types of physics analyses and decay channels. Since the HLT is implemented in software, it is flexible, allowing the triggering strategy to be changed if necessary during the running of the experiment.

## 3.10 Other LHC Experiments

LHCb is one of four large LHC experiments. ATLAS and CMS, the two general purpose, high luminosity experiments are located at opposite points on the LHC ring, intersection points 1 and 5 respectively. ALICE, the heavy-ion physics experiment, is located at intersection point 2. In addition, there are two smaller experiments, LHCf and TOTEM which share intersection points with ATLAS and CMS respectively.

### 3.10.1 ATLAS

The ATLAS (A Toroidal LHC ApparatuS) experiment encompasses an Inner Detector, which uses pixel, silicon microstrip, and straw tube detectors. It provides pattern recognition, vertex and momentum measurements, and electron identification. The Inner Detector is held within a 2 T magnetic field provided by a superconducting solenoid magnet that surrounds it. Electromagnetic calorimetry is provided by high-granularity liquid argon sampling calorimeters. For hadrons in the barrel region of the detector, a scintillator-tile calorimeter is used, while in the end caps, liquid argon technology provides both electromagnetic and hadronic measurements. The final layer of the detector is the muon system, which uses an air-core toroid magnet to provide strong bending power (up to 7.5 Tm) for muons which are detected by three layers of high-precision tracking chambers.

The ATLAS detector is forward-backward symmetric, and operates in the pseudorapidity region $|\eta| < 4.9$ ($< 2.5$ for the tracking), with almost full azimuthal angle coverage. This design will allow ATLAS to pursue a broad physics program, investigating QCD, electroweak, and flavour physics [63]. The LHCf (LHC-forward) experiment, which shares intersection point 1 with ATLAS, is designed to measure the energy spectra of LHC interactions at very forward angles [64].

### 3.10.2 CMS

The CMS (Compact Muon Solenoid) experiment shares many of the physics goals of ATLAS, but takes a complementary approach in its detector design. A powerful, 4 T superconducting solenoid provides 12 Tm of bending power. The solenoid is surrounded by 4 muon stations, incorporating aluminium drift tubes in the barrel region, with cathode strip and resistive plate chambers in the endcap regions. The large bore of the magnet allows the inner tracker and calorimetry to be located within its volume.

The tracking system consists of 10 layers of silicon microstrips, and 3 layers of silicon pixels in the region closest to the interaction point, allowing precise impact parameter and secondary vertex measurements. The electromagnetic calorimeter uses lead tungstate crystals, with silicon avalanche photodiodes and vacuum phototriodes used for detecting scintillation light in the barrel and endcap regions respectively. A preshower detector is used in the endcap region for $\pi^0$ identification. The hadronic calorimeter is a brass/scintillator sampling calorimeter, using hybrid photon detectors, while the forward calorimeters use iron/quartz-fibre technology [65]. The TOTEM experiment, which also located at intersection point 5, and partially embedded within the CMS detector, is designed to make measurements of the total proton-proton cross section [66].

### 3.10.3 ALICE

The ALICE (A Large Ion Collider Experiment) experiment will study heavy-ion collisions produced by the LHC in addition to the proton-proton collisions, in order to investigate the QCD sector and the quark-gluon plasma at extreme energy densities. The detector consists of a barrel part and a forward muon spectrometer.

The ALICE barrel contains an inner tracking system, which uses silicon pixel, drift and strip detectors. This is surrounded by a cylindrical time-projection chamber, followed by three particle identification systems; time-of-flight, RICH, and transition radiation detectors. The outer layer houses two electromagnetic calorimeters. The forward muon arm uses 14 layers of tracking and triggering chambers, along with absorbers and a large dipole magnet [67].

# Chapter 4

# The RICH System

## 4.1 Hybrid Photon Detectors

A crucially important aspect of the LHCb RICH detectors are the photosensors used to detect the Cherenkov photons; there are a number of criteria which these photosensors must fulfill, with the most important factors being

- single photon sensitivity
- excellent spatial resolution
- a sensitive wavelength range matching the emission spectra of the Cherenkov radiators (approximately 200 - 700 nm)

The solution chosen for the photosensitive elements of the LHCb RICH system is Hybrid Photon Detectors (HPDs), which combine vacuum photocathode and pixelated solid-state detector technologies.

Each HPD consists of an S20-type[68] ($Na_2SbK$:Cs) multialkali photocathode deposited onto the inside of a quartz entrance window. The photocathode has an active wavelength range of approximately 200-900 nm. The quartz window is attached to the HPD tube body by an indium seal. The tube body encapsulates the HPD electrostatics; the photoelectrons ejected from the photocathode are accelerated through a $\sim$20 kV potential, with two intermediate electrodes responsible for steering the photoelectrons, these are called the Focus and Zoom electrodes. The photoelectrons are focused onto the HPD silicon sensor, as shown in figure 4.1, which is a demagnification of the photocathode area by a factor $\sim$5.

The HPD anode consists of two parts; the sensor chip and the readout chip. The sensor chip is 300 $\mu$m thick silicon, reverse biased at 80 V. It is divided into 8192 pixels of size 500 $\times$ 62.5 $\mu m^2$. Approximately 5000 electron-hole pairs are produced by every 20 keV photoelectron striking the silicon sensor. The sensor chip is bump-bonded to

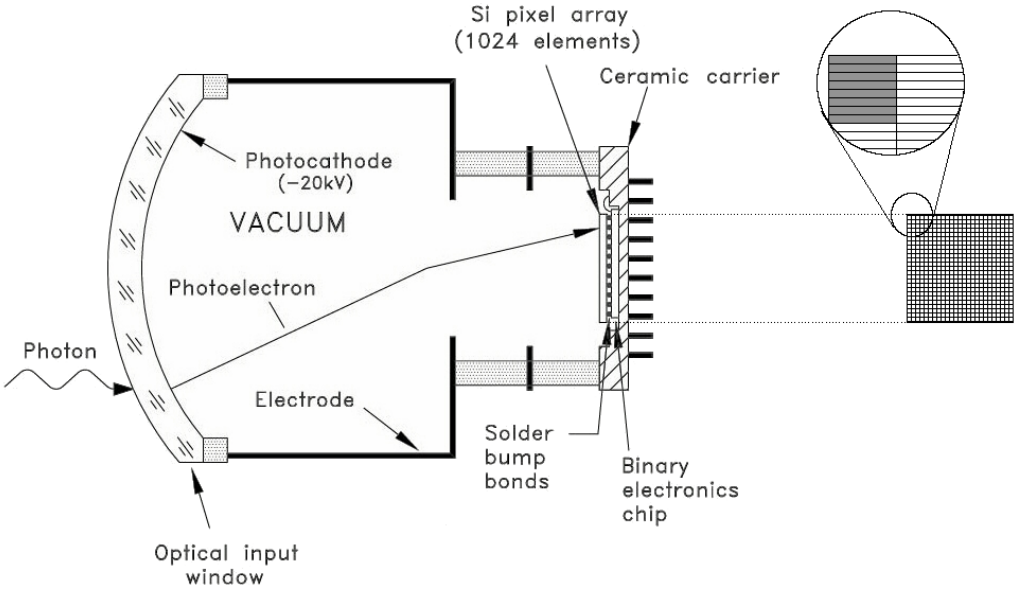


**Figure 4.1:** HPD Schematic Diagram, showing 8-fold pixel ORing (expanded section).

a binary readout chip, the LHCBPIX1 chip, which converts signals above threshold in the silicon to digital hits in the pixels. The readout chip is a 0.25 $\mu$m CMOS chip, and was developed in collaboration with the ALICE experiment, where it is used as part of their tracking system. The radiation tolerance requirements of the chip are based on an expected radiation dose of 30 kRad in the detector's 10 year lifetime; a full list of the performance specifications for the HPD binary readout electronics is shown in table 4.1. The chip has two operational modes, to reflect its two applications; in ALICE mode (only used in LHCb for diagnostic purposes), each of the 8192 channels is read out separately, while in LHCb mode, an 8-fold logical OR is applied to groups of 8 neighbouring pixels, as shown in figure 4.1. This forms a 32 $\times$ 32 array of 500 $\times$ 500 $\mu$m$^2$ superpixels. This pixel size corresponds to a granularity of 2.5 $\times$ 2.5 mm$^2$ for photon hits on the photocathode, which fulfills the spatial resolution requirements for the effective reconstruction of Cherenkov rings.

The readout chip is compatible with the 25 ns LHC clock, corresponding to the bunch-crossing rate of 40 MHz. The chip was designed to operate with an average Level-0 trigger rate of 1 MHz in LHCb mode, although it has been found that the chip cannot correctly read out events which were triggered on consecutive clock cycles, due to a fault in its design. The chip is read out sequentially by 32 parallel lines, taking 825 ns to read out an event in LHCb mode (32 rows @ 25 ns each, plus one additional clock cycle) and similarly 6425 ns to read out an event in ALICE mode, which has 256 pixel rows [70].

The readout sensor is bump-bonded [71] to the readout chip, and this assembly is packaged on a ceramic carrier and wire-bonded to a pin-grid array of 321 pins. This provides the interface between the binary readout chip and the external readout electronics [72].

**Table 4.1:** Specifications for the HPD Binary Readout Electronics [69].

| | |
|---|---|
| Operational Threshold | $<2000\ e^-$ |
| Max. Noise Occupancy | 1% |
| Time Resolution | 25 ns |
| Channel Size (LHCb Mode) | $500 \times 500\ \mu m^2$ |
| Maximum Time-Averaged Pixel Occupancy | 4% |
| Bunch Crossing Rate | 40 MHz |
| Average L0 Trigger Rate | 1 MHz |
| Level-0 Latency | 4 $\mu$s |
| L0 Derandomizer Depth | 16 |
| Max. Readout Time | 900 ns |
| Rad. Dose in 10 Years | 30 kRads |

The pin-grid array is compatible with 'Socket 7' Zero-Insertion-Force (ZIF) sockets. A kovar ring is brazed onto the ceramic carrier, and provides the base on which the tube body is built. The tube body and quartz window undergo a vacuum bake-out to remove residual gas molecules, and the photocathode is deposited on the quartz window prior to it being affixed to the tube body with an indium seal. Finally, the HPD is cabled and the bottom is sealed within a protective 'potting'. The manufacture of the HPD components takes place in five different countries, coordinated by the LHCb RICH group, with the final construction carried out by Photonis Netherlands[1] [73]. A completed HPD is shown in figure 4.2.

The HPD tube body and quartz window are porous to Helium, and so must be stored in Helium-free conditions. The effects of residual gas molecules in the HPD vacuum will be discussed in section 4.2. Both Nitrogen and reconstituted air were used to store the completed HPDs.

**Figure 4.2:** A completed HPD.

[1]Formerly Delft Electronic Products (DEP).

### 4.1.1 Photon Detector Test Facilities

In order to ascertain that all of the HPDs produced were suitable for use in the RICH detectors, a comprehensive set of tests was devised to characterise the performance of each HPD. These tests were performed at dedicated test centres in Edinburgh and Glasgow; the Photon Detector Test Facilities (PDTFs).

Procedures were designed to test each aspect of the HPD:

- Photocathode: Dark Count, Response to Photons, Quantum Efficiency
- Electron Optics/Tube Volume: Imaging, Demagnification, High Voltage Stability, Field Distortions, Ion Feedback, Vacuum Quality
- HPD Body: Physical Dimensions, Quartz Window, Pin Grid Array, Sensor Position
- Silicon Sensor: Characteristic IV Curve, Depletion, Bump Bonding, Efficiency
- Readout Chip: Connections, Communications, DAC Linearity, Readout Modes, Dead Channels, Noisy Channels, Pixel Masking, Threshold, Noise

HPDs must be satisfactory in all of the above aspects in order to be approved for use in the RICH detectors.

The physical aspects of the HPD are checked first, to ensure that its dimensions are correct, allowing it to be correctly integrated into the RICH framework. The quartz window is examined to check for imperfections both in the quartz itself and also in the indium seal to the tube body. The pin-grid array on the ceramic carrier is examined for faulty pins before the HPD is installed in the test station.

The test station consists of a light-tight box, in which the HPD is mounted. Light from a pulsed LED is introduced into the box via an optical fibre for illuminating the photocathode. Also inside the box are a photodiode to monitor light levels, temperature sensors and a retractable mask with an array of holes, which is used to test for electrostatic field distortions and chip rotations [74]. Two external power supplies are required to power the HPD; one for the High Voltage, supplying the electrodes for the accelerating and focusing electrostatic field, and another for the Low Voltage, which powers the HPD readout chip and electronics.

The data read out from the HPD under test is collected and analysed by a DAQ PC, running a LabView program which automates the test procedure. The HV is ramped up slowly, and the response to photons during the process is measured by illuminating the photocathode with the LED. A similar procedure is performed while ramping the bias voltage applied to the silicon sensor chip. These scans allow the onset of photoelectron response to be seen. The leakage current, the current in the chip in the absence of photoelectrons is also measured as a function of bias voltage applied.

Tests are performed on the pixel chip by injecting charge directly into the pixels in order to measure the thresholds and electronic noise, and find dead, faulty or noisy pixels. Long data-taking runs are taken both with and without illumination. The former allow the imaging to be investigated, and measurements such as the size of the photocathode image, and relative offset of the pixel chip. The latter allows the dark count rate to be measured; dark counts are expected to be the main source of noise in the HPD. Another important parameter of the HPD performance that is measured is the Ion Feedback, which is discussed in section 4.2.

The quantum efficiency of the HPD is measured by the manufacturers (as are several other HPD parameters), and is corroborated by measurements taken at the Edinburgh PDTF. The average quantum efficiency spectra for a number of HPD delivery batches can be seen in figure 4.3. The PDTF quantum efficiency tests are time consuming, and so are performed on a sample of HPDs, corresponding to approximately 10% of the delivered HPDs. Good agreement has been observed between the two sets of measurements [75].

The photoelectron detection efficiency was measured through tests at the Glasgow PDTF [76]; this 'backpulse' measurement compares the number of digital hits recorded per event to the integrated analogue signal seen on the bias line of the silicon sensor, while the HPD is under constant illumination. Like the quantum efficiency, this measurement was performed on a subset of HPDs.

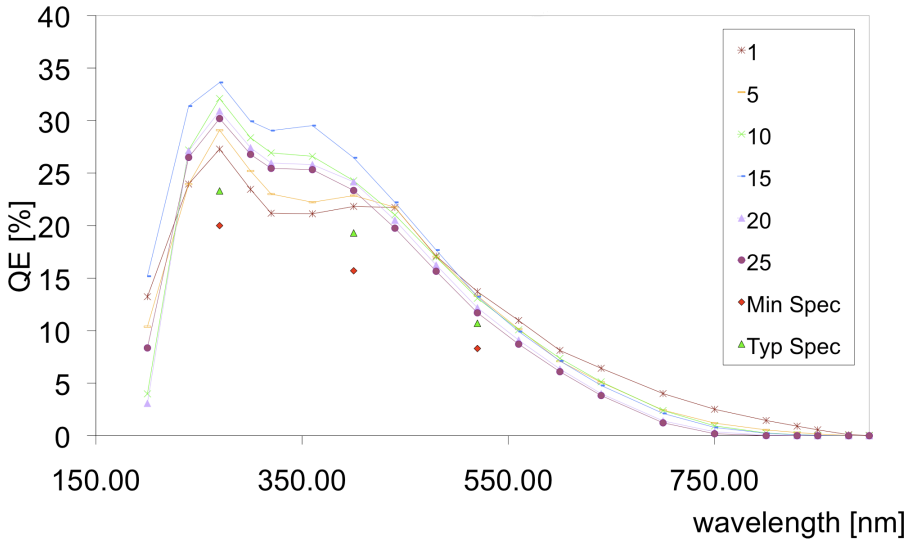


**Figure 4.3:** Average quantum efficiencies for a number of HPD delivery batches as a function of wavelength, from the manufacturer's measurements. The minimum and typical specifications required from the manufacturer are also shown.

Once the HPDs have been fully tested, they can be categorised based on how they performed in a number of specific tests. Some of the main criteria on which they are

judged are [77]:

- Dark count $< 5$ kHz/cm$^2$, corresponding to a <1% probability for 1 hit/HPD/event
- Leakage current $< 5$ $\mu$A
- Less than 1% faulty channels
- Photocathode image centre offset <2 LHCb pixels
- Quantum efficiency @ 270 nm $> 20\%$
- Ion feedback <1 %

There are four primary categories of HPDs; Category A HPDs are within specifications in all tests, category B HPDs have fallen marginally outside specifications in one test (usually the dark count limit) but have still generally behaved well, category E HPDs have fallen significantly outside specifications in one test (often the leakage current or the number of faulty channels) but are still functional, while category F HPDs have failed the criteria to a degree that makes them unusable. Category A, B and E HPDs are all passed for use in the RICH detectors, but category F HPDs cannot be used and, depending on the nature of the fault, are returned to the manufacturer to be reprocessed or replaced. There is also an additional A+ category, which was added after the initial 4, denoting HPDs which have behaved excellently in all tests, and in addition have high (>30%) quantum efficiency at 270 nm.

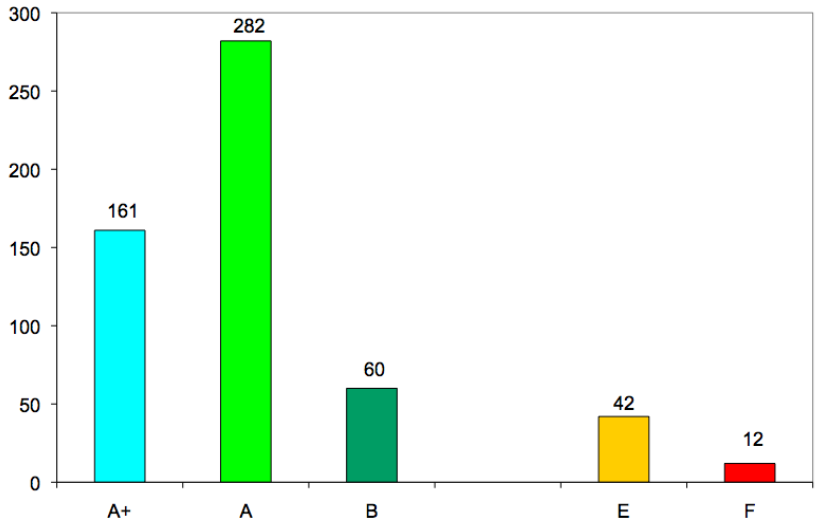


**Figure 4.4:** Breakdown of the HPD categories following PDTF tests.

Figure 4.4 shows the number of HPDs assigned to each category after all 557 HPDs produced were tested. Approximately 98% of the HPDs produced were suitable for use in the RICH detectors when tested [78], and more than 80% of those were classified as category A or A+.

### 4.1.2 HPD Integration

Once HPDs have been tested, they must be integrated into the RICH framework. The RICH photodetector planes are made up of columns of HPDs, each column comprising 14 HPDs for RICH1 and 16 HPDs for RICH2. For both RICH detectors, there are two types of columns, 'up' and 'down' columns. These differ in the position of the HPDs on the column, with a relative offset of approximately 1 HPD radius between the two. Consequently, when the columns are arranged 'up-down-up-down' the hexagonal close-packed arrangement required for the photodetector planes is formed. For RICH2, the two photodetector planes are referred to as the 'A' and 'C' sides (a convention for naming the sides of the detector dating back to the Delphi experiment which formerly occupied the LHCb cavern, with 'C' denoting the side towards the centre of the LHC ring) and each consisting of 9 HPD columns, giving a total of 288 HPDs. For RICH1, the planes are designated as 'Top' and 'Bottom', each containing 7 HPD columns (although the columns here are aligned horizontally), giving a total of 196 HPDs.

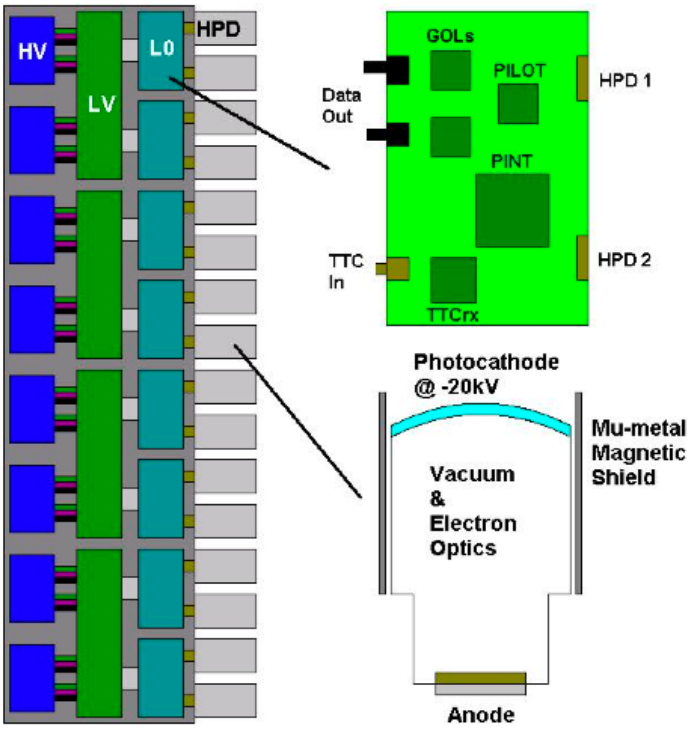


**Figure 4.5:** A diagram showing the layout of a RICH2 column.

The RICH columns are comprised of a number of elements: the physical structure of the HPD column is provided by an anodised aluminium ladder, onto which the other components are fixed. The first components installed on the ladder are the High Voltage (HV) distribution boards, which provide the potentials for the photocathode, focus and zoom electrodes. Each HV board supplies two HPDs. The Level-0 electronics boards provide the interface to a number of systems; the Timing and Fast Control

(TFC) system responsible for providing clock and trigger pulses, the Experimental Control System (ECS) which is used for slow control of detector elements, and the Data Acquisition (DAQ) system which reads out the data from the sensitive elements [79]. The L0 electronics react to the L0 (hardware) trigger, and also provide Low Voltage (LV) reference signals for calibrating the HPD chip electronics. Each L0 board controls two HPDs, which are connected to the L0 board by two flat kapton cables[2]. The L0 boards are powered by the LV distributions boards, each of which supplies two L0 boards, with the exception of the 'half' LV boards used as the final board on RICH1 columns which power only one due to the odd number of L0 boards on these columns. The layout of a RICH column is shown in figure 4.5. In figure 4.6, the mumetal magnetic shielding can be seen surrounding the HPDs. This shielding is intended to reduce the effect of the fringe field from the LHCb dipole magnet, which causes distortions to the HPD electrostatic field. The magnetic shielding protrudes slightly beyond the HPD quartz window.

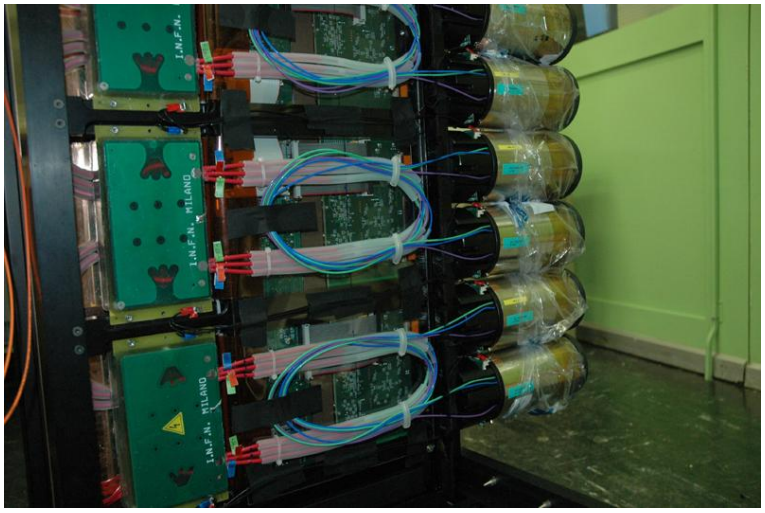


**Figure 4.6:** A completed HPD column before its cooling plate is attached.

The position of the HPDs in the columns is not arbitrary, from simulation studies [35] it is clear that the occupancy in the central regions of the RICH1 and RICH2 photodectector planes is far higher than in the outer regions, due to the strongly forward nature of b-quark production (and the associated background) discussed in chapter 3. In order to take advantage of this, it is preferable to place HPDs with high quantum efficiency and low background noise in this region. To do this, category A+ and A HPDs are installed in the central positions on the column where possible, and category E HPDs are installed in the edge positions. Another consideration when placing the HPDs on the column is the leakage current; HPDs with similar leakage currents were paired together on L0 boards to ensure similar timing of the readout signals. This will be discussed further in chapter 5.

[2]Copper connections embedded in kapton insulation.

The last stage in the construction of an HPD column is the installation of the cooling plate. The cooling plate consists of two copper sheets, with channels in between through which coolant is passed. Heat interfaces are attached to the LV board in order to conduct heat away though these cooling plates. Temperature sensors are also placed on the LV voltage regulators, so that their temperatures can be monitored.

### 4.1.3 Testing and Commissioning

The HPD columns are tested at several stages during their construction in order to check that all of the components are functioning correctly. The first check made once the elements are all installed is to test that all of the HPDs are correctly grounded through the ladder. Next, the voltage regulators on the LV distribution boards are adjusted; once this is complete, communication with the readout electronics is tested via the JTAG[3] protocol. Once this is established, the register contents of the Pilot chips on each L0 board are set in order that the correct DAC reference voltages are provided for the HPD readout chip, and the signal thresholds from the PDTF tests are applied. At this stage, data can be read out from the HPDs themselves; this is done without any High Voltage applied and so any data read out will be from either noise hits or charge injection. The level of noise hits can be increased by collecting data without the silicon bias voltage applied, but a more useful diagnostic tool is to use direct charge injection (test pulses) in a known pattern. This test reveals any readout problems such as missing columns of pixels, which is a common symptom of an incorrectly attached kapton cable. The readout tests are initially performed with the optical data fibres loosely in place on the column, and are repeated once these fibres have been routed into their final positions, in order to check that the fibres have not been damaged in the process, or dislodged any other connections.

Completed HPD columns are placed in the SSB (Small Simple Box, a RICH test bench, see section 4.3), for further testing. This is the first time that the HPD column is tested with HV applied. At this stage, the HPDs are again tested using test pulses, and a dark count run is also taken. This dark count run is used as a correction to the final test, which uses a pulsed laser to check the timing. A timing procedure working on a similar basis for the entire RICH will be discussed in chapter 5.

## 4.2 Ion Feedback Studies

In addition to the columns constructed to populate the RICH detectors, a spare column was also constructed to be used for testing the RICH ECS/DCS (Experimental and Detector Control) systems. During routine use of this column, a highly elevated noise

[3]Joint Test Action Group.

level was observed for three of the HPDs mounted on it. This column was tested at various High Voltage settings; at 3 kV the photocathode image was entirely saturated during dark count conditions, and at 6 kV the entire silicon sensor was saturated. A possible cause for this behaviour was proposed to be high levels of ion feedback. This observation led to the study of these and other HPDs which showed similar behaviour once mounted on the RICH columns, in order to investigate their failure mode.

Ion feedback is a useful parameter to measure, in order to track the changes in performance of HPDs as they age. Understanding and monitoring the evolution of the HPDs is essential for ensuring the continued high performance of the RICH detectors through their lifetime. Consequently, it was hoped to apply the knowledge gained from studying both the malfunctioning HPDs in the SSB, and the fully-functional HPDs at the PDTF stations, to develop tools for monitoring the ion feedback in the RICH detectors.

#### Ion Feedback

Ion feedback occurs when a residual gas molecule in the HPD volume is ionised by an incident photoelectron. This positive ion drifts in the electrostatic field towards the photocathode. Once this ion strikes the photocathode, it liberates several secondary electrons which are then accelerated back onto the silicon sensor. Due to the multiple electrons liberated at the photocathode, ion feedback causes a cluster of adjacent hits on the silicon sensor. As a result of the cross-focusing field, ions are most likely to be produced at the crossing point of the field, and drift back towards the centre of the photocathode. Consequently, ion feedback appears concentrated in the centre of the photocathode image.

Ion feedback occurs in all HPDs at some level, but this is generally extremely low. As was discussed in section 4.1.1, the PDTF criteria for ion feedback is that it should be less than 1%. Figure 4.7 shows the results obtained from the PDTF ion feedback tests, typically performed about one month after HPD production. It can be seen that all of the HPDs tested had ion feedback rates well below the 1% level at this point.

At low levels such as these, ion feedback cannot cause the behaviour that was seen in the malfunctioning HPDs, it will simply add a small contribution to the overall dark count rate. However, at very high ion feedback rates, the product of the ionisation probability and multiplicity of secondary electrons can exceed unity, leading to a self-sustaining cycle of increasing ion feedback. This renders the HPD unusable due to the extremely high noise levels and rapidly deteriorating photocathode. This is the regime in which the malfunctioning HPDs were eventually confirmed to be operating. It is referred to as the 'Glow Discharge' regime, since HPDs displaying this behaviour exhibit a faint blue emission of light in the centre of their quartz window, thought to be due to the ions recombining at the photocathode [80].

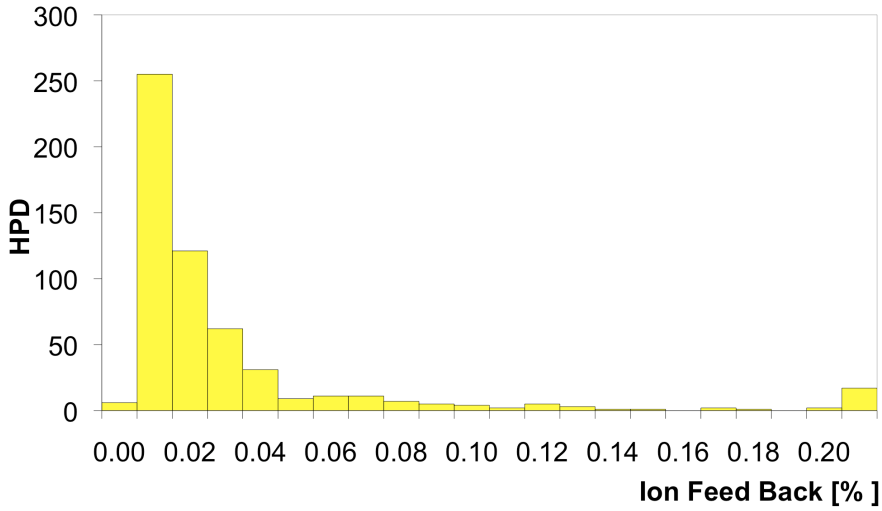


**Figure 4.7:** Results from the HPD ion feedback tests performed at the PDTF.

#### Identifying Ion Feedback

Ion feedback has two characteristic features which allow it to be isolated and investigated: large clusters of hits in adjacent pixels, and the time delay of these clusters with respect to the ionising photoelectron. Due to the generally low noise and dark count levels in the HPD, clusters of hits due to independent photoelectrons striking adjacent pixels (or electronic noise in adjacent pixels) are infrequent. Hits on adjacent pixels can be caused by charge sharing, in which the charge carriers produced in the silicon by a single photoelectron are distributed over multiple pixels, due to charge diffusion effects, and may exceed the hit threshold in several of them. However, this effect will only produce small (generally 2 ALICE pixel) clusters, while the clusters produced by ion feedback hits are larger (generally between 10 and 40 ALICE pixels). Thus, ion feedback can be identified by looking for 'large' clusters of hits in a single event.

The second feature, a delay of typically 200-300 ns between the ionising photoelectron and the ion feedback cluster, can be used to identify ion feedback if a carefully controlled, pulsed light source is available (as is the case in the PDTF). By increasing the timing delay of the light pulse with respect to the readout strobe, the ion feedback clusters can be temporally separated from the 'direct' signal hits.

### 4.2.1 Studies from SSB data

In order to understand the nature and potential cause of the effects observed, the behaviour of the HPDs during testing in the SSB was investigated. At this point, a number of HPDs already installed in RICH2 had also begun to show similar behaviour, giving a total of 9 malfunctioning HPDs by August 2007. The dark count runs taken for

these HPDs during SSB column tests provide an extra datapoint to study the evolution of the HPD performance between the PDTF measurements, in which the HPDs behaved normally, and the 'in situ' tests, in which the HPDs exhibited high levels of noise. In these dark count runs no time information on the ionising photoelectron is available, and so ion feedback is identified exclusively by cluster size.

The definition of a cluster used in this analysis is unambiguous and robust; a hit pixel belongs to a cluster if it is immediately adjacent (including along diagonals) to at least one other hit pixel in the cluster, while isolated hit pixels are considered as clusters of size one. The clustering is performed by a simple algorithm, which checks the neighbouring pixels of each hit pixel in turn, while ensuring that each hit pixel is assigned to exactly one cluster.

The criteria for what is classed as a large cluster depends on the operational mode of the HPD; in ALICE mode, the threshold for ion feedback clusters is 5 pixels, while in LHCb mode it is 3 pixels. The same definitions are used in the PDTF test procedure. In this analysis, the data was taken in ALICE mode and the ion feedback rate (from cluster size alone) is defined as:

$$\text{Ion Feedback Rate (\%)} = \frac{\text{Large Clusters}}{\text{All Clusters}} \times 100 \tag{4.1}$$

The DAQ system used for the SSB tests, described in section 4.1.3, does not use the standard LHCb readout framework, instead a LabView system, based on the one developed for the (pre-2006) RICH testbeams is used. As a consequence, the data files produced are not compatible with the LHCb Gaudi software framework, and so a stand-alone ROOT-based framework is used to analyse the data.

To obtain an accurate measurement of the ion feedback rate, it is important to separate out genuine dark count hits from other effects that may contribute to the overall occupancy. The two effects which are likely to affect the dark count rates in the SSB are noisy pixels and light leaks. A pixel is classified as noisy, and its hits are ignored in the analysis, if it fulfils both of the following criteria:

- The average number of hits per event on the pixel is $> 5 \times 10^{-5}$
- The number of hits per event on the pixel is more than 20 times larger than the average number of hits per event per pixel for that HPD

The first condition is mainly useful for identifying noisy pixels in low dark count HPDs, like the one shown in figure 4.8(c), while the latter is generally useful for identifying noisy pixels in higher dark count HPDs, such as the one shown in figure 4.8(a). Light leaks can affect the dark count rate, but for the extraction of ion feedback rates they are largely irrelevant as the probability of an ion feedback event occurring does not depend on whether the photoelectron responsible resulted from thermionic emission

or was caused by an incident photon. An exception is when light leaks cause localised 'hot spots' on the HPD image, which may result in clusters of hits. Unfortunately, such leaks were observed in the SSB dark count runs, however, these localised hot spots were generally classified as noisy pixels resulting in their exclusion form the analysis, and so do not have a large effect on the results.

The purpose of these studies was twofold; to investigate whether the malfunctioning HPDs entered the observed failure mode suddenly, or as the result of a steady degradation in performance, and secondly to try to identify HPDs which may fail in the future. The ion feedback of the malfunctioning HPDs was extracted from the SSB dark count runs, and compared to the ion feedback rates of the remaining, fully functional, HPDs on the same columns. The dark count runs for 5 RICH2 columns were analysed, giving a total of 79 HPDs in the sample (one HPD had to be excluded due to data corruption).

### Results

It was observed that the 9 malfunctioning HPDs did indeed all show ion feedback rates that were above the sample means for the columns investigated. Examples of the HPD hits maps and distributions of ion feedback clusters for these HPDs are shown in figure 4.8, demonstrating high ion feedback behaviour with a variety of dark count rates. The ion feedback rates extracted are shown in figure 4.9. However, whether these higher

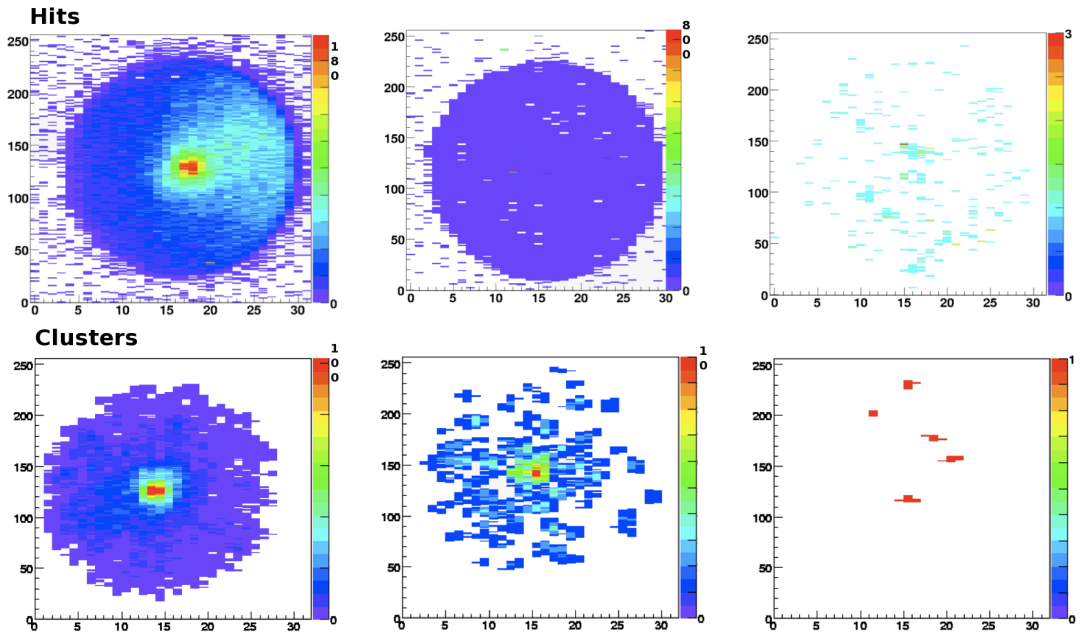


(a) high dark count HPD (b) medium dark count HPD (c) low dark count HPD

**Figure 4.8:** HPD hit maps (top) and ion feedback cluster distributions (bottom) for three of the malfunctioning HPDs, with a variety of dark count rates.

ion feedback rates are statistically significant was not obvious at the time, as there

were several other HPDs with similar (or even higher) ion feedback rates that had not displayed the glow discharge behaviour seen in the malfunctioning HPDs. However, these were considered candidates for future failure.

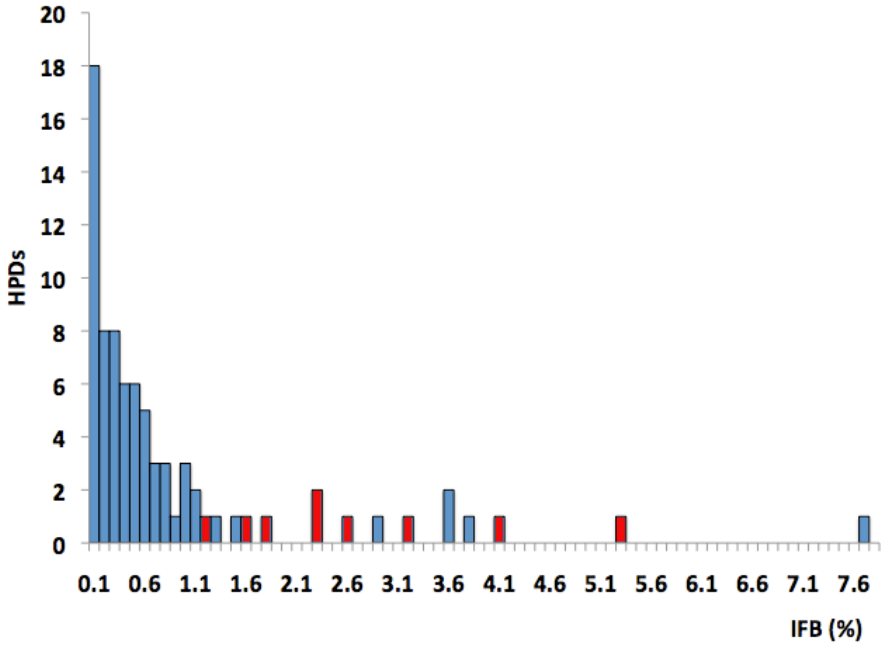


**Figure 4.9:** Ion feedback rates extracted from the SSB dark count runs of 79 HPDs from RICH2 in August 2007. The points marked in red represent the malfunctioning HPDs.

The ion feedback rates are significantly higher in the SSB tests than those observed in the PDTF tests. The two ion feedback measurements for each HPD were compared, and no good correlation was found between the two data sets. The rate difference was initially thought to be due to the different methods used in the two analyses. The PDTF measurements use the delayed response of ion feedback clusters discussed earlier to obtain a more accurate measurement (referred to as a 'strobe scan').

Ion feedback rates are also extracted from the dark count runs taken at the PDTF, which are generally higher than those extracted using the strobe scan method, which in principle should be be more compatible with the SSB data. However, no correlation was seen between this data set and the SSB data either, suggesting that another factor, most likely the different environment in which the data was taken, is responsible for the incompatibility of the measurements.

To conclude; the limited data sample provided by the two measurements of the ion feedback for the HPDs under investigation is insufficient to draw detailed conclusions regarding the failure mode of the malfunctioning HPDs. More data points under consistent conditions are needed, which can be provided by monitoring the HPDs within the RICH detectors, as described in the following section.

### 4.2.2 Online Monitoring

A procedure was developed to monitor the ion feedback online for HPDs installed in the RICH detectors. The environment within the RICH detectors is carefully controlled, and so repeated observations should provide compatible measurements which will allow the evolution of the HPD performance to be investigated. This ion feedback monitor was developed using the Brunel [81] reconstruction package in the LHCb Gaudi software framework. The clustering algorithm used for this monitor comes from the LHCb RICH core software, and works slightly differently from the algorithms used for the PDTF and SSB analyses. While the definition of a cluster remains the same, this algorithm makes use of the ordering of hit pixels in the data. This means that fewer neighbours must be checked for each pixel hit.

Since the definition of a cluster used is unambiguous, all of the algorithms should return the same results when running over the same data. This was verified by producing a Gaudi implementation of the PDTF clustering algorithm, allowing the two algorithms to be directly compared. Initial comparisons showed that the RICH algorithm found fewer ion feedback clusters, and more total clusters than the PDTF algorithm. This indicated that the core software algorithm was splitting large clusters into multiple smaller clusters. This problem identified a bug in the core software's ordering of hits prior to clustering, and once this was corrected the two algorithms gave identical results.

In contrast to several other parameters that are monitored by the RICH online monitoring package, PANOPTES, the ion feedback rate cannot be extracted on an event-by-event basis. The ion feedback monitor calculates the ion feedback rate every N events, where N is set by the user, and outputs histograms displaying the results. These histograms can be set to either display results averaged over the entire run or the results from the last N events. Figure 4.10 shows two of the histograms available from the ion feedback monitoring. Additional histograms showing the cluster size distribution and number of clusters per event are also available. The fraction of events monitored by this algorithm can also be set, in order to reduce load on the monitoring farm.

It is anticipated that warnings will be sent to the user via the CAMERA tool (an application for reporting the detector status to the operator) if the ion feedback of any HPD exceeds a certain threshold, the value of which is to be decided. It is already possible to send the ion feedback rates calculated, along with their statistical errors, to the user via CAMERA, while in offline running these are output to a text file.

This algorithm has also been modified for offline use, and used to perform a detailed analysis of the evolution of the ion feedback rates for the HPDs mounted in the RICH detectors. Runs were taken at periods of approximately a month apart, and analysed to investigate how the ion feedback had changed. The data from these runs showed a good degree of correlation, with HPDs at higher (>1%) ion feedback rates generally

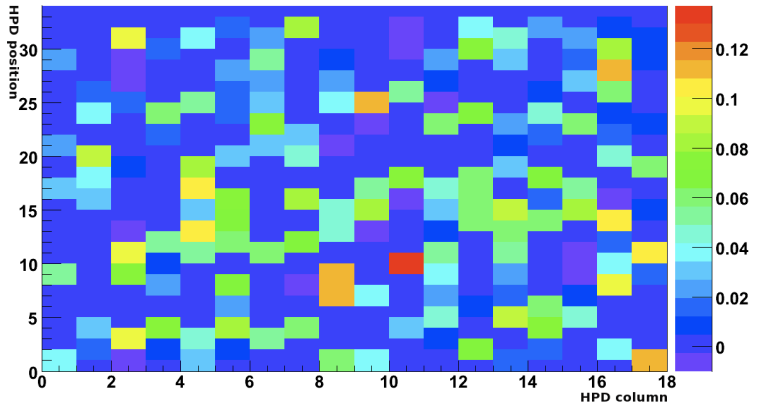


(a) Ion feedback rates

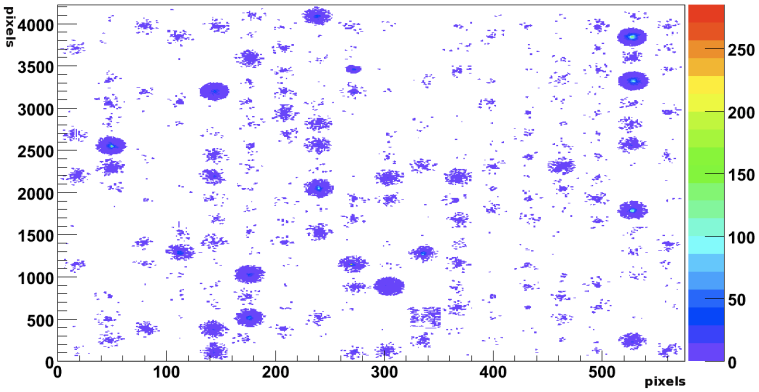


(b) cluster positions

**Figure 4.10:** Online monitoring histograms showing the ion feedback rate for individual HPDs and cluster position for each HPD in RICH2.

showing increases over time, suggesting degradation in performance perhaps linked to problems with the HPD vacuum. A number of HPDs have had to be replaced when they entered the glow discharge regime (52 as of May 2009, with approximately 55 additional HPDs expected to be replaced over LHCb's lifetime), although the majority of HPDs are still performing excellently. These studies are ongoing, and HPDs will continue to be replaced if more begin to malfunction.

## 4.3 RICH Test Beam

Several particle beams have been used to test the components of the RICH system in conditions approaching those they will face in final LHCb running. In October 2006 the final LHCb RICH test beam period took place at CERN. The particle beam was provided by the CERN SPS accelerator. A beam of $\pi^-$ particles at an energy of 80 GeV was used. The bunch spacing was 25ns, the same as will be provided by the LHC in full running. The bunches occurred in groups of 48, separated by a period of 23 $\mu$s, within a 2.2 s SPS spill, with the spills separated by a period of 12 s. The TTC

(Timing and Triggering Control) signals used by the readout electronics were provided by the SPS machine clock, meaning that the trigger is synchronous with the arrival time of the bunches.

### 4.3.1 Test Beam Detector Setup

The SSB was used as a scaled-down prototype RICH detector for these tests, and is shown in figure 4.11. The HPD enclosure of the SSB can accommodate 3 fully populated HPD columns, with feed-throughs from the exterior for all power supplies (high voltage (HV), low voltage (LV) and silicon bias) and data fibres (readout and TTC). The particle beam enters the SSB through the aluminium entrance window,

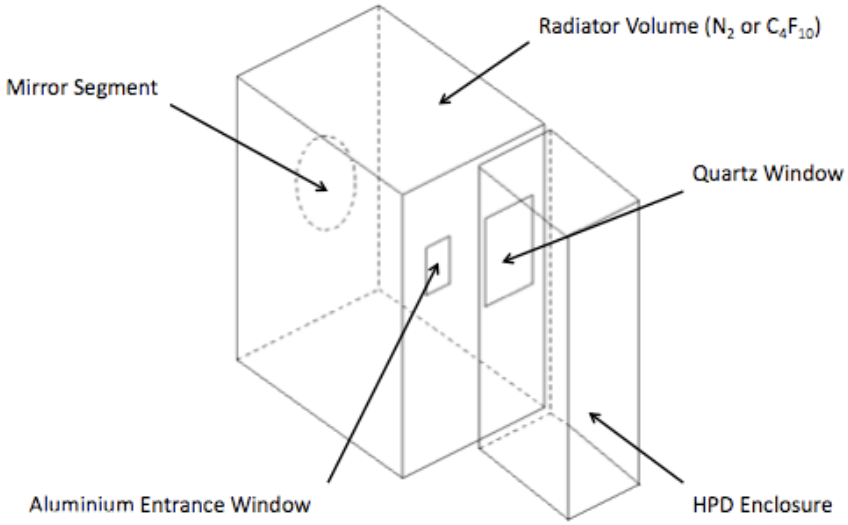


**Figure 4.11:** The SSB (Small Simple Box).

through which it passes into the radiator volume. The Cherenkov photons emitted in the radiator are focused into a ring by the spherical mirror segment, and reflected through the quartz window. They pass into the HPD enclosure where they strike the photodetector plane and are detected. The spherical mirror segment was mounted on three screws, which allowed the inclination of the mirror to be adjusted, and the Cherenkov ring to be positioned on different HPDs. A laser was used to find the vernier gauge settings for a variety of photon paths, which allowed the desired position to be set before starting a run.

The radiator volume was filled with one of two gas radiators, initially $N_2$ and later $C_4F_{10}$. These gases were chosen as radiators since their refractive indices (1.0003 and 1.0014 respectively) mean that they produce saturated ($\beta \approx 1$) Cherenkov photons at

significantly different angles. The saturated Cherenkov angle for $N_2$ results in photons that, in the SSB geometry, form a ring of approximately half the radius of the HPD photocathode, allowing the Cherenkov rings to be situated on a single HPD at a time. This is shown in figure 4.12(c). The saturated Cherenkov angle for $C_4F_{10}$ is higher, and so the Cherenkov rings produced in this radiator extend over several HPDs, as shown in figure 4.13.

Two bare HPD anodes were used for particle tracking. One anode was placed upstream and the other downstream of the SSB. The $\pi^-$ beam deposited energy in these anodes prior to entering and after leaving the SSB. These trackers were read out in an identical fashion to the HPDs (figures 4.12(a) and 4.12(b)), and the position of the hits on the anodes was used to infer the direction of the particles as they travelled through the SSB. Two scintillators were used to trigger on the bunches. Both scintillator paddles were placed upstream of the SSB and the tracking anode. A coincident signal in both of the scintillators was required to produce a trigger pulse.

The full LHCb readout and data acquisition system was used. The data received by the L0 boards was sent to the off-detector Level-1 (L1) electronics boards [82]. Each L1 board can receive data from up to 36 HPDs, and is responsible for selectively reducing the data, performing error checking, and sending the remaining data to the event builder. The data is zero-supressed and multiplexed before being sent on. In the context of the full LHCb experiment, the event builder sends the data to the HLT farm [83], however, no HLT was applied for the test beam, and so all data received by the event builder were recorded. The triggers from the scintillators were interpreted, and sent to the L0 boards by the 'ODIN' readout supervisor [84], which provided a link to the machine clock through the TTCmi (Timing and Trigger Control Machine Interface). The trigger rate that could be obtained within the test beam set-up was limited to 1-2 kHz due to the limited processing power of the single PC running the event builder. This PC was simultaneously used to run the online monitoring, which was also being used for the first time within the context of the full RICH readout chain[4]. Additional PCs were used to run the LV and HV controls, and to configure and monitor the L0 and L1 boards.

Runs were taken with beam for both $N_2$ and $C_4F_{10}$, under dark count conditions and with the HPDs under illumination from an LED within the SSB. Due to the size of the quartz window between the radiator volume and the HPD enclosure, and the limited movement range of the spherical mirror segment, only a small number of the HPDs mounted on the columns in the SSB could receive Cherenkov photons. Only 4 HPDs could be illuminated with $N_2$ Cherenkov rings, while 5 different mirror positions were possible with $C_4F_{10}$, illuminating 6 different HPDs with partial Cherenkov rings (either 3 or 4 HPDs could be illuminated at a time depending on the position chosen).

[4]This was used sparingly, since it further limited the throughput of the data acquisition.

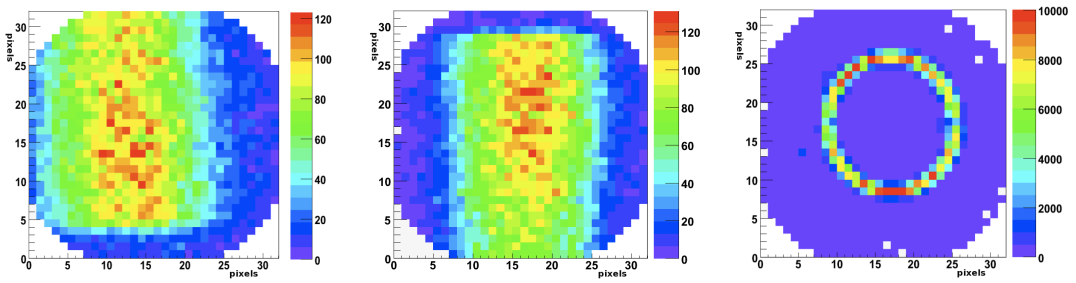


(a) Upstream Tracker (b) Downstream Tracker (c) $N_2$ Cherenkov Ring

**Figure 4.12:** Hit maps from an $N_2$ run of approximately 10k events, showing hits on the two trackers and a full Cherenkov ring on one HPD. The tracker images show the shape of the scintillator tiles used for triggering.

The test beam period was very successful; all elements of the detector and readout chain were fully functional, and a large amount of useful data was obtained from the HPDs. This data was subsequently used for a number analyses in order to assess various parameters of the detector performance. The Cherenkov angle resolution was investigated, along with the Cherenkov photon yields, and the rate of charge-sharing in the HPD silicon sensor. The test beam data was also used to investigate the RICH alignment procedure.

### 4.3.2 Test Beam Simulation

Simulated test beam data was also produced for use in various analyses. This was performed using the LHCb simulation package, Gauss [81]. There are two phases in a standard Gauss process; the generation phase and the simulation phase. The generation phase is responsible for the production of Monte Carlo (MC) particles, either by modelling p-p collisions using Pythia or Herwig and the subsequent b-decays with EvtGen, or by generating stable particles directly using a particle gun. During the simulation phase, the interaction of these particles with a detailed software detector description takes place. The interactions of the particles with matter are modelled using the Geant4 framework [85].

The software description of the test beam set-up is based on a modified version of the DC06 (Data Challenge 06, the LHCb simulation framework for Monte Carlo generation developed in 2006) RICH detector description. The trackers were implemented by adding two additional HPDs to the detector description in the correct position along the beam line in the global coordinate system. The HPDs in the photodetector planes have their MC hits assigned to the correct channel through comparing the position of the Geant4 (G4) hit to a list of HPD positions in the Conditions Database, which also stores the value of parameters such as gas pressure, temperature, refractive index, to be used by the simulation. This is not possible for the tracking HPDs which are outside

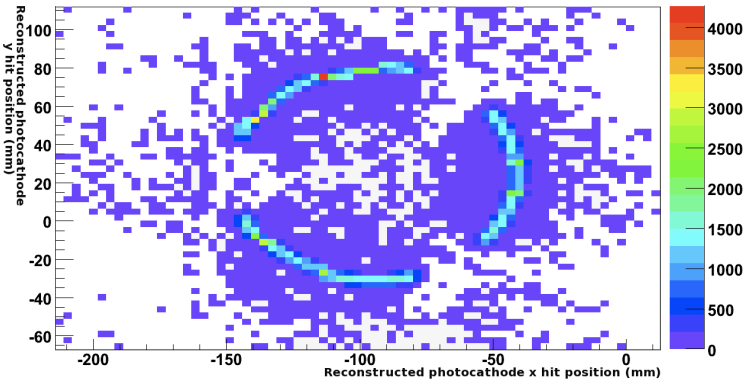


**Figure 4.13:** A reconstructed $C_4F_{10}$ ring from simulation, extending over 3 HPDs, shown in the local coordinate system of the photodetector plane. 5000 events were generated.

the RICH photodetector plane, and therefore do not have an entry in the database. Hence, the hits for these non-standard tracking HPDs had to be identified by their global position, and assigned to the correct HPD channel 'by hand', hard-coding the channel identifiers based on the global position of the hits.

An additional complication caused by the tracking HPDs is the extra background hits caused by scattering from unphysical volumes. Multiple particles are produced by interactions between the $\pi^-$ beam and HPD volumes that are not present for the bare HPD anodes, in particular the quartz windows. Particles resulting from the unwanted interactions are identified by the global position of their origin, and the volume which they originated in, and removed from the simulation to prevent them from generating Cherenkov photons or interacting with other volumes within the HPD. The G4 photoelectric process was also disabled for the tracking HPDs in order to prevent unphysical hits in the trackers.

The generation phase for the test beam simulation uses a particle gun to produce the 80 GeV $\pi^-$ beam. A number of adaptations were made to the particle gun in order to accurately match the beam produced by the SPS. The particle beam was not exclusively $\pi^-$, there was also contamination from other particles (although for $\pi^-$ the contamination was less than for $\pi^+$ from the SPS, which is why the negative beam was used). The beam was composed of 80 % pions, 10 % electrons, 7 % kaons and 3 % protons. This composition was also used for the simulated beam. Modifications were also made to allow multiple particles per event with different trajectories, setting the two and three particle contributions independently, and to provide a gaussian beam divergence. Once the Gauss output has been processed by Boole [81] (the LHCb digitisation package) the data can be analysed in an identical way to the real data. A fully digitised and reconstructed $C_4F_{10}$ ring from simulation is shown in figure 4.13.

Simulated datasets were produced for a range of scenarios, reflecting the various data runs taken during test beam period. The simulated events were analysed in parallel

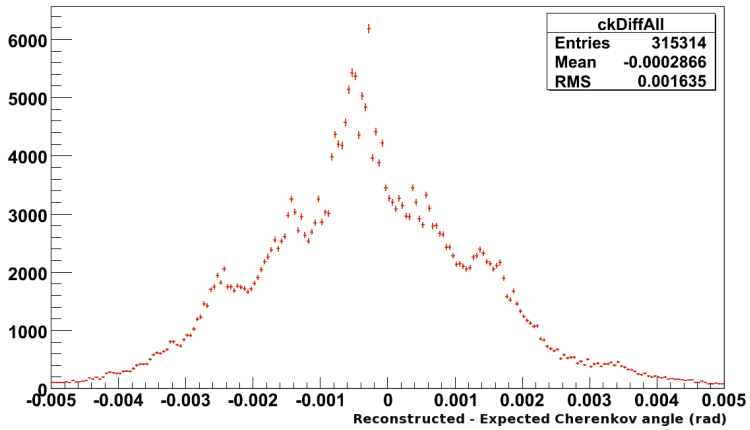


(a) Real Data

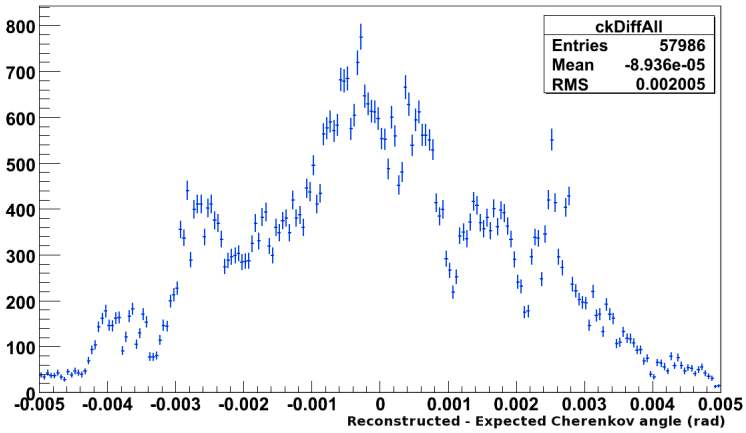


(b) MC Data

**Figure 4.14:** Comparison of (Reconstructed - Expected) Cherenkov angle for real (top) and simulated (bottom) $N_2$ data. The structure seen in both plots is due to pixelisation effects in the HPD anode.

with the real data, to aid in the understanding of various features of this data. This can be seen, for example, in figure 4.3.2 which shows the effect of HPD anode pixelisation on the reconstructed Cherenkov angle. Additionally, the comparison between simulated and real events allowed the validation of the simulation framework.

### 4.3.3 Results

Good agreement was found between the results from data and those from simulation. One of the key paramters to be measured was the Cherenkov angle resolution. The Cherenkov angle resolution obtained with $N_2$ (for which the mean Cherenkov angle $\langle\theta_c\rangle = 23.4$ mrad) was $\sigma = 0.296 \pm 0.003$ mrad, compared to $\sigma = 0.290 \pm 0.003$ mrad from simulation, where the errors quoted are statistical.

For $C_4F_{10}$, resolutions of $\sigma = 0.166 \pm 0.002$ mrad and $\sigma = 0.174 \pm 0.005$ mrad were found for data and simulation respectively. The mean Cherenkov angle in $C_4F_{10}$ initially

showed considerable disparity between simulation and data, but this was largely due to the unknown concentration of the radiator medium in this instance. The concentration finally used in the simulation was fine-tuned until the mean Cherenkov angle agreed for both data and simulation, at a value of $\langle\theta_c\rangle = 50.5$ mrad.

The unknown radiator purity also provided an additional complication in the analysis of the photoelectron yields in $C_4F_{10}$. Once this was taken this into consideration, the photoelectron yields from data for both radiators were compatible with the expected values, approximately 12 photons per ring in $N_2$, and 28 in $C_4F_{10}$. A full discussion of all the test beam analyses can be found in [86].

## 4.4 Conclusions

The RICH system is an essential element of the LHCb detector, and its performance will be crucial if LHCb is to fulfil its physics goals. The various components of the RICH detectors have been comprehensively tested at a number of stages throughout their integration, and large amounts of commissioning data have been taken.

As a result, the performance of the RICH detectors is well understood, and is expected to provide the necessary particle identification power for LHCb's physics measurements. The evolution of the HPD ion feedback characteristics is of concern, but continues to be carefully monitored, with HPDs being replaced if their performance degrades unacceptably. However, the vast majority of HPDs are still behaving well, and the RICH detectors are ready for physics data from the first LHC collisions.

# Chapter 5

# RICH Time Alignment

In order for any particle physics experiment to achieve optimum performance, each of the subdetectors must be carefully calibrated to operate with maximum efficiency. Throughout the construction and commissioning of the RICH detectors, many steps have been taken to ensure that each component is used as effectively as possible. An example of this is the preferential placement of high quantum efficiency, low background noise HPDs in the highest occupancy regions of the RICH detectors, as described in section 4.1.2.

An important aspect of the RICH detector calibration is time alignment. Each HPD has different timing properties, mainly due to variations in drift time for electrons in the silicon sensor. If the RICH detector is not correctly time aligned, the overall photon collection efficiency will be reduced, and there is the possibility that photons may be assigned to the wrong event, effectively increasing the number of background hits.

Ideally, each HPD would be individually adjusted to correct for timing variations, by setting the delay between the trigger signal and the beginning of the 25 ns wide strobe signal sent to the HPDs to trigger the readout. Unfortunately, this is not possible at the HPD level, as the delay of the strobe signal is set per L0 electronics board, each of which has two HPDs attached sharing a common timing, meaning that the L0 board is the smallest unit of the RICH detector that can be time aligned. To minimize the effects, HPDs with similar timing properties were paired together on L0 boards where possible. This is done by matching the leakage current of the two HPDs on the L0 board. The leakage current, measured in the silicon sensor in the absence of signal electrons, reduces the effective bias voltage over the silicon, and hence lowers the drift time for electrons.

To measure the timing profiles, allowing the optimum timing position for each L0 board to be found, and hence perform adjustments to maximise the timing overlap over the entire RICH detector, it was essential to design and implement a system to perform timing scans. The system uses a pulsed laser in order to test the HPD response obtained

when the delay between the pulse and the readout strobe is varied. The laser pulses are introduced into the RICH detector volumes via optical fibres, allowing the majority of the system to be kept remote from high-radiation areas.

## 5.1 Simulation

Simulations were carried out using the LHCb Gauss package, allowing the feasibility and expected performance of the laser pulser system to be assessed. For the simulation studies, a particle gun was used as the generation phase, and the simulation phase used the LHCb RICH subdetector description from DC06, neglecting the unnecessary subdetectors to decrease the CPU time required per event. Modifications had to be made to the standard Gauss ParticleGun to carry out these studies, as optical photons, which in Geant4 are classed as a different particle than gamma ray photons, could not be generated by the standard ParticleGun. The necessary interaction between Gauss and Geant4 was developed, allowing the generation of optical photons, and it is now available in more recent versions of the Gauss package.

In order to model the expected distribution of photons produced by the laser pulser, another modification to the ParticleGun was required, to produce a gaussian beam profile. The beam profile was extracted from data shown in figure 5.1.

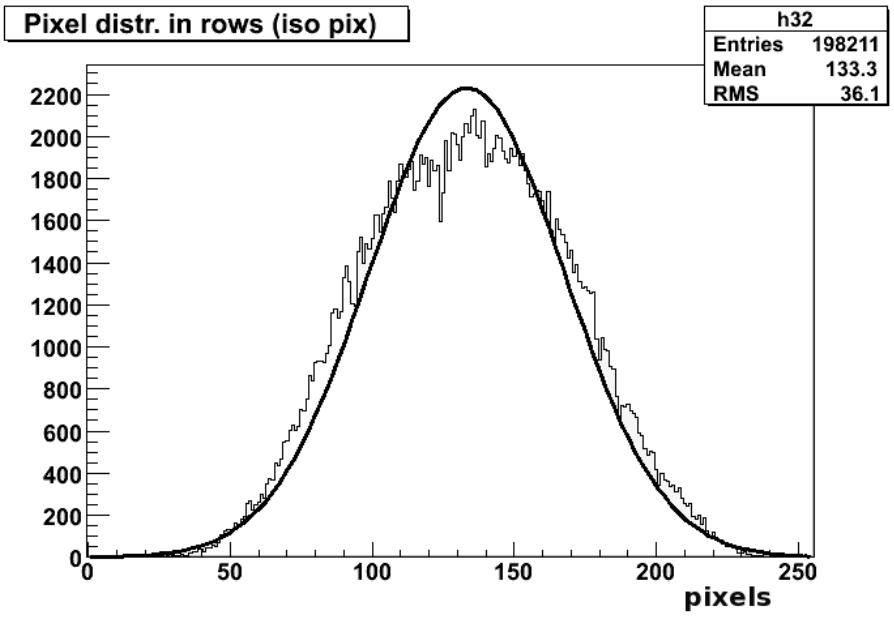


**Figure 5.1:** Beam profile of the bare optical fibre as seen by a HPD 9cm from the fibre. The profile is taken along the HPD x axis, in which direction the silicon sensor is divided in 256 ALICE pixels, compared to 32 pixels in the y direction.

This data was obtained by shining a bare optical fibre onto a single HPD from a fixed distance of 9cm. The spread of the beam therefore comes from the numerical

aperture of the fibre. It shows that the beam profile is only approximately gaussian, but fitting with a gaussian function was deemed to be satisfactory for the purposes of the feasibility studies to be carried out. The beam profile from the data using a gaussian approximation has an opening angle of $\sigma = 17.1$ mrad. This number was input into the simulation as the gaussian width of the photon beam.

The purpose of the simulation studies was to establish the effectiveness of various fibre positions, and hence find the ideal position for the optical fibres given the physical restrictions imposed. The main restrictions are that the fibre must be outside the detector acceptance during physics running, and must be in an accessible area. Another consideration is that the light intensity on each HPD is sufficiently high that the signal is above the background dark count noise rate, without increasing the power of the laser to a degree where the HPDs in the peak of the distribution are in danger of being saturated.

The favoured position would be to allow the reflection of the photons off both the spherical and plane mirrors prior to their incidence on the HPD plane, in order to mimic the path of Cherenkov photons in the RICH2 detector. However, this was found to be unfeasible as the angle necessary for reflection off both mirrors was too steep for the photons to reach the HPD plane. As a result, the notional position of the fibres was moved from a central position close to the beam pipe, to near the outer edge of the plane mirrors, from where the HPD plane will be illuminated directly, rather than via the mirrors.

Consequently, a scheme with two fibre positions was devised; a 'commissioning position' and a 'physics position'. During the commisioning of RICH2, no collisions will be taking place and so the constraint to be outside of the acceptance can be relaxed. By mounting the fibre within a simple mechanical support structure, it can be raised to a position where the entire HPD plane can be easily illuminated; this is the 'commissioning position'. This support structure will be removed after the comissioning phase, and subsequently the 'physics position', shown in figure 5.2, will be used. An optical splitter is used to provide a separate photon source for each side of RICH2.

From the 'physics position', all HPD columns can be illuminated, but with a significant variation in hit rates between columns. However, in combination with electronic calibrations from test pulse injections, illumination from this position should be adequate to identify any timing drifts given that a full timing scan has been performed previously from the commissioning position.

A related issue is the 'shadowing' of the photocathodes by the HPD mu-metal shields, discussed in section 4.1.2. The mu-metal is used as shielding from the magnetic fields produced by the LHCb dipole magnet, and protrudes several centimetres beyond the HPD tube body, potentially preventing light from the laser pulser reaching the HPD photocathode. This effect can be seen from the simulation in figure 5.3; the bottom

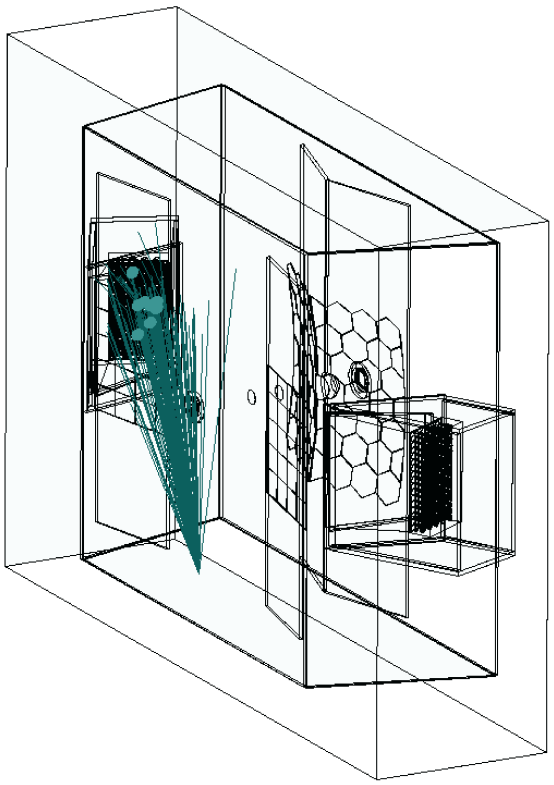

**Figure 5.2:** A visualisation of the RICH2 detector within the Gauss simulation package, showing a beam of photons being projected from the 'physics position' onto one of the HPD planes.

portions of the HPDs receive no hits, causing the photocathode image shapes to differ from the expected ellipses. However, for all HPDs in the photodetector plane, the majority of their photocathode can be illuminated by photons from the fibre in the physics position.

Another parameter than can be extracted from the simulation is the time spread of photons reaching the HPD plane due to different optical path lengths. This time spread, once considered in combination with the intrinsic pulse shape in time of the laser driver, must be much smaller than the L0 timing plateau for an accurate scan to be performed. This issue was of greater concern for the initial solution of reflecting the photons off both sets of mirrors; this solution gave a much greater optical path length overall, and greater potential path length differences for photons taking extreme paths. For the chosen positions, the full spread of hit times is very small, approximately 1.5 ns for the physics position, as can be seen in figure 5.4.

In RICH1, the space is extremely limited, and so there was no flexibility in the fibre placement. A detailed simulation study was not performed for the fibre positions in the RICH1 detector. The beam pipe runs inbetween the two RICH1 boxes, and this contributes to the geometric complications which make multiple fibres necessary for all

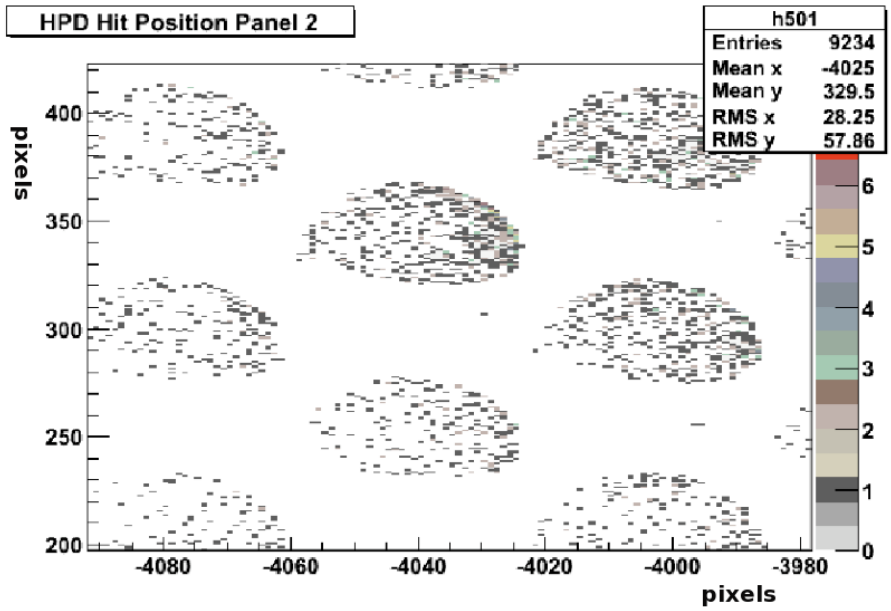


**Figure 5.3:** Simulated HPD hits demonstrating shadowing by the mu-metal magnetic shielding, for photons originating from the physics position. The x and y axes represent the x and y hit positions in the local photodetector plane.

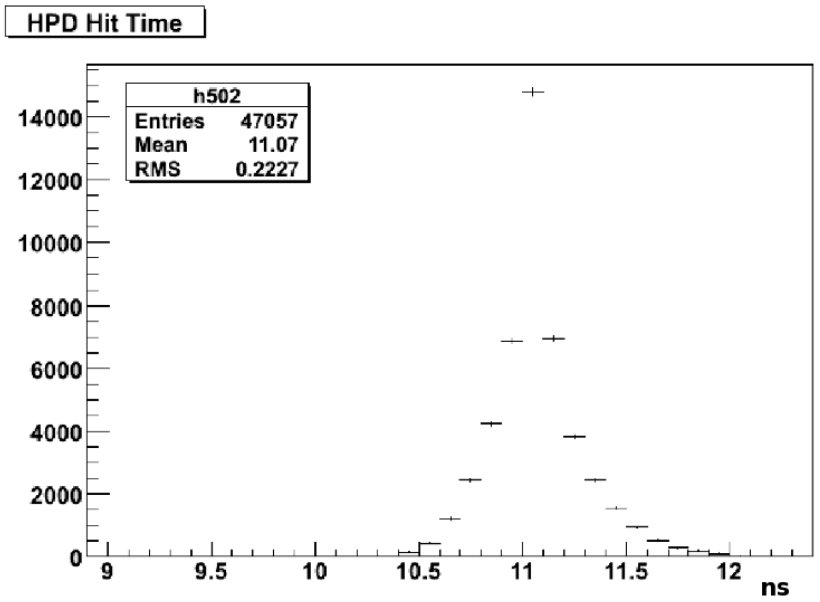


**Figure 5.4:** Simulated HPD hit arrival times in ns, for photons originating from the physics position.

of the RICH1 HPDs to be illuminated. Eight fibres were used to illuminate the RICH1 photodetector planes, four for the upper plane and four for the lower plane. The fibres are attached via a bracket to the inside of the HPD box, two at the 'top' and two at the 'bottom' (where top and bottom here refer to the top and bottom of the HPD columns) in pairs. This is shown in figure 5.5, in which the fibres are circled in red. The fibres

shine through the quartz entrance window to the HPD enclosure onto the HPDs in the opposite photodetector plane.

**Figure 5.5:** Position of laser pulser fibres in the RICH1 upper box. The fibres are held in place by a bracket.

## 5.2 Hardware

The following section outlines the various hardware elements of the laser pulser system. A custom-designed electronics board, which plugs into a standard VME crate, has been produced to house the majority of the electronics. This board was designed by Johan Morant, and is known as the JOLI (JOhan Laser Interface) board.

### 5.2.1 TTCrx Chip

The TTCrx ASIC[1] is responsible for receiving clock and trigger signals, providing an interface to the LHC TTC (Timing and Triggering Control) system. Each L0 board has its own TTCrx chip, as shown in figure 4.5, and one is used by the JOLI board also. The TTC data stream is divided into 2 communication channels; channel A contains trigger decisions (in the case of the RICH it will tell the HPDs whether they should read out the event or not, and for the laser system it will determine whether the laser is pulsed or not) and channel B contains configuration commands for the TTCrx chip. Channel B data can be sent to all TTCrx chips via a broadcast command, or to specific chips via individually-addressed commands, using the 14-bit TTCrx ID to specify which chip the data is destined for. The internal registers of the TTCrx chip can be set either via the optical fibre link or an I2C bus.

The length of the interval between receipt of a trigger signal in channel A, and the subsequent relaying of the trigger by the TTCrx chip is determined by two delay pipelines - a coarse delay and a fine delay. The coarse delay can be incremented in 25 ns steps;

[1] Application Specific Integrated Circuit.

since the frequency of bunch crossings at the LHC is 40 MHz, varying the coarse delay essentially has the effect of moving between different events. The maximum delay that can be implemented via the coarse delay is 0.375 $\mu$s (15 bunch crossings). If we consider coarse delay as moving in time from event to event, then fine delay controls the timing within that event. The fine delay can be varied in steps of 104 ps between 0 and 25 ns, hence the total delay that can be applied by the TTCrx chip is 0.4 $\mu$s. A useful additional output of the TTCrx chip is the TTC Ready signal, which is high or low depending on whether there is a TTC signal present. The JOLI board is the only piece of RICH electronics that allows this signal to be monitored, and so is used by the RICH to ensure that a TTC signal is available during operation.

### 5.2.2 SPECS

SPECS (Serial Protocol for the Experimental Control System) is used for the slow control of the experiment electronics. The system is comprised of SPECS masters, 4 of which are combined to make up a SPECS master board, and SPECS slaves which are located in close proximity to the detector electronics. The SPECS master board is based on a standard PCI card, and is generally located in a control Room PC. Each of the SPECS masters on the board operates separately, and can control up to 32 separate SPECS slaves. Communication between master and slaves is based on 4 lines (MS_SDA, MS_SCL, SM_SDA and SM_SCL, the data and clock signals respectively for master-to-slave and slave-to-master communication) transmitted via a standard category 5 network cable.

The SPECS slave is built as a mezzanine card and can communicate with the detector electronics via a number of different buses; there are 16 JTAG outputs, 16 I2C (Inter-Integrated Circuit) outputs (15 long distance plus 1 short distance 'internal' bus) and a parallel bus. It also has 32 I/O pins each of which can be set to read or write by changing the contents of a configuration register in the SPECS slave. One of these pins will be used to monitor the state of the TTC Ready signal mentioned previously. Due to the high-radiation environment the SPECS slave will be required to work in, the SPECS slave is designed to be radiation tolerant up to 10 krad.

### 5.2.3 Pulsed Laser

The source used to produce the laser pulses is a Hamamatsu picosecond light pulser (PLP10-065C). The unit consists of a controller and a laser diode head. The pulses produced have a wavelength of 655 nm, which is well within the sensitive rage of the HPD photocathode (although not at the peak efficiency range), and have a pulse width $<$100 ps.

The data flow for the laser pulser system is as follows: Control software → SPECS → TTCrx → Pulsed Laser

## 5.3 Software Design and Implementation

### 5.3.1 PVSS

The software for controlling the laser pulser system was created using PVSS[2], a Supervisory Control And Data Aquisition (SCADA) System that has been adopted throughout the LHC project as the software interface to both detector and accelerator hardware. PVSS allows users to create GUIs (Graphical User Interfaces) for the controlling, data monitoring and archiving, and error handling of hardware devices. Drivers to interface a large number of standard commercial units are supported by PVSS , and components for these systems and common CERN proprietary systems are available as part of the JCOP (Joint Controls Project) framework [87].

These components include libraries and scripts in a 'C-like' control language, Data Point types and instances and panels. Panels are what make up the GUI for PVSS projects. Data Points are where PVSS stores all of the information about the state of a system; Data Point Types are similar to objects in object-oriented programming, having a number of data members of various types, although do not have their own methods. The JCOP framework also provides guidelines for users creating their own PVSS projects, in order that they can be more easily integrated into the overall system.

### 5.3.2 Laser Pulser Controls

The software controls for the laser pulser must interface with SPECS, which in turn will communicate with the dedicated TTCrx chip for the system. Communication between the SPECS slave and TTCrx is implemented via the internal, short-range I2C bus.

The PVSS control panel for the system first selects the correct SPECS server, and then allows the user to select a SPECS master from the 4 available on the master board. Once the desired master is selected, a reset command is sent to it and the clock speed for this master is set to 60 kHz, as the TTCrx chip does not respond to data being sent at higher rates. Buttons are available on the User Interface panel that allow both the master and slave to be reset should that become necessary. The SPECS write function requires the slave to which the data is to be sent to be specified, but this can safely be hard-coded as the SPECS for this sytem will always be between a single master and slave. The correct bus is also hard coded so that all data will be sent via the internal I2C bus. Once set-up in this way, the SPECS slave can send data to the TTCrx chip.

[2] An acronym from its German name, "Prozess Visualisierungs und Steuerungs System".

### Writing/Reading Registers

Writing and reading the TTCrx registers via I2C is slightly different to doing so via JTAG or the parallel bus; rather than sending a single write command containing the internal register address and the data to be written to this address, writing to I2C is a two step process, involving two I2C-specific registers, I2C_pointer and I2C_data. Firstly, a command is sent to write into the I2C_pointer the address of the register to which the data is to be written (or read back). The appropriate read or write command is then sent addressed to I2C_data, which stores the data associated with the register addressed by I2C_pointer. Whenever reading or writing to a TTCrx register is referred to in this document, this method (shown in figure 5.6) is implied.

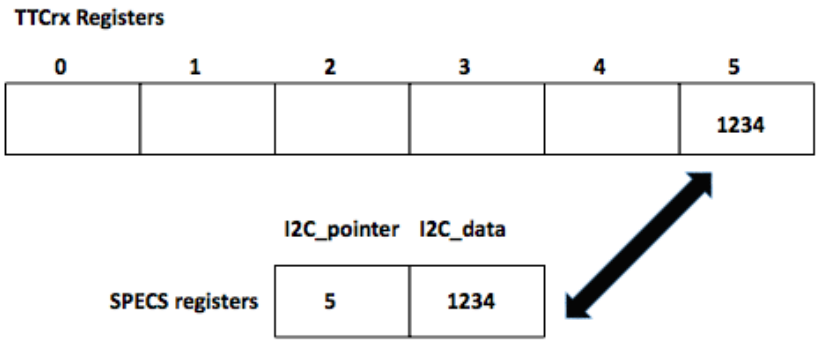


**Figure 5.6:** Writing to the TTCrx via I2C.

The first action that should be carried out is to set the TTCrx configuration register, which ensures that the correct clock is used by the chip. As the contents of this register do not need to change, reading it back and checking the contents is a good test that communication through the entire system is working correctly, and this is implemented as a test button on the UI panel.

### Setting Delays

The other important registers are the coarse and fine delay. The coarse delay is simple to set, the contents of four bits (corresponding to 16 possible coarse delay settings) in the relevant register being directly proportional to the coarse delay that is implemented. However, the fine delay architecture is based on two delay loops and so the register content is a function of the settings of these two loops ($n$ and $m$), rather than the overall delay value.

A calculation must be performed to transform the user-input $K$ value ($K \times 104.17$ ps gives the total fine delay) into the $n$ & $m$ values which are concatenated as $nm$ to give the final register content. As a result, simply reading back the register content is not useful to the user. To overcome this, when the fine delay is written, the delay $K$ value

and the $nm$ register content are both stored in a data point; when the fine delay is read back the register content is compared to the content stored in the data point. If the two $nm$ values match, the $K$ value stored in the data point is returned to the user. A look-up table converting $K$ to $nm$ values and vice-versa could be used instead, but the chosen procedure has a useful feature; if the stored and read-back values do not match, this means that there was a problem reading the register or there has been an upset to the chip, since the fine delay is only set via the UI panel. An error message will be returned instead of a delay value immediately alerting the user to the fact that the operation was not completed correctly.

Functionality was also included to allow the coarse and fine delay to be written via a TCP connection from another PC. This was required for the laboratory tests that will be discussed later. Toggling between 'interactive' control via the UI panel and 'TCP control' from a remote PC was implemented, with write actions to the TTCrx from the UI panel disabled when in TCP control mode; read actions can still be carried out to check that the correct values are stored. In order to write via TCP, a simple concatenation of the desired coarse and fine settings must be sent in the format ccfff (with c & f representing the digits of the coarse and fine settings respectively).

## 5.4 Preliminary Laboratory Tests

The first tests of the system were performed in the laboratory using the SSB. A system was already in place in the SSB to perform timing scans on individual columns, and the framework of this test procedure was used to test the new system. Within the SSB, the optical fibre carrying the light pulses from the laser diode is coupled to an optical splitter, which allows a separate fibre to be positioned in front of every HPD in order to provide optimal illumination for the scan. The control of the standard HPD column tests and interpretation of the readout from the protype L1 boards used in the SSB lab was handled by a set of LabView applications.

In the final system, there are two possible methods of varying the timing of the laser pulse relative to the readout strobe; one can vary either the delay of the laser or the delay in the TTCrx chips on the L0 boards. The former option was chosen for the laboratory tests. This provided a more robust test of the laser pulser system, and was less computationally intensive than automating a procedure for setting the L0 TTCrx chips in the SSB lab[3]. The same procedure was used for the individual column test, mentioned in section 4.1.3, and so the only change that needed to be made to the test program was the way in which the delay of the laser pulses was set. The LabView controls write to a TTCrx chip via the TTC fibre, so an option was added to send these delay settings to the PVSS pulser controls via a TCP connection.

[3]This facility is available in the full ECS at the LHCb pit, but not in the SSB system.

The first version of the system tested was composed of discrete components chained together; the SPECS slave was mounted on a 'croquette' test board provide by the Orsay group who are responsible for the SPECS protocol. This board allowed easy access to test points in order that the TTCrx could be probed to ensure that signals were being correctly sent and received.

### 5.4.1 Laboratory Test Results

The preliminary laboratory tests were very useful for finding bugs in the system. Once these bugs were solved, it was possible to carry out successful timing scans on a column in the SSB. The shape of the profile, and the width of the timing overlap for HPDs on the same L0 board (approximately 16 ns) were both consistent with data obtained from the timing scans performed as part of the HPD column tests. The position of the plateau, however, was shifted by several nanoseconds due to changes in cable lengths.

Timing scans we performed varying the delay of the laser in steps of approximately 1 ns (10 fine delay divisions) over a range of 70 ns. 1000 triggers were taken at each setting, which provided sufficient data to ascertain that the system was working satisfactorily.

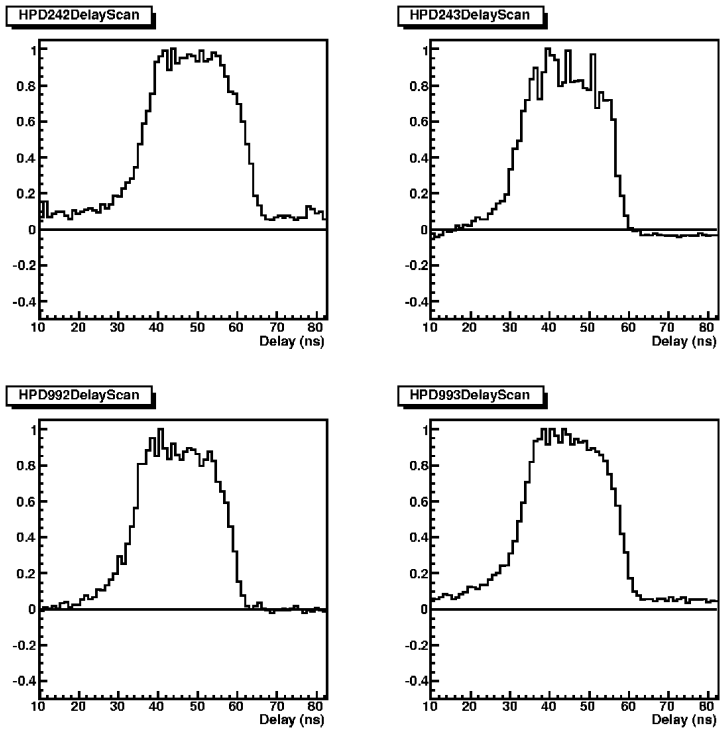


**Figure 5.7:** A selection of HPD timing scans from laboratory system tests. The timing profiles have been normalised and had their dark count rates - extracted from a separate dark count run - subtracted. This can be seen from the fact that the upper right scan dips below zero at the extremes of the scan range; this would imply that the dark count rate from the dedicated run was higher than that observed during the timing scan.

The data were analysed using stand-alone code based on a framework developed for LHCb RICH testbeam DAQ[4]. The results of this analysis can be seen in figure 5.7. The effect of charge sharing and backscattering of photoelectrons on the shape of the timing scan can be observed from these results. In both these effects, the number of electron/hole pairs produced in the silicon sensor for any given pixel is reduced compared to a 'standard' hit. Consequently, the signal rise time in each of these pixels is increased, and it takes longer for the discrimination level[5] to be reached. As a result, these hits are time-walked, appearing later in the scan than would otherwise be expected. This effect is visible as an excess of hits on the trailing (ie lower delay, on the left-hand side of the plots) edge of the distribution.

## 5.5 Installation and Integration

The hardware for the system was successfully installed at the LHCb pit in late 2007. The laser driver and JOLI control board are located in point D3, which also houses the high voltage controls for the RICH. Aside from the pulsed laser, there is also a continuous wave laser present for general illumination of the two RICH detectors (such as during HV ramping, to ensure proper operation of the HPDs). The continuous laser light is introduced into the RICH volume via the same optical fibres as the pulsed laser, and so the two must be physically swapped in order to move between pulsed and continuous wave illumination. These fibres are part of the fibre bundles used to send the data from the L0 GOL (Gigabit Optical Link) to the L1 readout electronics. The intensity of the pulse can be varied from the laser driver head, and was adjusted to provide the maximum number of photons per pulse possible without activating the RICH light leak detector, or saturating any HPDs. This level resulted in an average of approximately 180 HPD hits in RICH2 per pulse. The continuous laser was adjusted similarly using an air gap attenuator system.

The triggering of the HPDs and the laser is controlled by the LHCb TFC (Timing and Fast Control) project. A specific Channel A TTC command, designated trigger type C, is required to pulse the laser and is selected in the ODIN readout supervisor for the RICH. The 'Trigger Delay' parameter in the TFC was set in order to compensate for the time required for propagation of signals and arrival time of the laser pulses. The facility exists to automate timing scans, by using 'recipes' from the RICH ECS to step through L0 TTCrx settings. This automation was used for the RICH1 scan, and will be used for all subsequent scans, while for the RICH2 scan (which was performed earlier) the settings for the TTCrx laser were set manually at each timing step.

[4]Prior to October 2005, when a final testbeam took place using the Gaudi framework.
[5]Determined by the threshold settings in the pixel chip.

## 5.6 RICH Timing Scans

A timing scan was first performed for the RICH2 detector, varying the laser delay over a range of 50 ns, in steps of 2 ns. 100k triggers were recorded for each timing setting. The range for the scan was established by finding at which points the average HPD occupancy, taken from the RICH online monitoring, returns to the same level as is seen without any illumination, approximately 30 hits per event over the whole of RICH2. This background comes partly from HPD dark counts, partly from stray light within the RICH2 volume, and partly from the HPDs which were operating in the glow discharge regime, discussed in chapter 4.

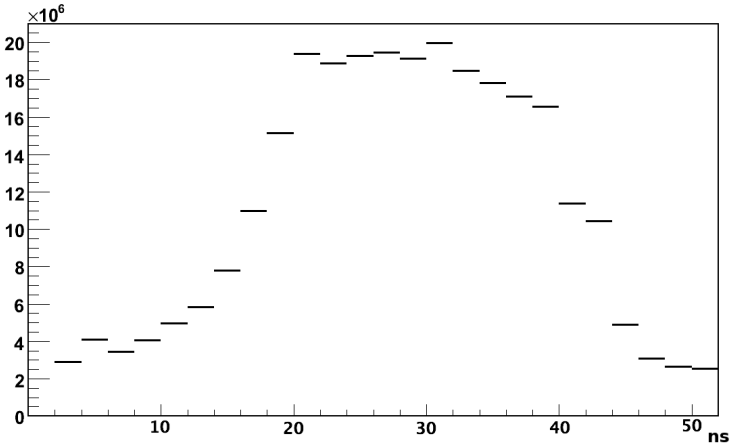


**Figure 5.8:** A plot showing the total number of hits in RICH2 for each laser delay setting, displayed in ns.

Figure 5.8 is an integrated timing scan, showing the overall timing profile for the RICH2 detector. It can be seen that this overall timing scan, showing the combined contribution from nearly 300 HPDs, is slightly broader than the timing scans for individual HPDs shown in figure 5.7, as would be expected. Since HPDs cannot be individually adjusted, the timing scan data is analysed by L0 board. Figure 5.9 shows the timing scans for two typical L0 boards. It can be seen that the background levels in 5.9(a) and 5.9(b) are significantly different, approximately 0.15 hits/event and 1.1 hits/event respectively. These differences are consistent with variations in HPD performance, and a range of background levels are observed in the timing scan data. Time walk effects resulting from charge-sharing and backscatter can be seen very clearly in this data, not only in the excess of hits on the trailing edge, but also in the slope of the plateau of the distribution.

### 5.6.1 Analysis

In order to determine the timing adjustments which must be applied to the L0 TTCrx settings, it is necessary to define and locate the beginning and end of the timing plateau

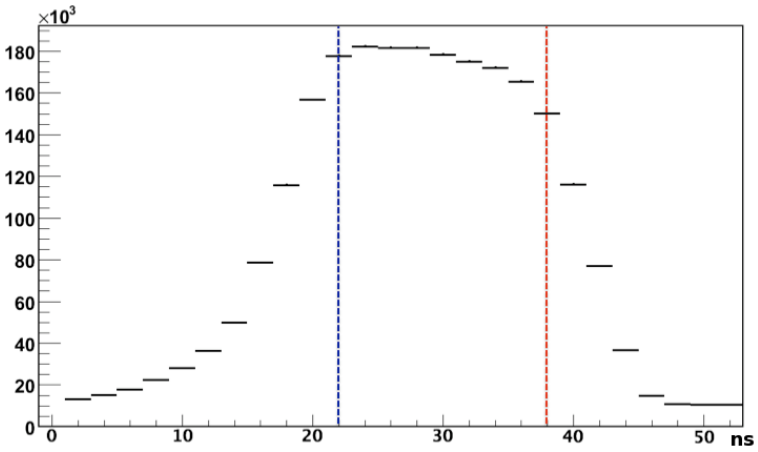


(a) Timing scan for L0 board 118

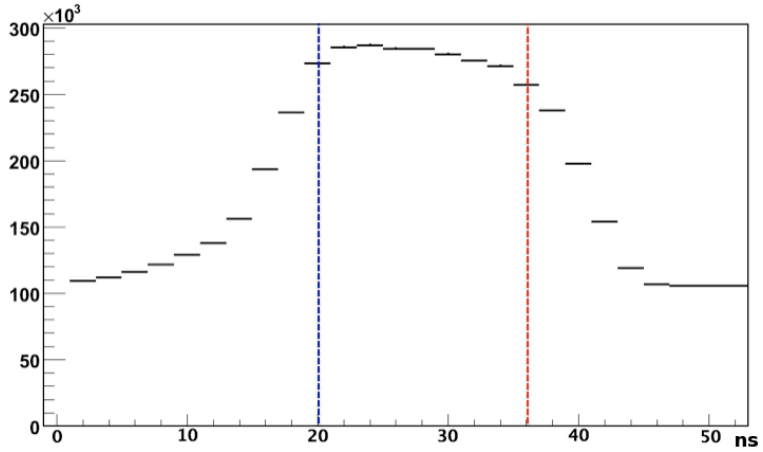


(b) Timing scan for L0 board 152

**Figure 5.9:** Timing scans for 2 L0 boards with different background levels, with the 'turn on' and 'turn off' points of the plateau marked.

for each board. The timing scan analysis algorithm first locates the maxiumum and minimum of a given L0 profile. The 'turn on' and 'turn off' of the timing plateau are defined as the points at which the profile rises above or drops below 90% of the maximum height of plateau above the background level, ie $0.9 \times (N_{max} - N_{min})$. The algorithm then scans through the entries and looks for the first point at which this criteria is met, defining this as the 'turn on' time; the 'turn off' time is then defined as the first point at which this criteria is no longer met, given that the 'turn on' time has already been located. These are represented by the blue and red lines on figure 5.9.

For several of the L0 boards, the analysis procedure did not immediately yield sensible figures for the timing plateau position; this was due to intermittently noisy pixels, which caused sharp spikes in the timing profile. By masking these pixels in the data, the timing profile could be recovered, and useful results were obtained. However, for one of the boards, L0 89 which is shown in figure 5.10, it was not possible to extract a timing plateau from the data. This was due to one of the HPDs on the board showing 'glow

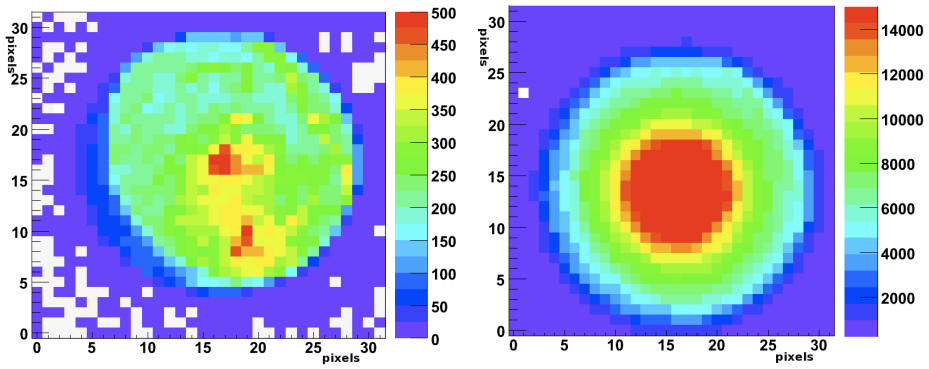


(a) HPD 0, behaving normally

(b) HPD 1, in 'glow discharge' regime

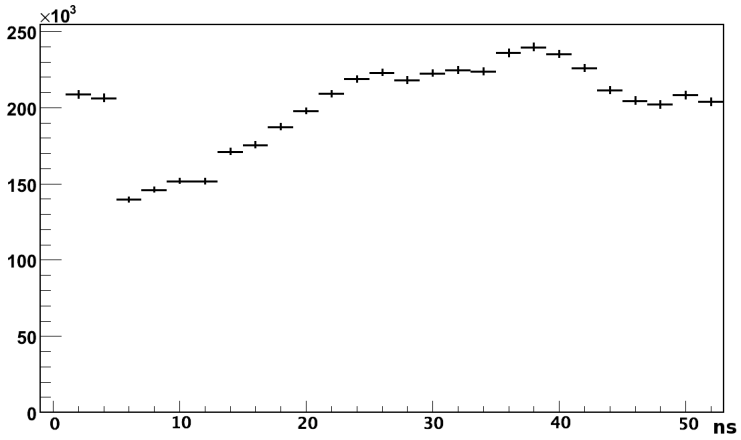


(c) Timing scan for L0 board 89

**Figure 5.10:** The HPD hit maps and timing scan for L0 board 89, for which the plateau position could not be extracted. The extremely large central peak is typical behaviour for an HPD with very high ion feedback.

discharge' behaviour; figures 5.10(a) and 5.10(b) show the two HPDs on the board, the former is behaving normally whereas the latter is demonstrating undesirable ion feedback characteristics.

The extremely high occupancy, largely concentrated in the centre of the HPD, is typical behaviour for a high ion feedback HPD. The 'glow discharge' behaviour results in an elevated and variable noise level, which can be seen in figure 5.10(c). This behaviour is not correctable offline, and so a plateau position for this board cannot be found. This L0 board, along with another board which was disconnected due to a readout problem, were both excluded from the analysis. These boards were assigned the average timing properties from the RICH2 sample as a temporary setting. Careful monitoring of the RICH performance will mean that malfunctioning HPDs and L0 boards can be identified, and will be removed from the RICH detectors and replaced at the first available opportunity.

### 5.6.2 Results

The compiled results for the RICH2 scan can be seen in figure 5.11. These results show that all of the L0 boards have plateaus which at least partly overlap with the nominal readout strobe position. However, it is also obvious that for most L0 boards, adjustments are possible which will increase the proportion of hits falling within the readout strobe. Additionally, we have seen that the low-delay edge contains a larger proportion of the hits than the high-delay edge, due to time-walk effects, and so it is preferable to include this portion of the profile in the readout strobe if complete inclusion of the timing plateau is not possible.

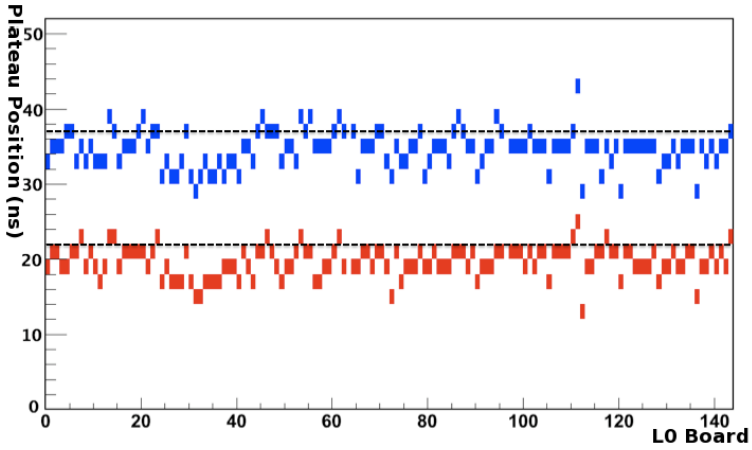


**Figure 5.11:** Timing plateau positions for all L0 boards in RICH2. The x axis shows an L0 board reference number, internal to the analysis algorithm and mapped to the hardware L0 ID numbers, while the y axis shows the position in ns of the timing plateau, with red and blue representing 'turn on' and 'turn off' points respectively. The dotted lines show the nominal position of the HPD readout strobe, which the L0 board timing should be adjusted with respect to.

A timing scan was also performed for RICH1. This timing scan used the automated procedure that will be adopted for all subsequent timing scans. The laser timing remains constant and the delays within the L0 TTCrx chips are varied. Consequently, the timing profiles obtained using this scheme are flipped along the y-axis compared to the RICH2 profiles. This scan used timing steps of 1 ns, with 10k triggers for each step, and was analysed in the same way as the RICH2 timing scan. Several HPDs in the RICH1 data did not have sufficient hits for an accurate timing profile to be extracted due to their position in the photodetector plane; these L0 boards were assigned the timing adjustments corresponding to the average for RICH1 overall. A $\sim$6 ns systematic shift was observed between the timing properties for the RICH1 upper and lower boxes; this shift has been attributed to differences between the fibres used to transport the laser pulses to the upper and lower boxes, and has been compensated for in the timing adjustments. The timing profiles for all the included L0 boards can be found in Appendix A.

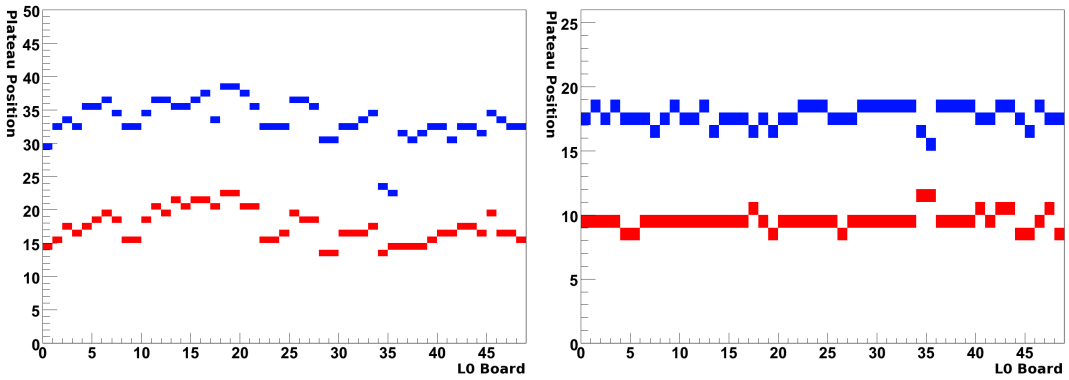


(a) Before Alignment (b) After Alignment

**Figure 5.12:** Plots showing the plateau positions for the upper RICH1 box before and after alignment. The different y-scales reflect the coarseness of the scans (following alignment, the scan was performed in steps of 2 ns). The deviation post aligment of L0 boards 36 and 37 is due to their narrow timing profiles.

## 5.7 Conclusions

The laser pulser timing system has been installed in the RICH detectors, timing scans have been successfully performed, the data analysed, and the necessary timing adjustments applied to the L0 boards. Both the manual procedure used for RICH2 and the automated technique used for RICH1 worked very well. The results of these scans show that the fine time adjustments required to maximise the timing overlap of the L0 boards are generally small, and the RICH detectors already had reasonably good timing properties. Nevertheless, as figure 5.12 shows, an improvement is achieved by applying the time alignment procedure. The system will be very useful in the future, when it can be used during periods with no LHC beam in order to test whether any timing drifts have occurred during the running of the experiment. The timing scans will also be repeated as HPD replacements are made to remove the malfunctioning glow discharge HPDs.

The pulsed laser has also been used to make more accurate measurements of the ion feedback for the HPDs in the RICH detectors. The readout strobe was delayed with respect to the laser pulse in order to collect only the delayed ion feedback hits, rather than the ion feedback hits plus direct signal hits that are collected when using continuous wave illumination. This will also aid the identification of HPDs that may malfunction in the future.

# Chapter 6

# $B_s^0 \to \phi\phi$ Event Selection Studies

## 6.1 Introduction

The RICH particle identification system is of crucial importance for many of the analyses LHCb will undertake, and this is especially true for purely hadronic decays such as $B_s^0 \to \phi\phi$, which has four kaons in its final state. This channel offers an opportunity to search for effects of physics beyond the Standard Model through measurements of the total weak phase in the decay.

### 6.1.1 $B_s^0 \to \phi\phi$ in the Standard Model

$B_s^0 \to \phi\phi$ is a flavour-changing neutral current (FCNC) decay, and hence is forbidden at tree level in the Standard Model. It proceeds via loop diagrams, with the gluonic penguin shown in figure 6.1(a) expected to be the dominant contribution, due to the relative strengths of the strong and weak couplings at the LHC energy scale.

Since the same final state is accessible to both $B_s^0$ and $\overline{B}_s^0$, CP violation can occur in this channel through interference between the contributions from decays with and without mixing, as discussed in section 2.3.4. These interfering amplitudes can introduce a phase to to CP violation parameter $\lambda_f$, where $\lambda_f$ has the same definition as in section 2.3.4, i.e.

$$\lambda_f \equiv \frac{q}{p}\frac{\overline{A}_f}{A_f} \tag{6.1}$$

The phase of $\lambda_f$ is an observable, and represents the total weak phase for the decay.

In this channel, the $B_s^0$ meson decays to a CP eigenstate,

$$\mathcal{CP}|f\rangle = \pm|f\rangle \tag{6.2}$$

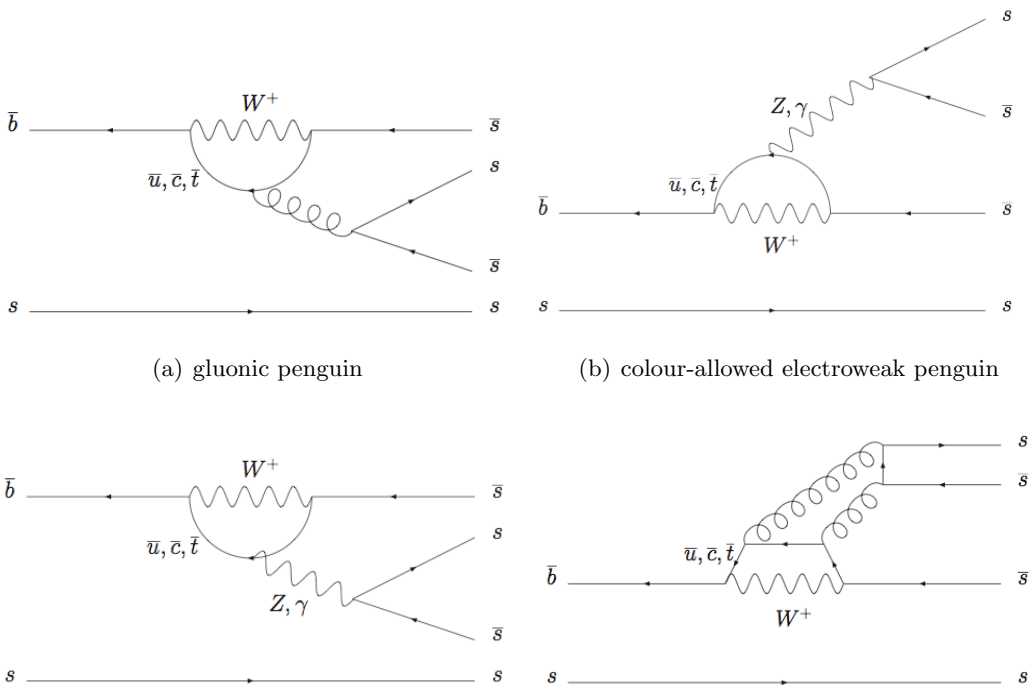


(a) gluonic penguin

(b) colour-allowed electroweak penguin

(c) colour-suppressed electroweak penguin

(d) singlet penguin

**Figure 6.1:** Possible diagrams for for $B_s^0 \to \phi\phi$.

and consequently,

$$\lambda_f \equiv (\eta_{CP}) \frac{q}{p} \frac{\overline{A}_{\overline{f}}}{A_f} \tag{6.3}$$

Where $\eta_{CP}$ can take values $\pm 1$ depending on whether the final state is CP-even or CP-odd. CP violation arising from the $B_s^0 - \overline{B}_s^0$ mixing amplitude is assumed to be small,

$$\left|\frac{q}{p}\right| \approx 1 \tag{6.4}$$

therefore,

$$\frac{q}{p} = e^{-i\Phi_M} \tag{6.5}$$

where $\Phi_M$ is the weak phase due to mixing.

Considering now the decay process, we can define the decay amplitudes as follows:

$$\begin{aligned} A_f &= e^{+i\varphi_f} |M_f| e^{i\delta_f} \\ \overline{A}_f &= e^{-i\varphi_f} |M_f| e^{i\delta_f} \end{aligned} \tag{6.6}$$

Here, $|M_f|e^{i\delta_f}$ is the hadronic matrix element, containing the hadronic dynamics of the decay, which is common to both amplitudes, and $e^{\pm i\varphi_f}$ comes from the CKM contribution. These amplitudes are a simplified version of the more general form of the amplitudes for $B$ meson decays, which includes two CKM factors - no more than

two contributions can be included, due to the unitarity constraint on the CKM matrix elements:

$$\sum_{q=u,c,t} V_{qs}^* V_{qb} = 0 \tag{6.7}$$

Penguin processes in $B_s^0 \to \phi\phi$ are dominated by the contribution from the $t$ quark, so the amplitudes reduce to those in equation 6.6. By substituting equations 6.5 and 6.6 into equation 6.3, we obtain

$$\begin{aligned} \lambda_f &= \pm e^{-i\Phi_M} \left( \frac{e^{-i\varphi_f}}{e^{+i\varphi_f}} \right) \\ &= \pm e^{-i(\Phi_M - 2\varphi_f)} \\ &= \pm e^{-i(\Phi_M - \Phi_D)} \end{aligned} \tag{6.8}$$

where $\Phi_D$ is the contribution to the total weak phase due to the decay amplitudes. The sign of the expression is due to the value of $\eta_{CP}$. Both $\Phi_M$ and $\Phi_D$ are subject to an arbitrary phase arising from the $\mathcal{CP}$ convention of the $B_s^0$ meson, and so cannot be separately measured. However, this common $\mathcal{CP}$ phase cancels in expression 6.8, allowing an observable CP-violating weak phase to be defined:

$$\Phi = \Phi_M - \Phi_D \tag{6.9}$$

By considering the Feynman diagrams associated with $B_s^0 - \overline{B}_s^0$ mixing, shown in figure 6.2, the CKM elements contributing to the mixing part of the process can be determined. The box diagrams are dominated by the contribution from the $t$ quark due to

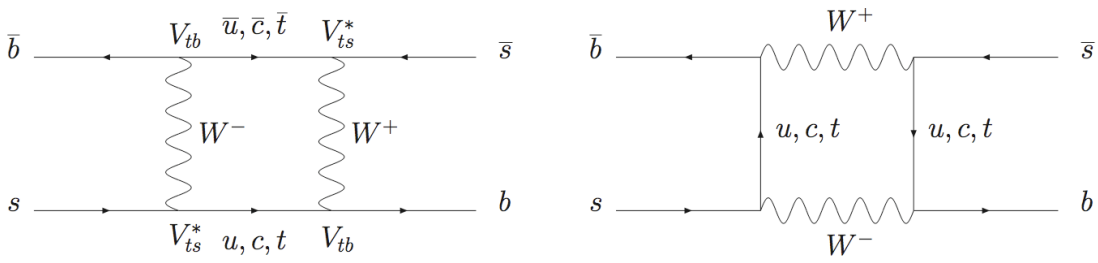


**Figure 6.2:** Box diagrams contributing to $B_s^0 - \overline{B}_s^0$ mixing.

its large mass, and so contributions from the lighter quarks can be neglected. Thus, by simply reading off the CKM element associated with each vertex, the CKM contribution is given by

$$V_{tb} V_{ts}^* V_{tb} V_{ts}^* \tag{6.10}$$

and the phase is therefore

$$\Phi_M = 2\ arg(V_{tb} V_{ts}^*) \tag{6.11}$$

Likewise, the CKM contribution from the decay process can be determined by consid-

ering the penguin diagram shown in figure 6.1(a), which as has already been stated, is also dominated by the $t$ quark contribution:

$$\begin{aligned} A_f &\propto V_{tb}V_{ts}^* \\ \overline{A}_f &\propto V_{tb}^*V_{ts} \end{aligned} \tag{6.12}$$

resulting in the phase

$$\begin{aligned} \Phi_D &= arg\left(\frac{V_{tb}V_{ts}^*}{V_{tb}^*V_{ts}}\right) \\ &= arg(V_{tb}V_{ts}^*V_{tb}V_{ts}^*) \\ &= 2\ arg(V_{tb}V_{ts}^*) \end{aligned} \tag{6.13}$$

Hence, it can be seen that there is a cancellation between the phases arising from mixing and decay, and consequently the total CP-violating weak phase, $\Phi$, is equal to zero in the Standard Model for this channel.

### 6.1.2 Experimental Status

The first evidence for the existence of the $B_s^0 \to \phi\phi$ decay mode was observed by the CDF experiment [20]. A sample of 180 $pb^{-1}$ yielded 8 signal candidate events, which are shown in figure 6.3. This signal yield is estimated to be significant at a level of 4.7 $\sigma$.

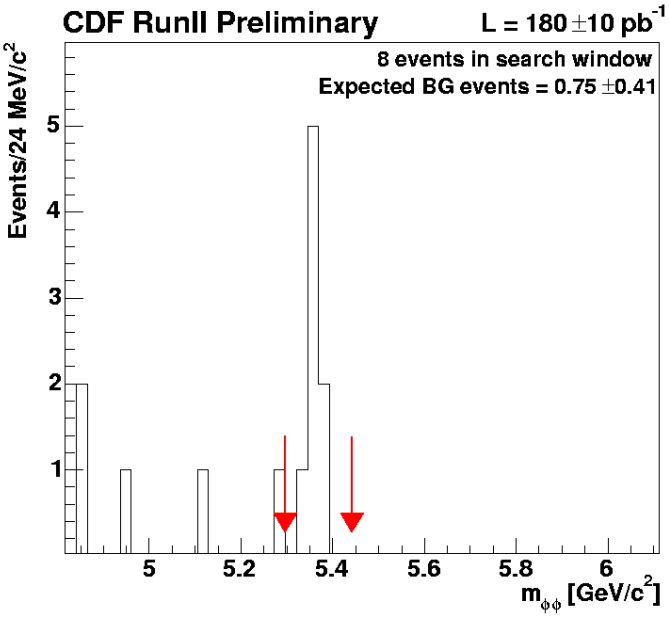


**Figure 6.3:** Mass distribution for $B_s^0 \to \phi\phi$ signal candidates from the CDF analysis, the arrows represent the signal search region [20].

The measurement allowed an estimation of the branching ratio for this channel, through comparison with the number of $B_s^0 \to J/\psi\phi$ events selected in a similar region of phase space. The branching ratio measurement obtained was:

$$BR(B_s^0 \to \phi\phi) = (1.4 \pm 0.6^{stat} \pm 0.2^{syst} \pm 0.5^{BR(B_s^0 \to J/\psi\phi)}) \times 10^{-5} \tag{6.14}$$

## 6.2 Extracting Φ

$B_s^0 \to \phi\phi$ is a Pseudoscalar to Vector Vector ($P \to VV$) decay; $B_s^0$ is a pseudoscalar meson with 0 overall spin, while the $\phi$ resonances are vector mesons each with an overall spin of 1. As a result, there are three possible spin configurations allowed by angular momentum conservation, shown in figure 6.4.

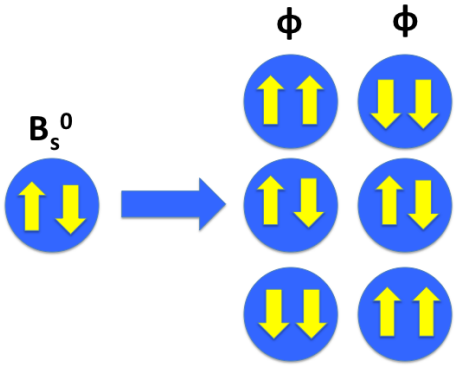


**Figure 6.4:** Possible spin configurations for $B_s^0 \to \phi\phi$.

These spin configurations manifest themselves as three possible helicity states, with amplitudes denoted $H_{+1}$, $H_{-1}$ and $H_0$. In this analysis, it is useful to also refer to linear polarisation amplitudes, which are related to the helicity amplitudes through the following transformations:

$$A_{||} = \frac{H_{+1} + H_{-1}}{\sqrt{2}} \tag{6.15}$$

$$A_{\perp} = \frac{H_{+1} - H_{-1}}{\sqrt{2}} \tag{6.16}$$

$$A_0 = H_0 \tag{6.17}$$

These states are referred to as Parallel, Transverse and Longitudinal respectively. The different linear polarisation states transform differently under CP; $A_0$ and $A_{||}$ are CP-even, while $A_{\perp}$ is CP-odd. Consequently, the final state will contain a mixture of CP eigenstates. In order to extract Φ from this decay the fraction of each CP eigenstate must be known.

This is done by performing an angular analysis of the decay products [88]; the angular distributions are different for the various linear polarisation states, and so allow the

different states to be disentangled. Two common bases for defining the angular variables are the helicity and transversity bases [89]; the helicity basis will be used in this analysis, as it treats the two (identical) $\phi$ particles symmetrically.

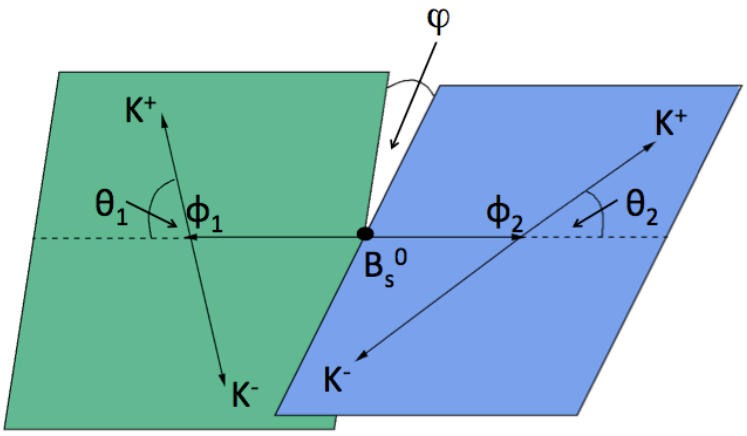


**Figure 6.5:** Definition of angular variables in the helicity basis.

Figure 6.5 shows the helicity basis, and the angular variables that will be used to characterise the decay, $\theta_1$, $\theta_2$ and $\varphi$. The $\theta$ angles are defined as the angle between the momentum vector of the $K^+$, and that of the $B_s^0$ meson in the $\phi$ rest frame. The third angle defining this basis is the $\varphi$ angle, defined as the angle between the decay planes of the two $\phi$ resonances. Since the $\phi$ particles are identical, the angular distributions of $\theta_1$ and $\theta_2$, should also be identical, although small differences may occur due to the ordering of the reconstructed $\phi$ candidates.

The angular distribution for a $P \to VV$ decay has the following form:

$$\frac{d^3\Gamma}{d(\cos\theta_1)\; d(\cos\theta_2)\; d\varphi} \propto \left| \sum_{h=0,\pm1} H_h \times Y_{1,h}(\theta_1,\varphi_1) \times Y_{1,-h}(\theta_2,\varphi_2) \right|^2 \tag{6.18}$$

Here the $Y_{a,b}$ functions are spherical harmonics. Equation 6.18 can be expanded and re-arranged in order to obtain 6 angular functions, $f_n(\theta_1,\theta_2,\varphi)$:

$$\begin{aligned}
f_1(\theta_1,\theta_2,\varphi) &= 4\cos^2\theta_1\cos^2\theta_2 \\
f_2(\theta_1,\theta_2,\varphi) &= \sin^2\theta_1\sin^2\theta_2(1+\cos 2\varphi) \\
f_3(\theta_1,\theta_2,\varphi) &= \sin^2\theta_1\sin^2\theta_2(1-\cos 2\varphi) \\
f_4(\theta_1,\theta_2,\varphi) &= -2\sin^2\theta_1\sin^2\theta_2\sin 2\varphi \\
f_5(\theta_1,\theta_2,\varphi) &= \sqrt{2}\sin 2\theta_1\sin 2\theta_2\cos\varphi \\
f_6(\theta_1,\theta_2,\varphi) &= -\sqrt{2}\sin 2\theta_1\sin 2\theta_2\sin\varphi
\end{aligned} \tag{6.19}$$

The coefficients of each of the angular functions in the overall angular distribution is

determined by the linear polarisation amplitudes. The first three angular functions describe the angular distributions of the $A_0$, $A_{||}$ and $A_\perp$ respectively, while the remaining three are cross terms.

These angular functions can then be used to construct a differential decay rate:

$$\frac{d^3\Gamma(t)}{d(cos\theta_1)\ d(cos\theta_2)\ d\varphi} \propto \sum_{n=1}^{6} K_n(t) f_n(\theta_1, \theta_2, \varphi) \tag{6.20}$$

The time-dependent $K_n(t)$ functions describe the time evolution of the linear polarisation states.

$$\begin{aligned} K_1(t) &= |A_0(t)|^2 \\ K_2(t) &= |A_{||}(t)|^2 \\ K_3(t) &= |A_\perp(t)|^2 \\ K_4(t) &= Im(A^*_{||}(t)A_\perp(t)) \\ K_5(t) &= Re(A^*_0(t)A_{||}(t)) \\ K_6(t) &= Im(A^*_0(t)A_\perp(t)) \end{aligned} \tag{6.21}$$

By fitting for the components of each of the 6 $f_n$ functions in the overall angular distribution, the amplitudes and phases of the linear polarisation states can be extracted. The fitting procedure will be discussed in chapter 7.

The total weak phase, Φ, appears in the lifetime distribution of the $B^0_s$ meson. The time-dependent $K_n(t)$ functions can be expanded in terms of the $B^0_s/\overline{B}^0_s$ lifetime distributions thus:

$$\begin{aligned} K_1(t) &= \frac{1}{2}A_0^2[(1+\cos\Phi)e^{-\Gamma_L t} + (1-\cos\Phi)e^{-\Gamma_H t} \pm 2e^{-\Gamma_s t}\sin(\Delta m_s t)\sin\Phi] \\ K_2(t) &= \frac{1}{2}A_{||}^2[(1+\cos\Phi)e^{-\Gamma_L t} + (1-\cos\Phi)e^{-\Gamma_H t} \pm 2e^{-\Gamma_s t}\sin(\Delta m_s t)\sin\Phi] \\ K_3(t) &= \frac{1}{2}A_\perp^2[(1-\cos\Phi)e^{-\Gamma_L t} + (1+\cos\Phi)e^{-\Gamma_H t} \mp 2e^{-\Gamma_s t}\sin(\Delta m_s t)\sin\Phi] \\ K_4(t) &= |A_{||}||A_\perp|[\pm e^{-\Gamma_s t}\{\sin\delta_1\cos(\Delta m_s t) - \cos\delta_1\sin(\Delta m_s t)\cos\Phi\} \\ &\quad -\frac{1}{2}(e^{-\Gamma_H t} - e^{-\Gamma_L t})\cos\delta_1\sin\Phi] \\ K_5(t) &= \frac{1}{2}|A_0||A_{||}|\cos(\delta_2-\delta_1) \\ &\quad [(1+cos\Phi)e^{-\Gamma_L t} + (1-\cos\Phi)e^{-\Gamma_H t} \pm 2e^{-\Gamma_s t}\sin(\Delta m_s t)\sin\Phi] \\ K_6(t) &= |A_0||A_\perp|[\pm e^{-\Gamma_s t}\{\sin\delta_2\cos(\Delta m_s t) - \cos\delta_2\sin(\Delta m_s t)\cos\Phi\} \\ &\quad -\frac{1}{2}(e^{-\Gamma_H t} - e^{-\Gamma_L t})\cos\delta_2\sin\Phi] \end{aligned} \tag{6.22}$$

Here, $\Gamma_s$ is the mean decay width of the $B^0_s$ while $\Gamma_H$ and $\Gamma_L$ are the decay widths of the heavy and light mass eigenstates respectively. The mass difference between these

eigenstates is denoted by $\Delta m_s$. The strong phase differences $\delta_1$ and $\delta_2$ are defined:

$$\begin{aligned} \delta_1 &= arg(A_\perp / A_{||}) \\ \delta_2 &= arg(A_\perp / A_0) \end{aligned} \tag{6.23}$$

### 6.2.1 $B_s^0 \to \phi\phi$ as a New Physics Probe

In the Standard Model, the CKM matrix acts as the sole source of CP-violation. However, contributions from New Physics particles could potentially affect this channel, and modify the measured weak phase, $\Phi$.

A typical way in which FCNC processes can be affected is by New Physics particles appearing in the loops. Alternatively, New Physics models may include new FCNC processes with non-zero tree-level amplitudes. The time dependent $K_n(t)$ functions of equation 6.22 assume Standard Model-like weak phases, which affect each linear polarisation component equally. In principle, CP violating New Physics phases may contribute differently to each polarisation component.

However, assuming different New Physics contributions for each polarisation state results in a larger number of parameters than measurements that can be made [90]. As a result, the approach applied in this analysis is to take the validity of the Standard Model (and hence the absence of New Physics contributions) as the null hypothesis which is to be disproved.

In $B_s^0 \to \phi\phi$, New Physics effects can manifest themselves in both the mixing box diagrams and the penguin decay. As a result, both the mixing and decay contributions can acquire a New Physics correction:

$$\begin{aligned} \Phi_M &= \Phi_M^{SM} + \Phi_M^{NP} \\ \Phi_D &= \Phi_D^{SM} + \Phi_D^{MP} \end{aligned} \tag{6.24}$$

Assuming that the New Physics contribution to the mixing and decay do not cancel, this will result in an overall measurable New Physics contribution to the total weak phase:

$$\Phi = \Phi^{SM} + \Phi^{NP} \tag{6.25}$$

Consequently, given that $\Phi^{SM} = 0$, a non-zero measurement of the total weak phase in this channel would imply the existence of physics Beyond the Standard Model. The analysis of this channel can be complemented by results from the analysis of the channel $B_s^0 \to J/\psi\phi$, a tree-dominated $B_s^0$ meson decay. The penguin contribution to $B_s^0 \to J/\psi\phi$ is highly suppressed compared to the tree, and therefore New Physics effects of the kinds mentioned above can only manifest themselves in the mixing box diagram (i.e. $\Phi_M$ only), providing an interesting comparison to $B_s^0 \to \phi\phi$.

## 6.3 Data Samples

In the absence of physics events from LHC collisions, events from Monte Carlo simulations are studied. These simulated events allow analysis procedures to be developed and evaluated. Many millions of Monte Carlo events were produced for the 2006 data challenge, DC06. The aims of DC06 were to test the LHCb computing model [91], and to provide a consistent set of data samples for analysis, based on the most up-to-date (at the time of production) detector model and values of B hadron decay parameters. The Monte Carlo data samples used in this study were produced using the DC06 detector description, and DC06 compatible versions of the simulation (Gauss), digitisation (Boole) and reconstruction (Brunel) packages.

### 6.3.1 Signal Sample

The sample of 100 k signal events was generated according to the PVV_CPLH model in EvtGen [92]. This model allows lifetime distributions with CP violation and non-zero lifetime differences to be generated for pseudoscalar to vector-vector decays. It also allows specification of the linear polarisation amplitudes and phases, and the amount of CP violation.

For the signal sample, the CP violating weak phase, $\Phi$, was set to zero in accordance with the Standard Model prediction for this channel. The mean $B_s^0$ decay width used was $\Gamma_s = 0.6852$ ps$^{-1}$, with $\Delta\Gamma_s/\Gamma_s = 0.1$, and $\Delta m_s = 20$ ps$^{-1}$.

The EvtGen input parameters relating to the linear polarisation amplitudes have the following definitions:

$$\begin{aligned} f_{||} &= |A_{||}|^2/(|A_{||}|^2 + |A_\perp|^2 + |A_0|^2) \\ f_\perp &= |A_\perp|^2/(|A_{||}|^2 + |A_\perp|^2 + |A_0|^2) \\ \phi_{||} &= arg(A_{||}/A_0) \\ \phi_\perp &= arg(A_\perp/A_0) \end{aligned} \tag{6.26}$$

No measurement has yet been made of the linear polarisation amplitudes, and so the generated values of these parameters were based on Heavy Flavour Averaging Group results for the topologically similar channel $B^0 \to \phi K^{*0}$, which proceeds via the same set of diagrams as $B_s^0 \to \phi\phi$, differing only in the spectator quark [38]. These values are shown in table 6.1.

### 6.3.2 Background Samples

The main background sample used was the stripped DC06 $b\bar{b}$-inclusive sample. In this sample, each event contains a $b\bar{b}$ pair, with at least one B hadron within the

**Table 6.1:** Generated Linear Polarisation Amplitudes.

| Parameter | Value |
|---|---|
| $f_\perp$ | 0.25 |
| $f_{\|\|}$ | 0.25 |
| $\phi_\perp$ | 2.36 |
| $\phi_{\|\|}$ | 2.37 |

detector acceptance, and has passed at least one of the preselections included in the stripping. This sample of approximately 80k stripped background events is equivalent to approximately 22M unstripped events. A sample of minimum bias events, required to have passed the Level 0 hardware trigger, was also used in order to ensure that the event selection has sufficient rejection power.

## 6.4 Event Selection

In this section, the distinction between the 'offline' and 'online' contexts is important. 'Offline' refers to studies performed on data that has been written to tape for permanent storage, while 'online' refers to actions carried out on data prior to it being sent to storage, i.e. in the trigger. Event selection is optimised first in the offline context.

### 6.4.1 Event Preselection

The first stage of offline event selection is a loose set of cuts to provide a 'preselected' sample of events. In principle all of the available signal events should be used, but in practice many of the events will not be reconstructible due to a lack of hits in the detector. Cuts are applied in order to reduce the number of background candidates to a manageable level, while retaining most of the reconstructible signal candidates.

Many of the cuts applied at the preselection stage come from shared selections for common particles. The kaons candidates used to reconstruct the $\phi$ resonances come from the 'StdLooseKaons' selection, which applies the following cuts:

- Long Tracks only, meaning the reconstructed track used for the kaon candidate must have hits in all of the LHCb tracking detectors (Velo, TT and downstream T stations) as shown in figure 6.6
- The difference in the particle identification log likelihoods for the kaon and pion hypotheses, DLL(K - $\pi$), is greater than -5, passing some kaon candidates for which the pion hypothesis is slightly more likely, in order to increase the kaon efficiency

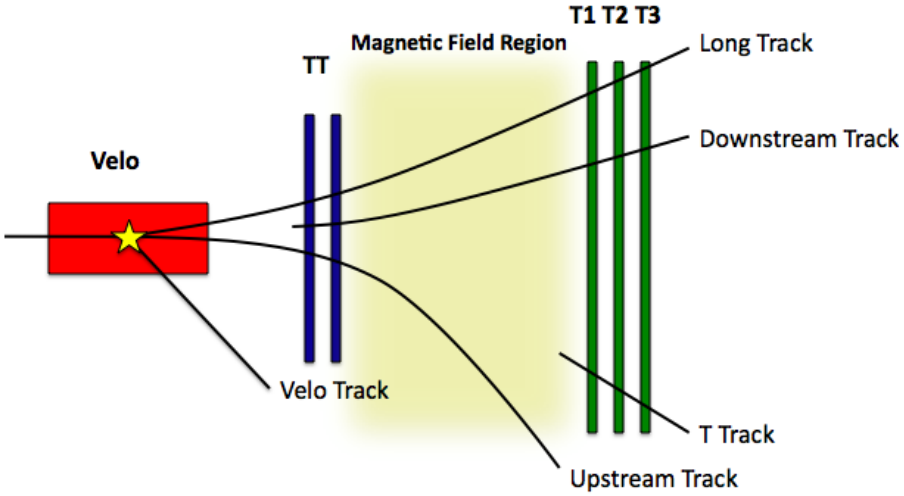


**Figure 6.6:** Track classification in LHCb.

The selected kaon candidates are then combined to produce $\phi$ resonances according to the cuts defined in the 'StdLoosePhi2KK' selection:

- The Impact Parameter (IP) significance of the kaon candidates with the respect to the Primary Vertex (PV) is greater than $2\sigma$
- The mass difference of the reconstructed $\phi$ candidate from the nominal $\phi$ mass is less than 50 MeV/c$^2$
- The $\chi^2$ per degree of freedom from the vertex fit of the kaon candidates to form a $\phi$ candidate is less than 25

The $\phi$ candidates passing these cuts are used to form the $B_s^0$ candidates subject to a final preselection cut:

- The mass difference of the reconstructed $B_s^0$ candidate from the nominal $B_s^0$ mass is less than 500 MeV/c$^2$. This wide mass window is necessary in order to allow sufficient sideband data for background shapes to be studied.

Applying the preselection defined above to the 100k events in the signal MC sample yields 25229 $B_s^0 \to \phi\phi$ candidates. By using the MC truth information, 14582 of these candidates are classified as true signal. When applied to the 80k stripped $b\bar{b}$-inclusive events, 20153 background candidates are returned.

Of the background candidates (including the non-truth matched candidates from the signal sample), the majority are classified as ghosts, where at least one reconstructed final state particle could not be matched to a true MC particle. There is also a significant number of candidates for which at least one reconstructed final state particle comes directly from a primary vertex (or a short lived resonant state), and there are a small fraction of these for which all of the final state particles originate from the same

primary vertex. The remaining candidates come either from partially-reconstructed physics backgrounds, in which not all of the final state particles from a B-decay are correctly reconstructed, or from $b\bar{b}$, $c\bar{c}$ or light flavor events.

### 6.4.2 Event Selection

The events passing the preselection cuts were used for the tuning of the final offline event selection. The aim of the event selection is to produce a clean, well understood sample of signal candidates on which the proposed physics studies can be performed.

The simplest way to do this is to define a set of cuts that are tight enough to ensure that no background candidates pass, resulting in a data sample containing only signal candidates. However, tuning the selection cuts simply to remove all background events is unlikely to result in a data set that will allow the best physics results to be obtained, as a significant proportion of the signal candidates will often be removed also, limiting the statistical precision on any measurements to be made.

Consequently, the optimisation of the selection should consider both the background rejection and the signal retention of the cuts applied. A common method for this is to select the cut values which maximise the signal significance, $\frac{S}{\sqrt{S+B}}$, where $S$ and $B$ represent the number of signal and background candidates respectively passing the cut. Maximising this parameter corresponds to obtaining the maximum possible significance for measuring cross sections and branching fractions.

Since the number of events in the signal and background samples available correspond to different integrated luminosities, the events must be appropriately weighted to compensate for this. The 100k signal events correspond to an integrated luminosity of 1.32 $fb^{-1}$, or approximately $6.6 \times 10^6$ s of data taking. The 800k $b\bar{b}$-inclusive events are equivalent to $1 \times 10^{-4}$ $fb^{-1}$, or approximately 500 s of data taking[1]. Together, this means that the actual parameter to be maximised in this case is $\frac{S}{\sqrt{S+13000B}}$. This will be the starting point for the optimisation. However, for the maximum likelihood fit performed on the data, this does not guarantee the best statistical precision on the parameters to be measured, and so where possible an overall high signal efficiency was maintained.

The most obvious parameters to provide separation between signal and background are the measured masses of the $B_s^0$ and $\phi$ resonances. Due to the relatively narrow width of the $\phi$ mass peak, tight cuts can be applied on this parameter, and a mass window of 20 MeV/c$^2$ either side of the nominal $\phi$ mass was chosen. This is shown in figure 6.7.

For the $B_s^0$ candidates a mass window of 50 MeV/c$^2$ was used. In order to improve the uncertainty on the background statistics, this $B_s^0$ mass cut was not applied to the

[1] Although this depends heavily on the $b\bar{b}$ cross-section at 14 TeV which is currently not well known.

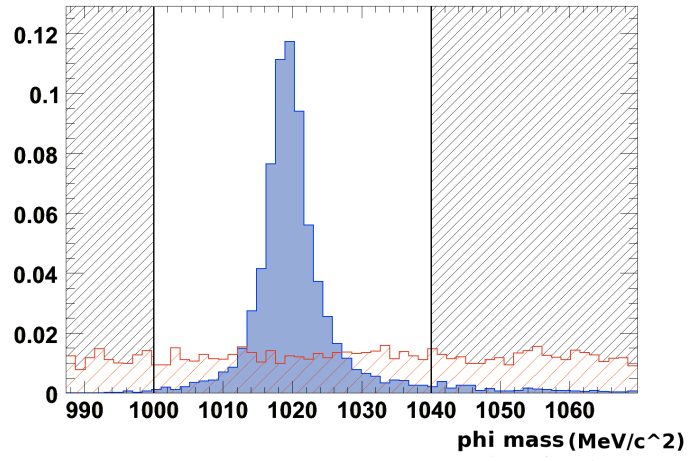


**Figure 6.7:** $\phi$ mass distributions for signal, shown in blue, and $b\bar{b}$-inclusive events, shown in red, in MeV/c$^2$. The hatched areas represent the regions excluded by the cuts. The necessary background weighting is not applied in these plots. The $\phi$ mass has a resolution of approximately 5 MeV/c$^2$.

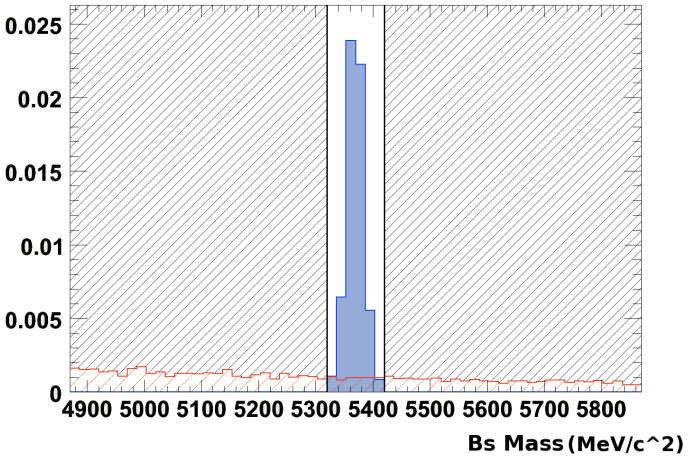


**Figure 6.8:** $B_s^0$ mass distributions for signal (blue) and $b\bar{b}$-inclusive (red) events in MeV/c$^2$, showing the applied mass window. The $B_s^0$ mass has a resolution of approximately 15 MeV/c$^2$.

background sample. The background shape in this variable is well-behaved, and it is largely uncorrelated with other variables, so the number of background candidates expected and the background shape in the signal mass region, shown in figure 6.8, is well understood.

For true signal candidates, the momentum vector of the reconstructed $B_s^0$ should point in the same direction as the vector between the primary vertex and the $B_s^0$ decay vertex. This requirement can be quantified by cutting on the cosine of the angle $\theta$ between the two vectors. Figure 6.9 shows the signal significance ($\frac{S}{\sqrt{S+B}}$), which is maximised

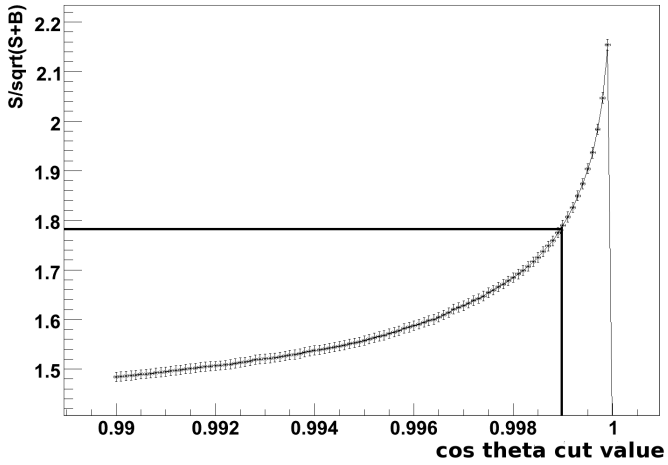


**Figure 6.9:** Variation of signal significance for different $B_s^0$ $\cos\theta > x$ cut values, showing the applied cut.

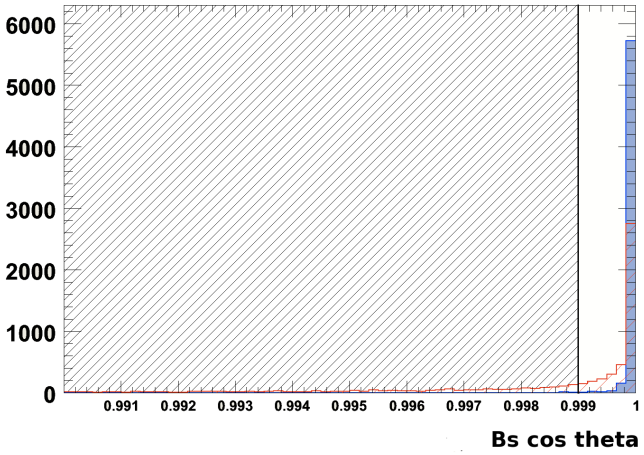


**Figure 6.10:** $B_s^0$ $\cos\theta$ distributions for signal (blue) and $b\bar{b}$-inclusive (red) events, showing the applied cut.

by the tightest possible cut value on this parameter, at $\cos\theta = 1$. A looser cut at $\cos\theta > 0.999$ was chosen to be applied in the final selection, to increase the signal

efficiency. Applying this cut, 99% of the signal candidates are retained. The signal and background distributions in this parameter can be seen in figure 6.10.

Aside from the mass windows, the most commonly applied cuts are on the particle momentum. In this selection, cuts are applied on the $\phi$ and kaon transverse momenta. The distributions in signal and background for the lowest transverse momentum $\phi$ and kaon candidates are shown in figures 6.11 and 6.12 respectively. Maximising the signal significance for these parameters results in cuts that are much too tight for the purposes of the analysis (due in part to the high weighting applied to the background events), and so looser cuts at $p_T(\phi) > 1.5$ GeV/c and $p_T(K) > 500$ MeV/c were chosen.

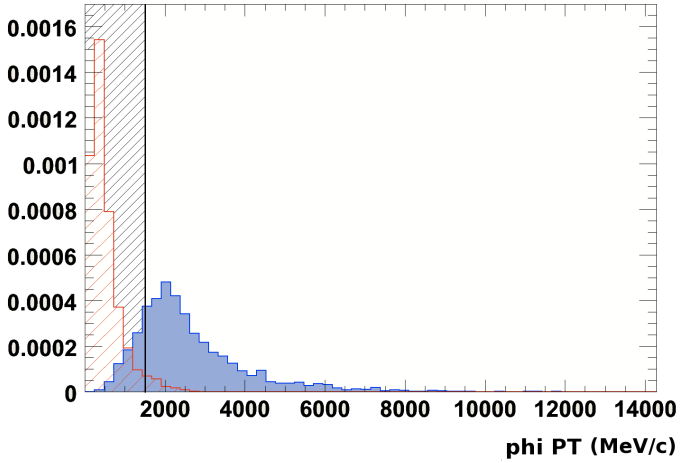


**Figure 6.11:** $\phi$ transverse momentum distributions for signal (blue) and $b\bar{b}$-inclusive (red) events in MeV/c, showing the applied cut.

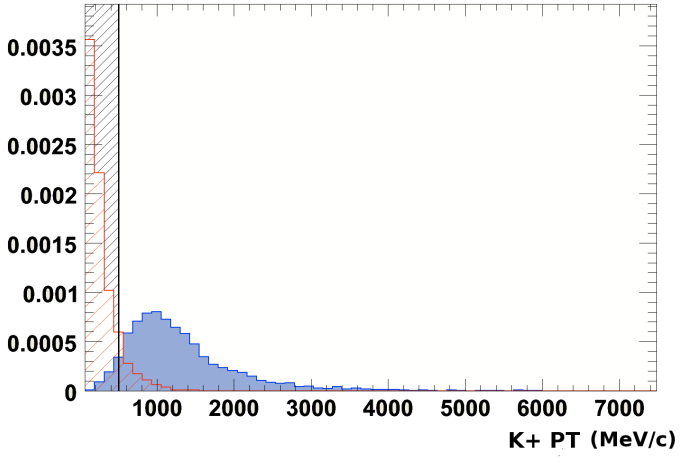


**Figure 6.12:** Kaon transverse momentum distributions for signal (blue) and $b\bar{b}$-inclusive (red) events in MeV/c, showing the applied cut.

The distribution of the higher transverse momentum $\phi$ candidate is used to discriminate between signal and background, by applying a cut on the product of the transverse momentum of the two $\phi$ candidates. As shown in figure 6.13, this parameter shows good separation between signal and background; like the $\cos\theta$ cut, the signal significance continues to improve as the cut is tightened.

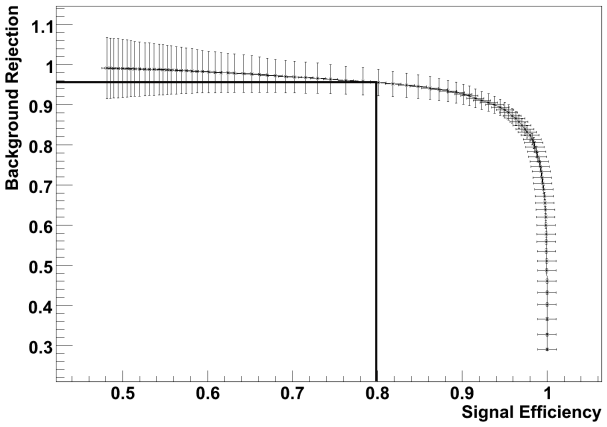


**Figure 6.13:** Background rejection against signal efficiency for different $\phi$ transverse momentum product $> x$ cut values, showing the applied cut.

Cutting on both the lowest $\phi$ transverse momentum and the product of the two $\phi$ transverse momenta provides better performance than cutting on either parameter alone, and also better performance than applying different transverse momentum cuts to the two $\phi$ candidates (within regions with acceptable signal efficiencies). A cut at $p_T(\phi_1) \times p_T(\phi_2) > 6 \times 10^6$ $(\mathrm{MeV/c})^2$ is applied for this selection. The signal and background distributions in this parameter are shown in figure 6.14.

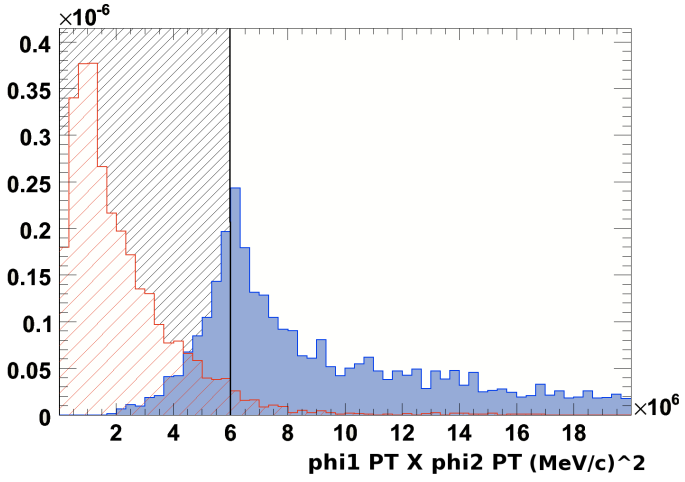


**Figure 6.14:** $\phi$ transverse momentum product distributions for signal (blue) and $b\bar{b}$-inclusive (red) events in $(\mathrm{MeV/c})^2$, showing the applied cut.

The final cut applied is a $\chi^2$ cut on the $B_s^0$ decay vertex. The signal and background distributions in this parameter are shown in figure 6.15. The cut is applied at $\chi^2(B_s^0) < 25$, which is equivalent to a $\chi^2$ per degree of freedom of 6.25, since the $B_s^0$ vertex is formed from 4 final state kaons.

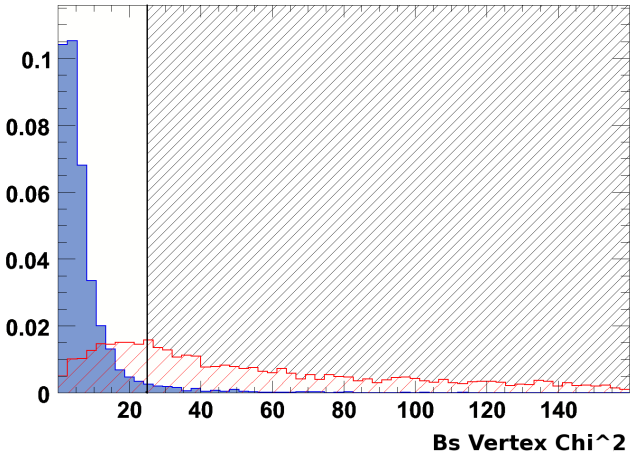


**Figure 6.15:** $B_s^0$ vertex $\chi^2$ distributions for signal (blue) and $b\bar{b}$-inclusive (red) events, showing the applied cut.

The signal efficiency and background rejection for each of these cuts is shown in table 6.2. Of the 14582 preselected true signal candidates, 9753 pass all of the offline selection cuts, corresponding to an efficiency of $67 \pm 0.4\%$. From 20153 preselected background candidates, 4 pass all of the offline selection cuts, giving a background rejection of $99.98 \pm 0.01\%$. When the selection is run over the 2.9M L0-accepted minimum bias events, no candidates are selected.

In table 6.2, it can be seen that there are multiple signal candidates per event. Since the small branching fraction ensures that the probability of multiple signal decays in a single event is negligible in both signal and background, these multiple candidates should be reduced to a single candidate. A significant fraction of events ($\sim 10\%$) contain 'velo clone' events; in these events, the two kaons from the $\phi$ resonance have such a small spatial separation that they cannot be separated in the Velo. Consequently, these clones cannot be killed by the track reconstruction algorithms without seriously impacting the $\phi$ reconstruction efficiency. To distinguish and select the best candidate in the event, the mass resolution is used. The $B_s^0$ candidates with the lowest total difference between the reconstructed mass and the expected mass for the two $\phi$ candidates is selected. While this can distort the shape of the $\phi$ mass peak, this will not affect the measurement of the total weak phase, since the $\phi$ mass is not used in the maximum likelihood fit described in chapter 7.

There may also be a contribution to the signal sample from 'self cross-feed'; this occurs

when a kaon is reconstructed as originating from the incorrect $\phi$. From looking at the Monte Carlo truth information, this contribution was found to be very small. Only 8 $\phi$ candidates from the entire preselected signal sample were found to be due to self cross-feed.

**Table 6.2:** Cut efficiencies from the offline event selection.

| | Signal | | | $b\bar{b}$-inclusive | |
|---|---|---|---|---|---|
| Cut | Candidates | per Event | Efficiency | Cands. | Eff. |
| Preselected | 14582 | 1.38 | 15% | 20153 | N/A |
| $\Delta M\left(B_s^0\right) < 50$ MeV/c$^2$ | 14233 | 1.21 | 98% | - | - |
| $\Delta M\left(B_s^0\right) < 500$ MeV/c$^2$ | - | - | - | 20153 | 100% |
| $\Delta M\left(\phi\right) < 20$ MeV/c$^2$ | 13473 | 1.30 | 92% | 5421 | 27% |
| K $p_T > 500$ MeV/c | 13222 | 1.21 | 91% | 1227 | 6% |
| $\phi$ $p_T > 1500$ MeV/c | 12070 | 1.21 | 83% | 684 | 3% |
| $\phi$ $p_T$ prod. $> 6 \times 10^6$ (MeV/c)$^2$ | 11630 | 1.24 | 80% | 897 | 4% |
| $\cos\theta\left(B_s^0\right) > 0.999$ | 14438 | 1.27 | 99% | 6403 | 32% |
| $\chi^2\left(B_s^0\right) < 25$ | 14083 | 1.26 | 97% | 6313 | 31% |
| All Cuts | 9753 | 1.12 | 67 % | 4 | <1% |

Figure 6.16 shows the correlations between the cut parameters. It can be observed that there are no significant correlations between any of the parameters, with the exception of the three transverse momentum cuts, which are highly correlated with each other in both signal and background, as would be expected.

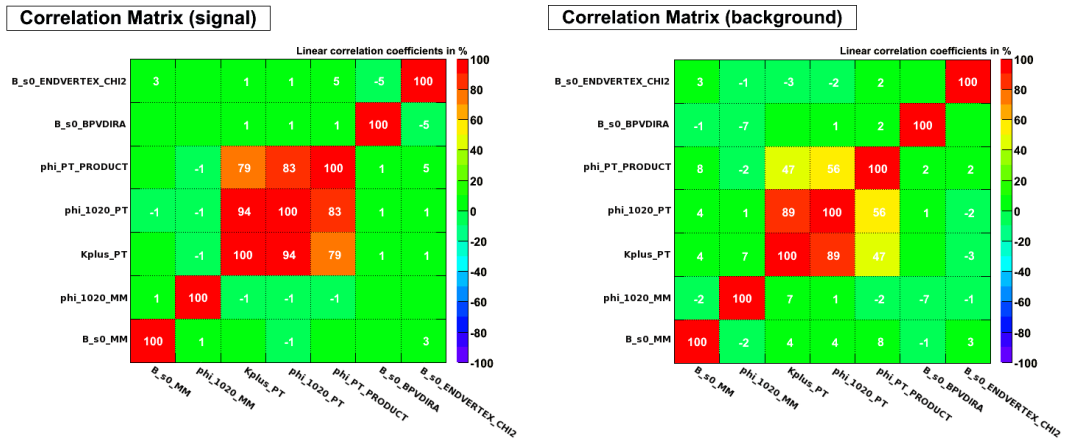


(a) signal (b) background

**Figure 6.16:** Correlations between cut parameters.

The effectiveness of each cut was tested in combination with the other cuts, to investigate whether the performance could be improved by changing the value of this cut once the other cuts are applied. In this way, an optimal ensemble of cuts was arrived at.

### 6.4.3 High Level Trigger

For events to be present in the data sample, they must be selected online by the LHCb trigger. The L0 hardware trigger and HLT1 software trigger both have a common implementation for all LHCb analyses (as described in section 3.9), while the HLT2 consists of a range of exclusive and inclusive online selections that can be optimised for specific analyses. An exclusive online HLT2 selection was designed for $B_s^0 \to \phi\phi$.

An effective HLT2 selection will retain as many signal events as possible, in particular those events which will be selected offline, while keeping the total rate down to an acceptable level. Due to differences between the online and offline reconstruction algorithms, simply running the event selection described in section 6.4.2 in HLT2 does not provide the optimum performance, and so the cuts values were re-assesed for use in the online context.

The principal differences between the online and offline event reconstruction are the vertexing and the particle identification. In the online context, a fast vertexing procedure is used which has reduced performance compared to the full offline vertex reconstruction. Therefore, cuts on parameters such as vertex $\chi^2$, or impact parameter significance are less effective when used in HLT2 selections than in offline selections. RICH information is unavailable for the online reconstruction, as the necessary algorithms are too CPU intensive, and so there is no particle identification to distinguish between kaons and pions in the HLT.

The allowed rate for an HLT2 exclusive selection is a few Hz from the 2 kHz total bandwidth for all exclusive selections. The signal sample used to optimise the HLT2 selection consisted of the signal events passing the offline selection, and the background came from the L0-accepted minimum bias sample. Since $B_s^0 \to \phi\phi$ has a small branching ratio ($\sim 10^{-6}$), signal decays will be a negligible contribution to the overall rate and so only the rate from background is of concern.

The starting point for the HLT2 selection is the online $\phi$ reconstruction from the 'Hlt2SharedPhi2KK' stream. The kaons use to construct the $\phi$ candidates come from 'Hlt2GoodKaons', which have the following cuts applied:

- The momentum of the kaon candidate is greater than 3 GeV/c
- The transverse momentum of the kaon candidate is greater than 500 MeV/c
- The impact parameter $\chi^2$ of the kaon candidate with respect to the primary vertex is greater than 4

The $\phi$ resonances are then constructed subject to the following:

- The mass difference of the reconstructed $\phi$ candidate from the nominal $\phi$ mass is less than 20 MeV/c$^2$

- The $\chi^2$ per degree of freedom of the vertex formed from the kaon candidates is less than 25

The final selection cuts are then applied to the $B_s^0$ candidates constructed from two $\phi$ candidates:

- The mass difference of the reconstructed $B_s^0$ candidate from the nominal $B_s^0$ mass is less than 500 MeV/c$^2$
- The cosine of the angle between the vector from the primary vertex to the $B_s^0$ decay vertex, and the $B_s^0$ momentum is less than 0.999
- The product of the transverse momenta of the two $\phi$ candidates is greater than $6 \times 10^6$ (MeV/c)$^2$
- The $\chi^2$ of the vertex formed from the $\phi$ candidates is less than 50

A wide mass window for the $B_s^0$ is applied in this HLT2 selection, to allow mass sideband regions to be selected so that backgrounds can be studied from data. The $\phi$ transverse momentum product and $B_s^0$ direction $\cos\theta$ cuts are retained from the offline selection, since the distribution of these parameters does not vary significantly when measured in online and offline contexts. The $B_s^0$ vertex $\chi^2$ cut is loosened significantly from the offline selection, reflecting the differences in vertex reconstruction.

**Table 6.3:** Trigger efficiencies on offline selected events.

| | Candidates | Efficiency |
|---|---|---|
| Offline Selected | 9753 | - |
| Passing Level 0 | 3718 | 38% |
| Passing L0+HLT1 | 2007 | 21% |
| Passing HLT2 | 8443 | 87% |
| Total | 1825 | 19% |

Running over the $\sim$ 2.9M L0-accepted minimum bias events, 15 $B_s^0$ candidates in 11 events pass this HLT2 selection. Of these 15 candidates, 9 are classified as ghosts with the remainder of the candidates being reconstructed from particles or short-lived resonances coming from the primary vertex. Once HLT1 is applied in addition to HLT2, this is reduced to 2 candidates (both ghosts) from 2 events. The L0-accepted minimum bias sample corresponds to approximately 3.3 seconds of data taking, and so this represents a trigger rate of <1 Hz.

Of the 9753 signal events passing the offline selection, 8443 (87%) of these are also selected online by the HLT2 selection (independent of the other triggers). The L0 trigger passes 3718 (38%) of the offline selected events, and 2007 (54%) of these L0 accepted events are confirmed and passed by HLT1. The HLT2 selection passes 1825 (91%) of the L0+HLT1 accepted events. The full online performance is shown in

table 6.3. The HLT2 efficiency quoted in this table is from the Global HLT2 decision, including the decision from all HLT2 selections.

When run over the $b\bar{b}$-background sample, 1 candidate passes the L0, HLT1 and HLT2. The low efficiency of the L0 and HLT1 trigger stages is a common issue for purely hadronic modes.

### 6.4.4 Event Yields

In order to assess the number of signal events expected for a given integrated luminosity, and the signal to background ratio, a calculation must be performed taking into account the number of $B_s^0$ mesons produced, the branching ratio for the signal channel, and the selection efficiency. The calculation will assume an integrated luminosity of 2 fb$^{-1}$, which is expected in a nominal year of LHCb data-taking.

#### Signal

The product of the integrated luminosity ($\mathcal{L}_{int} = 2$ fb$^{-1}$) with the $b\bar{b}$ cross-section ($\sigma_{b\bar{b}} = 500$ $\mu$b) gives the number of $b\bar{b}$ events expected in a nominal year. The factor $f_s$ represents the probability of a $b/\bar{b}$ quark hadronising into a $\overline{B}{}_s^0/B_s^0$, which is multiplied by a factor of 2 due to the fact that either of the quarks in the $b\bar{b}$ pair can hadronise. The total signal efficiency ($\epsilon_{tot}^{sig}$) is the product of two contributions, the geometric acceptance ($\epsilon_{\theta}^{sig}$) which reflects the fact that the generated events are forced to decay within the LHCb detector acceptance[2], and the efficiency ($\epsilon_{sel}^{sig}$) from both online and offline selections. The final contribution is from the visible branching ratio ($BR^{vis}$) for $B_s^0 \to \phi\phi$ with $\phi \to K^+K^-$.

$$\begin{aligned} N_{sig} &= \mathcal{L}_{int} \times \sigma_{b\bar{b}} \times 2 \times f_s \times BR^{vis} \times \epsilon_{tot}^{sig} \\ \mathcal{L}_{int} \times \sigma_{b\bar{b}} &= 1 \times 10^{12} \\ f_s &= 0.104 \pm 0.014 \text{ [28]} \\ \epsilon_{tot}^{sig} &= \epsilon_{\theta}^{sig} \times \epsilon_{sel}^{sig} \\ &= (0.2057 \pm 0.0021) \times \frac{1825}{100000} \\ &= 0.0038 \pm 0.0005 \end{aligned} \tag{6.27}$$

$$\begin{aligned} BR^{B_s^0 \to \phi\phi} &= (1.4 \pm 0.6^{stat} \pm 0.2^{syst} \pm 0.5^{BR(B_s^0 \to J/\psi\phi)}) \times 10^{-5} \\ BR^{\phi \to KK} &= 0.492 \pm 0.006 \\ BR^{vis} &= (3.4 \pm 2.1) \times 10^{-6} \\ N_{sig} &= 2670 \pm 1690 \end{aligned} \tag{6.28}$$

[2]This value and its error are taken from the MC generator statistics

The quoted uncertainty does not take into account the poor knowledge of $\sigma_{b\bar{b}}$, the 500 $\mu$b value used is a conservative estimate.

**Background**

The estimated combinatoric background yield is determined using the $b\bar{b}$-inclusive Monte Carlo sample. The total background efficiency includes an extra contribution compared to the signal efficiency; in addition to the geometric acceptance and selection efficiency there is a term due to the relative size of the $B_s^0$ mass windows for signal and background ($\frac{\Delta M_{sig}}{\Delta M_{bkg}}$). Again, the yield estimate is subject to a large uncertainty on $\sigma_{b\bar{b}}$ but this will not affect the B/S ratio estimate since it is a common factor in both the signal and background estimates.

$$\begin{aligned} N_{bkg} &= \mathcal{L}_{int} \times \sigma_{b\bar{b}} \times \epsilon_{tot}^{bkg} \\ \epsilon_{tot}^{bkg} &= \epsilon_{\theta}^{bkg} \times \epsilon_{sel}^{bkg} \times \frac{\Delta M_{sig}}{\Delta M_{bkg}} \\ &= 0.434 \times \frac{1}{21388889} \times 0.1 \\ &= \left(2.03^{+9.28}_{-1.98}\right) \times 10^{-9} \\ N_{bkg} &= 2029^{+9281}_{-1979} \end{aligned} \tag{6.29}$$

Due to the low background statistics, the uncertainty on the background yield comes from a 95% Poissonian confidence limit on 1 event. These results suggest a B/S ratio of $0.76^{+3.5}_{-0.74}$. The large uncertainty on this ratio is a consequence of the relatively small size of the $b\bar{b}$-inclusive sample.

Once data from LHC collisions are available, the background yield can be estimated by studying events in mass sideband regions. This will allow the background yield to be far better understood, as the size of the DC06 $b\bar{b}$-inclusive data set will be exceeded within 10 minutes of LHC data-taking.

### 6.4.5 Specific backgrounds

In addition to combinatoric backgrounds, which are selected based on final state particles originating from a number of separate processes (or from tracks constructed from a selection of hits not arising from a single physical particle in the case of ghost tracks) the final event selection is expected to contain background candidates arising from specific B-meson decays. In order to interpret the effect of these 'peaking' backgrounds they must first be identified.

To identify potential peaking backgrounds, the offline selection was run over the biased $b\bar{b}$-inclusive sample. This sample consists of $b\bar{b}$ events in which generator-level cuts have been applied to the B hadron which will increase the likelihood of the event

retained in the sample containing a B hadron that can be reconstructed and selected. Cuts are applied on pseudorapidity ($2.2 < \eta < 4.7$), transverse momentum ($p_T > 8.4$ GeV), flight distance ($c\tau > 0.16$ mm) and the sum of transverse momentum and pseudorapidity ($p_T + 5.36\eta > 26$ GeV/c). These cuts result in a generator-level efficiency of 3.25%, compared to the 43.7% generator-level efficiency from the acceptance cuts for the unbiased events. The sample consists of $\sim$ 1.9M stripped events, with a stripping retention rate of 12%, corresponding to an unstripped sample of $\sim$15.8M events.

The MC information was used to identify the B-hadron decays in the events that pass the offline selection; none of the reconstructed decays in the accepted events are completely associated to a single Monte Carlo decay. As would be expected, Monte Carlo associated kaons mostly came from decays that proceed via a $\phi$ resonance, although some were observed that originated from $K^{*0}$ resonances, or directly from the B-hadron decay vertex.

One decay that is expected to contribute to the analysis of $B_s^0 \to \phi\phi$ is the topologically similar decay $B^0 \to \phi K^{*0}$. The final state of this decay is comprised of a $K^+K^-$ pair from the $\phi$ and a $K^+\pi^-$ ($K^-\pi^+$) pair from the $K^{*0}$ ($\overline{K}^{*0}$); mis-identifaction of the pion will result in the same final state as $B_s^0 \to \phi\phi$. In addition to pion misidentification, decays in which an additional kaon (from the opposite-side decay or the primary vertex) is picked up can contribute to the background, as will other four-kaon final states.

Based on these possibilities, a selection of potential background modes is shown in table 6.4. A number of these modes were part of the LHCb DC06 production and so samples were already available, if not, DC06 compatible data samples were generated. The $B_s^0 \to \phi\phi$ selection was run over these samples to allow estimation of their contribution to the selected data sample.

**Table 6.4:** Predicted contributions (upper limits at 95 % C. L.) from specific backgrounds to data sample. Branching ratios marked † are estimates.

| Decay Channel | $BR$ [$\times 10^{-6}$] | $BR$ [prod] | Sample Size | Candidates Selected | Contribution in 2 fb$^{-1}$ |
|---|---|---|---|---|---|
| $B^0 \to K^+K^-K^+K^-$ | 1$^\dagger$ | N/A | 100000 | 0 | $< 5.51$ |
| $B^0 \to \phi(KK)K^{*0}(K\pi)$ | 4.674 | 0.328 | 100000 | 0 | $< 20.62$ |
| $B^0 \to f_0(KK)f_0(KK)$ | $< 0.23$ | (see text) | 100000 | 20 | $<8.21$ |
| $B^0 \to K^{*0}(K\pi)K^+K^-$ | 27.5 | 0.67 | 100000 | 0 | $< 104.01$ |
| $B^0 \to K^{*0}(K\pi)\overline{K}^{*0}(\pi K)$ | 1.28 | 0.45 | 250487 | 0 | $< 1.27$ |
| $B^0 \to \rho^0(\pi\pi)\rho^0(\pi\pi)$ | 0.73 | $\sim 1$ | 254415 | 0 | $< 1.82$ |
| $B_s^0 \to K^+K^-K^+K^-$ | 1$^\dagger$ | N/A | 100000 | 0 | $< 1.60$ |
| $B_s^0 \to K^{*0}(K\pi)\overline{K}^{*0}(\pi K)$ | $< 1680$ | 0.45 | 306163 | 0 | $< 381.79$ |
| $B^+ \to \phi(KK)K^+$ | 4.08 | 0.489 | 100000 | 0 | $< 13.22$ |

With the exception of $B^0 \to f_0(KK)f_0(KK)$, none of these samples contained any events that passed the trigger and offline selection, and so upper limits on the contri-

bution to a 2 fb$^{-1}$, offline selected sample at a 95% confidence level are given. The branching ratios marked with † are estimates, as no branching ratio is published. The branching ratio for $B_s^0 \to K^{*0}\overline{K}^{*0}$ is given as an upper limit due to poor knowledge of its value.

For $B^0 \to f_0(KK)f_0(KK)$, 20 candidates passed the selection and trigger. The branching ratio used for this channel assumes that one $f_0$ resonance decays to $\pi^+\pi^-$ and the other to $K^+K^-$; the product branching ratios for the $f_0$ resonance are not well known, and so it is not possible to disentangle the branching ratio for the four-kaon final state from the stated result.

The list of decays shown in table 6.4 is not exhaustive. There are a number of additional decays that may contribute to the background, such as $B^0 \to \phi f_0$, and others may be identified if a larger generic background sample is made available.

## 6.5 Conclusions

The decay $B_s^0 \to \phi\phi$ is sensitive to New Physics effects in both mixing and decay. By measuring the total weak phase in this channel, it may be possible to see visible New Physics effects at LHCb. The expected annual signal yield following online and offline event selection is $2670 \pm 1690$ events, with a B/S ratio of $0.76^{+3.55}_{-0.74}$, based on data from DC06 simulations.

There is a large uncertainty on the background yield due to the size of the DC06 $b\bar{b}$-inclusive sample, but this can be well established with early LHC data. However, the generation of large MC samples will still be required in order to identify and assess the impact of specific backgrounds. Since the majority of the specific backgrounds studied yielded no selected candidates from data samples of size $\sim 10^5$ events, larger data samples will be required in order to fully understand their contribution to the background.

# Chapter 7

# $B_s^0 \rightarrow \phi\phi$ Fit Model and Estimated Sensitivities

## 7.1 Fit Methodology

In order to extract $\Phi$ and other parameters of interest, the six time-dependent functions defined in section 6.2, define a combined Probability Density function (PDF), which is fit to the selected events. The PDF describes the probability of an event being found at a given point in a multi-dimensional space of observables. Six observable properties of the reconstructed events are used as input variables for the fit, these are:

- The proper lifetime of the reconstructed $B_s^0/\overline{B}_s^0$ candidate
- The three decay angles $\theta_1$, $\theta_2$ and $\varphi$ as defined in figure 6.5
- The flavour tag decision, and associated tagging category (see section 7.2.2)

These variables are used to construct a Likelihood surface in terms of the remaining constant parameters on which the PDF depends. These parameters can either be fixed, if their value is known, or can be 'floated' to extract the parameter's value using Maximum Likelihood Esimation, if there is sufficient sensitivity and large enough statistics. For these studies, the fixed parameters are:

- The mixing parameters: $\Gamma_L$, $\Gamma_H$ and $\Delta m_s$
- The acceptance parameters: the parameters defining the propertime and angular acceptance functions
- The resolution parameters: the parameters defining the propertime and angular resolutions

The parameters that will be floated in the fit are:

- The physics parameters of interest: $\Phi$, the linear polarisation amplitudes $A_{||}$ and $A_{\perp}$ (from which $A_0$ can also be inferred) and the strong phases of the decay, $\delta_1$ and $\delta_2$
- The tagging parameters: the true $\omega_{tag}$ for each tagging category (section 7.2.2)

### 7.1.1 Maximum Likelihood Fitting

If an event $x$ is assumed to be drawn from a PDF which can be defined as

$$f_x = f(x; \alpha_1, \alpha_2, ..., \alpha_n) \tag{7.1}$$

Where the $\alpha_i$ are the parameters to be estimated, the Likelihood function for a sample of events $x_1$ to $x_k$ is then given by

$$\mathcal{L} = \prod_{j=1}^{k} f_{x_i} \tag{7.2}$$

The values of the $\alpha_i$ which maximise this function provide our best estimate for the true values of these parameters. To simplify the computation involved, the Log Likelihood can be used instead:

$$\ln \mathcal{L} = \sum_{j=1}^{k} \ln f_{x_i} \tag{7.3}$$

In the fitting package RooFit [93], which was used for these studies, it is in fact $-\ln \mathcal{L}$, the Negative Log Likelihood (NLL), which is minimised.

## 7.2 Signal Model

Various inputs to the signal PDF used in the maximum likelihood fit are estimated based on the results from DC06 simulations; these include the tagging performance, resolutions, and acceptance funtions. These estimates allow the sensitivity of the fit with the expected LHCb performance to be investigated. Results from simulations will also be relied upon for some of these inputs (such as the resolutions for the observables) when performing the fit on data from LHC collisions.

### 7.2.1 Resolutions

Some of the principal limitations on how well LHCb will be able to measure $\Phi$ arise from how accurately we are able to determine the value of parameters such as the proper lifetime of the $B_s^0$, and the decay angles in the helicity basis.

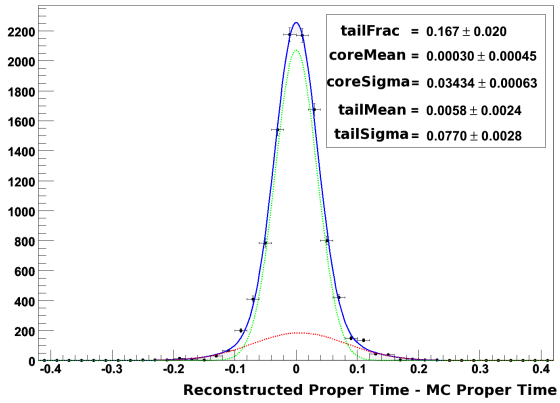


**Figure 7.1:** $B_s^0$ proper lifetime resolution (ps), fit with a double gaussian.

Figure 7.1 shows the estimated resolution in the $B_s^0$ proper lifetime. The resolution is calculated using the difference between the measured lifetime and the true lifetime from the particle's MC information. The distribution is fit with a double gaussian PDF. The core gaussian (in green) has a width of 34 fs, and the tail gaussian (in red) has a width of 77 fs. The contribution to the total PDF from the core gaussian is approximately 5 times that from the tail. The fit gives a $\chi^2$ per degree of freedom of 1.362 with 100 bins.

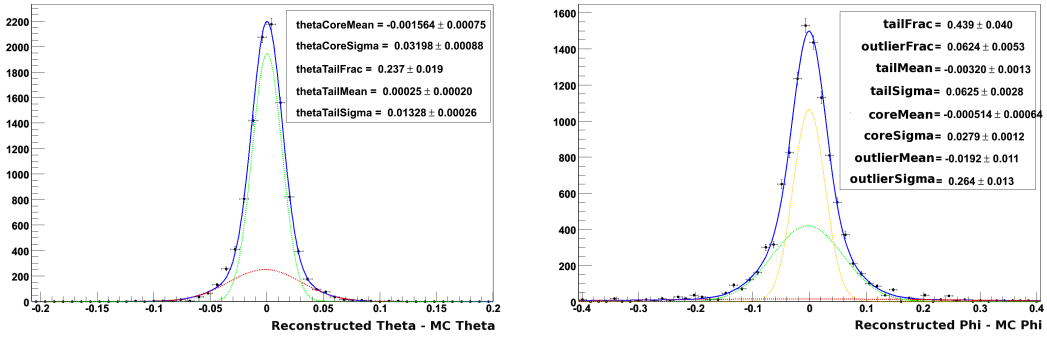


(a) $\theta$ (b) $\varphi$

**Figure 7.2:** Angular resolutions for $\theta$ and $\phi$ (rad), fit with double and triple gaussians repectively.

The angular resolutions are determined in a similar way. The true decay angles are calculated from the MC momentum information, and compared to the reconstructed decay angles. Figure 7.2(a) shows the resolution in determining the $\theta$ angle for the lowest $p_T$ $\phi$, which we define as $\theta_1$. It is fit with a double gaussian PDF. The core (green) and tail (red) gaussians have widths of 0.013 and 0.032 rad respectively, with a ratio of 3.2 in the size of their contributions to the total PDF. A $\chi^2$ per degree of freedom of 1.328 is obtained with 100 bins. Similar results are obtained by fitting to $\theta_2$, the angle for the higher $p_T$ $\phi$.

For the resolution in the angle $\varphi$, it was necessary to add an extra, broad gaussian to the total PDF, in order to fit for the outlying contribution. For this distribution, the core (orange) and tail (green) gaussian have widths of 0.028 and 0.066 rad respectively, with a ratio approximately 1.1, with the outlier (red) gaussian having a width of 0.264 rad, giving a contribution 12.5% of that of the core gaussian. This fit results in a $\chi^2$ per degree of freedom of 2.41 with 100 bins.

There is no evidence of any significant correlations between the resolutions in these three parameters. Additionally, no significant correlations are observed between the resolutions and any other measurable parameters, with the exception of a 30% correlation between the $B_s^0$ proper lifetime resolution and the $B_s^0$ measured mass.

### 7.2.2 Tagging

The LHCb flavour tagging system uses a number of methods to determine the flavour of the $B_s^0$ candidate, by looking at both the same-side (i.e. the signal $b$ quark) and opposite-side (the non-signal $b$ quark, also within the detector acceptance) decays. Several of these methods may contribute to the flavour tagging of single $B_s^0$ candidate. These methods are [94]:

- **Opposite side kaon:** This tagger uses the charge of the kaon in opposite-side $b \to c \to s$ decays to determine the charge of the same-side $b$ quark.
- **Opposite side electron/muon:** As above, except using the charge of the muon/electron from opposite-side semileptonic decays.
- **Same side kaon:** This tagger works by using correlations in the fragmentation decay chain; The additional $\overline{s}$ quark produced in hadronisation of a $\overline{b}$ to a $B_s^0$ (or the charge conjugate process) will frequently ($\sim$50 % of the time) result in a charged kaon following hadronisation, the charge of which provides the flavour tag for the same-side decay.
- **Vertex Charge:** This tagger identifies the flavour of the same-side decay by performing an inclusive reconstruction of the opposite-side secondary vertex. The normalised sum of the track charges, weighted by a function of their transverse momentum, is used to determine the flavour of the opposite-side decay.

The flavour tagging performance will have a significant effect on the precision with which $\Phi$ can be determined. The two indicators of the tagging performance are the tagging efficiency and the mistag rate. Both tagged and untagged candidates are used in the analysis. For correctly tagged candidates, the $B_s^0$ proper lifetime distribution is determined by the 6 time-dependent $K_n(t)$ functions expressed in equation 6.22. For the untagged events, since the flavour of the $B_s^0$ is unknown, the sign of the terms in equation 6.22 related to $\Delta m_s$ cannot be assigned.

In the offline selected signal sample there is a very small asymmetry in the true $B_s^0$ flavour; 49.3±0.5% of the candidates are $B_s^0$, and 50.7±0.5% are $\overline{B}_s^0$.

### Tagging Efficiency

In total, 5901 of the 9753 true signal candidates are tagged, giving an overall tagging efficiency $\epsilon_{tag} = 60.5 \pm 0.5\%$. Of these tagged events, 2892 (49.0±0.6%) are tagged as $B_s^0$, and 3009 (51.0±0.6%) are tagged as $\overline{B}_s^0$ .

Comparing these results with the true composition of the sample, the tagging efficiency appears to be the approximately equal for both $B_s^0$ and $\overline{B}_s^0$. Of the 4805 true $B_s^0$ candidates in the sample, 2896 are tagged, giving an efficiency $\epsilon_{tag}(B_s^0) = 60.3 \pm 0.7\%$. For the $\overline{B}_s^0$ candidates, 3005 from 4948 are tagged, corresponding to an efficiency of $\epsilon_{tag}(\overline{B}_s^0) = 60.7 \pm 0.7\%$. The remaining untagged event sample is comprised of 1909 (49.6±0.8%) $B_s^0$ candidates and 1943 (50.4±0.8%) $\overline{B}_s^0$ candidates.

### Mistag Rate

The true flavour of some of the candidates does not match the flavour with which they are tagged. Overall, 2148 of the 5901 tagged candidates are tagged incorrectly, giving a mistag rate of $\omega_{tag} = 36.4 \pm 0.9\%$. Like the tagging efficiency, the mistag rate can also be considered separately for the two flavours. Of the 2892 candidates tagged as $B_s^0$, 1072 of these are incorrectly tagged, giving a mistag rate of $\omega_{tag}(B_s^0) = 37.1 \pm 1.3\%$. For those tagged as $\overline{B}_s^0$, 1076 of the 3009 candidates are tagged incorrectly, giving a mistag rate of $\omega_{tag}(\overline{B}_s^0) = 35.7 \pm 1.3\%$. This suggests that the mistag rate is independent of the B-meson flavour in this channel.

These mistag rates are calculated by averaging over all events. However, the flavour tagging system also provides a per-event probability of the tag being correct. This per-event $\omega_{tag}$ rate comes from the output of the neural net which combines the tag decision from the different tagging methods in order to produce an overall tagging decision.

Figure 7.3 shows the comparison between the per-event $\omega_{tag}$ for the offline selected events, divided into 5 bins, and the true (i.e. from comparing the flavour tag to the MC truth flavour of the particle) $\omega_{tag}$ in those bins. Comparing these results to the line showing $y = x$, a strong correlation can be seen. The per-event $\omega_{tag}$ deviates slightly from the true $\omega_{tag}$ in the lowest bin, this is likely to be a consequence of the fact that these events are less common, and so there are fewer events for the neural net to be trained on.

The tagging efficiency and mistag rate can be combined, in order to give an effective tagging efficiency, the tagging power. It is defined thus:

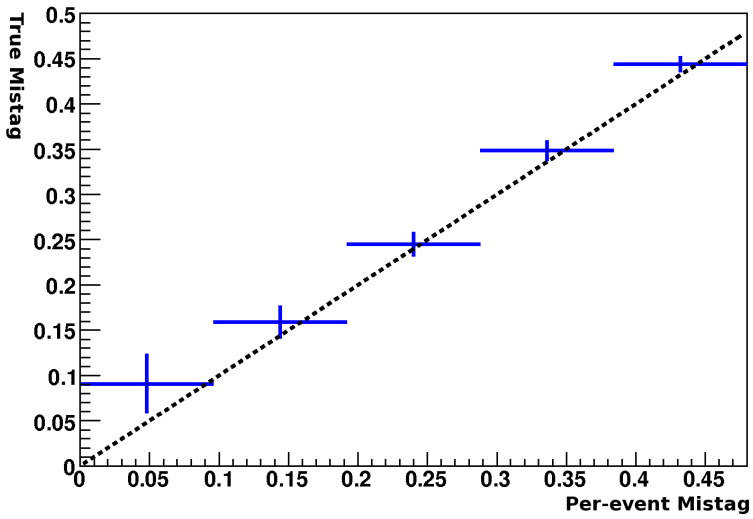


**Figure 7.3:** True mistag rate as a function of per-event mistag.

$$\epsilon_{tag}^{eff} = \epsilon_{tag}\,(1 - 2\omega_{tag})^2 \tag{7.4}$$

Using the overall efficiency and mistag rates, the estimated tagging power in this channel is $\epsilon_{tag}^{eff} = 4.5 \pm 0.7\%$. By separating the tagged sample into five bins of per-event $\omega_{tag}$, according to the tagging category output by the flavour tagging system [94], the tagging power can be significantly increased, as shown in table 7.1. The total tagging power when separating the tagged events in this way is $\epsilon_{tag}^{eff} = 6.8 \pm 0.5\%$. This increase in the tagging power is equivalent to reducing the overall $\omega_{tag}$ rate to 33.3%. It should be noted that these bins are of varying widths, and do not correspond to the binning shown in figure 7.3 (or the different tagging algorithms in table 7.2).

**Table 7.1:** Tagging performance on offline selected events.

| | | $N_{tag}$ | $\epsilon_{tag}$ | $\omega_{tag}$ | $\epsilon_{tag}^{eff}$ |
|---|---|---|---|---|---|
| $B_s^0$ | Bin 1 | 1669 | 34.7±1.0% | 44.2±2.0% | 0.5±0.2% |
| | Bin 2 | 489 | 10.2±0.5% | 37.0±3.2% | 0.7±0.32% |
| | Bin 3 | 359 | 7.5±0.4% | 25.1±2.9% | 1.9±0.4% |
| | Bin 4 | 223 | 4.6±0.3% | 21.1±3.4% | 1.6±0.4% |
| | Bin 5 | 156 | 3.2±0.3% | 12.8±3.0% | 1.6±0.4% |
| | Sum | 2892 | 60.3±0.7% | - | 6.4±0.7% |
| $\overline{B}_s^0$ | Bin 1 | 1659 | 33.5±1.0% | 43.4±1.9% | 0.5±0.2% |
| | Bin 2 | 547 | 11.1±0.5% | 31.6±2.8% | 1.5±0.3% |
| | Bin 3 | 367 | 7.4±0.4% | 28.3±3.1% | 1.4±0.3% |
| | Bin 4 | 230 | 4.6±0.3% | 21.3±3.4% | 1.5±0.3% |
| | Bin 5 | 202 | 4.1±0.3% | 12.9±2.7% | 2.3±0.4% |
| | Sum | 3005 | 60.7±0.7% | - | 7.3±0.8% |

**Individual Tagger Performance**

Table 7.2 shows the number of candidates tagged by each individual tagging algorithm. Each candidate can be tagged by more than one of these algorithms, and the overall tagging decision for each candidate is formed using the combined results of these five algorithms. The first set of results shows the number of candidates tagged overall as $B_s^0/\overline{B}_s^0$ that were tagged as the same flavour by each individual algorithm. The second set shows the number of true $B_s^0/\overline{B}_s^0$ candidates that were tagged as their correct flavour by each algorithm. The third set shows the number of true $B_s^0/\overline{B}_s^0$ candidates, tagged as their correct flavour overall, that were tagged as their correct flavour by each algorithm. In each case, the numbers in brackets represent the number of candidates tagged by that algorithm only.

**Table 7.2:** Summary of individual tagging algorithms used.

| | Tagged as $B_s^0$ | Tagged as $\overline{B}_s^0$ |
|---|---|---|
| Vertex Charge (only) | 1505 (954) | 1631(982) |
| Same Side Kaon (only) | 1131 (620) | 1072 (586) |
| Opposite Side Kaon (only) | 783 (223) | 834 (233) |
| Opposite Side Electron (only) | 57 (10) | 24 (5) |
| Opposite Side Muon (only) | 169 (41) | 192 (57) |
| | True $B_s^0$ | True $\overline{B}_s^0$ |
| Vertex Charge (only) | 908 (521) | 1029 (545) |
| Same Side Kaon (only) | 1139 (413) | 796 (390) |
| Opposite Side Kaon (only) | 620 (143) | 608 (153) |
| Opposite Side Electron (only) | 88 (7) | 17 (4) |
| Opposite Side Muon (only) | 131 (29) | 156 (39) |
| | Both | Both |
| Vertex Charge (only) | 908 (521) | 1029 (545) |
| Same Side Kaon (only) | 766 (402) | 745 (380) |
| Opposite Side Kaon (only) | 521 (142) | 579 (152) |
| Opposite Side Electron (only) | 34 (7) | 16 (4) |
| Opposite Side Muon (only) | 124 (29) | 145 (39) |

These results highlight the importance of good RICH particle ID performance to the analysis of this channel; a large fraction of the $B_s^0$ candidates are tagged by the same-side and opposite-side kaon taggers which rely heavily on the performance of the RICH.

### 7.2.3 Acceptance

Both the online and offline event selections remove a fraction of signal events in addition to suppressing the background events. Some cuts will remove events uniformly with respect to a certain observable, while other cuts will remove events primarily in certain regions of an observable's phase space. In the latter case, the distributions of these

observables will be modified, which can affect the fit results if not accounted for in the fit model. These changes can be modelled by applying an acceptance function.

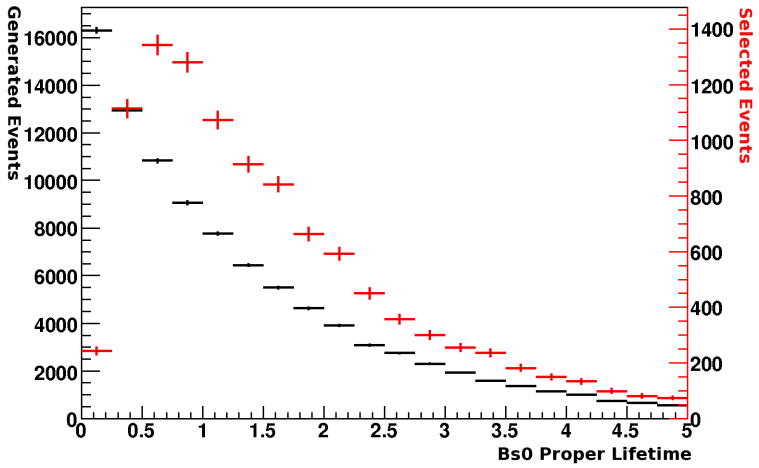


**Figure 7.4:** $B_s^0$ Proper lifetime (ps) distributions for generated (black) and offline selected (red) events.

### Proper Time Acceptance

Figure 7.4 shows the comparison between the proper lifetime distribution for the generated events (for which the lifetime information is taken from the MC truth) and the offline selected events (for which the reconstructed lifetime is used). It can be observed that there is a significant difference between the two distributions at short lifetimes (<1 ps). This difference is caused by cuts applied relating to the $B_s^0$ vertex; impact parameter significance, vertex $\chi^2$ and the direction angle.

Dividing the selected lifetime distribution by the generated distribution (both binned) provides an acceptance efficiency distribution, to which a function can be fitted. The initial form assumed for the acceptance function was [35]

$$\epsilon_{acc}(\tau) = \frac{a\tau^3}{b+\tau^3} \tag{7.5}$$

Fitting to the binned data using this function is shown as the red line on figure 7.5. It returns values for the parameters of $a = 0.141 \pm 0.001$ and $b = 0.030 \pm 0.002$.

From looking at the data, there is also evidence that the acceptance efficiency decreases for long $B_s^0$ proper lifetimes. This is likely to be due to a decrease in tracking efficiency for $B_s^0$ candidates with longer flight distances, whose decay products pass through fewer Velo sensors. This loss of efficiency can be accounted for by adding an additional term to the acceptance function, giving it the form

$$\epsilon_{acc}(\tau) = \frac{a\tau^3}{b+\tau^3}(1+c\tau) \tag{7.6}$$

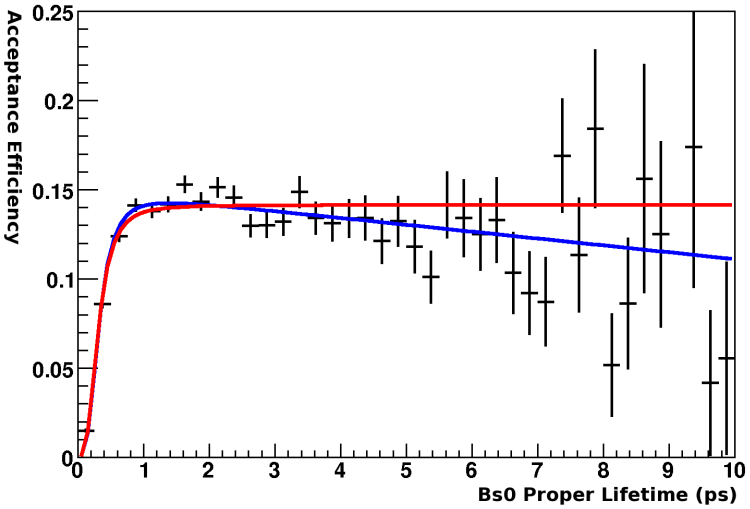


**Figure 7.5:** Acceptance efficiency as a function of $B_s^0$ proper lifetime (ps), fit with two different acceptance functions.

Fitting using this function results in the parameter values $a = 0.150 \pm 0.003$, $b = 0.034 \pm 0.002$ and $c = -0.026 \pm 0.006$. Using this acceptance function gives a $\chi^2$ per degree of freedom of 1.39, improving on the 1.73 obtained using the initial acceptance function.

### Angular Acceptance

A similar procedure can be followed to investigate acceptance effects in the decay angles. Since the decay angles are calculated from the particle momenta, it is the transverse momentum cuts that are likely to have the largest effects on the angular distributions. The order of the two angles $\theta_1$ and $\theta_2$ is randomized with respect to the order from the reconstruction; this is to remove any asymmetries caused by the highest momentum $\phi$ candidate always being reconstructed first. The $\theta$ angles can be swapped freely, since the angular distributions given in equation 6.19 are invariant under the exchange of $\theta_1$ and $\theta_2$. The angular acceptance distributions are shown in figures 7.6(a) and 7.6(b).

These distributions appear to be flat, to a reasonable approximation. Fitting a constant efficiency to the data gives a $\chi^2$ per degree of freedom of 0.92 and 1.9 for $\theta$ and $\varphi$ respectively. It should be noted that these acceptance plots only reflect the effect of selection cuts applied to $B_s^0$ mesons decaying within the detector acceptance, as the decay products are forced to be within the detector acceptance at generation. Therefore, there may be additional acceptance effects due to this geometric constraint, but these are expected to be small.

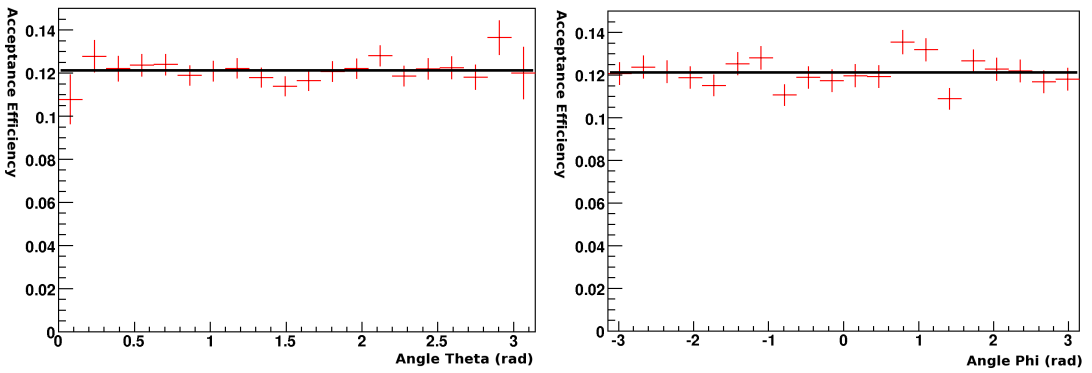


(a) $\theta$ (b) $\varphi$

**Figure 7.6:** Acceptance efficiencies as a function of the decay angles.

## 7.3 Background Model

Since the data sample includes background events in addition to the signal events of interest, the total PDF which is fit to the data must allow contributions from both signal and background. Hence, it is necessary to define a PDF which describes the background events.

The background PDF described here is based on the distributions of $b\bar{b}$-inclusive events passing the preselection described in section 6.4.1. These distributions may be expected to be different once the final event selection has been applied, however, the low background statistics in the selected sample make estimating a PDF based on these events unfeasible. Thus, the preselected background events are used to provide the best estimate of the final offline selected combinatoric background distributions, although for investigating the proper time background, the $\chi^2$ and $\cos\theta$ cuts were applied in addition, as these cuts have a large effect on this distribution.

### 7.3.1 Proper Time Background

To estimate the $B_s^0$ proper lifetime distribution from the $b$-inclusive data, the $\chi^2 < 25$ and $\cos\theta > 0.999$ cuts described in section 6.4.2 were applied. Based on fits to this data, the background PDF has a distribution in this input variable with the form

$$P(\tau) \propto e^{-\Gamma_1 \tau} + C e^{-\Gamma_2 \tau} \tag{7.7}$$

where $\Gamma_1 = 0.252$, $\Gamma_2 = 1.291$ and $C = 3.848$, as shown in figure 7.7. An acceptance function of the form

$$\epsilon_{acc}^{bg}(\tau) = \frac{a\tau^3}{b + \tau^3} \tag{7.8}$$

where $a = 1$ and $b = 1.5 \times 10^{-4}$, is also applied.

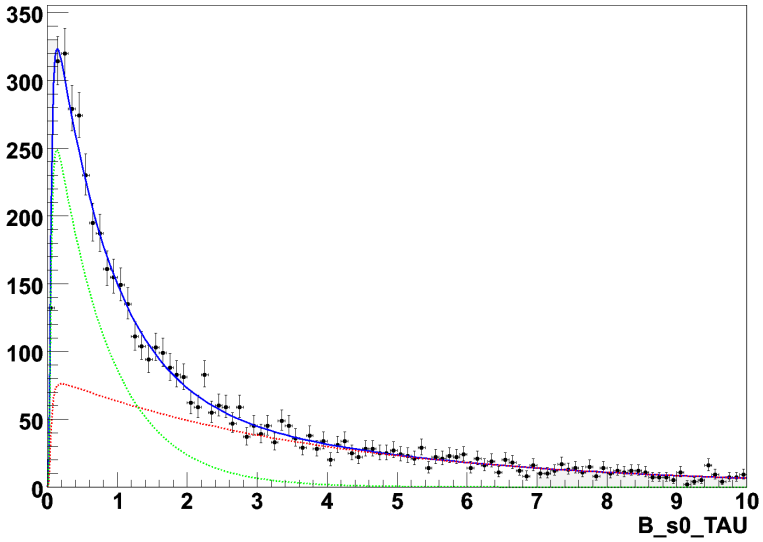


**Figure 7.7:** $B_s^0$ proper lifetime distribution from $b\bar{b}$-inclusive background with preselection plus $B_s^0$ $\chi^2$ and $\cos\theta$ cuts from section 6.4.2 applied.

### 7.3.2 Angular Backgrounds

The background distributions in the decay angles extracted from the preselected $b\bar{b}$-inclusive sample are shown in figure 7.8. The background distribution in the two angles $\theta_1$ and $\theta_2$ are significantly different; this is due to the ordering of the $\phi$ candidates by the reconstruction software. Consequently, there are a significantly larger number of true background $\phi$ resonances contributing to the distribution of $\theta_1$ than to that of $\theta_2$. The average of these two distributions is taken by randomizing the order of the background $\phi$, and this is what is shown in figure 7.8(a). The background PDF contribution fit to

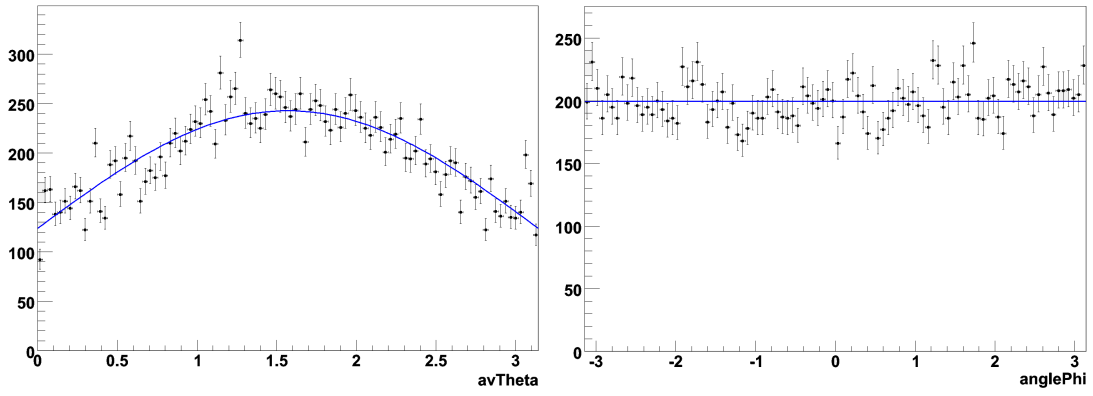


(a) $\theta_{av}$ (b) $\varphi$

**Figure 7.8:** Angular distributions from preselected $b\bar{b}$-inclusive background.

this average distribution is

$$P(\theta_{av}) \propto 1 + \sin(\theta_{av}) \tag{7.9}$$

The background distribution in the decay angle $\varphi$ is fit with a flat PDF contribution.

### 7.3.3 $B_s^0$ mass background

The distributions of the previous four input variables ($\tau$, $\theta_1$, $\theta_2$ and $\varphi$) do not offer good separation between signal and background, and so a contribution to the PDF from the $B_s^0$ mass distribution is also added. As can be seen in figure 7.9, this variable provides good separation between signal and combinatoric background. The background

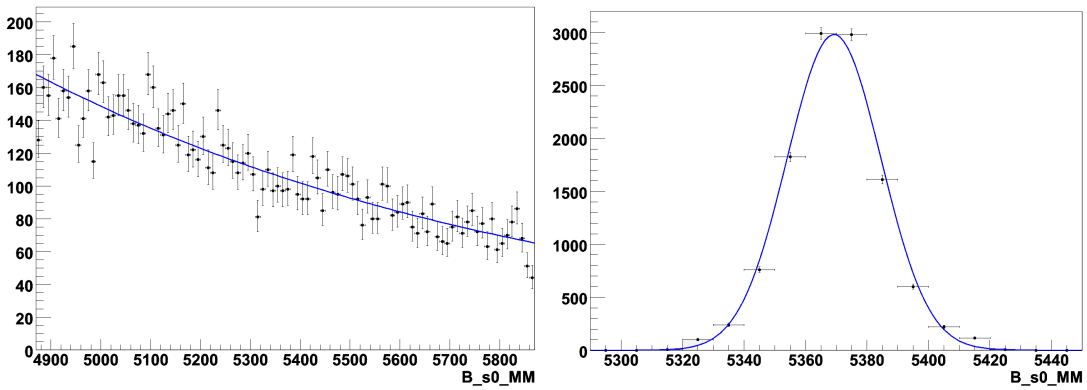


(a) preselected $b$-inclusive (b) signal

**Figure 7.9:** $B_s^0$ mass distributions.

distribution is fit with a shallow exponential (with exponent coefficient $-9.75 \times 10^{-4}$), while the signal distribution is fit with a gaussian of width 15.3 MeV, centred about the nominal $B_s^0$ mass of 5366 MeV.

### 7.3.4 Combining PDFs

The $B_s^0$ mass distribution is assumed to be independent of other input variables, and so the total signal PDF is formed from the product of the four-dimensional PDF used to extract $\Phi$, defined by equations 6.19 and 6.22, with the mass PDF:

$$P_{sig}(\tau, \theta_1, \theta_2, \varphi, m) = P_{sig}(\tau, \theta_1, \theta_2, \varphi) \times P_{sig}(m) \tag{7.10}$$

In the absence of a priori knowledge of their interdependence, the input variables to the background PDF are all assumed to be uncorrelated, and so the total background PDF is formed from the product of independent PDFs in each variable:

$$P_{bg}(\tau, \theta_1, \theta_2, \varphi, m) = P_{bg}(\tau) \times P_{bg}(\theta_1) \times P_{bg}(\theta_2) \times P_{bg}(\varphi) \times P_{bg}(m) \tag{7.11}$$

The two PDFs are combined simply by adding together their values at each point in the multi-dimensional space of the input variables, scaled by the size of their contributions. This can be done in terms of a single parameter, the B/S ratio, or the number of signal and background events in the sample can both be floated. It is the latter approach,

called an Extended Likelihood, which is used in these studies.

Information from the flavour tagging system is also included in the fit, but since this divides the data into discrete categories it is treated differently to the other, continuous input variables. The 4-dimensional PDF chooses the correct form of the lifetime distributions depending on the tag decision, and separate PDFs are created within RooFit for each tag category, which are then fitted as a simultaneous set, each with a different $\omega_{tag}$. The background model assumes the same distribution over the tag categories as for signal, so that each simultaneous PDF will have the same B/S ratio.

## 7.4 Estimated Sensitivities

This model can be used to estimate the expected statistical error on the physics parameters to be measured. This is done by generating so-called 'toy' Monte Carlo datasets; toy data contains events that have been produced according to the PDF, rather than by modeling the underlying physics processes and detector interactions and responses as is done in full Monte Carlo data such as DC06. This allows large data samples to be produced quickly, and by fitting the PDF back to these samples, and repeating this process on a large number of samples (referred to as 'experiments'), the distributions of the fit results can be studied. These toy events can also be generated with a range of values for the input parameters, allowing the dependence on the underlying value of the parameters to be investigated.

For these toy studies, the floated parameters for the likelihood to be maximised with respect to are

- The total weak phase, $\Phi$
- The linear polarisation amplitudes, $A_{||}$ and $A_{\perp}$
- The strong phases, $\delta_1$ and $\delta_2$
- The mistag rate, $\omega_{tag}$ for each tagging category
- The number of signal and background events, $N_{sig}$ and $N_{bg}$

The remaining parameters have their values fixed. The decay widths of the $B_s^0$ mass eigenstates, $\Gamma_L$ and $\Gamma_H$ are set to 0.738 and 0.654 ps$^{-1}$ respectively, and $\Delta m_s = 17.77$ ps$^{-1}$ is used [28]. The proper time and angular resolutions used are taken from the DC06 results discussed in section 7.2 (although the resolution models applied in the PDF use only the core and tail contributions), as are the acceptance functions.

Figure 7.4 shows how the sensitivity to the Standard Model value of $\Phi$ $(= 0)$ is expected to scale as the LHCb data sample increases. The annual signal yield was assumed to

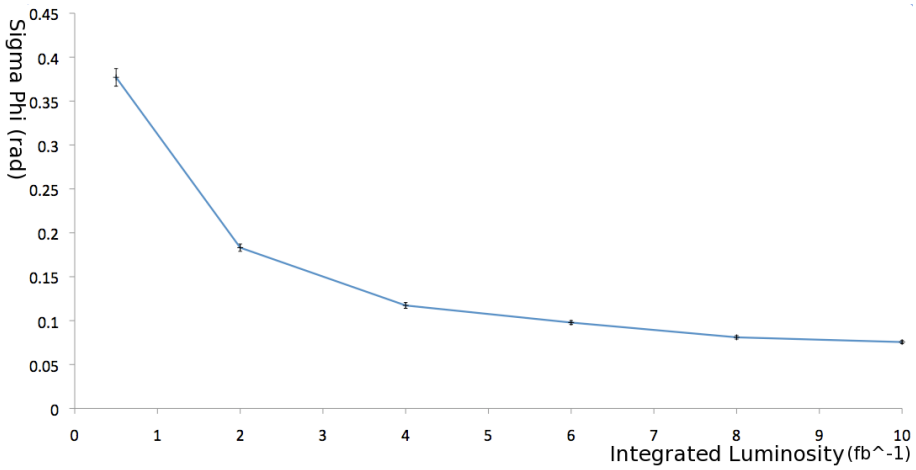


**Figure 7.10:** Variation of $\sigma(\Phi)$ with increasing integrated luminosity.

be 2936 with a B/S ratio of 0.69 for these experiments, and the linear polarisation and tagging parameters are taken from the values in tables 6.1 and 7.1[1] respectively.

Experiments were also performed with the $\omega_{tag}$ rates fixed, in order to compare the sensitivities obtained. Fixing all five $\omega_{tag}$ rates to their true, generated values, yields a sensitivity to $\Phi$ of $\sigma(\Phi) = 0.1667 \pm 0.004$ rad for an integrated luminosity of 2 fb$^{-1}$. Comparing this to the result of $\sigma(\Phi) = 0.1831 \pm 0.0042$ rad obtained for 2 fb$^{-1}$ when the five $\omega_{tag}$ rates are floated, it is clear that some sensitivity is lost if these parameters are floated. This sensitivity can also be compared with the result obtained when a single, fixed $\omega_{tag}$ representing the overall average mistag probability is used; this situation yields a sensitivity $\sigma(\Phi) = 0.2087 \pm 0.005$ rad, clearly demonstrating the advantage of using the tagging category information.

While the sensitivity obtained for 2 fb$^{-1}$ with five fixed $\omega_{tag}$ rates is significantly better than the result when these parameters are floated, increasing the size of the data sample to 10 fb$^{-1}$ allows sensitivities of $0.0752 \pm 0.0018$ rad and $0.0756 \pm 0.0018$ rad, with the $\omega_{tag}$ rates fixed and floated respectively, to be obtained. This suggests that once the dataset is sufficiently large to allow good determination of the $\omega_{tag}$ rates, floating these parameters does not impact the statistical precision on measuring $\Phi$.

The sensitivity achievable in measuring $\Phi$ may also depend on the value of $\Phi$ to be measured. Figure 7.11 shows the values of $\sigma(\Phi)$ for a number of generated values of $\Phi$ in the range $-0.3 < \Phi < 0.3$ rad with an integrated luminosity of 10 fb$^{-1}$ and B/S=0.69. Over this range there is a variation in sensitivity $0.0751 < \sigma(\Phi) < 0.083$ rad, without an obvious trend in the relationship between $\Phi$ and $\sigma(\Phi)$.

The measurement of $\Phi$ relies on knowledge of the linear polarisation state composition of the data sample, and so the precision in measuring $A_{||}$ and $A_{\perp}$ will have an effect on $\sigma(\Phi)$. Table 7.3 shows the sensitivity obtained for 10 fb$^{-1}$ and $\Phi = 0$ in generation,

[1]The average of the $B_s^0/\overline{B}_s^0$ values for $\omega_{tag}$ and $\epsilon_{tag}$ in each category were used.

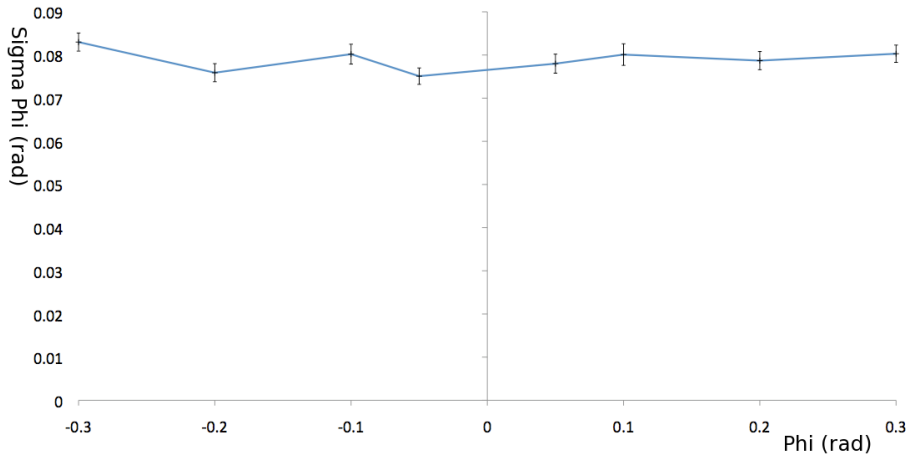


**Figure 7.11:** Variation of $\sigma(\Phi)$ with $\Phi$.

with a number of different scenarios for the linear polarisation coefficients $A_{||}$ and $A_{\perp}$, along with the resolutions, $\sigma(A_{||})$ and $\sigma(A_{\perp})$, in determining these parameters. The best sensitivity to all three parameters is obtained when $A_{||} = A_{\perp} = 0.15$, although an even greater sensitivity is expected for fully polarised scenarios.

**Table 7.3:** Variation of $\sigma(\Phi)$ with $A_{||}$ & $A_{\perp}$.

| $A_{\|\|}$ | $A_{\perp}$ | $\sigma(\Phi)$ (rad) | $\sigma(A_{\|\|})$ | $\sigma(A_{\perp})$ |
|---|---|---|---|---|
| 0.15 | 0.35 | 0.0788±0.0018 | 0.00474±0.00011 | 0.00568±0.00013 |
| 0.35 | 0.15 | 0.0732±0.0017 | 0.00572±0.00014 | 0.00481±0.00011 |
| 0.15 | 0.15 | 0.0697±0.0016 | 0.00459±0.00011 | 0.00449±0.00011 |
| 0.35 | 0.35 | 0.0784±0.0018 | 0.00614±0.00014 | 0.00583±0.00013 |

The B/S ratio will also affect the sensitivity to $\Phi$. Figure 7.12 shows the variation of $\sigma(\Phi)$ for 0 <B/S< 3.5, for the standard set of parameter values. The number of signal events is equivalent to 10 fb$^{-1}$, and is constant for all of the experiments. The B/S ratio is varied by changing the number of background events in the sample.

The sensitivities obtained range from 0.0629±0.0016 rad, when there are no background events in the sample, to $0.0959 \pm 0.0026$ rad, when the B/S ratio is 3.5.

## 7.5 Systematic Errors

Where possible, the fixed parameters of the fit model are set to the best measurements of their values, but where measurements do not exist, their values must be estimated. Since these estimates rely on the accuracy of the Monte Carlo simulation, or applicability of results from control channels, they may differ from the true values.

These differences may affect the values of the physics parameters returned by the fit,

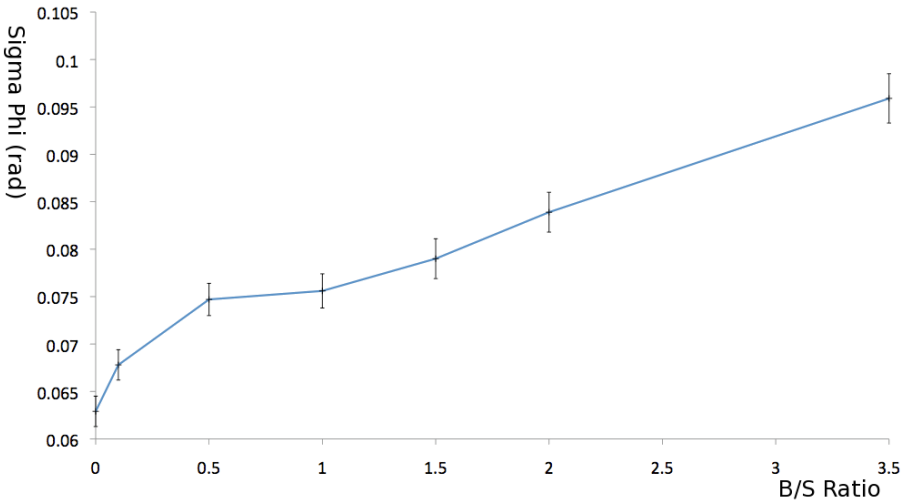


**Figure 7.12:** Variation of $\sigma(\Phi)$ with B/S ratio. These results deviate from the $\sigma(\Phi) \propto \sqrt{1+B/S}$ dependence that would be naïvely expected.

causing systematic biases. By generating toy Monte Carlo events with one set of values for these parameters (based on the uncertainty in the values of the parameters), and fitting with another (our best estimates of the parameters), these biases can be investigated. These studies were carried out on samples representing an estimated integrated luminosity of 10 fb$^{-1}$, to ascertain whether systematic effects are comparable to the statistical error for the total projected LHCb data sample.

### 7.5.1 Tagging

Incorrectly tagged candidates dilute the contribution of the $\sin(\Delta m_s t)$ terms in the time-dependent functions $K_n(t)$, defined in equation 6.23, the amplitude of which depend on the value of $\Phi$. For example:

$$\begin{aligned} K_1(t) &= \frac{1}{2}A_0^2[(1+\cos\Phi)e^{-\Gamma_L t} + (1-\cos\Phi)e^{-\Gamma_H t} \\ &\quad \pm(1-2\omega_{tag}) \times 2e^{-\Gamma_s t}\sin(\Delta m_s t)\sin\Phi] \end{aligned} \tag{7.12}$$

Where $(1-2\omega_{tag})$ represents the dilution factor. Hence, using incorrect mistag rates can cause a systematic bias in the value of $\Phi$ returned by the fit. By fitting for the 5 mistag rates, this issue is avoided. However, the form of the dilution factor shown here assumes identical tagging performance for both $B_s^0$ and $\overline{B}_s^0$, which may not necessarily be the case, although the DC06 results discussed in section 7.2.2 suggest they should be very similar. To allow for tagging asymmetries additional parameters, $\Delta\omega_{tag}$ and $\Delta\epsilon_{tag}$ are added for each tagging category. The parameter $\Delta\omega_{tag}$ describes differences between the dilution factors for $B_s^0$ and $\overline{B}_s^0$, while $\Delta\epsilon_{tag}$ describes differences in the number of $B_s^0$ and $\overline{B}_s^0$ in the untagged sample. The value of each will be zero in the case that the tagging performance is identical for both flavours.

Possible systematic effects due to these parameters can be estimated by generating toy MC events with non-zero values of $\Delta\omega_{tag}$ and $\Delta\epsilon_{tag}$ (using variations of several percent in both the positive and negative directions for different tag categories) and fitting with the values set to zero. The value of $\Phi = 0.3$ rad was used for the 1000 experiments, as for values of $\Phi$ close to zero, the size of the tagging-dependent terms is very small, and biases will be correspondingly small.

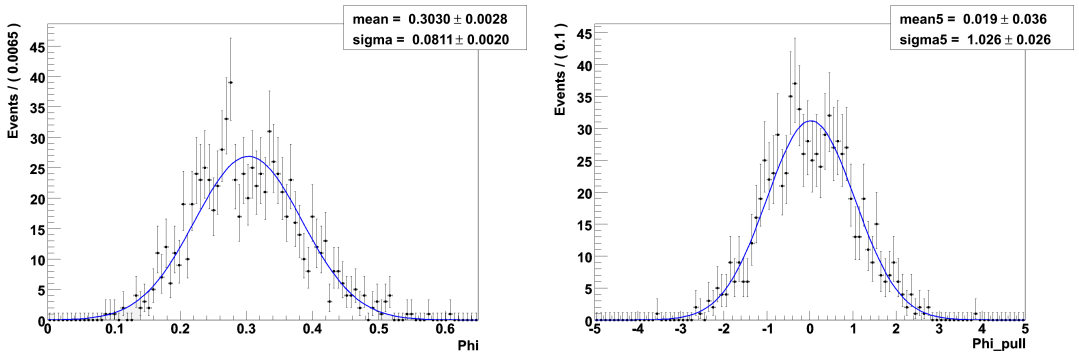


(a) $\Phi$ Distribution (b) $\Phi$ Pull

**Figure 7.13:** Distribution and Pull of $\Phi$ fit results for the case in which all $\Delta\omega_{tag}$ and $\Delta\epsilon_{tag}$ are generated with non-zero values, and are fixed to zero in fitting.

The results obtained from these experiments are shown in figure 7.13, and they show only a small bias (+0.003 rad) in the values of $\Phi$ returned by the fit, which is comparable in size to the error on the mean of the gaussian distribution fitted to the results, and is $< 5\%$ of the size of the statistical error on $\Phi$. Experiments were also run with each $\Delta\omega_{tag}$ and $\Delta\epsilon_{tag}$ set to twice the original values; the results from these experiments also showed a bias comparable to the error on the mean, and $\sigma(\Phi)$ consistent with the results shown in figure 7.13.

### 7.5.2 Resolution Models

Lack of knowledge regarding the true proper time resolution for the reconstructed $B_s^0/\overline{B}_s^0$ candidates affects the fit in a similar way to the mistag rate. The finite proper time resolution has the effect of 'smearing' the $\sin(\Delta m_s t)$ oscillations, reducing the effective amplitude, as shown in figure 7.14(a). Hence, the effect of an incorrect proper time resolution is similar to that of an incorrect tagging dilution factor.

Consequently, by fitting for the mistag rates, any potential bias due to an incorrect proper time resolution can be minimised, as it will be absorbed into the value of the fitted parameters. This can be seen in figure 7.14(b), in which no significant bias can be observed in the fit results of 1000 experiments, where a 10% reduction in the proper time resolution[2] from the expected value extracted from the DC06 MC is applied between

[2]I.e. an increase in the width of both of the gaussian PDFs in the resolution model.

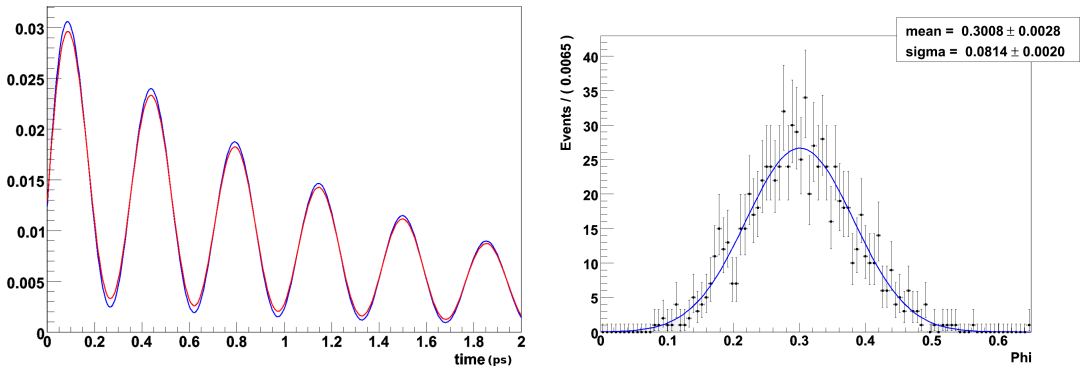


(a) Effect on lifetime component $K_1(t)$ of 10% decrease in resolution (lower resolution in red), demonstrating the reduction in oscillation amplitude.

(b) Distribution of values of $\Phi$ returned by the fit.

**Figure 7.14:** Effects of a 10% error in proper time resolution.

generation and fitting, for $\Phi = 0.3$ rad. Reducing the proper time in generation further, to 20% lower than the fitted value, also gives results consistent with no systematic bias on the fitted values of $\Phi$.

The angular distributions $f_n(\theta_1, \theta_2, \varphi)$, defined in equation 6.19 are slowly-varying functions of the decay angles, and so the effect of angular resolutions (of the order shown in section 7.2) on these distributions is negligible. As a result, lack of knowledge regarding these resolutions does not affect the fit results for $A_{||}$, $A_\perp$, or $\Phi$.

### 7.5.3 $B_s^0$ Lifetime and Mixing Parameters

The $B_s^0$ lifetime parameters and mass difference will be fixed in the fit. These parameters are among the first measurements LHCb hopes to make, and so they should be very well determined by that time that a sufficiently large $B_s^0 \to \phi\phi$ sample is available to allow the maximum likelihood fit to be performed.

In order to assess the systematic effects that fixing the $B_s^0$ lifetimes in the fit could have, fits were performed where the lifetime difference $\Delta\Gamma_s/\Gamma_s$ was varied by the expected LHCb sensitivity to this parameter, $\sigma(\Delta\Gamma_s/\Gamma_s) = 0.018$ [53], between generation and fitting. Systematic effects due to fixing the $B_s^0$ mass difference $\Delta m_s$ were also investigated in the same way. In this case, the expected LHCb sensitivity to the parameter is $\sigma(\Delta m_s) = 0.011$ ps$^{-1}$.

The results can be seen in figure 7.15. Reducing $\Delta\Gamma_s/\Gamma_s$ by 0.018 between generation and fitting causes a bias in $\Phi$ of +0.0057 rad on the generated value $\Phi = 0.3$ rad. Increasing $\Delta m_s$ by 0.011 ps$^{-1}$ results in a bias of -0.0013 rad. These biases are relatively small, and in the case of $\Delta m_s$, is within the fit error on the mean value of $\Phi$. The sensitivities used for the fixed paramters are those expected for 2 fb$^{-1}$, and these

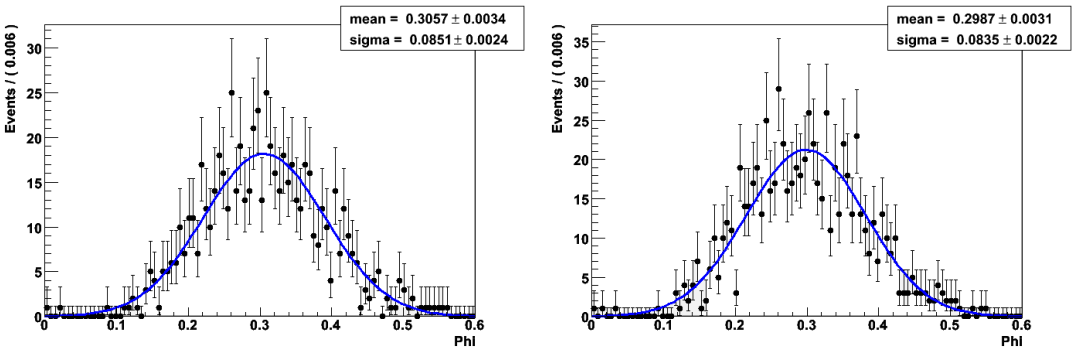


(a) Varying $\Delta\Gamma_s/\Gamma_s$ (b) Varying $\Delta m_s$

**Figure 7.15:** Distribution of $\Phi$ fit results, with the lifetime and mixing parameters varied between generation and fitting.

measurements will improve as more data is collected. When the studies are repeated, using the expected sensitivities for 10 fb$^{-1}$ (extrapolated assuming standard scaling, $\sigma(x) \propto \frac{1}{\sqrt{N_{evts}}}$) as the size of the variation, the biases reduce to $-0.0009$ rad and $-0.0006$ rad for varying $\Delta\Gamma_s/\Gamma_s$ and $\Delta m_s$ respectively. These results are consistent with no bias on the mean value of $\Phi$ returned by the fit.

### 7.5.4 Acceptances

To investigate the effect of an incorrect proper time acceptance function, the parameters $a$ and $b$ that define the shape of the acceptance were varied between generation and fitting. Initially, $a$ was increased by 10%, and $b$ decreased by 10%. The resulting values of $\Phi$ returned by the experiments, which were generated with $\Phi = 0.3$ rad, are shown in figure 7.16(a). A small bias (+0.0034 rad) is suggested by these results, while increasing the variation in the acceptance parameters to 20% results in an increased bias (+0.0088 rad) as shown in figure 7.16(b). The effect of varying the parameter $c$, which determines the slope of the acceptance function at larger proper times, was also investigated. Generating toy data with this parameter set to its value from the DC06 studies, and fitting with it set to zero, (i.e. a flat acceptance for $\tau$ >2 ns) results in a bias of +0.01214 rad on $\Phi = 0.3$ rad.

As discussed in section 7.2, the angular acceptance functions are assumed to be flat. Toy MC events with non-flat angular acceptances were generated to assess the effect of ignoring them in fitting. The acceptance surface with respect to the three decay angles is composed of the product of three one dimensional acceptance functions:

$$\epsilon_{acc}(\theta_{1,2}) = 1 - D(\theta_{1,2} - \frac{\pi}{2})^2 \quad \& \quad \epsilon_{acc}(\varphi) = 1 - D\varphi^2 \tag{7.13}$$

A value of $D \sim 0.003$ was used initially, as this level of deviation from a flat acceptance

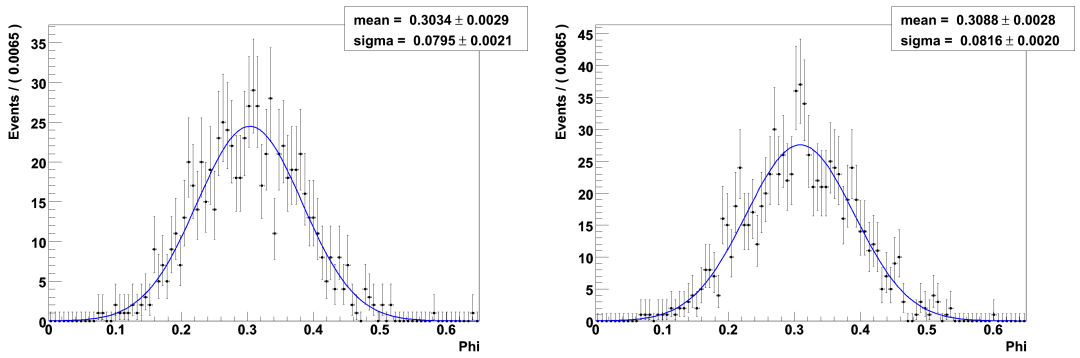


(a) 10 % variation between generation and fitting (b) 20 % variation

**Figure 7.16:** Distributions of $\Phi$ fit results, with proper time acceptance function parameters varied by 10% between generation and fitting.

function does not significantly affect the $\chi^2$ per degree of freedom when fit to the DC06 data shown in figures 7.6(a) and 7.6(b). The effect of this acceptance function will depend upon the value of the linear polarisation amplitudes $A_{||}$ and $A_{\perp}$, and so toys were generated with a variety of values for these parameters. The largest effect was observed with $A_{\perp} = 0.35$ and $A_{||} = 0.15$, the results of which are shown in figure 7.17.

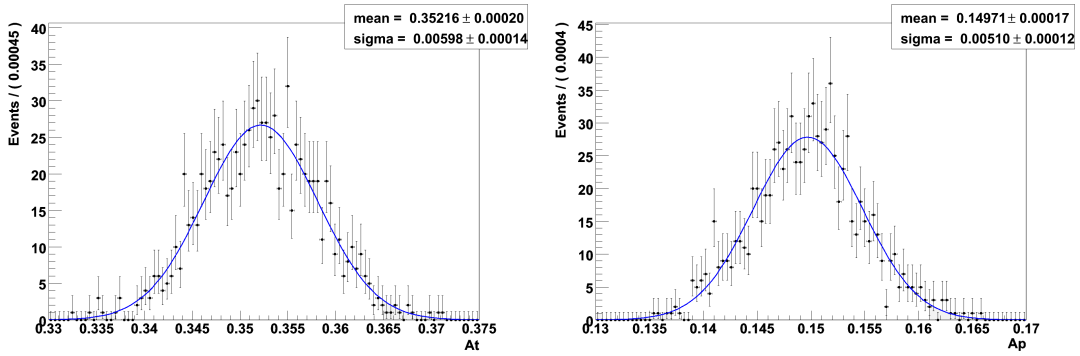


(a) $A_{\perp}$ (b) $A_{||}$

**Figure 7.17:** Distributions of linear polarisation amplitudes, with $\theta$ and $\varphi$ angular acceptance functions applied in generation and ignored in fitting.

From biases on $A_{\perp}$ and $A_{||}$ of +0.00216 rad and -0.00029 rad respectively, the resulting bias on $\Phi = 0.3$ was -0.0039 rad. Increasing the value of $D$ to $\sim 0.015$, the biases on the linear polarisation amplitudes are increased to +0.0101 rad and -0.00213 rad. However, the bias on $\Phi$ decreases to -0.0020 rad; this suggests that the relationship between biases in the linear polarisation amplitudes and in $\Phi$ is non-trivial. This is due to the multiple dependencies of $\Phi$ on the different linear polarisation amplitudes in the six time-dependent $K_n(t)$ functions.

### 7.5.5 Background Model

As was mentioned earlier, the background PDF is not based on theoretical prediction, but on recreating observed distributions from data. In creating the background PDF used for these studies, in addition to being unable to use the full offline selection to produce the distributions, it is also probable that the simulated $b\bar{b}$-inclusive events will differ from the combinatoric background observed in real data from collisions. Studying events in sideband regions from data will allow the background distributions to be better parameterised, but there are still likely to be differences between the model used in the fit and the true underlying distributions.

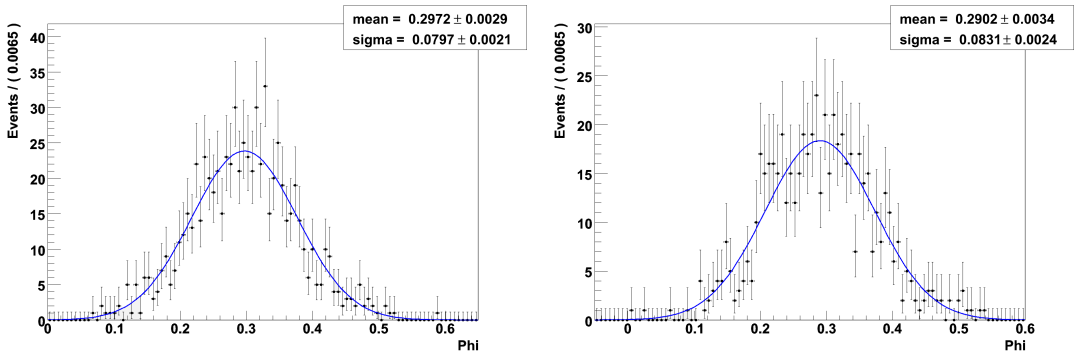


(a) B/S = 0.69 (b) B/S = 1.5

**Figure 7.18:** Distributions of $\Phi$ fit results, with proper time background parameters varied by 10% between generation and fitting.

For the proper time background, the parameters defining the distribution were again varied by 10% (increasing the decay width and coefficient of the short lived component, and decreasing the decay width of the long lived component), between generation and fitting. Experiments were performed with B/S ratios of 0.69 and 1.5. The results are shown in figure 7.18. Biases of -0.0028 rad and -0.0098 rad were returned for B/S ratios of 0.69 and 1.5 respectively on $\Phi = 0.3$ rad.

The effect of varying the background shape in $\theta_{1,2}$ was also investigated. The relative amplitude of the sinusoidal component was varied between generation and fitting from 1 to 0.5. A few values of $A_{||}$ and $A_{\perp}$ were used; the largest bias on the linear polarisation amplitudes was observed with $A_{||} = 0.35$ and $A_{\perp} = 0.15$, -0.0233 and +0.01651 respectively, although the bias on $\Phi = 0.3$ rad of +0.0475 rad is smaller than that observed for the scenario $A_{||} = A_{\perp} = 0.25$ of +0.0779 rad (for which the biases on the linear polarisation amplitudes were +0.00152 and 0.00208 respectively). These results, for which a B/S ratio of 0.69 was used, are shown in figure 7.19. Increasing the B/S ratio to 1.5 results in the biases on $\Phi = 0.3$ rad increasing to +0.0765 and +0.1059 rad for the two different linear polarisation scenarios .

Table 7.4 summarises the results of the studies on systematic errors in this channel.

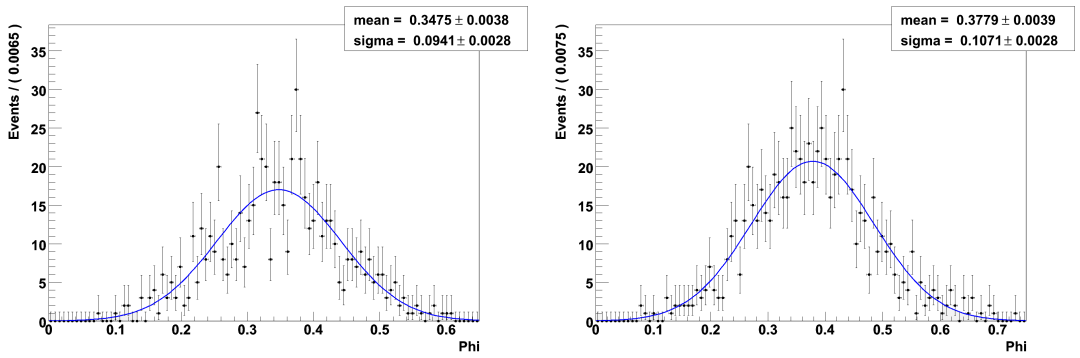


(a) $A_{||} = 0.35$, $A_{\perp} = 0.15$ (b) $A_{||} = A_{\perp} = 0.25$

**Figure 7.19:** Distributions of $\Phi$ fit results, with amplitude of sinusoidal component of $\theta$ background varied by 50% between fitting and generation.

**Table 7.4:** Summary of systematic errors on $\Phi$.

| Fit Input | Potential Systematic Error |
|---|---|
| Lifetime Resolution | negligible |
| Tagging Asymmetry | $\pm$0.003 rad |
| Lifetime Difference $\Delta\Gamma_s$ | $\pm$0.006 rad |
| Mass Difference $\Delta m_s$ | $\pm$0.001 rad |
| Decay Angle Acceptance Function | $\pm$0.004 rad |
| Lifetime Acceptance Function | $\pm$0.01 rad |
| Lifetime Background Model | $\pm$0.01 rad |
| Decay Angle Background Model | $\pm$0.1 rad |

### 7.5.6 Embedded Toy Studies

While toy events generated from the PDF are highly useful, they do not fully reproduce the correlations between all of the input observables that will be present in the real data. These correlations can be studied by using fully simulated, offline selected events. In order to make the most of the limited number of events available, resampling of the data set is used to create 'bootstrap' samples which can be used as a single experiment.

Signal data sets equivalent to 2 fb$^{-1}$ are produced by this method, and the standard fit is performed on each data set. Initially, the distribution of fit results returned from these studies showed ambiguities in fitting the strong phases, resulting in a small secondary peak in $\Phi$, as shown in figure 7.20. When the $\omega_{tag}$ rates are fixed, rather than floated in the fit, this ambiguity is removed, and the fit results return a mean value of $\Phi$ that is biased by -0.04628 rad from the expected mean, $\Phi = 0$.

These fully simulated signal events were then 'embedded' within background events generated from the background PDF, and the fits repeated. The results for these fits with background included showed a larger bias (-0.11571 rad) than for the fits using

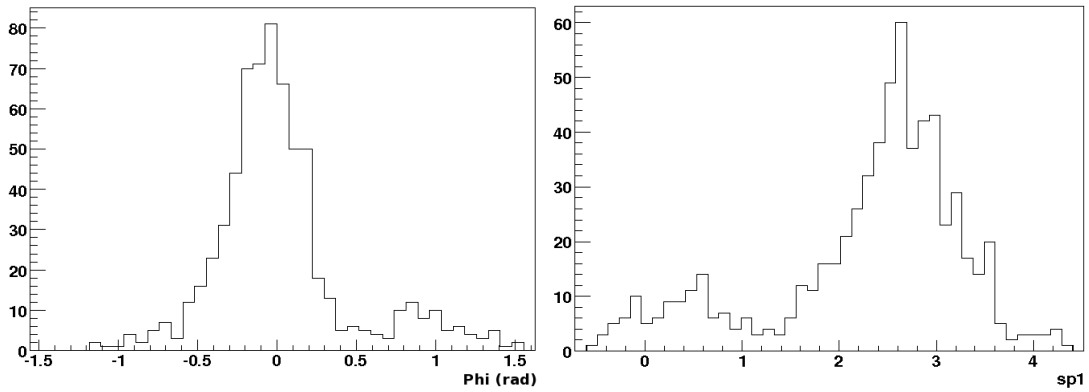


(a) $\Phi$ (b) $\delta_1$

**Figure 7.20:** Fit results from bootstrap samples of fully simulated data.

only the fully-simulated signal data. Multiple peaks in the distributions of the strong phase fit results also appear when background is included, and in this case are not resolved by fixing the $\omega_{tag}$ rates. It is likely that these ambiguities will be resolved with a larger data sample (this is suggested by repeating the study with bootstrap samples equivalent to 4 fb$^{-1}$) but studies of larger data samples are limited by the size of the offline selected signal sample.

These results illustrate some of the difficulties that will be encountered when performing an analysis on real data from collisions. While the observed biases may partly be due to systematic errors of the kind already discussed in this section (for instance, in the acceptance functions), there may also be an 'irreducible' bias present due to correlations between the input observables. These studies can be repeated with background data from sidebands with early LHCb data, and will be crucial in understanding the full systematics of the fit.

## 7.6 Conclusions

The estimated sensitivity to the total weak phase, using the total expected LHCb dataset of 10 fb$^{-1}$, is approximately $\sigma(\Phi) = 0.08$ rad, from pure toy studies assuming the Standard Model value for the weak phase, $\Phi = 0$. This result makes use of improved tagging power made possible by splitting the tagged events based on their per-event $\omega_{tag}$ rate. Variations in sensitivity of order $\sim 10\%$, are observed for scenarios in which $\Phi$ is moved away from zero, corresponding to measuring a total weak phase augmented by contributions from New Physics processes. Changes in the linear polarisation coefficients from their estimated values ($A_{||} = A_{\perp} = 0.25$) can also affect the sensitivity to $\Phi$ by a similar amount.

Floating the five $\omega_{tag}$ rates is found to have a negligible effect on the sensitivity for a

sufficiently large data sample, and in addition to removing the necessity to estimate the value of these parameters, means that potential biases on the fitted value of $\Phi$ due to incorrectly assigning the $B_s^0$ proper lifetime resolution (which would scale proportionally with the value of $\Phi$) are also avoided. However, the results from embedded toy studies suggest that fitting for the $\omega_{tag}$ rates with smaller data samples can introduce ambiguities in the fit results, and these should be studied further. Biases due to the tagging asymmetry parameters, $\Delta\omega_{tag}$ and $\Delta\epsilon_{tag}$ for each tagging category, are small. Systematic errors are also possible due to fixing the $B_s^0$ lifetime and mixing parameters in the fit. However, LHCb aims to make precise measurements of these parameters in other channels which will ensure that these effects are small.

Non-negligible systematic effects are observed if the acceptance functions for the $B_s^0$ proper lifetime and decay angles are incorrectly specified. Procedures are being developed to allow these functions to be extracted from the data directly, and in combination with improved Monte Carlo simulations will allow these functions to be well determined it is hoped.

Large effects are also possible if the background model used in the fit is incorrect. However, it is expected that it will be possible to parameterise well the combinatoric background shapes by studying events in mass sideband regions. Specific backgrounds of the kind discussed in section 6.4.5 will also have an effect; larger background Monte Carlo samples will allow the determination of the decays that contribute, which can then be modelled individually with appropriate PDF contributions.

The measurements that LHCb will be able to make are unprecedented in this channel, not only of the total CP-violating weak phase $\Phi$ but also of the linear polarisation coefficents, and will be very useful facet of LHCb's indirect search for New Physics.

# Chapter 8

# Conclusions

The LHCb detector has been installed and commissioned at IP 8 on the LHC ring, and is currently awaiting its first data from collisions. Among the fully installed subdetectors is the RICH system, which provides the particle identification that is crucial for the physics performance of LHCb. The photodetector elements of the RICH system, the HPDs, have shown excellent performance in tests at the dedicated test facilities in Edinburgh and Glasgow.

These HPDs have been installed on specially designed columns, to allow their integration, along with the necessary offboard electronics and power supplies, into the RICH system. These columns were subjected to a variety of tests prior to their use in the RICH detectors, in order to ensure their full functionality. Dark count runs taken during these tests allowed early diagnosis of increased ion feedback, the increased occurrence of which was thought to lead to an effect known as 'glow discharge'. While studies on a limited set of HPDs did not reveal a conclusive link between ion feedback and glow discharge, it allowed tools to be developed in order for the ion feedback to be continuously monitored for HPDs installed in the RICH detectors. By monitoring this parameter, HPD replacements can be made as required during shutdown periods to maintain the optimum RICH performance.

Prior to the filling of the RICH detectors, several HPD columns were tested in beam conditions, using a $\pi^-$ beam produced by the CERN SPS accelerator. Measurements were made of the Cherenkov angle and resolution (for the two radiator gases used), as well as dark count rates and charge sharing percentages for each of the HPDs used. Detailed simulations of the test beam were also performed, in order to aid understanding of features of the data, such as pixelisation effects. The experience gained during test beam periods proved useful during the commissioning period, and the results obtained help the expected performance of the RICH detectors to be understood.

The two RICH detectors are now fully populated with HPD columns, and have been collecting large amounts of data from dark count runs, and runs with both pulsed and

continuous laser light. The data obtained during commissioning have also allowed the evolution of the HPD ion feedback behaviour to be studied, and these results have been carefully monitored, allowing HPDs that have begun to malfunction to be replaced. A system was designed, using a pulsed laser, in order to allow the timing properties of the HPDs within the RICH detectors to be established, and adjustments implemented to offer a common timing solution. The RICH laser pulser system has been successfully used in order to perform and verify the time alignment of the two RICH detectors. This system will remain in place, and will be used periodically to find and correct for potential timing drifts during the detector lifetime.

The powerful particle identification provided by the RICH system will be essential for the reconstruction of the $b \to s$ penguin decay $B_s^0 \to \phi\phi$. Measurements of the total weak phase, $\Phi$, in this decay offer a sensitive probe for potential New Physics effects. An offline selection and high level trigger for this decay at LHCb has been developed. Based on the available branching ratio measurements, cross-section estimates and the DC06 detector simulation, an annual yield of $2670 \pm 1690$ events is predicted, with a background to signal ratio of approximately 0.76.

The total weak phase $\Phi$, will be obtained from the data by using a maximum likelihood fit. This fit uses angular information in order to determine the linear polarisation coefficients which describe the admixture of CP eigenstates in the final state. Based on the yield estimate, plus tagging and resolution estimates also obtained from DC06 Monte Carlo data, a sensitivity[1] to the Standard Model weak phase, $\Phi = 0$, of $\sigma(\Phi) = 0.18$ rad is predicted for an integrated luminosity of 2 fb$^{-1}$, increasing to $\sigma(\Phi) = 0.08$ rad for 10 fb$^{-1}$. These results use per-event estimates of the mistag rate in order to separate the tagged candidates into 5 bins, which allows the overall tagging power to be increased with respect to using a single average mistag rate. Small variations in the sensitivity are observed for different values of $\Phi$ and the linear polarisation coefficients $A_{||}$ and $A_{\perp}$.

Floating the mistag rates in the fit allows potential biases due to lack of knowledge of these parameters to be avoided. Since varying the $B_s^0$ proper lifetime resolution affects the fit in the same way as a change in the mistag rate, leaving these parameters free also removes biases due to using an incorrect resolution. Non-negligible biases are possible if the background model or acceptance functions used in the fit differ from their true forms.

Correctly parameterising the background model will require a large sample of background events. This can come both from data sideband events, once full-energy LHC collisions are being produced, and also from larger Monte Carlo samples than are currently produced. In particular, large Monte Carlo $b\bar{b}$-inclusive samples will allow additional potential peaking backgrounds to be identified. This will allow further studies of

[1] Assuming an annual yield of 2936 signal events, with a B/S ratio of 0.69.

the kind shown in section 6.4.5, which can also be expanded to use larger data samples for the most important modes.

In the case of the acceptance functions, large samples of generator-level (i.e. prior to simulating the interactions of the generated particles with the detector) Monte Carlo data can be produced in order to investigate in greater detail the effect of various cuts on the distributions of the $\phi$ decay angles and the $B_s^0$ proper lifetime. Techniques for extracting the acceptance functions from data are in development, and in combination with information form Monte Carlo events will hopefully allow biases due to these factors to be avoided.

A larger background sample will allow more sophisticated, multivariate event selection procedures such as Boosted Decision Trees to be investigated. The sensitivity to $\Phi$ may also be improved further by considering a different parameter to maximise when performing the event selection. Suggestions have been made that it could be possible to select events based on a 'per-event power'. This method is based on the idea that some events improve $\sigma(\Phi)$ more than others, and thus requires a weighting factor to be calculated for each event that reflects its contribution. This weighting factor will be based upon the mistag rate and local B/S ratio. The former can be estimated based on per-event mistag rates, while the latter requires the multi-dimensionally binned B/S rates to be re-calculated after each optimisation step. It is therefore a far more complicated procedure than maximisation with respect to parameters based on overall signal and background yields. This approach, as with all other selection studies, will be improved by a larger background sample.

Recent results from the CDF experiment suggest that the $B_s^0 \to \phi\phi$ branching ratio is larger than previously expected:

$$BR(B_s^0 \to \phi\phi) = (2.4 \pm 0.2^{stat} \pm 0.3^{syst} \pm 0.8^{BR(B_s^0 \to J/\psi\phi)}) \times 10^{-5} \text{ [95]}$$

This measurement is close to the theoretical predictions for the branching ratio in this channel, $2.18^{+0.11+3.04}_{-0.11-1.7} \times 10^{-5}$ [96]. The central value of this new measurement is a factor of $\sim 1.7$ larger than that used to estimate the signal yield in chapter 6. This increased yield will reduce the statistical error on $\Phi$ by a factor of $\sim 0.77$, neglecting any additional improvement due to an improved B/S ratio. The B/S ratio obtained in the CDF study was $< 0.25$.

The LHC will usher in a new era for experimental particle physics, and LHCb will capitalise on this to drive forwards the field of B-physics. The huge volume of data that will be produced requires novel computing methods in order to allow efficient data access and processing to be available to all of the physicists wishing to perform analyses. These analyses will be highly challenging, but the results will offer fresh and invaluable insights into the fundamental nature of our Universe.

# Appendix A

# Timing Scan Results

## RICH 2

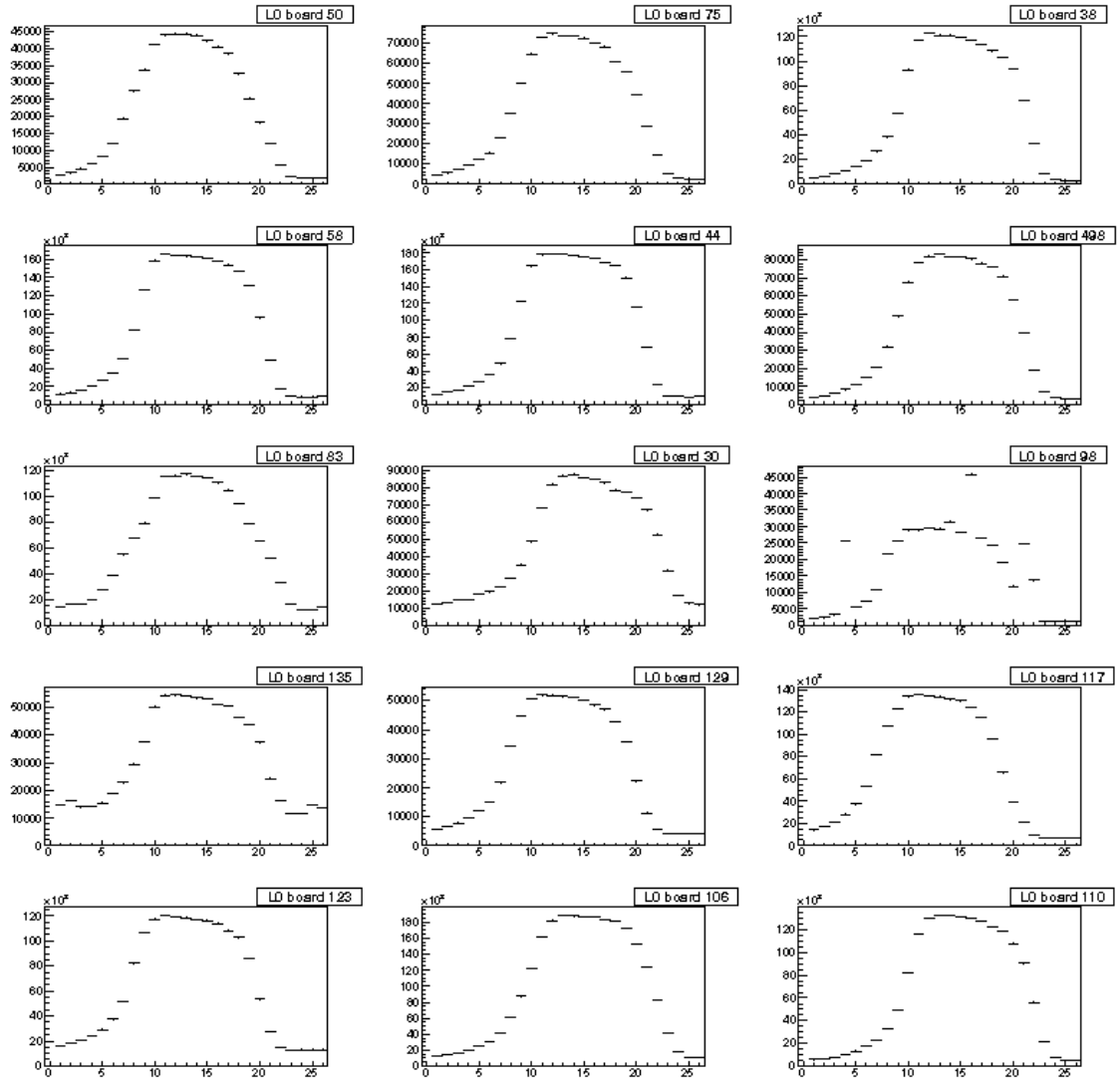

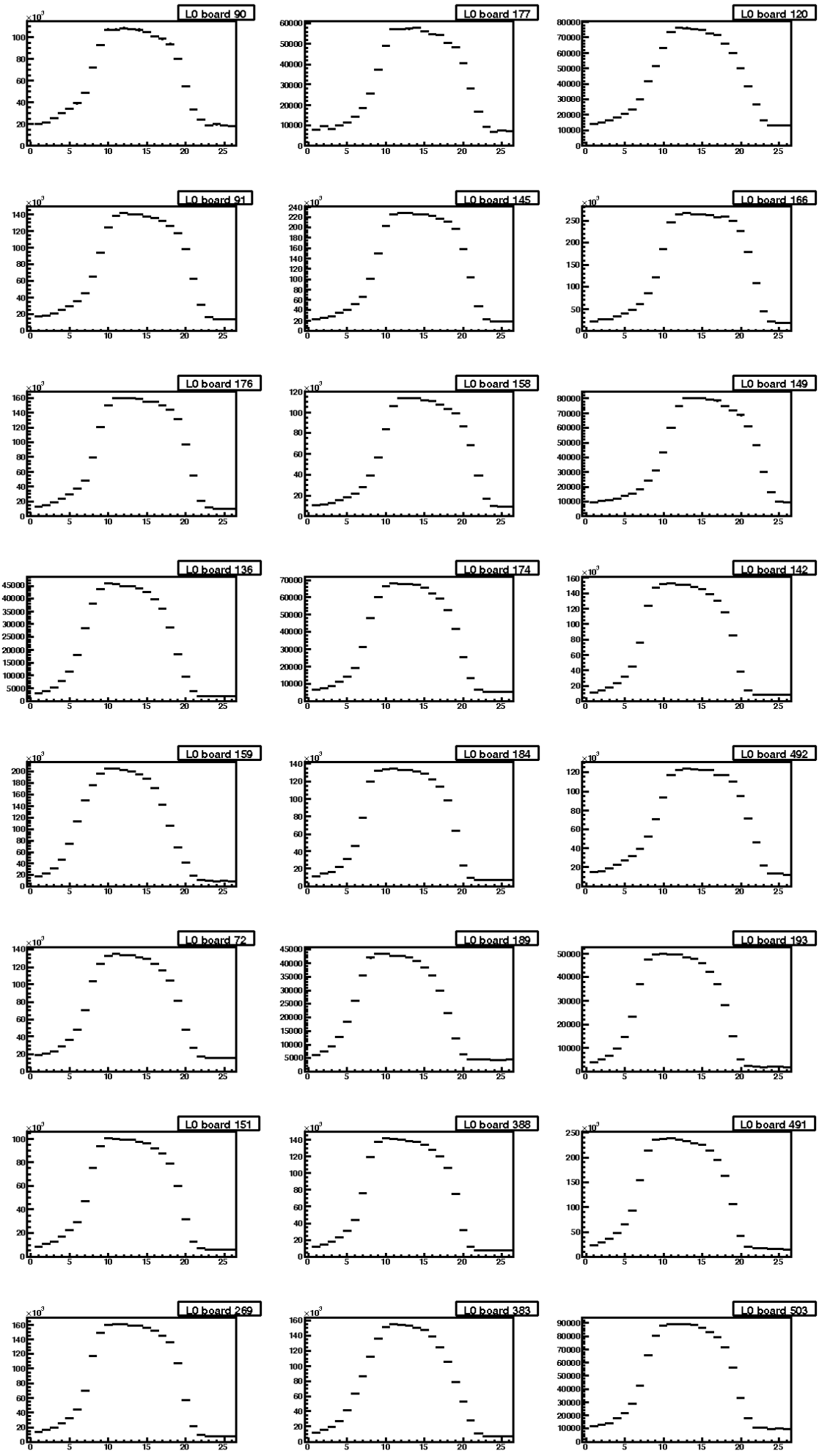
L0 board 90
L0 board 177
L0 board 120
L0 board 91
L0 board 145
L0 board 166
L0 board 176
L0 board 158
L0 board 149
L0 board 136
L0 board 174
L0 board 142
L0 board 159
L0 board 184
L0 board 492
L0 board 72
L0 board 189
L0 board 193
L0 board 151
L0 board 388
L0 board 491
L0 board 269
L0 board 383
L0 board 503

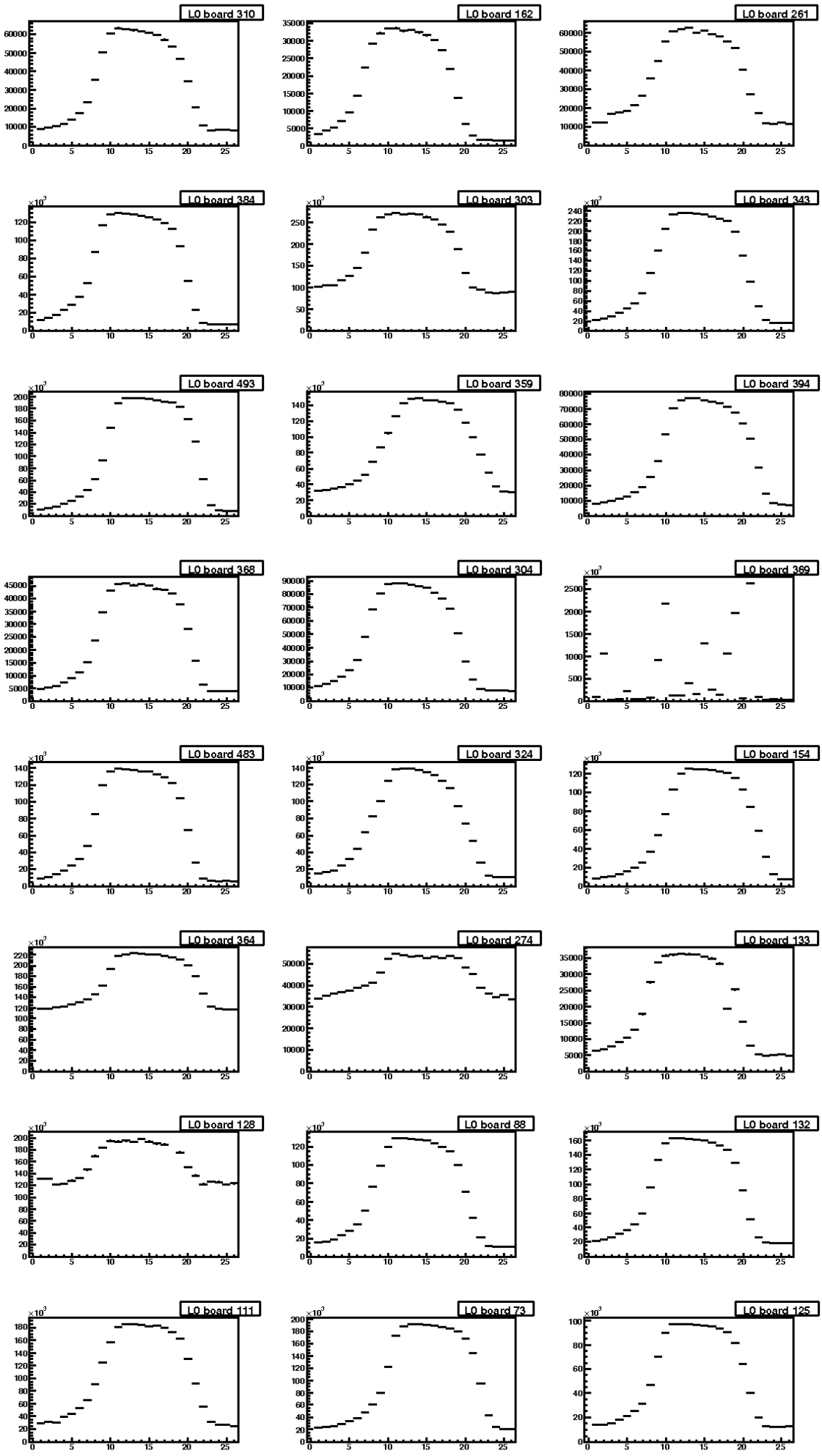
L0 board 310
L0 board 162
L0 board 261
L0 board 384
L0 board 303
L0 board 343
L0 board 493
L0 board 359
L0 board 394
L0 board 368
L0 board 304
L0 board 369
L0 board 483
L0 board 324
L0 board 154
L0 board 364
L0 board 274
L0 board 133
L0 board 128
L0 board 88
L0 board 132
L0 board 111
L0 board 73
L0 board 125

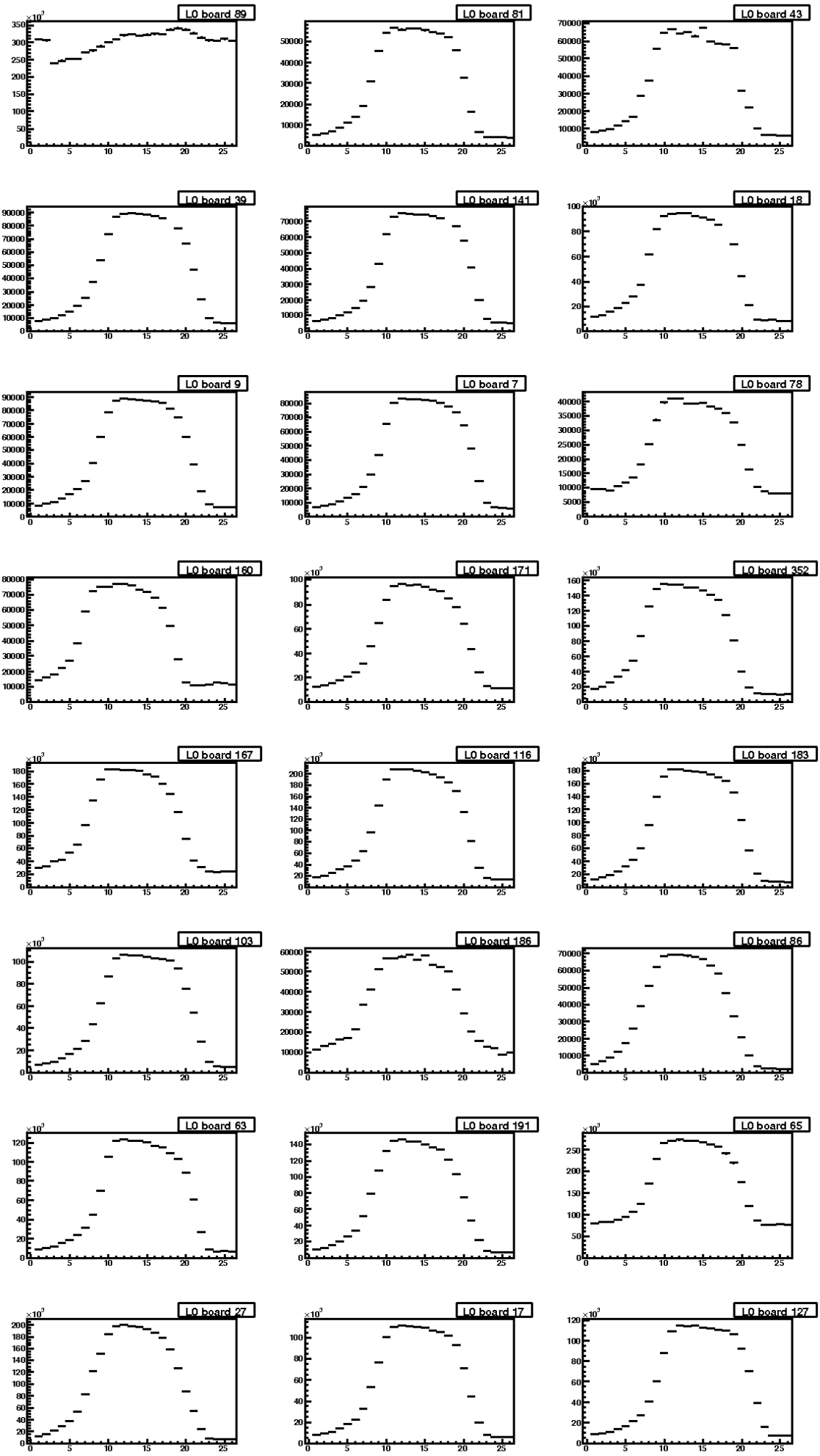
L0 board 89
L0 board 81
L0 board 43
L0 board 39
L0 board 141
L0 board 18
L0 board 9
L0 board 7
L0 board 78
L0 board 160
L0 board 171
L0 board 352
L0 board 167
L0 board 116
L0 board 183
L0 board 103
L0 board 186
L0 board 86
L0 board 63
L0 board 191
L0 board 65
L0 board 27
L0 board 17
L0 board 127

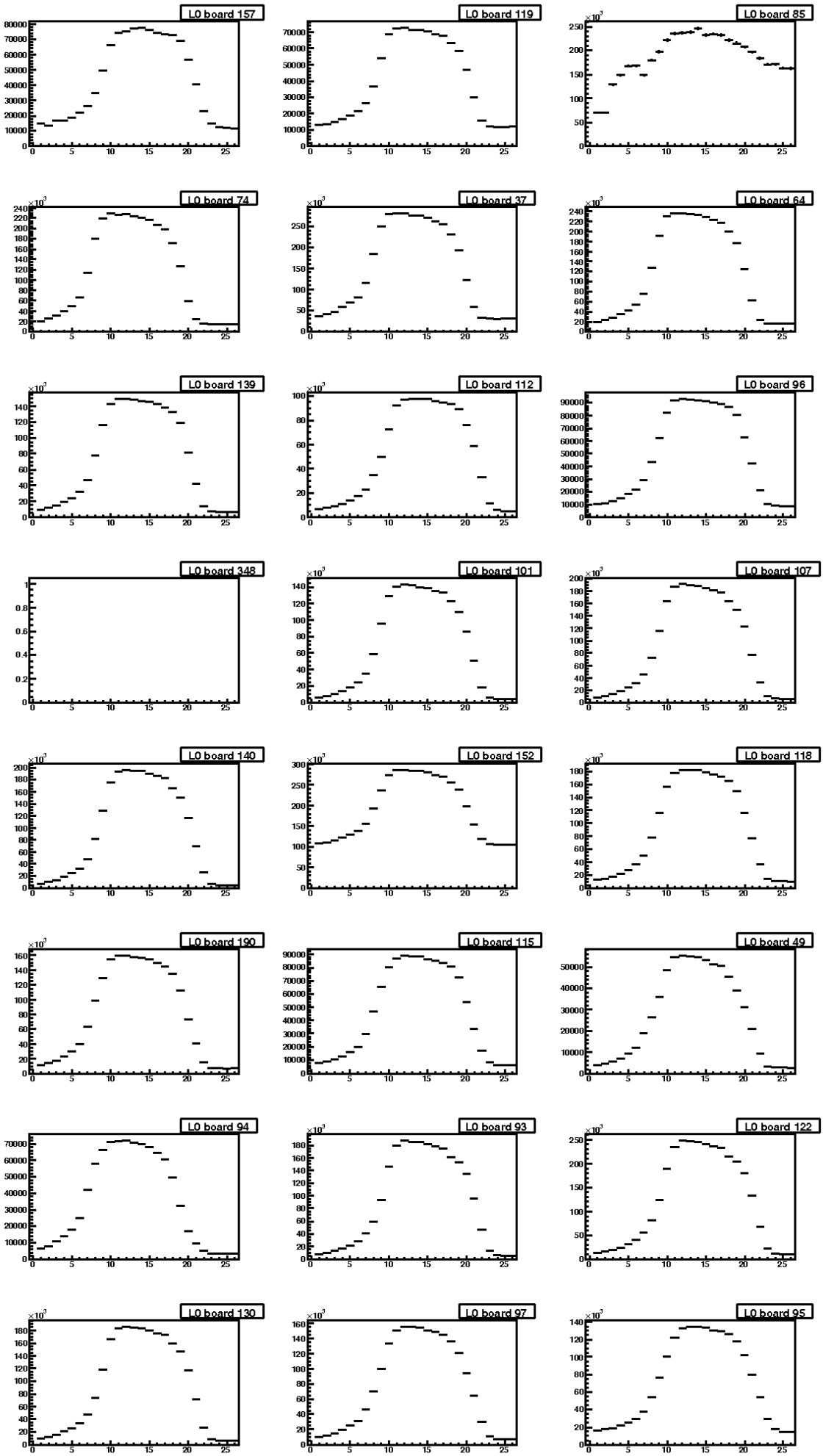
L0 board 157
L0 board 119
L0 board 85
L0 board 74
L0 board 37
L0 board 64
L0 board 139
L0 board 112
L0 board 96
L0 board 348
L0 board 101
L0 board 107
L0 board 140
L0 board 152
L0 board 118
L0 board 190
L0 board 115
L0 board 49
L0 board 94
L0 board 93
L0 board 122
L0 board 130
L0 board 97
L0 board 95

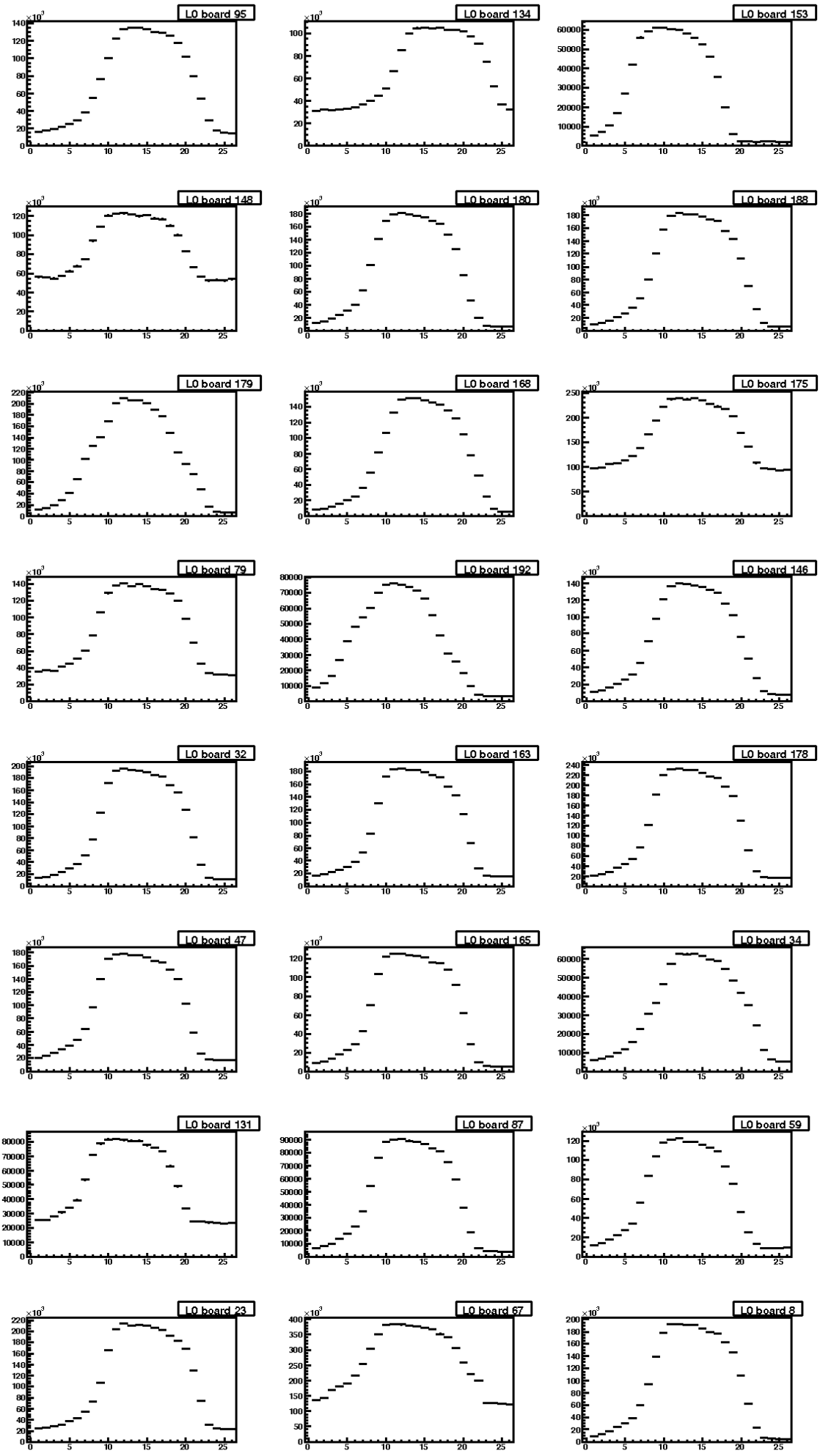
L0 board 95
L0 board 134
L0 board 153
L0 board 148
L0 board 180
L0 board 188
L0 board 179
L0 board 168
L0 board 175
L0 board 79
L0 board 192
L0 board 146
L0 board 32
L0 board 163
L0 board 178
L0 board 47
L0 board 165
L0 board 34
L0 board 131
L0 board 87
L0 board 59
L0 board 23
L0 board 67
L0 board 8

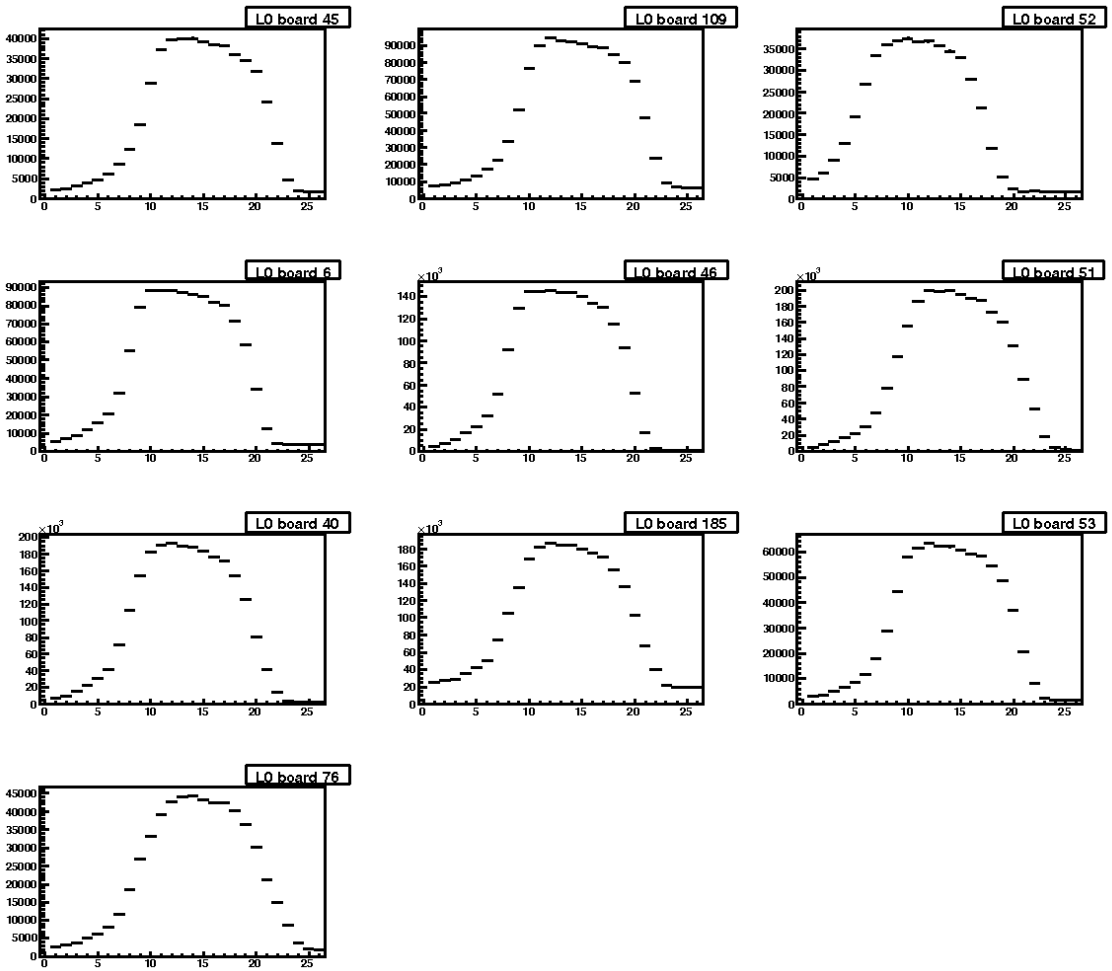


## RICH1

*N.B. The scans for the two RICH detectors used different time steps (The timing steps in the RICH2 scans are 2 ns, compared to 1 ns for RICH1) and different numbers of triggers per step (10k for RICH2 and 100k for RICH1).*

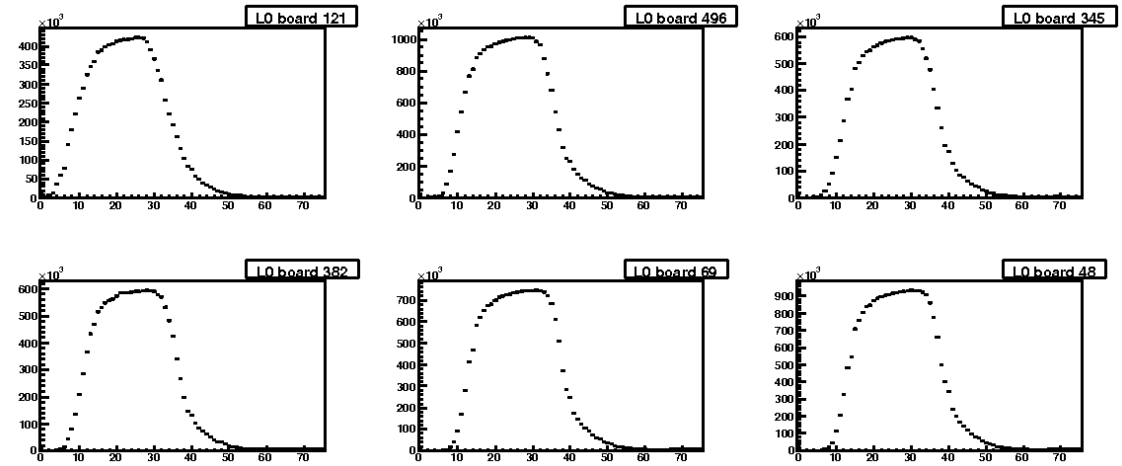

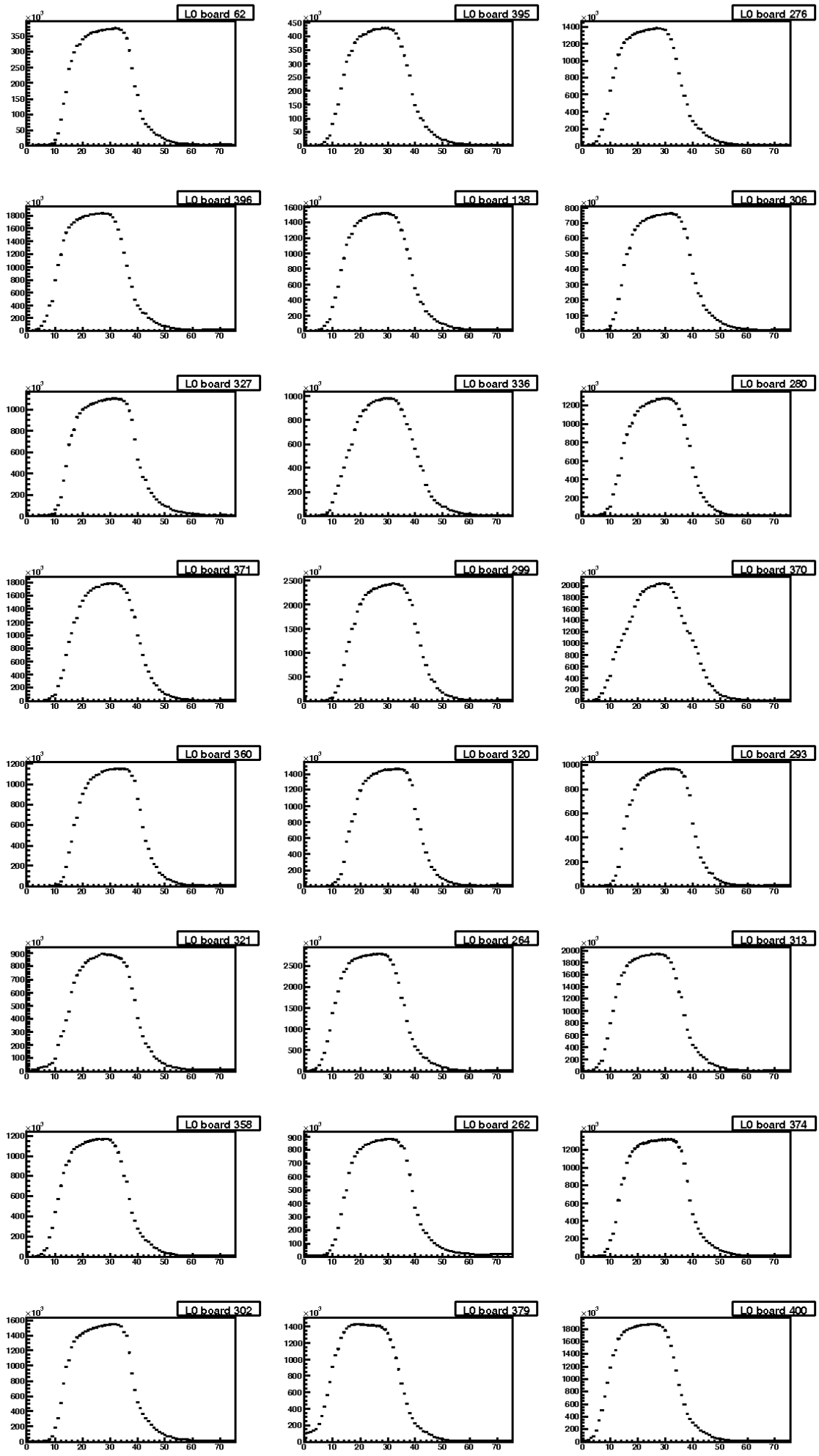
L0 board 62
L0 board 395
L0 board 276
L0 board 396
L0 board 138
L0 board 306
L0 board 327
L0 board 336
L0 board 280
L0 board 371
L0 board 299
L0 board 370
L0 board 360
L0 board 320
L0 board 293
L0 board 321
L0 board 264
L0 board 313
L0 board 358
L0 board 262
L0 board 374
L0 board 302
L0 board 379
L0 board 400

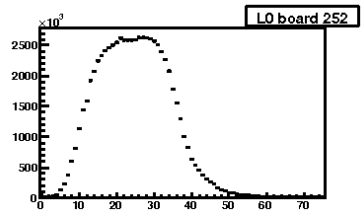
L0 board 252

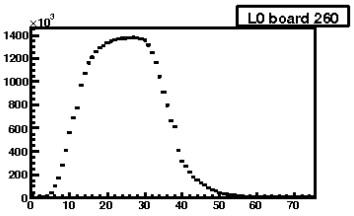
L0 board 260

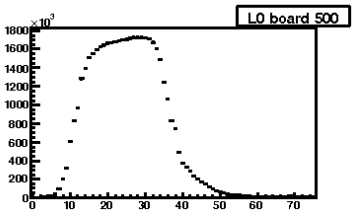
L0 board 500

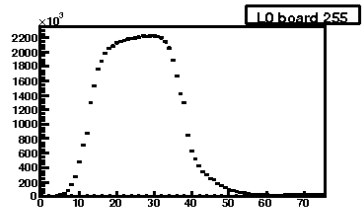
L0 board 255

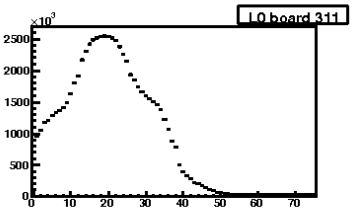
L0 board 311

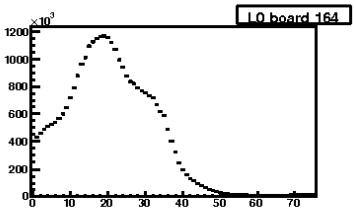
L0 board 164

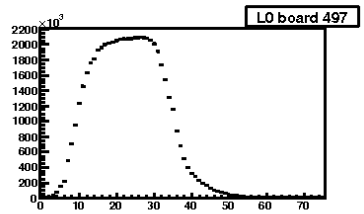
L0 board 497

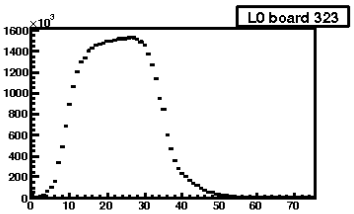
L0 board 323

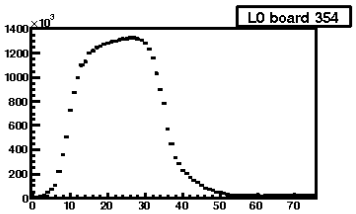
L0 board 354

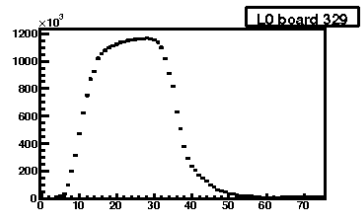
L0 board 329

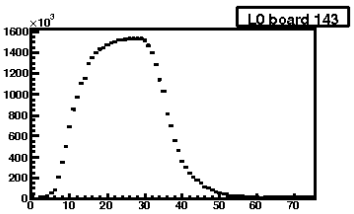
L0 board 143

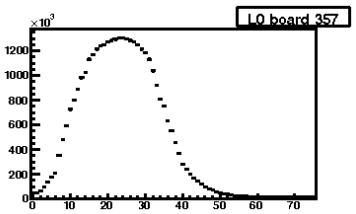
L0 board 357

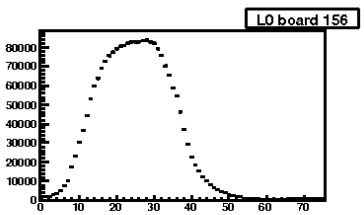
L0 board 156

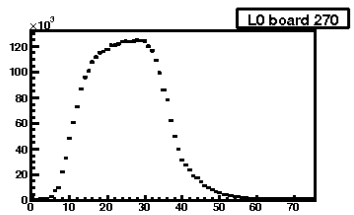
L0 board 270

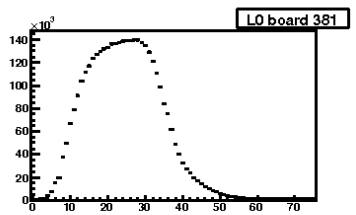
L0 board 381

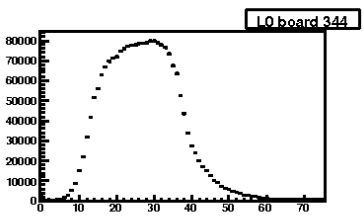
L0 board 344

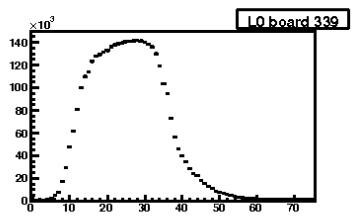
L0 board 339

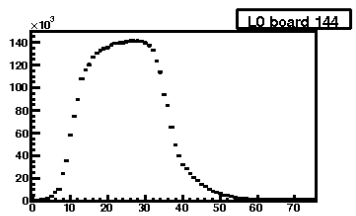
L0 board 144

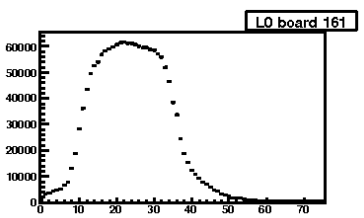
L0 board 161

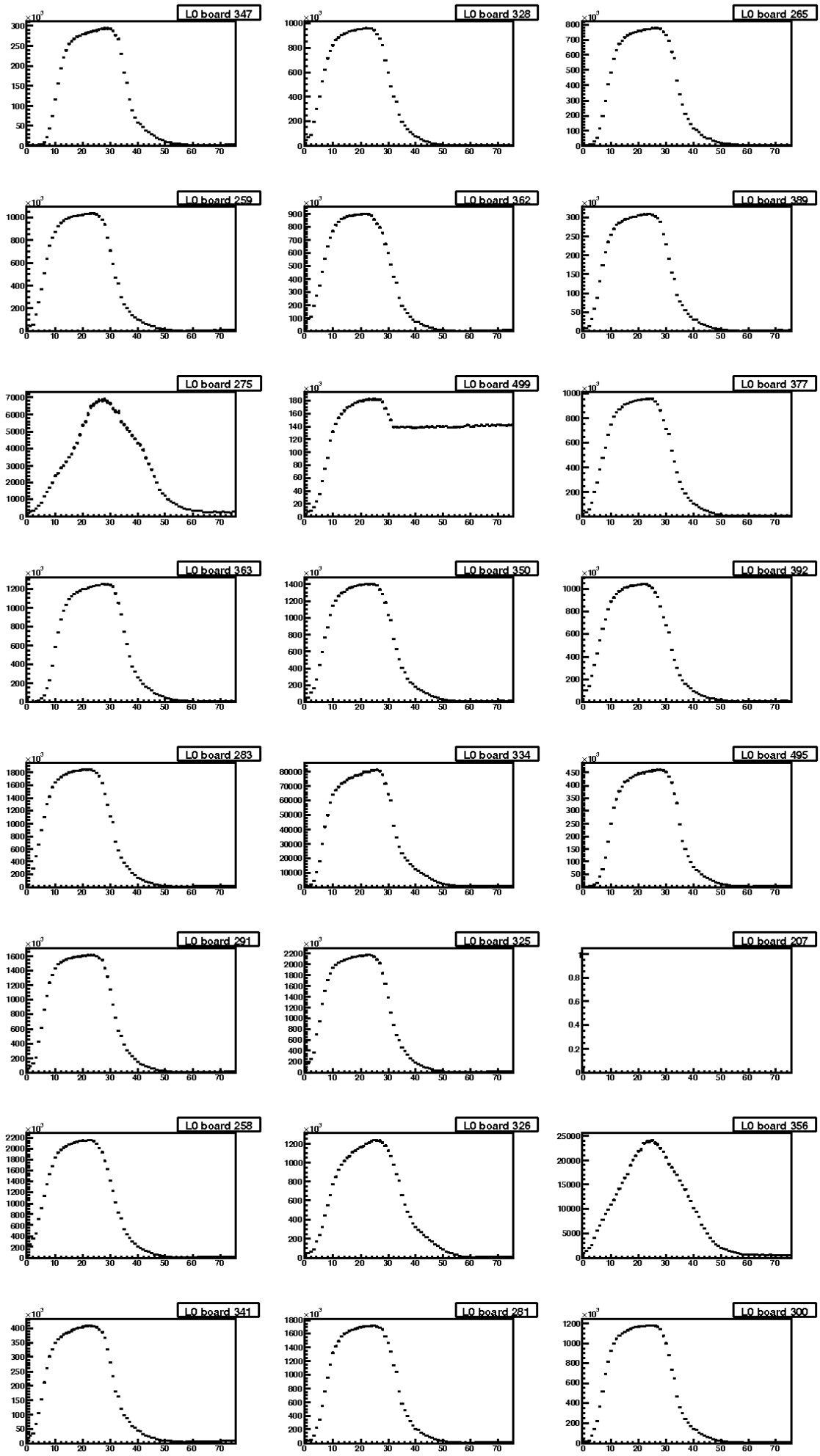
L0 board 347
L0 board 328
L0 board 265
L0 board 259
L0 board 362
L0 board 389
L0 board 275
L0 board 499
L0 board 377
L0 board 363
L0 board 350
L0 board 392
L0 board 283
L0 board 334
L0 board 495
L0 board 291
L0 board 325
L0 board 207
L0 board 258
L0 board 326
L0 board 356
L0 board 341
L0 board 281
L0 board 300

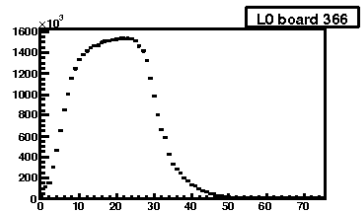
L0 board 366

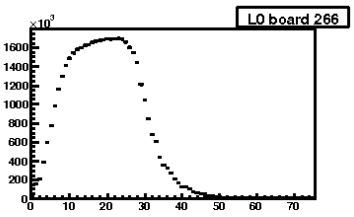
L0 board 266

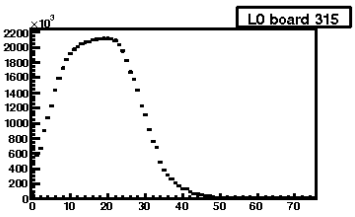
L0 board 315

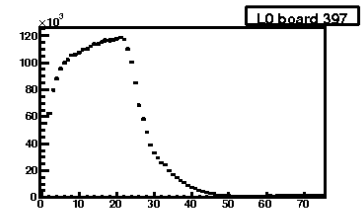
L0 board 397

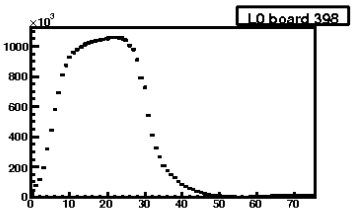
L0 board 398

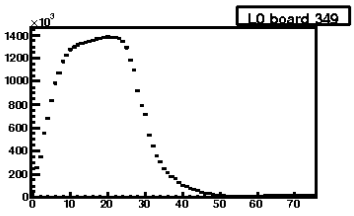
L0 board 349

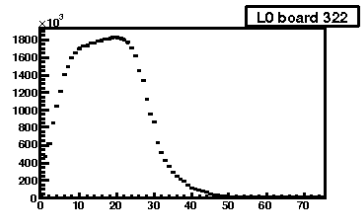
L0 board 322

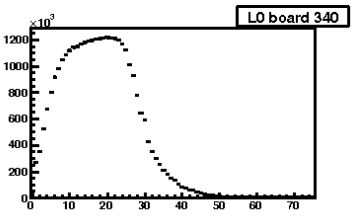
L0 board 340

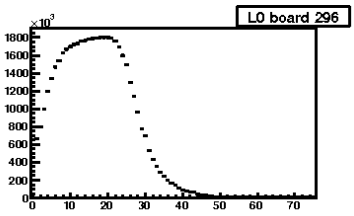
L0 board 296

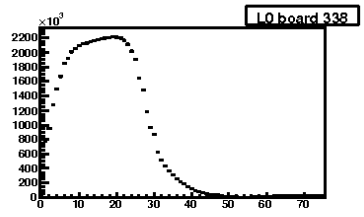
L0 board 338

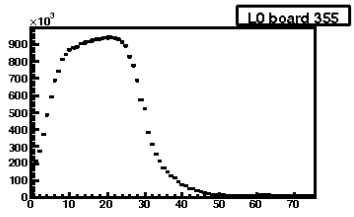
L0 board 355

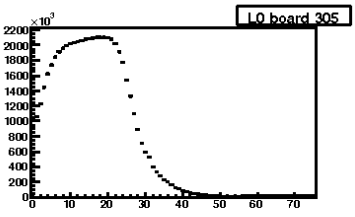
L0 board 305

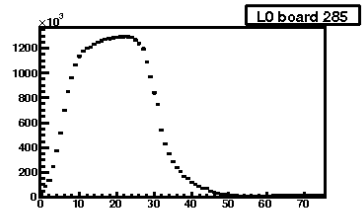
L0 board 285

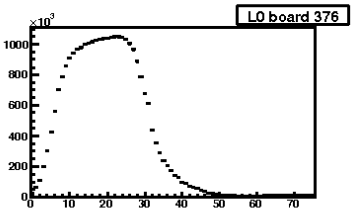
L0 board 376

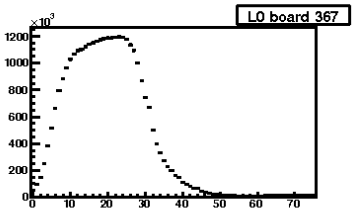
L0 board 367

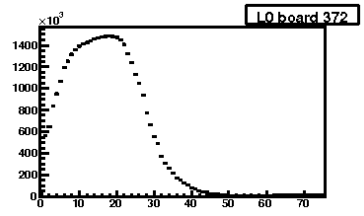
L0 board 372

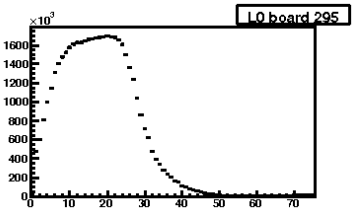
L0 board 295

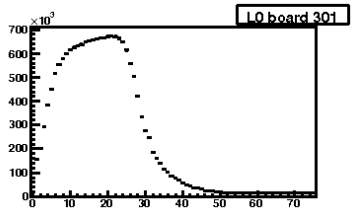
L0 board 301

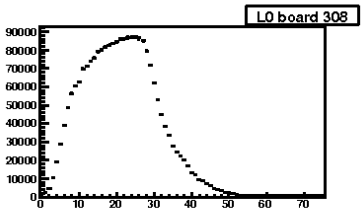
L0 board 308

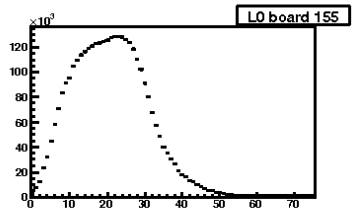
L0 board 155

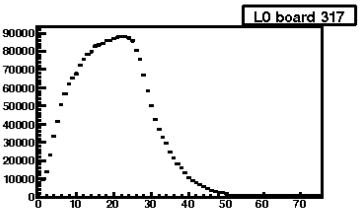
L0 board 317

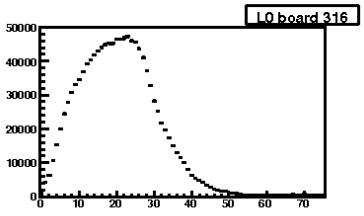
L0 board 316

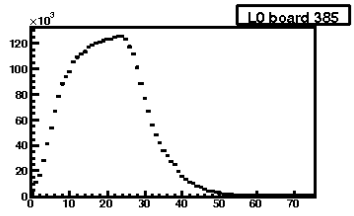
L0 board 385

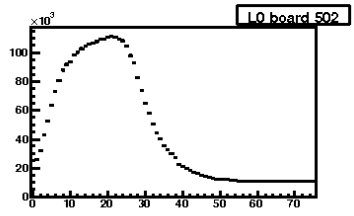
L0 board 502

# Bibliography


[1] L. Susskind. The gauge hierarchy problem, technicolor, supersymmetry and all that. In *Proceedings from the SLAC Summer Institute on Particle Physics: Physics at Very High Energies*, pages 197–209, 1982.

[2] G. Steigman. Observational tests of antimatter cosmologies. *Annual Review of Astronomy and Astrophysics*, 14:339–372, 1976.

[3] F. D. Steffen. Dark matter candidates - axions, neutralinos, gravitinos, and axinos. *The European Physics Journal C*, 59(2):557–588, 2009.

[4] C. S. Wu, E. Ambler, R. W. Hayward, D. D. Hoppes, and R.P. Hudson. Experimental test of parity conservation in beta decay. *Physical Review*, 105(4):1413–1415, 1957.

[5] J. Christenson, J. W. Cronin, V. L. Fitch, and R. Turlay. Evidence for the $2\pi$ decay of the $K_2^0$ meson. *Physical Review Letters*, 13(4):138–140, 1964.

[6] A. D. Sakharov. Violation of CP invariance, C asymmetry, and baryon asymmetry of the universe. *Journal of Experimental and Theoretical Physics Letters*, 5:24–27, 1967.

[7] M.B. Gavela, P. Hernández, J. Orloff, and O. Pène. Standard model CP-violation and baryon asymmetry. *Nuclear Physics B*, 430, 1994.

[8] H. Burkhardt et al (The NA31 Collaboration). The beam and detector for a high-precision measurement of cp violation in neutral-kaon decays. *Nuclear Instruments and Methods A*, 268:16–143, 1988.

[9] M. Jeitler for the NA48 Collaboration. The performance of the NA48 detector. *Nuclear Instruments and Methods A*, 478:404–410, 2002.

[10] A. Alavi-Harati et al (The KTeV Collaboration). Measurements of direct CP violation, CPT symmetry, and other parameters in the neutral kaon system. *Physical Review D*, 67, 2002.

[11] B. Aubert et al (The BaBar Collaboration). The BaBar detector. *Nuclear Instruments and Methods A*, 479:1–116, 2002.

[12] A. Abashian et al (The Belle Collaboration). The Belle detector. *Nuclear Instruments and Methods A*, 479:117–232, 2002.

[13] F. Abe et al (The CDF Collaboration). The CDF detector: An overview. *Nuclear Instruments and Methods A*, 271(3):387–403, 1988.

[14] V. M. Abazov et al (The D0 Collaboration). The upgraded D0 detector. *Nuclear Instruments and Methods A*, 565:463–537, 2006.

[15] B. Aubert et al (The BaBar Collaboration). Direct CP violating asymmetry in $B^0 \to K^+\pi^-$ decays. *Physical Review Letters*, 93(13), 2004.

[16] Y. Chao et al (The Belle Collaboration). Evidence for direct CP violation in $B^0 \to K^+\pi^-$ decays. *Physical Review Letters*, 93(19), 2004.

[17] B. Aubert et al (The BaBar Collaboration). Observation of CP violation in the $B^0$ meson system. *Physical Review Letters*, 87(9), 2001.

[18] K. Abe et al (The Belle Collaboration). Observation of large CP violation in the neutral B meson system. *Physical Review Letters*, 87(9), 2001.

[19] A. Abulencia et al (The CDF Collaboration). Observation of $B_s^0 - \overline{B}_s^0$ oscillation. *Physical Review Letters*, 97(24), 2006.

[20] M. Rescigno et al. First evidence for $B_s^0 \to \phi\phi$ and penguin B decays at CDF. In *Proceedings of the 32nd International Conference on High Energy Physics*, pages 1113–1117. World Scientific, 2004.

[21] O. W. Greenberg. Spin and unitary-spin independence in a paraquark model of baryons and mesons. *Physical Review Letters*, 13(20):598–602, 1964.

[22] D. Miller. An introduction to QED and QCD, 2006. Proceedings of the School for Experimental High Energy for Physics Students, CCLRC.

[23] S. Bethke. Experimental tests of asymptotic freedom. *Progress in Particle and Nuclear Physics*, 58:351–386, 2007.

[24] D. J. Gross and F. Wilczek. Ultraviolet behaviour of non-abelian gauge theories. *Physical Review Letters*, 30(26):1343–1346, 1973.

[25] H. D. Politzer. Reliable peturbative results for strong interactions? *Physical Review Letters*, 30(26):1346–1349, 1973.

[26] P. Renton. *Electroweak Interactions*. Cambridge University Press, 1990.

[27] S. Davidson. The standard model, 2006. Proceedings of the School for Experimental High Energy for Physics Students, CCLRC.

[28] C. Amsler et al (Particle Data Group). The review of particle physics. *Physics Letters B*, 667(1), 2008.

[29] P. W. Higgs. Broken symmetries and the masses of gauge bosons. *Physical Review Letters*, 13(16):508–509, 1964.

[30] N. Cabibbo. Unitary symmetry and leptonic decays. *Physical Review Letters*, 10(12):531–533, 1963.

[31] S. L. Glashow, J. Iliopoulos, and L. Maiani. Weak interactions with lepton-hadron symmetry. *Physical Review D*, 2(7):1285–1292, 1970.

[32] M. K. Gaillard and B. W. Lee. Rare decay modes of the K mesons in gauge theories. *Physical Review D*, 10(3):897–916, 1974.

[33] M. Kobayashi and T. Maskawa. CP-violation in the renormalizable theory of weak interaction. *Progress of Theoretical Physics*, 49(2):652–657, 1973.

[34] L. Wolfenstein. Parameterization of the Kobayashi-Maskawa matrix. *Physical Review Letters*, 51(21):1945–1947, 1983.

[35] S. Amato et al (The LHCb Collaboration). *LHCb Technical Proposal*. CERN, 1998. CERN LHCC 98-004.

[36] The CKM fitter group. *http://ckmfitter.in2p3.fr*.

[37] The UTfit group. *http://www.utfit.org*.

[38] E. Barbiero et al (The Heavy Flavour Averaging Group). Averages of b-hadron and c-hadron properties at the end of 2007, 2008. arXiv:hep-ex/0808.1297v3.

[39] B. Aubert et al (The BaBar Collaboration). Dalitz plot analysis of the decays $B^{\pm} \to K^{\pm}\pi^{+}\pi^{-}$. *Physical Review D*, 72, 2005.

[40] A. Garmash et al (The BELLE Collaboration). Evidence for large direct CP violation in $B^{\pm} \to \rho(770)^{0}K^{\pm}$ from analysis of three-body charmless $B^{\pm} \to K^{\pm}\pi^{+}\pi^{-}$ decays. *Physical Review Letters*, 96, 2006.

[41] G. C. Branco, L. Lavoura, and J. P. Silva. *CP Violation*. Oxford Science Publications, 1999.

[42] A. Masiero and O. Vives. CP violation in physics beyond the standard model. In *CP Violation: from Quarks to Leptons*, pages 133–173. International School of Physics Enrico Fermi, IOS Press, 2005.

[43] D. Wu. A brief introduction to the strong CP problem, 1991. SSCL-548.

[44] S. P. Martin. A supersymmetry primer, 2008. arXiv:hep-ph/9709356v5.

[45] S. Dimopoulos, S. Raby, and F. Wilczek. Supersymmetry and the scale of unification. *Physical Review D*, 24(6):1681–1683, 1981.

[46] G. Isidori. Kaon decays and the flavour problem. *Annales Henri Poincare*, 4(1):97–109, 2003.

[47] G. D'Ambrosio, G. F. Giudice, G. Isidori, and A. Strumia. Minimal flavour violation: An effective field theory approach. *Nuclear Physics B*, 645:155–187, 2002.

[48] J. Hewett et al. *The Discovery potential of a super B factory.* SLAC, 2004. SLAC-R-709.

[49] A. Martin. Technicolor signals at the LHC, 2008. arXiv:hep-ph/0812.1841v2.

[50] P.R. Barbosa Marinho et al (The LHCb Collaboration). *LHCb Vertex Locator Technical Design Report.* CERN, 2001. CERN LHCC 2001-0011.

[51] A. Augusto Alves Jr et al (The LHCb Collaboration). The LHCb detector at the LHC. *Journal of Instrumentation*, 3, 2008.

[52] M. Ferro-Luzzi, N. Van Bakel, and J. F. J. Van den Brand. A first study of wake fields in the LHCb vertex detector, 2000. CERN-LHCb-99-041.

[53] R. Antunes Nobrega et al (The LHCb Collaboration). *LHCb Reoptimised Detector Design and Performance Technical Design Report.* CERN, 2003. CERN LHCC 2003-064.

[54] P. A. Cherenkov. Visible radiation produced by electrons moving in a medium with velocities exceeding that of light. *Physical Review Letters*, 52:378–340, 1937.

[55] S. Amato et al (The LHCb Collaboration). *LHCb Magnet Technical Design Report.* CERN, 2000. CERN LHCC 2000-007.

[56] A. Franca Barbosa et al (The LHCb Collaboration). *LHCb Inner Tracker Technical Design Report.* CERN, 2002. CERN LHCC 2002-029.

[57] P. R. Barbosa et al (The LHCb Collaboration). *LHCb Outer Tracker Technical Design Report.* CERN, 2001. CERN LHCC 2001-024.

[58] S. Amato et al (The LHCb Collaboration). *LHCb Calorimeters Technical Design Report.* CERN, 2000. CERN LHCC 2000-036.

[59] P. R. Barbosa Marinho et al (The LHCb Collaboration). *LHCb Muon System Technical Design Report.* CERN, 2001. CERN LHCC 2001-010.

[60] P. R. Barbosa Marinho et al (The LHCb Collaboration). *LHCb Addendum to the Muon System Technical Design Report.* CERN, 2003. CERN LHCC 2003-002.

[61] P. R. Barbosa Marinho et al (The LHCb Collaboration). *LHCb Second Addendum to the Muon System Technical Design Report.* CERN, 2005. CERN LHCC 2005-012.

[62] R. Antunes Nobrega et al (The LHCb Collaboration). *LHCb Trigger System Technical Design Report.* CERN, 2003. CERN LHCC 2003-031.

[63] G. Aad et al (The ATLAS Collaboration). The ATLAS experiment at the CERN large hadron collider. *Journal of Instrumentation*, 3, 2008.

[64] O. Adriani et al (The LHCf Collaboration). The LHCf detector at the CERN large hadron collider. *Journal of Instrumentation*, 3, 2008.

[65] S. Chatrchyan et al (The CMS Collaboration). The CMS experiment at the CERN LHC. *Journal of Instrumentation*, 3, 2008.

[66] G. Anelli et al (The TOTEM Collaboration). The TOTEM experiment at the CERN large hadron collider. *Journal of Instrumentation*, 3, 2008.

[67] K. Aamodt et al (The ALICE Collaboration). The ALICE experiment at the CERN LHC. *Journal of Instrumentation*, 3, 2008.

[68] R. Driggers. *Encyclopedia of Optical Engineering.* CRC Press, 2003.

[69] S. Amato et al. *LHCb RICH Technical Design Report.* CERN, 2000. CERN LHCC 2000-037.

[70] K. Wyllie, G. Aglieri Rinella, M. Campbell, M. Castro Carballo, T. Gys, S. Jolly, M. Moritz, C. Newby, D. Piedigrossi, and L. Somerville. Silicon detectors and electronics for pixel hybrid photon detectors. *Nuclear Instruments ad Methods A*, 530:82–86, 2004.

[71] M. Campbell, G. Aglieri-Rinella, G. Arnau-Izquierdo, T. Gys, N. Kanaya, C. Newby, D. Piedigrossi, P. Riedler, J. Salmi, J. Salonen, S. Savolainen-Pulli, L. Somervile, I. Suni, S. Vahanen, and K. Wyllie. A fine pitch bump bonding process compatible with the manufacture of the Pixel-HPDs for the LHCb RICH detector. *IEEE Transaction on Nuclear Science*, 53(2):657–661, 2006.

[72] K. Wyllie, M. Campbell, T. Gys, C. Newby, D. Piedigrossi, and L. Somerville. Readout of the LHCb pixel hybrid photon detectors. In *Proceedings of the 6th International Workshop on Radiation Imaging Detectors*, pages 86–92. Nuclear Instruments and Methods A, 2004.

[73] PHOTONIS Netherlands B.V., Dwazziewegen 2, 9301 ZR Roden, The Netherlands.

[74] J. McCarron. *Characterisation of Hybrid Photon Detectors for the LHCb and an analysis of the rare decay* $B_s^0 \to \phi\phi$. PhD thesis, The University of Edinburgh, 2007.

[75] R. Lambert. Quantum efficiency of Hybrid Photon Detectors for the LHCb RICH. In *Astroparticle, Particle And Space Physics, Detectors And Medical Physics Applications: Proceedings of the 10th Conference*, pages 85–89. World Scientific, 2008.

[76] L. Carson. Hybrid photon detectors for the LHCb RICH: Performance and operational experience. In *Proceedings of the 8th International Conference on Position Sensitive Detectors*, pages 202–206. Nuclear Instruments and Methods A, 2009.

[77] R. Lambert. *LHCb Hybrid Photon Detectors and Sensitivity to Flavour Specific Asymmetry in Neutral B-Meson Mixing.* PhD thesis, The University of Edinburgh, 2008.

[78] S. Eisenhardt. Production and tests of hybrid photon detectors for the LHCb RICH detectors. In *Proceedings of the Sixth International Workshop on Ring Imaging Cherenkov Detectors*, pages 142–145. Nuclear Instruments and Methods A, 2008.

[79] M. Adinolfi, J.H. Bibby, S. Brisbane, V. Gibson, N. Harnew, M. Jones, J. Libby, A. Powell, C. Newby, N. Rotolo, N. Smale, L. Somerville, P. Sullivan, S. Topp-Jorgensen, S. Wotton, and K. Wyllie. The front-end (Level-0) electronics interface module for the LHCb RICH detectors. *Nuclear Instruments and Methods A*, 572(2):689–697, 2007.

[80] S. Eisenhardt. Private communications.

[81] R. Antunes Nobrega et al (The LHCb Collaboration). *LHCb Computing Technical Design Report.* CERN, 2005. CERN LHCC 2005-019.

[82] J. Bibby, M. Sannino, S. Wotton, and K. Wyllie. The readout electronics of the LHCb RICH detector, 2004. CERN EDMS 492255.

[83] B. Gaidioz, A. Barczyk, N. Neufeld, and B. Jost. High performance event-building in linux for LHCb. *IEEE Transactions on Nuclear Science*, 53(3):898–906, 2006.

[84] Z. Guzik and R. Jacobsson. LHCb readout supervisor 'ODIN' with a L1 trigger, 2005. CERN EDMS 704078.

[85] The GEANT4 Collaboration. GEANT4 - a simulation toolkit. *Nuclear Instruments and Methods A*, 506(3):250–303, 2003.

[86] M. Adinolfi, E. Albrecht, C. D'Ambrosio, T. Gys, J. Morant, D. Piedigrossi, M. Patel, K. Wyllie, M. Ameri, F. Fontanelli, G. Mini, M. Sannino, C. Arnaboldi, T. F. Bellunato, E. Fanchini, D. L. Perego, G. Pessina, C. Barham, C. Buszello, J. Dickens, V. Gibson, C. Jones, U. Kerzel, G. Rogers, H. Skottowe, S. Wotton, T. Blake, C. Eames, R. Plackett, S. Brisbane, N. Harnew, J. Libby, A. Powell, P. Sullivan, S. Topp-Jorgensen, S. Easo, A. Papanestis, Z. Zhang, S. Eisenhardt, F. Muheim, and N. Styles. Performance of the LHCb RICH photodetectors and readout in a system test using charged particles from a 25ns-structured beam. *Nuclear Instruments and Methods A*, 603(3):289–293, 2009.

[87] S. Schmeling. Common tools for large experiment controls a common approach for deployment, maintenance, and support. *IEEE Transaction on Nuclear Science*, 53(3), 2006.

[88] I. Dunietz, H. Quinn, A. Snyder, and W. Toki. How to extract CP-violating asymmetries from angular correlations. *Physical Review D*, 43:2193–2208, 1991.

[89] K. Abe, M. Satpathy, and H. Yamamoto. Time-dependent angular analyses of B decays, 2001. arXiv:hep-ex/0103002v1.

[90] D. London, N. Sinha, and R. Sinha. Probing new physics via an angular analysis of $B \to V_1 V_2$ decays. *Europhysics Letters*, 67(4):579–585, 2004.

[91] R. Nandakumar, S. G. Jimenez, M. Adinolfi, R. Bernet, J. Blouw, D. Bortolotti, A. Carbone, B. M'Charek, D. L. Perego, A. Pickford, C. Potterat, M. S. Miguelez, M. Bargiotti, N. Brook, A. Casajus, G. Castellani, P. Charpentier, C. Cioffi, J. Closier R. Graciani Diaz, G. Kuznetsov, S. Paterson, R. Santinelli, A. C. Smith, and A. Tsaregorotsev. The LHCb computing data challenge DC06. In *Proceedings of the International Conference on Computing in High Energy and Nuclear Physics (CHEP '07)*, volume 119. Journal of Physics: Conference Series, 2008.

[92] D. J. Lange. The EvtGen particle decay simulation package. In *Proceedings of the 7th International Conference on B-physics at Hadron Machines*, pages 152–155. Nuclear Instruments and Methods A, 2001.

[93] The RooFit Toolkit for data modeling. *http://roofit.sourceforge.net*.

[94] M. Calvi, O. Leroy, and M. Musy. Flavour tagging algorithms and performances in LHCb, 2007. CERN-LHCb-2007-058.

[95] Dominik Horn. Study of $B_s^0 \to D_s^{+(*)} D_s^{-(*)}$ and $B_s^0 \to \phi\phi$ decays at CDF II, 2009. Presented at the 2009 Europhysics Conference on High Energy Physics.

[96] M. Beneke, J. Rohrer, and D. Yang. Branching fractions, polarisation and asymmetries of $B \to VV$ decays. *Nuclear Physics B*, 774:64–101, 2007.